

APPENDIX E NFCSC DOCUMENT COVER SHEET¹

Name/Title of Deliverable/Milestone/Revision No. Preliminary Analysis of Postclosure DPC Criticality Consequences

Work Package Title and Number Probabilistic Postclosure DPC Criticality Consequence Analyses, SF-20SN01030506

Work Package WBS Number M2SF-20SN010305061

Responsible Work Package Manager Laura Price *Laura Price*
(Name/Signature)

Date Submitted December 20, 2019

Quality Rigor Level for Deliverable/Milestone ²	<input type="checkbox"/> QRL-1 <input type="checkbox"/> Nuclear Data	<input type="checkbox"/> QRL-2	<input checked="" type="checkbox"/> QRL-3	<input type="checkbox"/> QRL-4 Lab QA Program ³
--	---	--------------------------------	---	---

This deliverable was prepared in accordance with Sandia National Laboratories
(Participant/National Laboratory Name)

QA program which meets the requirements of
 DOE Order 414.1 NQA-1 Other

This Deliverable was subjected to:

Technical Review

Peer Review

Technical Review (TR)

Peer Review (PR)

Review Documentation Provided

Review Documentation Provided

- Signed TR Report or,
- Signed TR Concurrence Sheet or,
- Signature of TR Reviewer(s) below

- Signed PR Report or,
- Signed PR Concurrence Sheet or,
- Signature of PR Reviewer(s) below

Name and Signature of Reviewers

Hecho Park

Hecho Park

NOTE 1: Appendix E should be filled out and submitted with the deliverable. Or, if the PICS:NE system permits, completely enter all applicable information in the PICS:NE Deliverable Form. The requirement is to ensure that all applicable information is entered either in the PICS:NE system or by using the NFCSC Document Cover Sheet.

- In some cases there may be a milestone where an item is being fabricated, maintenance is being performed on a facility, or a document is being issued through a formal document control process where it specifically calls out a formal review of the document. In these cases, documentation (e.g., inspection report, maintenance request, work planning package documentation or the documented review of the issued document through the document control process) of the completion of the activity, along with the Document Cover Sheet, is sufficient to demonstrate achieving the milestone.

NOTE 2: If QRL 1, 2, or 3 is not assigned, then the QRL 4 box must be checked, and the work is understood to be performed using laboratory QA requirements. This includes any deliverable developed in conformance with the respective National Laboratory / Participant, DOE or NNSA-approved QA Program.

NOTE 3: If the lab has an NQA-1 program and the work to be conducted requires an NQA-1 program, then the QRL-1 box must be checked in the work Package and on the Appendix E cover sheet and the work must be performed in accordance with the Lab's NQA-1 program. The QRL-4 box should not be checked.

This page is intentionally left blank.

Preliminary Analysis of Postclosure DPC Criticality Consequences

Spent Fuel and Waste Disposition

***Prepared for
U.S. Department of Energy
Spent Fuel and Waste Science
and Technology***

***L.L. Price, A.A. Alsaed, A. Barela, P.V. Brady,
F. Gelbard, M.B. Gross, M. Nole, J.L. Prouty
Sandia National Laboratories***

***K. Banerjee, S. Bhatt, G.G. Davidson,
Z. Fang, R. Howard, S.R. Johnson,
S.L. Painter, and M. Swinney
Oak Ridge National Laboratory***

***E. Gonzalez
University of Michigan***

December 20, 2019

M2SF-20SN010305061

SAND2020-4106

CONTEXT FOR THIS STUDY

This is a technical paper that does not take into account contractual limitations or obligations under the Standard Contract for Disposal of Spent Nuclear Fuel and/or High-Level Radioactive Waste (Standard Contract) (10 CFR Part 961). For example, under the provisions of the Standard Contract, spent nuclear fuel in multi-assembly canisters is not an acceptable waste form, absent a mutually agreed to contract amendment.

To the extent discussions or recommendations in this paper conflict with the provisions of the Standard Contract, the Standard Contract governs the obligations of the parties, and this paper in no manner supersedes, overrides, or amends the Standard Contract.

This paper reflects technical work which could support future decision making by DOE. No inferences should be drawn from this paper regarding future actions by DOE, which are limited both by the terms of the Standard Contract and a lack of Congressional appropriations for the Department to fulfill its obligations under the Nuclear Waste Policy Act including licensing and construction of a spent nuclear fuel repository.

DISCLAIMER

This information was prepared as an account of work sponsored by an agency of the U.S. Government. Neither the U.S. Government nor any agency thereof, nor any of their employees, makes any warranty, expressed or implied, or assumes any legal liability or responsibility for the accuracy, completeness, or usefulness, of any information, apparatus, product, or process disclosed, or represents that its use would not infringe privately owned rights. References herein to any specific commercial product, process, or service by trade name, trade mark, manufacturer, or otherwise, does not necessarily constitute or imply its endorsement, recommendation, or favoring by the U.S. Government or any agency thereof. The views and opinions of authors expressed herein do not necessarily state or reflect those of the U.S. Government or any agency thereof.



Sandia National Laboratories

Sandia National Laboratories is a multimission laboratory managed and operated by National Technology and Engineering Solutions of Sandia LLC, a wholly owned subsidiary of Honeywell International Inc. for the U.S. Department of Energy's National Nuclear Security Administration under contract DE-NA0003525. Approved for Unclassified, Unlimited Release.

SUMMARY

One of the objectives of the United States (U.S.) Department of Energy's (DOE) Office of Nuclear Energy's Spent Fuel and Waste Science and Technology Campaign is to better understand the technical basis, risks, and uncertainty associated with the safe and secure disposition of spent nuclear fuel (SNF) and high-level radioactive waste. Commercial nuclear power generation in the U.S. has generated thousands of metric tons of SNF, the disposal of which is the responsibility of the DOE (Nuclear Waste Policy Act 1982). Any repository licensed to dispose the SNF must meet requirements regarding the long-term performance of that repository. For an evaluation of the long-term performance of the repository, one of the events that may need to be considered is the SNF achieving a critical configuration. Of particular interest is the potential behavior of SNF in dual-purpose canisters (DPCs), which are currently being used to store and transport SNF but were not designed for permanent geologic disposal.

A two-phase study has been initiated to begin examining the potential consequences, with respect to long-term repository performance, of criticality events that might occur during the postclosure period in a hypothetical repository containing DPCs. Phase I, a scoping phase, consisted of generating an approach intended to be a starting point for the development of the modeling tools and techniques that may eventually be required either to exclude criticality from or to include criticality in a performance assessment (PA) as appropriate; Phase I is documented in Price et al. (2019). The Phase I approach guided the analyses and simulations done in Phase II to further the development of these modeling tools and techniques as well as the overall knowledge base. The purpose of this report is to document the results of the analyses conducted during Phase II.

New modeling capability that has been developed thus far includes coupling Shift (a high-performance, Monte Carlo, neutronics solver) and COBRA-SFS (a subchannel, single-phase, thermal-hydraulics code) within the Terrenus framework and adding a submodule to PFLOTRAN (a three-dimensional [3D], multiphase, subsurface flow and radionuclide transport code) to model the additional heat and radionuclide inventory associated with a steady-state criticality event for a specified duration after repository closure. These new modeling capabilities represent significant progress toward being able to model the consequences of a postclosure criticality event on long-term repository performance.

Changes in the radionuclide inventory as a result of a 4 kW steady-state criticality event lasting from 9,000 to 19,000 years after closure in a hypothetical saturated shale repository were evaluated. Results of these analyses provide insight as to (1) which radionuclides not previously modeled in PA calculations might need to be considered if postclosure criticality is among the features, events, or processes (FEPs) included in a PA and (2) what the extent of inventory changes might be.

Several different thermal analyses were conducted to investigate the effects of heat produced by the steady-state criticality event on the waste package itself and on other waste packages. One conclusion from the analyses is that the power that can be generated by a 10,000-year criticality event in a breached waste package is much greater in a saturated environment than it is in an unsaturated environment. Accordingly, temperature increases in the hypothetical unsaturated repository are substantially less than those in the hypothetical saturated repository; inventory changes in the hypothetical unsaturated repository are also substantially less than those in the hypothetical saturated repository.

Even though the potential for criticality in a DPC cannot be completely ruled out, that potential can become very low because of the presence of absorbers, changes in geometry, and limited moderation. A preliminary investigation of in-package chemistry during a steady-state criticality event indicates that high temperatures, radiolysis, corrosion of stainless steel, and dissolution of SNF have competing effects on the pH inside the waste package and on radionuclide solubilities. Further study is needed to quantify these competing processes.

Several processes that could cause permanent criticality termination in disposed DPCs were also evaluated, including radioactive decay, additional burnup due to a steady-state postclosure criticality event, and changes in geometry due to grid spacer corrosion or collapse. These evaluations indicate that a theoretical steady-state criticality event could be sustained for hundreds of thousands of years for higher reactivity DPCs, assuming presence of moderation and no changes to fuel geometry configuration.

Base case and comparison simulations of radionuclide releases from a single waste package in a hypothetical saturated shale repository were performed with the new submodule developed in PFLOTRAN. The difference between the base case and comparison simulations is that the former does not include a steady-state criticality event while the latter does. A selected subset of ten radionuclides was chosen to evaluate the impact of a steady-state criticality event on the aqueous radionuclide concentrations in the shale surrounding the drift. In the comparison simulations, concentrations of the short-lived isotopes increase by several orders of magnitude relative to the base case until about a few thousand years after the criticality event ceases, depending on the half-life of the radionuclide. Concentrations of the longer-lived radionuclides increase over the course of a hundred thousand years, relative to the base case. The largest increases in concentrations (about an order of magnitude) occur for those radionuclides that exhibit the most retardation (i.e., have the highest distribution coefficient [K_d] values) in the backfill in the absence of a criticality event. For nonsorbing radionuclides, the increase in concentration is much smaller, only a few percent. Note that these concentrations are in the shale right next to the waste disposal drift, not in the far field where a potential exposure to a member of the public might occur at some time in the future. As such, it is not appropriate to use these near-field concentrations to estimate dose to a member of the public.

Further work was identified in the areas of (1) code development, including developing the technical bases for supporting this code development; (2) modeling a transient event; (3) investigating and parameterizing the cyclic nature of a “steady-state” criticality event; (4) evaluating the chemistry inside a DPC during a steady-state criticality event; (5) evaluating the geometry changes of the DPC baskets and fuel assemblies, and (6) developing an understanding of the processes that could permanently terminate a criticality event, in particular, cladding and grid spacer degradation.

ACKNOWLEDGEMENTS

This work was supported by the DOE Office of Nuclear Energy, through the Office of Spent Fuel and Waste Science and Technology.

The authors would like to thank Ernie Hardin from Sandia National Laboratories (SNL) for providing helpful technical input; Heeho Park for his thorough technical review; and Tim Gunter, Bob Clark, and Bill Spezialetti from the DOE for their suggestions and guidance.

This page is intentionally left blank.

CONTENTS

SUMMARY	v
ACKNOWLEDGEMENTS	vii
ACRONYMS	xvi
1. INTRODUCTION	1
1.1 Background	1
1.2 Objective	2
1.3 Scope	3
1.4 Assumptions	3
1.4.1 Assumption 1—A waste package has been breached and criticality occurs.	3
1.4.2 Assumption 2—Fuel assembly configurations remain intact, but cladding permits radionuclide transport.	4
1.4.3 Assumption 3—Postclosure performance requirements are similar to those for Yucca Mountain.	4
1.4.4 Assumption 4—Basket neutron absorbers are assumed to have degraded prior to the initiation of a criticality.	4
1.4.5 Assumption 5—The steady-state criticality event is not cyclic.	5
1.5 Approach	5
2. CRITICALITY ANALYSES DESCRIPTIONS	7
2.1 Neutronics	7
2.1.1 Methodology	8
2.1.2 Numerical Codes: Shift	11
2.1.3 Numerical Codes: COBRA-SFS	12
2.1.4 Assumptions	12
2.1.5 Initial Configuration and Input Data	13
2.1.6 Status of Transient Analysis Technique	15
2.2 Inventory	16
2.3 Thermal Effects	17
2.3.1 Analysis of Thermal-Hydrologic Constraints on Criticality Power Output for DPCs in Unsaturated Alluvium using PFLOTRAN	17
2.3.2 Analytical Models for Thermal Response to Steady-State Criticality in a Saturated Repository	19
2.3.2.1 Analytical Model with Heat Conduction Only	20
2.3.2.2 Analytical Model with Heat Conduction and Heat Convection	30
2.3.3 Thermal Analysis with PFLOTRAN	31
2.4 Chemistry	32
2.5 Solubility	32
2.6 EBS Degradation	32
2.7 Permanent Criticality Termination Processes	34

2.8	Repository Simulations.....	37
2.8.1	Base Case Simulations (without Criticality)	38
2.8.1.1	Introduction.....	38
2.8.1.2	Model Design.....	38
2.8.2	Comparison Simulations (with Criticality)	41
2.8.2.1	Criticality Submodule Development	42
2.8.2.2	Interface with Neutronics Codes	43
3.	CRITICALITY ANALYSES RESULTS	45
3.1	Neutronics.....	45
3.1.1	3×3 Assembly Power Distributions	45
3.1.2	3×3 Assembly Channel Temperature Distributions.....	46
3.1.3	3×3 Assembly Channel Density Distributions	47
3.1.4	Initial Use of Terrenus on a 17×17 PWR Assembly.....	48
3.1.5	Investigation of Negative Reactivity Phenomena.....	52
3.1.6	Calculating Critical Water Level	54
3.1.7	Critical Power Search.....	57
3.1.8	Conclusions and Future Work	57
3.2	Inventory.....	58
3.3	Thermal Effects.....	68
3.3.1	Thermal-Hydrologic Constraints on Criticality Power Output for DPCs in Unsaturated Alluvium.....	68
3.3.2	Computational Results for Analytical Models of Thermal Response to Steady-State Criticality	76
3.3.2.1	Results for Analytical Model with Heat Conduction	76
3.3.2.2	Results for Analytical Model with Heat Conduction and Heat Convection	83
3.3.3	Results for Thermal Analysis with PFLOTRAN without Criticality.....	85
3.4	Chemistry.....	89
3.4.1	Steel Corrosion	90
3.4.2	Radiolysis.....	91
3.4.3	CSNF Degradation.....	91
3.5	Solubility	92
3.6	EBS Degradation.....	92
3.7	Time of Termination.....	92
3.7.1	Reactivity Perturbations due to Fuel Geometry Changes.....	93
3.7.2	Reactivity Perturbations due to Burnup	95
3.7.3	Reactivity Changes due to Decay	98
3.7.4	Reactivity Perturbations due to Compositional Changes from Corrosion/Dissolution	101
3.7.5	Summary and Conclusions.....	103
3.8	Repository Simulations.....	104
3.8.1	Base-Case Simulations (without Criticality).....	104
3.8.2	Comparison Simulations (with Criticality)	109

4.	CONCLUSIONS.....	117
4.1	Summary of Results	117
4.2	Future Work.....	119
5.	REFERENCES.....	121
A-1.	Introduction.....	129
A-2.	Mathematical Derivation	129

LIST OF FIGURES

Figure 1-1. Conceptual Drawing of Hypothetical Reference Case for Saturated Shale/Argillite	6
Figure 1-2. Conceptual Drawing of Hypothetical Reference Case for Unsaturated Alluvium.....	6
Figure 2-1. Flowchart Showing Inner Radiation Transport Thermal-Hydraulic Coupling Loop, Outer Mechanics, and Nuclide Depletion Loop	8
Figure 2-2. Multiphysics Coupling for a DPC Simulator for Solving Steady-State or Gradual Approach to Critical Configuration Problems.....	10
Figure 2-3. Schematic of 3×3 Square Array of Spent Fuel Rods within a Canister	14
Figure 2-4. TML Time-stepping Scheme	16
Figure 2-5. Cut Through of the Computational Domain showing a 6×6×12 m Detail of the Mesh	18
Figure 2-6. Plan View of 11 DPCs for Thermal Response to a 4-kW Steady-State Criticality Only in the Central DPC	22
Figure 2-7. Heat Generation in the Critical DPC and in Adjacent DPCs, Based on the TSC-37 DPC	24
Figure 2-8. Illustration of Using Multiple Point Sources or Point Sinks to Represent the Variable Heat Output for the Thermal Conduction Model	26
Figure 2-9. Model Domain for a 3D, Single-Drift, Single-Waste Package Simulation using Quarter Symmetry Boundaries	39
Figure 2-10. Locations of Four Observation Cells: Center of the Waste Package, in the Drift near the Edge of the Waste Package, in the DRZ at the Edge of the Drift, and in the Host Rock at the Edge of the DRZ.....	41
Figure 2-11. Criticality Parameters Are Associated with Individual Waste Forms through a Submodule Built onto the Waste Form Process Model	42
Figure 3-1. 3×3 Radial Power Distribution over Two Iterations at $z = 185$ cm	46
Figure 3-2. 4×4 Channel Temperatures over Two Iterations at $z = 185$ cm.....	46
Figure 3-3. Axial Temperatures Distributions for Iterations 0 and 1	47
Figure 3-4. Channel Water Densities	47
Figure 3-5. Axial Channel Water Densities in a Central Channel.....	48
Figure 3-6. Pin Layout of a Standard 17×17 PWR Assembly.....	49
Figure 3-7. Pin Powers at the Axial Midplane (left) and Axial Distribution of Pin Power along a Fuel Pin adjacent to the Central Instrument Tube (right).....	49
Figure 3-8. Temperature of the Water Moderator in Each Channel at the Axial Midplane (left) and Axial Temperature Distribution in the Central Instrument Tube (right)	50
Figure 3-9. Water Moderator Density in Each Channel at the Axial Midplane (left) and Axial Distribution of the Moderator Density in the Central Instrument Tube (right).....	50

Figure 3-10. Pin Temperature in Each Pin Cell at the Axial Midplane (left) and the Axial Temperature Distribution in a Fuel Pin adjacent to the Central Instrument Tube (right).....	51
Figure 3-11. Axial Distribution of Temperature (left) and Moderator Density (right) in the Central Instrument Tube for Various Power Levels	51
Figure 3-12. Reactivity in a Fully Reflected 17×17 PWR Assembly at Various Power Levels	52
Figure 3-13. A Simplified Neutronic Model of a Loaded Canister.....	53
Figure 3-14. Effect of Moderator Density on Reactivity	53
Figure 3-15. Inventory of Actinides and Their Decay Products 19,000 Years after Repository Closure, with and without 10,000-Year Steady-State Criticality Event.....	60
Figure 3-16. Inventory of Radioactive Fission and Activation Products 19,000 Years after Repository Closure, with and without 10,000-Year Steady-State Criticality Event.....	62
Figure 3-17. Inventory of Stable Fission Products 19,000 Years after Repository Closure, with and without 10,000-Year Steady-State Criticality event.....	63
Figure 3-18. Comparison of Selected Radionuclide Mass Fractions in the DPC with and without a Steady-State Criticality Event.....	67
Figure 3-19. Waste package Temperature versus Time prior to Waste Package Breach	69
Figure 3-20. Liquid Saturation Index for the 10 mm/yr Case at 500 Years Postclosure, the Time of Maximum Dry-out.....	70
Figure 3-21. Liquid Saturation Index for the 2 mm/yr Case at 750 Years Postclosure, the Time of Maximum Dry-out.....	71
Figure 3-22. Waste Package Temperature versus Time after Waste Package Breach at 9,000 Years for the 10 mm/yr Case, 300 W Scenario	72
Figure 3-23. Waste Package Temperature versus Time after Waste Package Breach for the 10 mm/yr Case, 400 W Criticality Scenario	73
Figure 3-24. Liquid Saturation Index for the 10 mm/yr Scenario shown on Vertical Cross Section Perpendicular to Emplacement Drifts.....	74
Figure 3-25. Liquid Saturation Index for the 2 mm/yr Scenario in a Vertical Cross Section Perpendicular to the Emplacement Drifts at Different Times	75
Figure 3-26. Temperature History for 4 kW Criticality from 9,000 to 19,000 Years with Thermal Properties for Bentonite Backfill.....	77
Figure 3-27. Contribution to Temperature Change from the Central (Critical) DPC and from the Adjacent DPCs with the Thermal Properties for Bentonite Backfill.....	78
Figure 3-28. Temperature History for 4 kW Criticality from 9,000 to 19,000 years with Thermal Properties for Shale Host Rock	79
Figure 3-29. Temperature Change in Adjacent DPCs Separated by 20, 30, and 40 m from the Central (critical) DPC in Bentonite Backfill	80
Figure 3-30. Temperature Change in Adjacent DPCs Separated by 20, 30, and 40 m from the Central (critical) DPC in Shale Host Rock.....	80
Figure 3-31. Comparison of Temperature Change with Five Versus Nine Discrete Locations for Thermal Point Sources on the Axis of the Central (critical) DPC in Bentonite Backfill.....	82

Figure 3-32. Contours of Increased Temperature Above Ambient at 100, 1,000, and 10,000 years with Rock Permeabilities of $1 \times 10^{-15} \text{ m}^2$ and $5 \times 10^{-15} \text{ m}^2$ on the Left and Right Sides, Respectively 84

Figure 3-33. Snapshots of 3D Temperature Distribution..... 86

Figure 3-34. Snapshots of 3D Liquid Saturation Distribution 87

Figure 3-35. Temperature versus Time at Observation Points Specified in Figure 2-10 88

Figure 3-36. Liquid Saturation versus Time at Observation Points Specified in Figure 2-10 89

Figure 3-37. Normalized k_{eff} as a Function of Pin Pitch 94

Figure 3-38. Example Cladding Unzipping 95

Figure 3-39. Concentration of Fissile Isotopes as a Function of PWR SNF Burnup 96

Figure 3-40. Concentration of Neutron Absorber Isotopes as a Function of PWR SNF Burnup..... 97

Figure 3-41. k_{eff} as a Function of PWR Burnup for the TAD DB Configuration and Degraded IG Configuration with Varying Levels of Saturation 98

Figure 3-42. k_{eff} as a Function of Decay Time 99

Figure 3-43. Isotopic Concentrations of Radionuclides Important to Criticality 100

Figure 3-44. Initial Pressure and Temperature Conditions for Shale Case at the Time of Repository Closure 105

Figure 3-45. Temperature versus Time at Observation Points Listed in Figure 2-10 106

Figure 3-46. Gas Saturation versus Time at Observation Points Specified in Figure 2-10 107

Figure 3-47. Gas Pressure versus Time at Observation Points Specified in Figure 2-10 108

Figure 3-48. Concentrations of Selected Radionuclides in the Shale adjacent to the Drift Wall with no Criticality Event and a Waste Package Breach at 9,000 Years..... 109

Figure 3-49. Temperature versus Time at Observation Points Indicated in Figure 2-10, with a Criticality Event Lasting from 9,000 to 20,000 Years 111

Figure 3-50. Liquid Pressure versus Time at Observation Points Indicated in Figure 2-10, with a Criticality Event Lasting from 9,000 to 20,000 Years 112

Figure 3-51. Gas Saturation versus Time at Observation Points Indicated in Figure 2-10, with a Criticality Event Lasting from 9,000 to 20,000 Years 113

Figure 3-52. Concentration versus Time after Waste Package Breach in the Shale Host Rock at the Edge of the Drift for a Selection of Radionuclides, with and without a Criticality Event 115

LIST OF TABLES

Table 2-1. Description of the Fuel Rod	14
Table 2-2. Fuel Rod Material Properties.....	15
Table 2-3. Description of the Square Box and Canister	15
Table 2-4. Fluid Properties	15
Table 2-5. Heat without and with 4 kW Criticality Event in the TSC-37.....	23
Table 2-6. Thermal Properties for Calculations for Bentonite Backfill and Shale Host Rock.....	30
Table 2-7. Parameters for Determining Contours of Temperature Increase above Ambient for a Line Source in a Saturated Porous Medium.....	31
Table 2-8. Comparison of k_{eff} Values for PWR SNF Configurations	35
Table 2-9. Physical Properties of Model Materials	40
Table 2-10. Inputs to PFLOTRAN for Each Radionuclide.....	44
Table 3-1. Critical Water Level for the MPC-32-TSC 079 Sequoyah Canister.....	55
Table 3-2. Test Cases for Critical Water Level Search	56
Table 3-3. Inventory of Actinides and Their Decay Products 19,000 Years after Repository Closure, with and without 10,000-Year Steady-State Criticality Event.....	59
Table 3-4. Inventory of Radioactive Fission and Activation Products 19,000 Years after Repository Closure, with and without 10,000-Year Steady-State Criticality Event.....	61
Table 3-5. Inventory of Stable Fission Products 19,000 Years after Repository Closure, with and without 10,000-Year Steady-State Criticality Event.....	62
Table 3-6. Inventory of Selected Radionuclide Inventories as Input into PFLOTRAN, without Criticality	64
Table 3-7. Inventory of Selected of Radionuclides as Input into PFLOTRAN, with Criticality	65
Table 3-8. Fissile and Absorber Material Equivalency at 5 and 10,000,000 Years for PWR SNF (4.5 Wt.% ^{235}U and 40 GWd/MTU)	100
Table 3-9. Relative Worth of SNF Isotopes.....	102
Table 3-10. Criticality Parameters Specified in the Criticality Submodule.....	110
Table 3-11. Percentage Change in Concentrations of Selected Radionuclides at the Edge of the Drift Shale with a Postclosure Criticality Event from 9,000 to 20,000 Years after Repository Closure	116

ACRONYMS

2D	two-dimensional
3D	three-dimensional
ANS	American Nuclear Society
ANSI	American National Standards Institute
ASCR	Advanced Scientific Computing Research
API	application programming interface
BSC	Bechtel SAIC Company
BWR	boiling water reactor
CAD	computer-aided design
CASL	Consortium for Advanced Simulation of Light Water Reactors
CFD	computational fluid dynamics
CFR	Code of Federal Regulations
CMFD	coarse mesh finite difference
CNWRA	Center for Nuclear Waste Regulatory Analyses
COBRA	Coolant Boiling in Rod Arrays
COBRA-SFS	Coolant Boiling in Rod Arrays-Spent Fuel Storage
COBRA-TF	Coolant Boiling in Rod Arrays-Two Fluid
CRWMS	Civilian Radioactive Waste Management System
CY	calendar year
DABC	disposal analysis basis configuration
DB	design basis
DOE	Department of Energy
DPC	dual-purpose canister
DRZ	disturbed rock zone
EBS	engineered barrier system
ECP	Exascale Computing Project
ENDF	evaluated nuclear data file
EPA	Environmental Protection Agency
EPKE	exact point kinetics equations
EPRI	Electric Power Research Institute
FEP	feature, event, or process
FMDM	Fuel Matrix Dissolution Model

GPU	graphical processing unit
HDF	hierarchical data format
I/O	input-output
IBM	International Business Machines
IG	igneous
INEL	Idaho National Engineering Laboratory
LEU	low-enriched uranium
M&O	Management and Operating Contractor
MCNP	Monte Carlo N-Particle
MPACT	Michigan Parallel Characteristics Transport
MPC	multipurpose canister
MPI	message passing interface
MTU	metric tons of uranium
N/A	not applicable
NAC	Nuclear Assurance Corporation
NEA	Nuclear Energy Agency
NRC	Nuclear Regulatory Commission
OECD	Organisation for Economic Co-operation and Development
ORIGEN	Oak Ridge Isotope Generation
ORNL	Oak Ridge National Laboratory
PA	performance assessment
PARCS	Purdue Advanced Reactor Core Simulator
PCQM	Predictor-Corrector Quasi-static Method
PFLOTRAN	Parallel Flow and Transport
PWR	pressurized water reactor
RELAP	Reactor Excursion and Leak Analysis Program
RTK	reactor toolkit
SKB	Svensk Kärnbränslehantering AB (Swedish Nuclear Fuel and Waste Management Company)
SNF	spent nuclear fuel
SNL	Sandia National Laboratories
TAD	transportation, aging, and disposal
TML	transient multilevel
TSC	transportable storage canister

UNF-ST&DARDS	Used Nuclear Fuel – Storage, Transportation & Disposal Analysis Resource and Data Systems
U.S.	United States
VERA	Virtual Environment for Reactor Application
WP	waste package
wt. %	weight percent

SPENT FUEL AND WASTE SCIENCE AND TECHNOLOGY

PRELIMINARY ANALYSIS OF POSTCLOSURE DPC CRITICALITY CONSEQUENCES

1. INTRODUCTION

One of the objectives of the United States (U.S.) Department of Energy's (DOE) Office of Nuclear Energy's Spent Fuel and Waste Science and Technology Campaign is to better understand the technical basis, risks, and uncertainty associated with the safe and secure disposition of spent nuclear fuel (SNF) and high-level radioactive waste. Commercial nuclear power generation in the U.S. has resulted in thousands of metric tons of SNF, the disposal of which is the responsibility of the DOE (*Nuclear Waste Policy Act 1982*). Any repository licensed to dispose the SNF must meet requirements regarding the long-term performance of that repository. For an evaluation of the long-term performance of the repository, one of the events that may need to be considered is the SNF achieving a critical configuration. Of particular interest is the potential behavior of SNF in dual-purpose canisters (DPCs), which are currently being used to store and transport SNF but were not designed for permanent geologic disposal.

A two-phase study has been initiated to begin examining the potential consequences, with respect to long-term repository performance, of criticality events that might occur during the postclosure period in a hypothetical repository containing DPCs. Phase I, a scoping phase, consisted of developing an approach intended to be a starting point for the development of the modeling tools and techniques that may eventually be required either to exclude criticality from or to include criticality in a performance assessment (PA) as appropriate; Phase I is documented in Price et al. (2019). The Phase I approach guided the analyses and simulations done in Phase II to further the development of these modeling tools and techniques as well as the overall knowledge base. The purpose of this report is to document the results of the analyses conducted during Phase II.

The remainder of Section 1 presents the background, objective, and scope of this report, as well as the relevant key assumptions used in the Phase II analyses and simulations. Subsequent sections discuss the analyses that were conducted (Section 2), the results of those analyses (Section 3), and the summary and conclusions (Section 4).

This report fulfills the Spent Fuel and Waste Science and Technology Campaign deliverable M2SF-20SN010305061.

1.1 Background

The DOE submitted the Yucca Mountain Repository License Application (DOE 2008a) to the U.S. Nuclear Regulatory Commission (NRC) in 2008. An update to the license application was completed later in the same year (DOE 2008b) and submitted to the NRC in 2009. The license application included a PA that analyzed the long-term performance of the repository consistent with applicable requirements given in the Code of Federal Regulations (CFR): 10 CFR Part 63 and 40 CFR Part 197. In that PA, SNF was

assumed to be placed in transportation, aging, and disposal (TAD) canisters that were specifically designed to transport fuel from its current storage location to Yucca Mountain, store it for aging purposes (if needed), and dispose it in Yucca Mountain. These TAD canisters were designed such that the probability of an in-package criticality event during the repository postclosure period was sufficiently low to exclude it from consideration in the PA (DOE 2008b, Section 2.1.2.2). That is, the probability of a criticality event was less than one chance in 10,000 of occurring within 10,000 years after disposal.

However, the license application process was suspended in 2010, and TADs were never built; thus, utilities could not load SNF into TAD canisters. Rather, in general, utilities have continued the practice of storing SNF in DPCs that are designed to meet relevant NRC requirements for storage and transport of SNF (10 CFR Part 72 and 10 CFR Part 71, respectively). While DPCs were designed, licensed, and loaded to preclude the possibility of a criticality event during SNF storage and transport, they were not designed or loaded to preclude the possibility of a criticality event during the regulated postclosure period following disposal, which can be up to 1,000,000 years per Assumption 3 in Section 1.4.

As discussed in the Phase I report (Price et al. 2019), one of the requirements for assessing the long-term performance of a repository is that all features, events, or processes (FEPs) must be included in the PA unless the probability of occurrence of the FEP is below a specified limit or the consequences of its occurrence, however probable, can be demonstrated to not be significant (EPA 2008). As noted above, for the Yucca Mountain PA, the probability of in-package criticality in TAD canisters during the postclosure period was, by design, less than one chance in 10,000 in 10,000 years after disposal. Thus, postclosure criticality in TAD canisters was excluded from the Yucca Mountain PA on the basis of probability. Based on studies investigating the probability of occurrence of in-package criticality in DPCs during the postclosure performance period, it is not clear that in-package criticality in DPCs can be excluded from a PA on the basis of probability for all geologies (Hardin et al. 2015).

Therefore, if direct disposal of SNF in DPCs in a geologic repository is to be considered, the associated PA for the repository may have to include in-package criticality. The DOE has developed a methodology for addressing the consequences of in-package criticality during the postclosure period (YMP 2003). If the DOE pursues a disposal licensing strategy that excludes in-package criticality in DPCs from the PA on the basis of low consequence rather than low probability, the DOE will have to demonstrate that the consequences of an in-package criticality event are not significant in terms of repository performance. Alternatively, if the consequences of an in-package criticality event are included in the PA, then the DOE must demonstrate that the regulatory performance standards can still be met.

1.2 Objective

The objective of this Phase II report is to summarize the initial results of implementing the approach to modeling the consequences of criticality in DPCs after closure of a hypothetical repository (i.e., during the postclosure period) that were presented in the Phase I report (Price et al. 2019). The eventual goal is to build the capability of conducting a modeling analysis that can be used to either exclude criticality from a PA on the basis of consequence or be used in a PA if criticality is to be included. The approach implemented in this report is consistent with approaches developed in the past (YMP 2003; BSC 2005d). The work discussed herein represents a starting point and is subject to limitations, however. For example, if criticality is eventually included in a PA, then associated probabilities of occurrence must also be calculated. The work discussed in this report focuses solely on the consequences of criticality during the

postclosure period, not the probability of occurrence of criticality. Further limitations in the scope of work are described in Section 1.3.

1.3 Scope

The approach implemented in this report is consistent with relevant regulations and requirements (Price et al. 2019) and uses, to the extent possible, existing generic models. Only in-package criticality in DPCs is studied; that is, criticality events external to the waste package, either in the near field or far field, are not studied. The only type of waste form considered is commercial SNF in DPCs, and the DPCs are represented by a single selected DPC.

The approach identifies conceptual models that feature two different hypothetical repositories and the occurrence of both steady-state criticality events and transient criticality events (Section 1.5). As previously stated, the approach considers only the consequences of criticality, not the probability of occurrence of criticality. Consistent with DOE's methodology (YMP 2003), the primary consequence of a steady-state criticality event is a change in the radionuclide inventory, which could affect repository performance; however, other effects of a steady-state criticality event are considered as well, such as thermal and chemical effects. The same effects can also occur because of a transient criticality. However, for a transient criticality the primary consequence is a sudden power pulse, which might damage neighboring waste packages or damage the engineered barrier system (EBS) in the vicinity of the critical waste package.

Research efforts thus far have concentrated on building the capability to analyze steady-state criticality events for DPCs disposed in a geologic repository. Accordingly, while this report discusses both types of criticality events, the focus is on steady-state criticality events. An approach for addressing transient criticality events has been proposed and is being developed (Section 2.1.4). The effect of transient criticality events on direct disposal of DPCs will be examined after the appropriate tools and methodology become available.

1.4 Assumptions

The broad, overarching assumptions described below are simplifying or bounding in nature; they are necessary at this time because the work described herein represents a starting point. As the work in this area matures, one or more of these assumptions may no longer be required. In addition, there are other assumptions pertinent to specific analyses that are discussed in the subsections addressing those analyses.

1.4.1 Assumption 1—A waste package has been breached and criticality occurs.

To facilitate criticality calculations, it is assumed that a waste package has failed, water has entered the waste package, and the configuration of water and SNF in the waste package is such that the configuration has an effective neutron multiplication factor (k_{eff}) greater than or equal to 1.0. This combination of circumstances forms a conservative assumption for the purposes of this study. The probability that these conditions have occurred is not calculated. For the analyses described in this report, the waste package consists of the DPC inside a larger disposal overpack.

The analyses consider the timing of any criticality event in a manner that is consistent with 10 CFR 63.114, which limits the time period over which FEPs must be evaluated to 10,000 years. Therefore, the

steady-state criticality event is assumed to begin 9,000 years after the repository closes and to continue for approximately 10,000 years; that is, until 19,000 years after closure. Modeling the steady-state criticality event as lasting 10,000 years is consistent with previous studies (CNWRA 2005; Rechar et al. 2003; CRWMS M&O 1999). The transient criticality event is assumed to occur 9,000 years after the repository closes; it is a single event.

1.4.2 Assumption 2—Fuel assembly configurations remain intact, but cladding permits radionuclide transport.

Low enriched fuel (i.e., less than 5 wt.% ^{235}U) is more reactive in a lattice configuration (i.e., in fuel pins) compared to a homogeneous configuration (e.g., in solution). Additionally, commercial fuel assemblies are designed to be undermoderated. Configurations that involve decreased fuel pin pitch (i.e., damage to grid spacers) or degraded fuel (i.e., damaged cladding) are typically of lower reactivity than intact fuel assemblies because there is less water to moderate the neutrons. Mechanisms that could increase pin pitch relatively uniformly during disposal are not postulated. Therefore, for the criticality consequence analysis, it is assumed that the fuel pins and cladding remain intact such that the fuel pellets are retained in their original assembly lattice configurations. This conservative assumption will be investigated as the research effort moves forward.

For the purpose of examining criticality consequences relative to repository performance, it is further assumed that the cladding has holes that, while small enough to preserve the fuel assembly configuration, are also large enough to permit radionuclides to be released into a breached waste package and be transported into the EBS and beyond.

1.4.3 Assumption 3—Postclosure performance requirements are similar to those for Yucca Mountain.

To examine the consequences of criticality in a DPC on postclosure repository performance, it is necessary to define the metric against which this performance is to be measured. It is assumed for the purposes of the analyses described in this report that the postclosure performance requirements that will apply to a repository in which DPCs are disposed are similar to those for disposal of SNF and high-level waste in Yucca Mountain. In particular, it is assumed that the following performance metrics are the same as those for Yucca Mountain: dose to a member of the public, the period of postclosure performance (i.e., 1,000,000 years), and the limits on inclusion of FEPs in the postclosure PA. More details on repository performance requirements and the FEPs screening process are discussed in Price et al. (2019).

1.4.4 Assumption 4—Basket neutron absorbers are assumed to have degraded prior to the initiation of a criticality.

Because of the relatively high corrosion rate of aluminum-based materials, it is assumed that borated aluminum-based neutron absorbers degrade within tens or hundreds of years once water enters a DPC. Although borated aluminum corrosion products (e.g., B_4C) may remain in the DPCs, the presence of neutron absorber material conservatively is not credited in the k_{eff} calculations for the analyses described in this report. The location of neutron absorber material inside the basket is paramount for criticality control, and it is difficult to justify whether the absorber material would maintain its original location after corrosion over tens or hundreds of years in an aqueous atmosphere.

1.4.5 Assumption 5—The steady-state criticality event is not cyclic.

Under unsaturated conditions, an uncontrolled criticality in a DPC in the repository is likely to oscillate between being critical and subcritical as reactivity feedback mechanisms change the environmental conditions (e.g., water evaporates because of heat generated by criticality, rendering the system subcritical for an undefined period of time). Modeling this cyclic criticality in a waste package in a repository is beyond current modeling capabilities. Because work is being done in a separate research effort to develop such a capability, cyclic criticality may be included at some point in the future as the research in criticality consequences evolves. However, in the analyses discussed in this report, it is assumed conservatively that the heat generated by the steady-state criticality event is exactly balanced by heat loss through convection, conduction, radiation, and evaporation, such that there is no cyclic behavior.

1.5 Approach

Two different hypothetical repositories are considered as reference cases in the analyses discussed below: a saturated repository in shale and an unsaturated repository in alluvium. For each hypothetical repository, the effects of a steady-state criticality event are examined. The approach to modeling the effects of a transient criticality event in a disposed DPC is being developed; once this model has been developed, the effects of transient criticality events in a single waste package will be examined. The performance of the single waste package with and without the occurrence of a steady-state criticality event is measured by calculating radionuclide releases into the host rock with the occurrence of the steady-state criticality event, then calculating radionuclide releases without the occurrence of any criticality event, and then comparing these releases.

The hypothetical reference case for a repository in saturated shale, or argillite, is illustrated in Figure 1-1. For this reference case, the repository is placed at a depth of 500 m, the emplacement drifts are backfilled with bentonite as a buffer (Mariner et al. 2017), and the waste package center-to-center spacing is 20 m (Hardin and Kalinina 2016). It is assumed that the hydrostatic pressure at repository depth is 50 bar. At this pressure, water boils at approximately 264°C (Weast and Astle 1979); therefore, during the steady-state criticality event, the maximum temperature in the waste package is 264°C. Other characteristics of the host rock are given in relevant subsections of this report and in Section 4.2.2 of Mariner et al. (2017).

Figure 1-2 depicts the hypothetical reference case for a repository in unsaturated alluvium. The repository depth is 250 m, and waste drifts are backfilled with crushed alluvium (based on Mariner et al. 2018). The drift diameter is 4.5 m, and the percolation rate is 10 mm/yr. Hydrologic and thermal parameters are given below in relevant subsections and in Table 5-1 of Mariner et al. (2018).

As noted above, it is assumed that the steady-state criticality event begins 9,000 years after closure and continues for approximately 10,000 years.

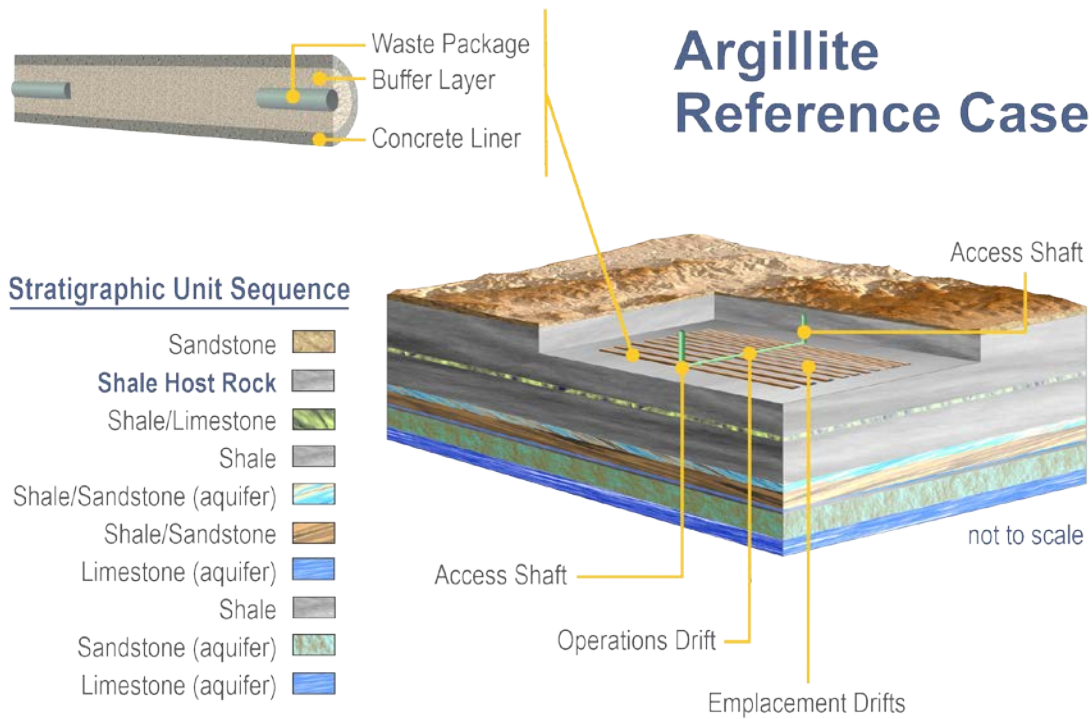


Figure 1-1. Conceptual Drawing of Hypothetical Reference Case for Saturated Shale/Argillite

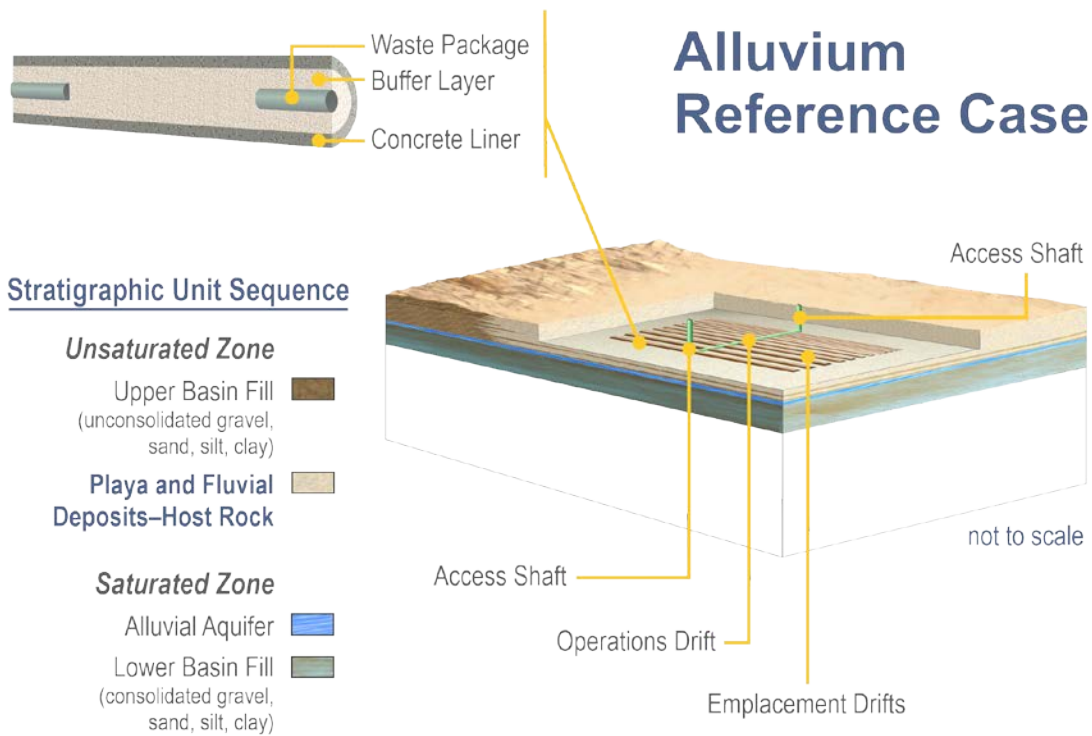


Figure 1-2. Conceptual Drawing of Hypothetical Reference Case for Unsaturated Alluvium

2. CRITICALITY ANALYSES DESCRIPTIONS

To understand the effects of postclosure criticality on different aspects of repository performance, several different analyses were conducted:

- **Neutronics**—Section 2.1 describes the development of high-fidelity, multiphysics simulation capability needed for neutronics calculations.
- **Inventory**—Section 2.2 examines changes in radionuclide inventory as a result of the criticality event.
- **Thermal Effects**—Section 2.3 presents various analytical and simulated thermal analyses.
- **Chemistry**—Section 2.4 focuses on the changes to the chemistry inside the waste package that may occur as a result of a steady-state criticality event.
- **Solubility**—Section 2.5 evaluates the impact of a steady-state criticality event on radionuclide solubility.
- **EBS Degradation**—Section 2.6 considers how a steady-state criticality event might affect the performance of the EBS.
- **Permanent Criticality Termination Processes**—Section 2.7 summarizes an analysis of mechanisms that might serve to permanently terminate the potential for criticality.
- **Repository Simulations**—Section 2.8 addresses the repository analyses that were conducted using PFLOTRAN, a massively parallel, subsurface flow and radionuclide transport code.

The results of these analyses are described in Section 3, with the subsection order corresponding to that in Section 2 such that Section 2.x provides the analysis description corresponding to the results given in Section 3.x.

2.1 Neutronics

Neutronics calculations of SNF in a DPC require high-fidelity multiphysics simulations. The relevant physics simulations include (1) radiation transport for calculating the system reactivity and the distribution of fission power throughout the fuel in a canister, (2) thermal hydraulics for calculating the density and temperature of any water within the canister, as well as the fuel temperature, (3) fuel depletion for calculating the changing nuclide inventory over time, and (4) mechanics for calculating the stress and strain on the canister walls and inner structure. This section presents an initial coupling capability between a high-performance Monte Carlo radiation transport solver (Shift) (Pandya et al. 2016) and a subchannel single-phase thermal-hydraulics code featuring natural circulation (Coolant Boiling in Rod Arrays-Spent Fuel Storage [Rector et al. 1986], also referred to as COBRA-SFS or simply COBRA in this document). This new multiphysics framework, Terrenus (Davidson et al. 2019), will initially provide a high-fidelity, steady-state criticality event simulation capability by coupling all of the associated physics and may be further extended to support a transient criticality event with a time-dependent neutronics solver.

2.1.1 Methodology

As described above, the relevant physics necessary for a DPC simulator include radiation transport, thermal hydraulics, depletion, and mechanics. For a steady-state or gradual approach to a critical configuration, the coupling between the physics packages is given in Figure 2-1. A transient or rapid approach to criticality involves different physics (radiation transport and kinetics), and the methodology being considered for handling this class of problem is still being investigated. A discussion on the current status of the solver under consideration to address transient criticality events is presented in Section 2.1.4.

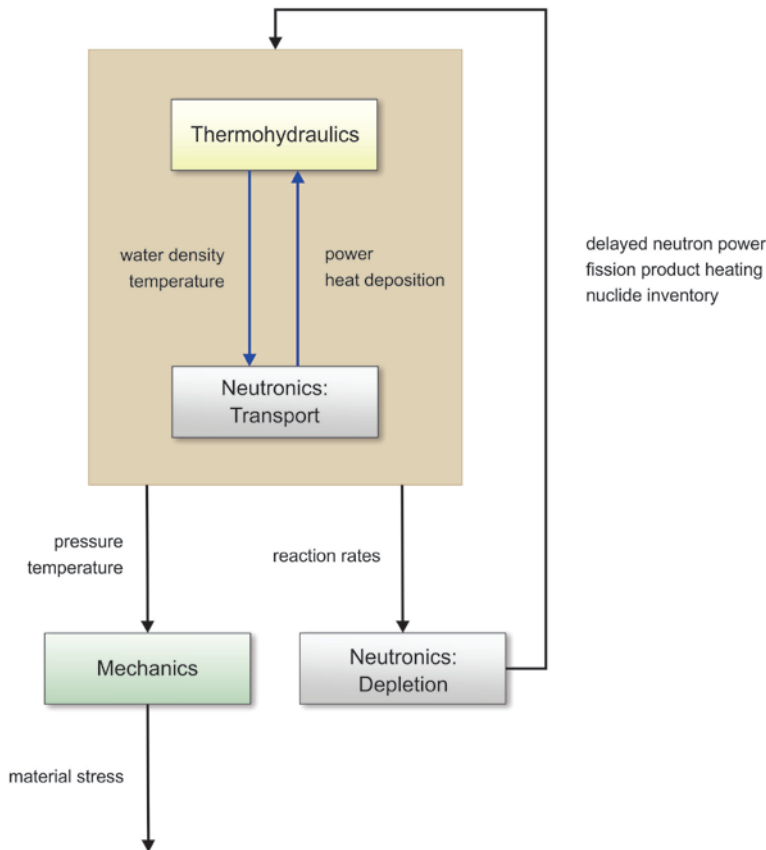


Figure 2-1. Flowchart Showing Inner Radiation Transport Thermal-Hydraulic Coupling Loop, Outer Mechanics, and Nuclide Depletion Loop

The coupling for a gradual approach to criticality in a DPC simulator is in two loops. The first inner loop couples the quasi-static radiation transport equations to a thermal-hydraulics solver. These two input-output (I/O) coupled physics packages are iterated to convergence for a particular point in time. The second outer loop involves the mechanics solver, which uses the converged fluid properties to calculate stress and strain on the DPC’s wall and internal structures, and the depletion solver, which uses the converged fission power to deplete the nuclide inventory and advance the simulation to the next time point.

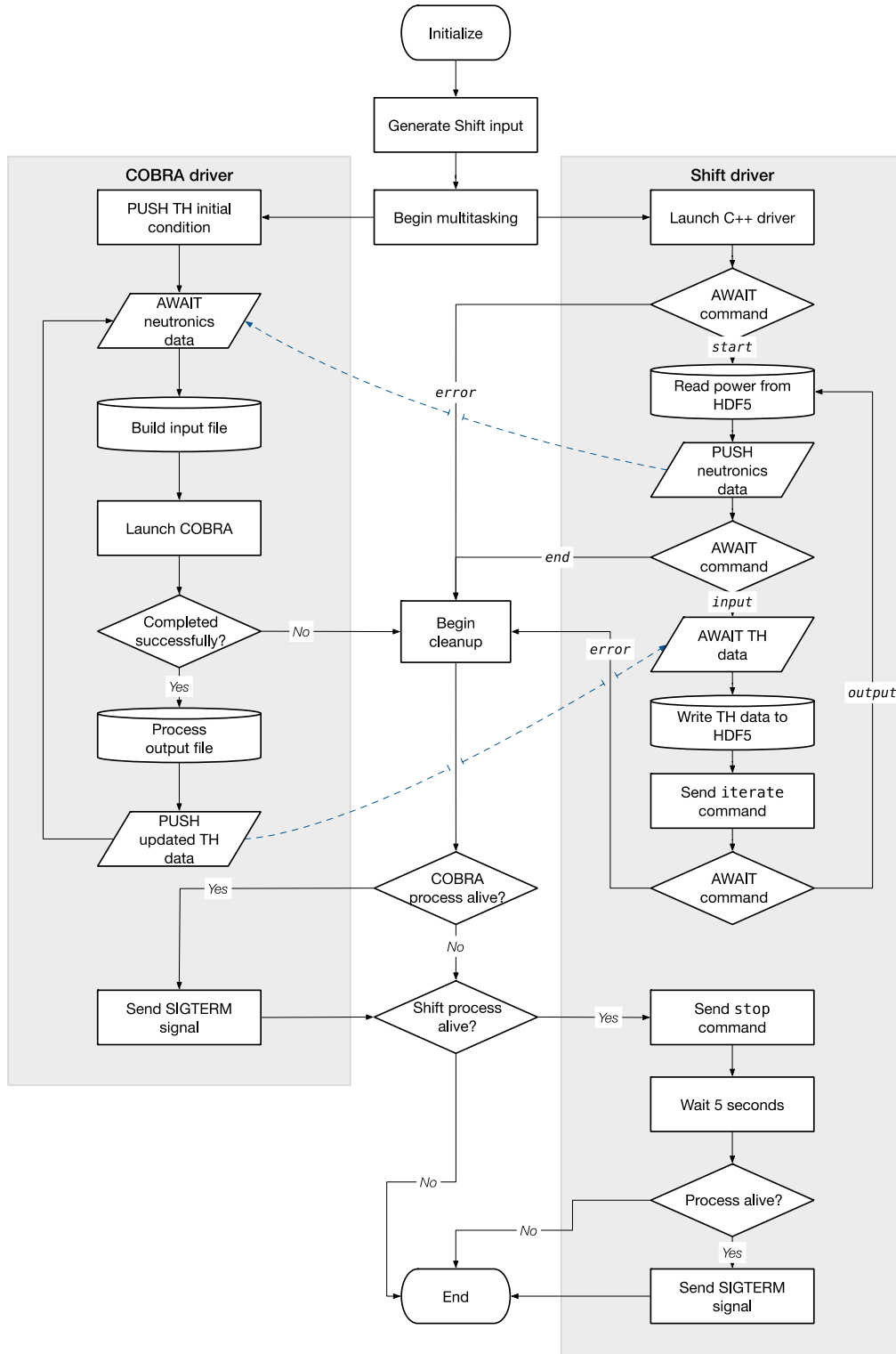
The current approach for addressing the inner loop involves coupling the quasi-static high-fidelity radiation transport code Shift to the subchannel natural circulation code COBRA-SFS. Coupling COBRA-SFS to Shift requires overcoming several technical hurdles. The primary difficulty is designing an efficient interface between a serial I/O-based process (COBRA) and a massively parallel framework (Shift). The parallel program has a comparatively large startup cost, so it is desirable to provide Shift an in-memory interface that allows the code to remain active but idling while COBRA generates updated thermal-hydraulics data. A Python-based driver code that launches and coordinates the Shift and COBRA processes achieves this design goal.

The Python driver code has three main responsibilities: interaction with COBRA, interaction with Shift, and coordination between the two. Since COBRA uses an inflexible input format and a human-readable output format, the driver must be able to generate text-based, fixed-column input from numerical data. The input format for COBRA has several limitations that affect the accuracy of the simulation. The most serious of these is that COBRA's input allows only an axial power profile and a separate radial power profile, implying that the three-dimensional (3D) power distribution calculated by Shift must be approximated by a separable function in r and z . An additional limitation is in the fixed-column input format: most variables must be represented in fixed-point notation inside five or ten columns, limiting both the accuracy and the range of values that can be provided to COBRA. Finally, since COBRA uses the imperial system of units, care must be taken to properly convert values to and from Shift. To ensure the validity of the conversions, the Python driver parses the units of each field in the output and uses an open source unit conversion package to maintain the integrity of the units throughout the code.

Shift's thermal-hydraulics application programming interface (API) uses a parallel, hierarchical data format 5 (HDF5)-format interface to efficiently read, distribute, and write its thermal hydraulics and neutronics data. Since it has this computer-readable, metadata-rich I/O interface, robustly providing input to and reading output from Shift is very simple. The major challenge of coupling to Shift is informing the code when new input is available and determining when newly generated output can be safely read. This challenge is addressed by using special command tokens piped through stdin and stdout between the Shift message passing interface (MPI) executable and the Python driver code.

The final task for the Python driver is to asynchronously run and coordinate the COBRA and Shift processes. Figure 2-2 represents the driver as a flow chart. The two gray regions are internal components that manage execution of COBRA and Shift. They run independently using Python's `asyncio` module, which allows the driver process to interleave input, output, and command execution between the two codes. This allows processing of the COBRA output file to complete while Shift is still solving the neutronics. In the flow chart, the dashed blue arrows represent the flow of data between the two processes. When Shift reports convergence, or if either code fails unexpectedly, then the driver cleanly terminates both codes.

The following two subsections briefly describe both of the numerical codes (Shift and COBRA-SFS) currently used in the development of Terrenus.



NOTE: TH = thermal-hydraulic.

Figure 2-2. Multiphysics Coupling for a DPC Simulator for Solving Steady-State or Gradual Approach to Critical Configuration Problems

2.1.2 Numerical Codes: Shift

Shift is a high-performance massively parallel Monte Carlo code featuring both continuous-energy and multigroup physics. Shift is capable of solving problems in both k-eigenvalue and fixed-source modes (Pandya et al. 2016). Shift can model coupled neutron/photon physics, including secondary particles born both by collisions and fission. Shift is also fully coupled to automatic cross-section generation capabilities in the SCALE code package, as well as to the Oak Ridge Isotope Generation code (ORIGEN) for nuclide depletion and decay (Davidson et al. 2018). Shift has previously been used for SNF canister dose analysis (Davidson and Banerjee 2017).

Shift is highly optimized to work on high-performance computing platforms using multiple parallelization strategies that can be tailored to the memory and performance requirements of the target architecture. Internode parallelism is managed using an MPI-based communication paradigm in which the problem is decomposed into N_s sets with N_b blocks per set such that the total number of processes is $N_s \times N_b$. Particles are decomposed across sets, while the spatial domain is decomposed across blocks. Thus, setting $N_b = 1$ reverts to the traditional *domain replication* parallelism model in which only particles are decomposed, while $N_b > 1$ implies *domain decomposition*. For problems with large tally requirements, which are typical in many full model depletion problems, multiple blocks can be used to enable the problem to fit within memory limitations on each process.

In addition, Shift has recently (Hamilton and Evans 2019) been enhanced with an intranode neutron transport algorithm that uses NVIDIA graphics processing unit (GPU) hardware. Recent performance analyses conducted using the latest NVIDIA compute GPU (Volta V100) show that, as the number of nuclides in the model increases, Shift achieves a particle tracking rate equal to between 100 and 175 IBM Power9 compute cores. Furthermore, the efficiency is highest when large numbers of particle histories are simulated. Therefore, Shift is ideally suited to efficiently run the large particle-count simulations necessary to reduce statistical convergence below the minimum uncertainty bounds required by this work.

The depletion package within Shift is also optimized to work on high-performance computing platforms. The depletion package does not attempt to maximize parallelism by simply evenly distributing the depletion regions among all available processes, since this would require the communication of the depletion results to be global. Rather, the depletion package exploits Shift's multilevel parallelism to reduce the amount of memory and communication required during solution of the depletion equations. A process only performs the depletion calculation on the depletable regions within its local block, with the depletion regions in a block evenly distributed across all sets. This depletion method maximizes the parallelism within a block while minimizing block-to-block communication. The depletion method has been shown to scale well to 10,000 cores (Davidson et al. 2018); however, since the depletion only constitutes a few percent (< 5%) of the total simulation time, this performance is considered sufficient for the work proposed here.

As part of DOE's Advanced Scientific Computing Research (ASCR) Exascale Computing Project (ECP), Shift is being coupled to Nek5000, a spectral finite-element computational fluid dynamics (CFD) code (Mersari et al. 2013) that can resolve turbulent flows using the large eddy simulation model. Capabilities developed during ECP will be leveraged for coupling to COBRA-SFS, including the use of on-the-fly doppler broadening of the cross sections, enabling tight coupling between the neutronics and thermodynamics. Currently, heat deposition is approximated by multiplying the fission rate by Shift's

internal fission heat library (the values ultimately come from ORIGEN-6.2; Davidson et al. 2018). These tallies are then scaled by the total power in the system. Therefore, this method is essentially assuming that all of the energy associated with the gammas is locally deposited in the fuel. In the future, a new, validated heat deposition data library will be added to Shift; this library will be used to calculate the decay and fission heat for each nuclide in the system. Instead of locally depositing the gamma energy in the fuel pins, an additional transport simulation will be performed to calculate where the gamma energy is deposited throughout the canister. In addition to providing the correct amount of energy deposited in the fuel channels for more accurate thermal-hydraulic inputs, this enhancement can also be used to perform high-fidelity calculations of neutron fluence and gamma energy deposition on the canister walls and interior structures. Since Shift also has advanced hybrid deterministic/Monte Carlo capabilities for automatic variance reduction, parameters of interest in low flux regions such as particle fluence on canister boundaries can be calculated (Wagner et al. 2011).

2.1.3 Numerical Codes: COBRA-SFS

COBRA-SFS is a program for steady-state and transient simulation of the thermal-hydraulic behavior of SNF systems (Rector et al. 1986; Michener et al. 2017a; Michener et al. 2017b). Like other codes in the COBRA family, such as COBRA-Two Fluid (COBRA-TF; Avramova 2009), COBRA-SFS solves a set of subchannel equations describing conservation of mass and momentum in the coolant flowing within fuel assemblies, as well as energy conservation within the fuel rods and other solid structures in the system. COBRA-SFS retains the validation history of other codes in the COBRA series, but it also provides additional validation specific to analysis of SNF systems. COBRA-SFS is distinguished from other COBRA variants by its treatment of features specific to SNF storage systems. This trait includes the ability to model natural circulation of coolant within a fuel canister, as well as simulation of radiative heat transfer between fuel rods and solid structures such as a SNF canister. It also extends the iteration scheme of other COBRA versions to be fully implicit in time to allow stronger coupling between equations governing fluid energy and heat transfer in solid components of the system.

2.1.4 Assumptions

Assumptions currently used in developing the Terrenus capability are discussed below. It is expected that some of these assumptions will change as the analysis and modeling evolve.

- **Single-Phase Liquid**—It is assumed that boiling does not take place and that temperature and Doppler reactivity coefficients are sufficient to maintain criticality.
- **Drift Airflow**—It is assumed that airflow through the repository drift is essentially stagnant and that no ventilation exists during the postclosure timeframe.
- **Water Temperature**—It is assumed that water enters the DPC at the ambient temperature of the surrounding media.
- **Water Flowrate**—It is assumed that inflow is equal to or greater than outflow, a condition necessary to maintain moderator presence within the DPC.
- **Configuration**—It is assumed that SNF is maintained at its original configuration.

2.1.5 Initial Configuration and Input Data

Shift supports a variety of geometric packages for modeling radiation transport scenes, including Monte Carlo N-Particle (MCNP) geometry, SCALE geometry, computer-aided design (CAD) geometry, and a reactor toolkit (RTK) geometry that was specifically designed for modeling pressurized water reactor (PWR) geometries for the Consortium for Advanced Simulation of Light Water Reactors (CASL) Virtual Environment for Reactor Application (VERA) code. The MCNP, SCALE, and CAD geometry packages enable modeling highly complex geometries, while the RTK package is limited to PWR geometries only.

However, there is much more to multiphysics simulations than simple geometric complexity. It is necessary to receive updated temperature and density information from the subchannel code and dynamically alter the model compositions. Because MCNP, SCALE, and CAD geometries are general purpose, they do not include the necessary model metadata denoting which geometric cells are fuel pins, which are guide tubes, which are moderator channels, etc. The only geometric package containing this metadata is the RTK geometry package. Therefore, it was decided that the more expedient and lower risk choice is to initially limit the Terrenus code to using RTK geometry models only. This choice enabled work to focus on the multiphysics coupling aspects initially, deferring geometric complexity to a later time. The choice comes at the expense of limiting the models that can be simulated. This restriction will be eliminated in the future by creating a DPC-aware metadata layer on top of the general geometry package.

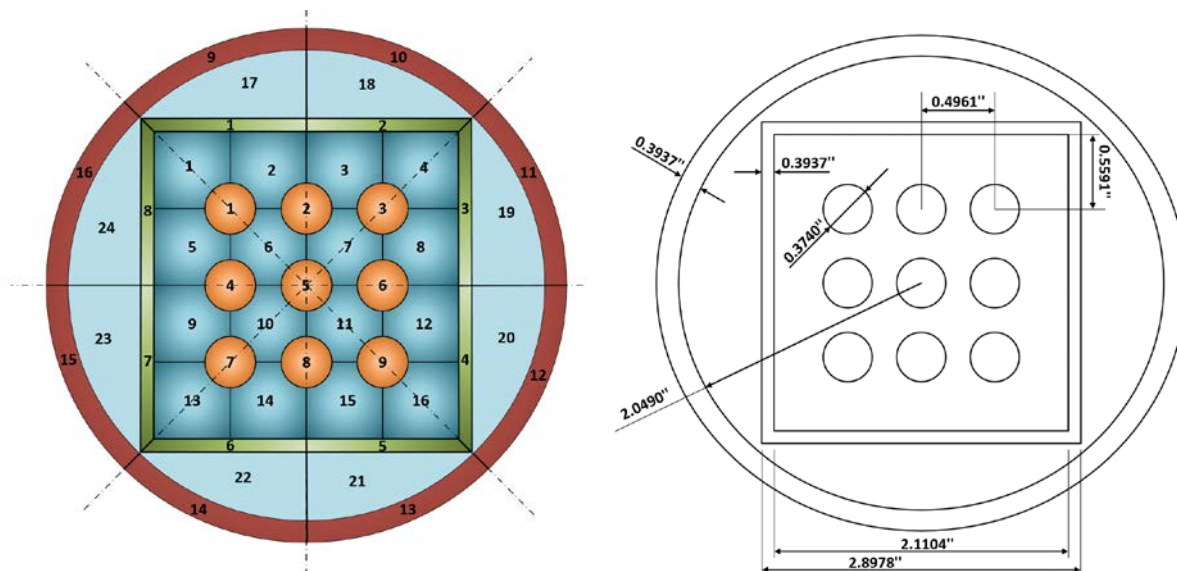
Several configurations (progression problems) have been developed and will be used to develop and demonstrate the progress of Terrenus multiphysics capabilities development. The selected configurations are listed below:

1. A 3×3 square array of fuel rods with surrounding stainless steel walls on four sides, enclosed within a cylindrical stainless steel canister (shown in Figure 2-3)
2. A 17×17 square array of fuel rods with surrounding stainless steel walls on four sides, enclosed within a cylindrical stainless steel canister
3. A 3×3 square array of fuel assemblies enclosed within a cylindrical stainless steel canister, with each fuel assembly surrounded by a square stainless steel box that represents the canister basket
4. A fully loaded canister with 37 PWR fuel assemblies, with each fuel assembly surrounded by a square stainless steel box that represents the canister basket
5. A fully loaded canister with 37 PWR fuel assemblies, including a stainless steel basket and supporting structures
6. A fully loaded canister with 89 boiling water reactor (BWR) fuel assemblies, including a stainless steel basket, supporting structures, and an outer canister
7. Additional configurations that may be used for benchmarking and validating various Terrenus modules

Currently, Terrenus is capable of modeling any single PWR assembly within a canister, including fuel pins and guide tubes. However, for simplicity, the first progression problem chosen is a single 3×3 array of PWR fuel rods within a canister. This problem is sufficient for demonstrating that the radiation transport and thermal-hydraulics modules are successfully coupled, but it does not require significant

effort to set up, nor does it require significant computational resources: a perfect demonstration problem on an initial enabling capability. The details of the 3×3 pin cell array are given below. For COBRA-SFS, the DPC canister walls were modeled explicitly, whereas with Shift, reflecting boundaries were set around the 3×3 array of pins. This approach gives the pin cell array a higher reactivity, which is more similar to what would be experienced by a fully loaded canister. When canister-aware metadata have been added to the SCALE geometry package, multiple assemblies as well as the DPC wall will be modeled explicitly, the geometric scene will extend beyond the boundary of the DPC, and either vacuum boundaries or an albedo condition tuned to the repository’s geology will be used.

The configuration is shown schematically in Figure 2-3. Table 2-1 presents various fuel rod parameters as modeled in COBRA and Shift. Table 2-2 shows the fuel rod material properties. Table 2-3 provides the square box and canister parameters. The moderator used is water at atmospheric pressure. Finally, Table 2-4 presents the moderator properties.



NOTE: The left image shows the COBRA-SFS channel, rod, and slab nodalization.

Figure 2-3. Schematic of 3×3 Square Array of Spent Fuel Rods within a Canister

Table 2-1. Description of the Fuel Rod

Description	Values
Fuel rod outer diameter (in.)	0.3740
Active fuel length (in.)	144.0
Cladding thickness (in.)	0.0243
Pitch (in.)	0.4961
Pellet material	UO ₂
Cladding material	Zircaloy
Enrichment (wt.%)	3% ²³⁵ U

Table 2-2. Fuel Rod Material Properties

Fuel Conductivity (Btu/[hr·ft·°F])	Fuel Specific Heat (Btu/[lbm·°F])	Fuel Density (lbm/ft ³)	Pellet Diameter (in.)	Cladding Conductivity (Btu/[hr·ft·°F])	Cladding Specific Heat (Btu/[lbm·°F])	Cladding Density (lbm/ft ³)	Cladding Thickness (in.)
2.8	0.0717	685	0.3669	9.540	0.0779	409	0.0243

Table 2-3. Description of the Square Box and Canister

Description	Values
Square box thickness (in.)	0.3937
Square box side length (in.)	2.1104
Square box material	stainless steel
Canister inside diameter (in.)	4.098
Canister thickness (in.)	0.3937
Canister material	stainless steel

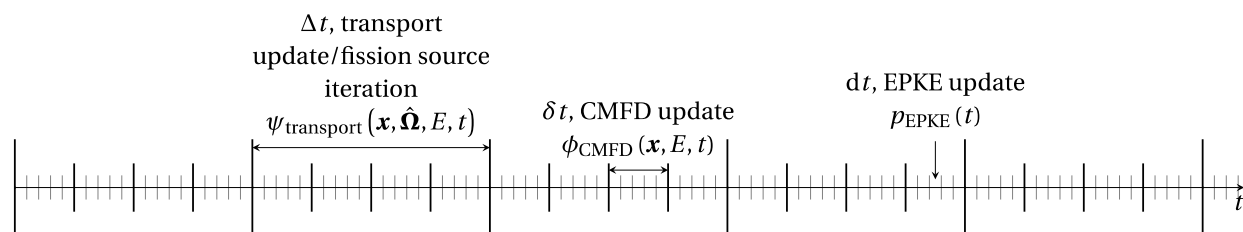
Table 2-4. Fluid Properties

Temperature (°F)	Enthalpy (Btu/lbm)	Conductivity (Btu/[hr·ft·°F])	Specific Heat (Btu/[lbm·°F])	Specific Volume (ft ³ /lbm)	Viscosity (lbm/[ft·hr])
40	8.08	0.329	1	0.016	3.744
60	28.1	0.341	1	0.016	2.7108
80	48.1	0.352	1	0.0161	2.0736
120	88	0.371	1	0.0162	1.3464
160	128	0.384	1	0.0164	0.9612
180	148	0.388	1	0.0165	0.8352
200	168	0.391	1.01	0.0166	0.7308
212	180.16	0.3912	1.01	0.01671	0.6809

2.1.6 Status of Transient Analysis Technique

The proposed technique for addressing a rapid approach to criticality involves implementing a transient multilevel (TML) method (Zhu 2016) to add nested time discretization loops (Figure 2-4) to a Predictor-Corrector Quasi-static Method (PCQM) algorithm (Dulla et al. 2008). In the TML method, the angular flux is computed on a fine spatial grid (with a high-order solver) and factorized into amplitude and shape functions. This same concept is used to factorize the scalar flux on a coarse spatial grid (coarse mesh finite difference [CMFD] grid flux). The inner loop of the algorithm computes the amplitude function using the exact point kinetics equations (EPKE) on a fine dt time step. This EPKE amplitude is then used to correct the CMFD flux on the δt time step. The outer loop of the TML algorithm then uses the CMFD updates to correct the transport flux on the Δt time step.

The code for the current EPKE solver has been validated with a one-group analytical solution as well as benchmarked against the Purdue Advanced Reactor Core Simulator (PARCS) spatial kinetics solver. The outputs are time-dependent power, reactivity, and delayed neutron precursor density.



NOTE: CMFD = coarse mesh finite difference.
EPKE = exact point kinetics equations.

Figure 2-4. TML Time-stepping Scheme

An implementation of the TML method has only been applied to a method of characteristics solver, Michigan Parallel Characteristics Transport (MPACT), and not a Monte Carlo solver. Additionally, the PCQM implementation into a Monte Carlo eigenvalue solver accomplished previously (Jo et al. 2016) was not coupled to a thermal-hydraulic solver to account for temperature feedback. An algorithm for a potential implementation of the TML into a Monte Carlo eigenvalue solver with temperature feedback is currently under development. While implementation of this algorithm will be nontrivial, additional branches of research from this method are available. These branches include the following:

1. Attempting to quantify uncertainty propagation through the PCQM/TML implementation
2. Adaptive time-step selection for the TML algorithm
3. Improved CMFD efficiency (CMFD solvers are often the bottleneck for TML transient runs [Zhu et al. 2016])
4. Development of a formalized method for trade-off of data between the Monte Carlo and thermal-hydraulics solvers (currently, there is no universally applied technique [Gill et al. 2017])

2.2 Inventory

Radionuclides with half-lives on the order of hundreds of years or more, or that are part of long radionuclide decay chains, are generally included in a repository PA. On the other hand, radionuclides with shorter half-lives that are not part of long decay chains (e.g., fission products) decay to insignificant quantities before waste packages fail and radionuclides are released from a repository. Therefore, these short-lived radionuclides are not included in a PA. A criticality event produces both additional quantities of those radionuclides that were already included in a PA and new quantities of those radionuclides that were not typically included in a PA. For example, a breached DPC in a steady-state criticality event during the postclosure period would generate additional short-lived radionuclides that might need to be included in a repository PA. A site-specific travel time from repository to receptor could be used to identify those short-lived radionuclides that could potentially be transported to the accessible environment and ingested by a member of the public.

The effects of a steady-state criticality on inventory were evaluated based on the data from actual assemblies of 37 Westinghouse 15×15 loaded in the NAC TSC-37 from a reactor that was shut down prior to calendar year 2000 (CY2000). The analysis assumes a steady-state criticality in a hypothetical shale repository with a 4 kW power distribution lasting from 9,000 to 19,000 years after closure. Section 2.3.2.1 presents the basis for assuming the steady-state criticality event generates 4 kW. The power distribution of 4 kW was applied among 37 assemblies using the burnup of the assemblies (i.e., the maximum power was assigned to the lowest burned assembly and the minimum power was assigned to the highest burned assembly). For compositions after a criticality event, the fuel is assumed to be approximately 20 years old with calculations beginning at 9,000 years after the repository closure in CY2100. The results of the inventory analysis, which are discussed in Section 3.2, were incorporated as appropriate in the repository simulations (Section 2.8 and Section 3.8).

2.3 Thermal Effects

Several analyses were completed as initial steps for understanding the effect on thermal behavior of a steady-state criticality event occurring in a DPC in a repository. Presented in Section 2.3.1, the first analysis uses PFLOTRAN, a massively parallel, subsurface flow and reactive transport simulator (Hammond et al. 2014; PFLOTRAN 2016), to explore the thermal-hydrologic constraints on criticality power output for DPCs disposed in unsaturated alluvium. The simulation results (Section 3.3.1) indicate what conditions might lead to retaining enough water in a breached waste package to maintain a criticality event.

The second analysis relies on analytical models to investigate the thermal response to a steady-state criticality event in a DPC disposed in a saturated, homogenous medium (e.g., saturated shale). Section 2.3.2.1 describes a model that considers conduction only; the results are provided in Section 3.3.2.1. The model described in Section 2.3.2.2 and Appendix A includes conduction and convection, with the associated results given in Section 3.3.2.2.

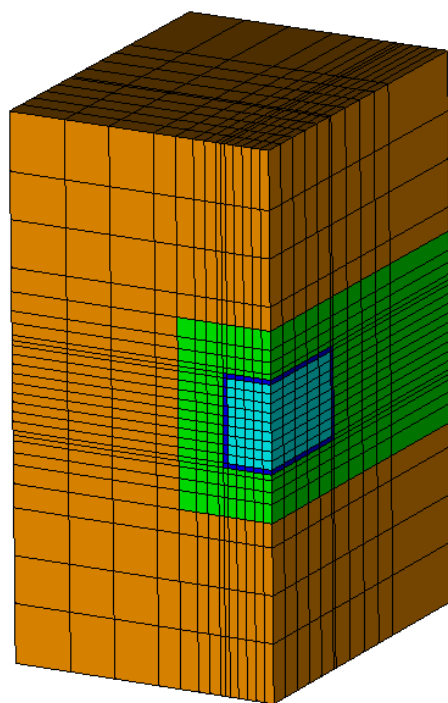
The final analysis is similar to the second except it uses PFLOTRAN to simulate the thermal response to a steady-state criticality in a DPC disposed in saturated shale. This analysis is described further in Section 2.3.3, and the results are provided in Section 3.3.3.

2.3.1 Analysis of Thermal-Hydrologic Constraints on Criticality Power Output for DPCs in Unsaturated Alluvium using PFLOTRAN

Preliminary analyses of generic disposal concepts in unsaturated alluvium formations have been undertaken previously (Mariner et al. 2018; Perry et al. 2018; Sevougian et al. 2019b; Hardin and Kalinina 2016) in part because alluvium may have thermal and hydrogeologic characteristics that are amenable for managing the challenges associated with geologic disposal of large DPCs. For a waste package criticality to occur, water would have to enter a breached waste package. Low infiltration rates and unsaturated conditions in alluvial deposits could diminish the probability that enough water would be available to fill a breached canister to cause a criticality event. This section describes initial exploration of those thermal-hydrologic processes and of the long-term average power output that could be sustained without driving water out of the package and terminating the criticality event.

The parallel subsurface multiphase thermal-hydrologic simulator PFLOTRAN (Hammond et al. 2014) was used for these analyses. PFLOTRAN solves the highly nonlinear conservation equations for mass and energy in variably saturated porous media. This work used PFLOTRAN's so-called general mode, which includes conservation equations for energy, water as liquid and vapor, and air as gas and dissolved in liquid.

The model domain includes a single waste package positioned in a backfilled emplacement drift (tunnel) in a repository situated in unsaturated alluvium at a depth of 250 m. The waste package and drift are both approximated as having square cross sections rather than the circular cross sections described for the reference case in Mariner et al. (2018). For this analysis, the cross sections are 1.67×1.67 m for the waste package and 4×4 m for the emplacement drift. The centerline-to-centerline drift spacing is 40 m. The waste packages are 5 m long with centers spaced at 40 m along the drift. The drift and waste package volumes are consistent with the GDSA unsaturated zone reference case design (Table 4.1 in Sevougian et al. 2019b; see also Hardin and Kalinina 2016). By symmetry, only half of the waste package and 20 m of the drift are modeled. In addition to the waste package internals, a shell/overpack with thickness of 0.1 m (assumed for ease of gridding) is included in the mesh. The model domain extends from the land surface to the water table in the vertical direction. Figure 2-5 shows a detail from the computational mesh in the vicinity of the waste package and drift.



NOTE: This 3D perspective is cut through the drift centerline and waste package midpoint and thus shows only one-quarter of the waste package. Green = backfilled drift, brown = host formation, light blue = waste package internals, and dark blue = waste package shell.

Figure 2-5. Cut Through of the Computational Domain showing a $6 \times 6 \times 12$ m Detail of the Mesh

The alluvium host medium for the repository is assumed to have a dry thermal conductivity of 1.0 W/(m·K) and a wet thermal conductivity of 2.0 W/(m·K). Backfill material is assumed to have the same thermal properties as the alluvium but with higher permeability (10^{-14} m² for the host medium versus 10^{-13} m² for the backfill). The internals of the waste package are assumed to have the same moisture retention properties as the backfill material. That assumption is conservative because it prevents the formation of a capillary barrier once the waste package fails. The waste package outer shell is assigned a very low permeability to prevent water from flowing through it.

The simulations were initially spun up without the repository. Repository closure is assumed at $t = 0$, using results from the spin-up phase as initial conditions, but with waste package internals, shell, and drift backfill in place. The DPCs are assumed to contain 37 PWR assemblies from a reactor that was shutdown prior to CY2000. Decay heat in the DPC produces about 4 kW at the time of repository closure (assumed to be in CY2100), but the value is only 249 W at 9,000 years postclosure, the assumed time of waste package breach in this work.

At 9,000 years, the top of the waste package shell is assumed to be breached, which is modeled by replacing the mesh cells associated with the waste package shell with those associated with drift backfill. The low permeability cells of the waste package shell sides and bottom remain intact, allowing the waste package to fill with water. The criticality event is assumed to start after the waste package has filled with water. Cases with two different deep percolation rates (approximately 10 mm/yr and approximately 2 mm/yr) are simulated. For each of the percolation rates, different power outputs from the criticality event are assumed. The objective is to identify the power output that could be produced by a criticality event without driving water out of the package.

2.3.2 Analytical Models for Thermal Response to Steady-State Criticality in a Saturated Repository

The objective of the thermal modeling of a steady-state criticality event in the hypothetical saturated repository is to incorporate the coupling of heat transfer by conduction and convection, with fluid migration, phase change such as boiling, chemical reactions, and criticality in heterogeneous porous media containing SNF. The model is needed to understand the consequences of postclosure criticality in an unsaturated repository. As a first-order assessment, a transient heat conduction-only model in a uniform homogeneous medium is used. In Section 2.3.2.1, a description is given of the conceptual and mathematical models for heat conduction from a group of 11 DPCs before and during a steady-state criticality. Section 3.3.2.1 presents the associated numerical results for temperature at the central (critical) DPC and at the nearest DPC in the same emplacement drift.

This conduction-only model provides a reasonable estimate of the temperature around a set of DPCs in a saturated medium. The model is analytic, and therefore provides a very rapid method to evaluate the effects of different DPC spacing, heating rates, and thermal properties of the host rock.

Section 2.3.2.2 addresses the next step in complexity for analytical evaluations, which is the inclusion of buoyancy-induced convection due to the nonuniform heating of the saturated medium. While this analysis includes both convection and conduction, it is limited to a saturated uniform homogeneous medium. In addition, the heating rate must be uniform with time. Presented in Section 3.3.2.2, the results provide a

strong basis for neglecting induced convection unless the backfill permeability increases by several orders of magnitude.

2.3.2.1 Analytical Model with Heat Conduction Only

The temperature field around a group of DPCs from decay and a steady-state criticality event has been analyzed using an analytic solution for heat conduction with multiple point sources in an infinite medium (Carslaw and Jaeger 1959). The thermal response to the heating from radioactive decay in a group of 11 DPCs determines the initial temperature change for the first 9,000 years after repository closure. The heat generation from radionuclide decay is based on a representative source term for 37 PWR SNF assemblies loaded in a NAC-MAGNASTOR TSC-37 manufactured by NAC-International (Price et al. 2019, Section 4.5). The thermal response at 9,000 years after closure provides the initial condition for predicting the thermal response to a steady-state criticality event in the central DPC. The steady-state criticality is assumed to have a constant power level of 4 kW from 9,000 to 19,000 years after closure; the basis for this assumption is presented below.

The thermal conduction calculations are based on the reference case for a fully saturated shale repository (Mariner et al. 2017), which was introduced in Section 1.5. There is a 20 m center-to-center spacing between adjacent DPCs in each emplacement drift, and 30 m spacing between adjacent emplacement drifts. Separate calculations determined the thermal response at the critical (central) DPC and at adjacent DPCs. The calculations used two sets of thermal properties (Mariner et al. 2017, Table 4-11): one set for the bentonite backfill, which directly surrounds the DPCs, and a second set for shale host rock, which surrounds the emplacement drifts. However, only one set of thermal properties is used throughout the domain for a calculation. Further details of the model are provided below.

Maximum Power Produced by Postclosure Criticality Event in Saturated Media

The duration of the current calculations for thermal response to heat conduction is 20,000 years. Heating from radioactive decay occurs throughout the 20,000 years, and heating from a 4.0 kW steady-state criticality event begins at 9,000 years and ends at 19,000 years. The assumed 4.0 kW power level during criticality is based on the model from Section 7.3 of CRWMS M&O (1996), but with parameter values that are specific to the hypothetical saturated shale repository. Specifically, CRWMS M&O (1996) calculated the maximum power that could be produced by a steady-state criticality event that occurs external to the waste package. In this model, fissile material is released from the waste package and accumulates in a reducing zone 500 m below the water table, forming a sphere. Assuming cooling by convection is negligible compared to cooling by conduction, the temperature can be determined by solving the steady-state heat conduction equation with a spherical source. This assumption of negligible convective cooling is justified based on the work given in this report in Section 3.7.2.

In applying this model to a steady-state postclosure criticality event in a DPC (which is a right circular cylinder, not a sphere) in a saturated shale repository, the DPC is represented by an equivalent spherical source. This equivalent spherical source is assumed to have a volume equal to that of the volume of the selected DPC; the radius of the equivalent spherical source can then be calculated for use in the steady-state heat conduction equation. The height of the DPC is 184.8 in. (4.69 m) and the diameter is 71 in. (1.80 m; Price et al. 2019); the diameter of the equivalent spherical source is thus 1.42 m.

CRWMS M&O (1996, Section 7.3.3) uses the following equation to calculate the power corresponding to a given average temperature of the critical equivalent sphere:

$$P = \frac{T_{av} - T_{\infty}}{\frac{1}{4k\pi R} + \frac{1}{14k\pi R}} \quad \text{Equation 2-1}$$

where

P = power (W)

T_{av} = average temperature in the equivalent sphere (K)

T_{∞} = ambient temperature of the shale far from the equivalent sphere (K)

k = thermal conductivity of the saturated shale (W/[m·K])

R = radius of the critical equivalent sphere (m)

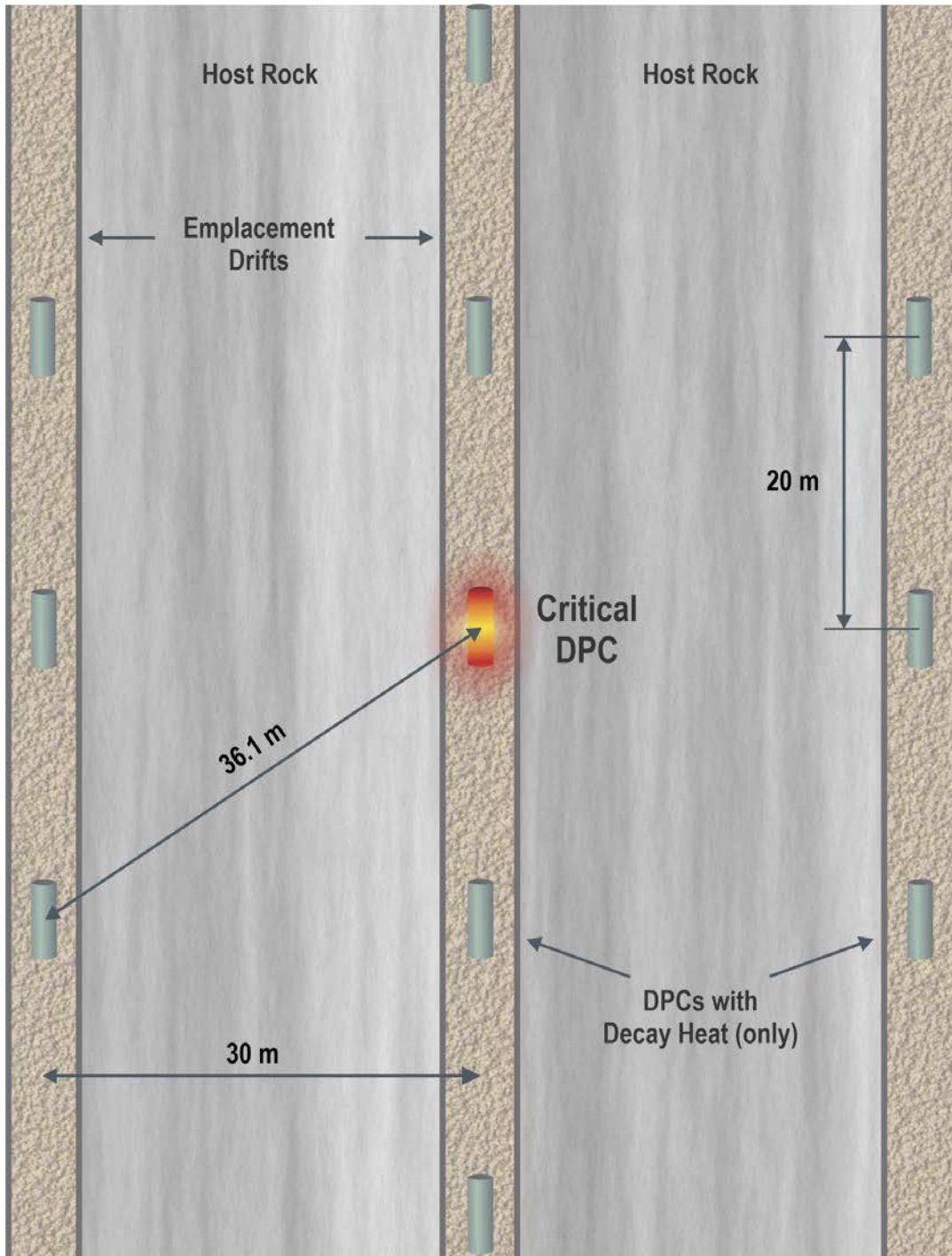
For the calculation in a saturated shale repository, it is assumed that the average temperature in the equivalent sphere is the boiling point of water at 50 bar, which is 264°C or about 537 K (Price et al. 2019), and that the ambient temperature of the shale far from the sphere (but at the same depth) is 30°C, or about 303 K. The thermal conductivity of the saturated shale is 1.2 W/(m·K) (Mariner et al. 2017). Given these values, the maximum power produced by a postclosure criticality event occurring in a DPC in the saturated shale is 3,895 W, which is rounded up to 4 kW for convenience.

Model for Temperature Change Due to Steady-State Criticality

The temperature rise at a central DPC with a 4 kW steady-state criticality event has been evaluated for a group of 11 DPCs that are located within 40 m of the central (critical) DPC. The 11 DPCs are located in 3 adjacent emplacement drifts, which are spaced 30 m apart (Figure 2-6). In the center emplacement drift, the critical DPC has four adjacent DPCs with 20 m center-to-center spacing. In each of the two adjacent emplacement drifts, there are 3 DPCs with 20 m center-to-center spacing between adjacent DPCs. Given the 30 m offset between emplacement drifts, the adjacent drifts have one DPC that is 30 m from the critical DPC and two DPCs that are $\sqrt{(30 \text{ m})^2 + (20 \text{ m})^2} = 36.1 \text{ m}$ from the central DPC. Figure 2-6 shows a plan view of the 11 DPCs and their spacing in the 3 emplacement drifts.

There are two potential sources of heat for each DPC in the model. The central DPC generates heat from radioactive decay and, in addition, generates 4 kW of heat from steady-state criticality between 9,000 and 19,000 years after closure. All other DPCs in the model generate heat from radioactive decay only.

Each DPC is represented by multiple thermal point sources at five discrete locations within each DPC. The strength of the multiple thermal point sources is varied to represent the time-dependent power level from radionuclide decay and criticality, as explained next.



NOTE: DPC = dual-purpose canister.

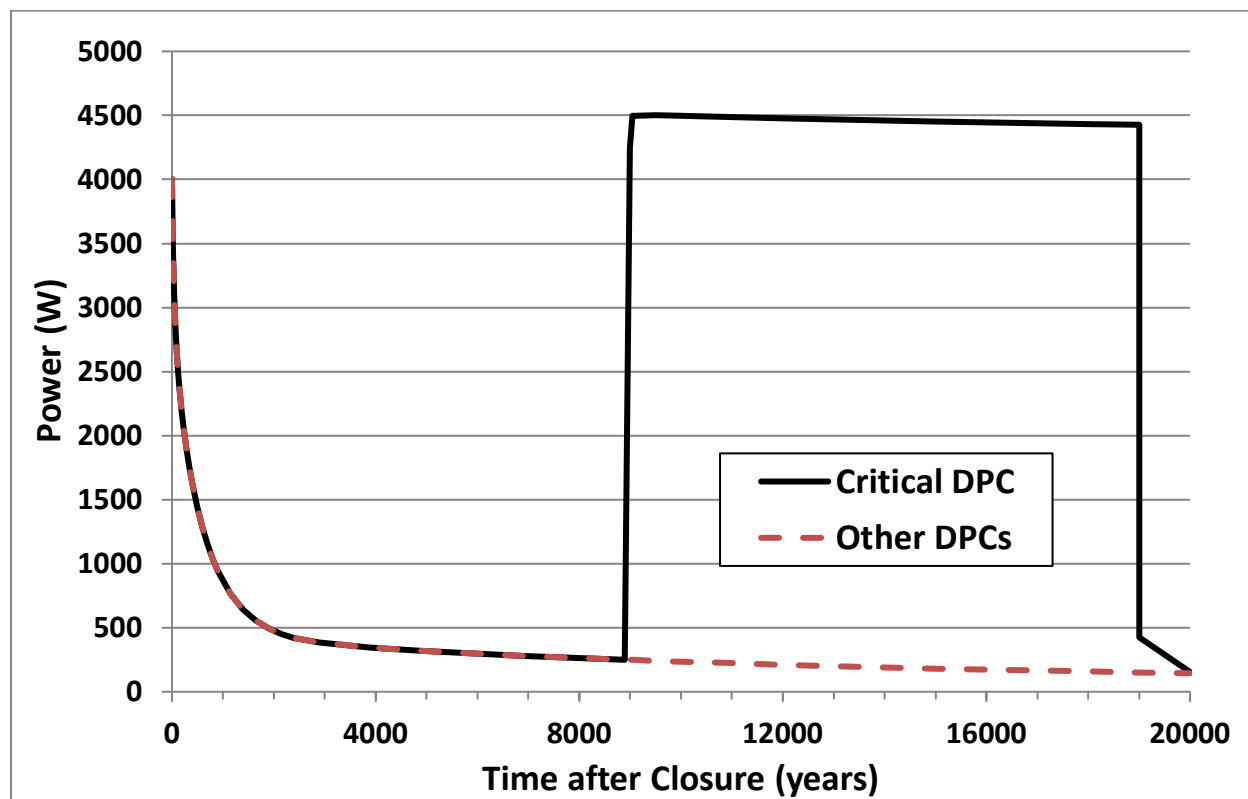
Figure 2-6. Plan View of 11 DPCs for Thermal Response to a 4-kW Steady-State Criticality Only in the Central DPC

The heat from radioactive decay has been calculated with the SCALE code for a 4 kW criticality event (Bhatt 2019). The decay heat is defined by a piecewise linear curve that decreases monotonically from 4,002.73 W at time 0 (closure) to 249.02 W at 9,000 years after closure (Table 2-5). Between 9,000 and 19,000 years, the central DPC also has a steady-state criticality that produces 4 kW plus a small increase in decay heat from criticality-generated fission products, shown in the sixth column in Table 2-5. DPCs that do not go critical continue to produce heat from radioactive decay (only) throughout the 20,000-year analysis period, as shown in the second and fifth columns in Table 2-5. Figure 2-7 illustrates the decay heat curves for 20,000 years.

Table 2-5. Heat without and with 4 kW Criticality Event in the TSC-37

Time after Closure (years)	Heat without Criticality (W)	Heat including Criticality (W)	Time after Closure (years)	Heat without Criticality (W)	Heat including Criticality (W)
0	4002.73	4002.73	2150	451.92	451.92
25	3459.25	3459.25	2400	421.97	421.97
50	3097.82	3097.82	2900	383.32	383.32
75	2843.38	2843.38	3900	343.34	343.34
100	2653.15	2653.15	4900	319.02	319.02
125	2502.66	2502.66	5900	299.20	299.20
150	2377.76	2377.76	6900	281.51	281.51
200	2174.78	2174.78	7900	265.36	265.36
250	2009.67	2009.67	8900	250.52	250.52
300	1868.45	1868.45	9000	249.02	4,249.92
350	1744.46	1744.46	9050	248.31	4,497.47
400	1633.90	1633.90	9100	247.61	4,499.16
500	1444.05	1444.05	9500	242.10	4,501.65
600	1286.46	1286.46	10000	235.47	4,498.92
700	1153.87	1153.87	11000	222.97	4,489.36
800	1041.46	1041.46	12000	211.43	4,479.13
900	945.72	945.72	15000	181.70	4,452.13
1150	762.89	762.89	18000	157.89	4,430.91
1400	638.45	638.45	19000	151.01	4,434.88
1650	552.99	552.99	20000	144.59	154.29
1900	493.68	493.68	—	—	—

NOTE: For the criticality case, the central DPC has two sources of heat generation: heat from radioactive decay and 4 kW of heat from steady-state criticality between 9,000 and 19,000 years after closure. All other DPCs in the model generate heat only from radionuclide decay.



NOTE: DPC = dual-purpose canister.

Figure 2-7. Heat Generation in the Critical DPC and in Adjacent DPCs, Based on the TSC-37 DPC

Conceptual Model for Thermal Response to Heat Conduction

The model for heat conduction from the DPC into the surrounding medium uses a superposition of the analytic solution for a continuous thermal point source to represent the finite heated length of each DPC, to represent the variable heat generated within each DPC, and to represent the 11 DPCs in the model. The details of this representation are as follows:

- At each instant in time, the heat output from a DPC is represented by point sources located at five discrete locations on the axis of each DPC: one location in the center of the DPC, two locations on axis at each end of the DPC, and two locations on axis and midway between the center and each end. The point sources at each of the five locations have a power output that is equal to one-fifth of the total power output from a DPC at any given time.

The uniform power release at the five locations is reasonable because each waste package has two Type 304 stainless steel shells with a combined thickness of approximately 2.5 in. (0.5 in. for the DPC and ~ 2 in. for the overpack). The thermal conductivity of Type 304 stainless steel sheet is 9.4 Btu/(hr·ft·°F) (16.3 W/[m·°C]) (Avallone et al. 2007, Table 6.1.9), which is approximately a factor of 10 greater than the thermal conductivity of bentonite backfill or of the shale host rock (Table 2-6). The high conductivity of the steel shells provides a relatively uniform thermal source along the axial length of each DPC, similar to the effect of having five

point sources with equal power along the axis of a DPC. The on-axis locations for the point sources is also reasonable because the analytical solution for a point source assumes a uniform, homogeneous medium, and it cannot represent the materials (such as UO₂ pellets, water, or the steel shells) in the DPCs.

A test calculation with nine discrete locations was performed and demonstrated only minor differences from the model with five discrete locations. A comparison of the outputs from both discretizations is presented in Section 3.3.2.1.

- The DPC has a variable heating rate from radionuclide decay and/or criticality (Table 2-5 or Figure 2-7) that cannot be represented by a single point source because the analytic solution is only valid for constant power. Given this constraint, the DPC model represents the variability in power output by superimposing multiple point sources with varying start times and varying power levels (both positive and negative) at each of the five discrete locations within each DPC. This approach is valid because solutions to the heat conduction equation (such as individual point sources) can be superposed provided the boundary and initial conditions are compatible, which is true for point sources. In particular, the temperature change at finite distance from a point source is 0 when a point source first turns on, so a new source does not (initially) perturb the existing temperature field, and the temperature field from a point source goes to 0 in the far field at all times. These features ensure that boundary and initial conditions are compatible with superposition of multiple point sources at a given location.

The variability in power output is represented by superposing multiple point sources or point sinks with varying start times. Figure 2-8 illustrates this approach using the data in Table 2-5. As shown in Figure 2-8, the first point source is at full power (4,002.73 W) and starts at time 0. After 25 years, a point sink is turned on with a negative constant power output of 3,459.25 W – 4,002.73 W = – 543.48 W that reduces the net power output to 4,002.73 W – 543.48 W = 3,459.25 W after 25 years, which is consistent with the data in Table 2-5. After 50 years, a second point sink is added with a negative constant power output of 3,097.82 W – 3,459.25 W = – 361.43 W, and so on. Each subsequent point source or point sink has a constant power output (positive or negative) that, when summed with all previous sources or sinks at a given location produces a net power output equal to the value on the power output data in Table 2-5.

In practice, the time intervals for the numerical solution are smaller than 25 years when the power output is changing rapidly. In this case, the piecewise linear power curve is interpolated between the data points in Table 2-5 to find the relevant power output for the numerical solution, which is then used to define the magnitude of the next thermal source or sink at that time.

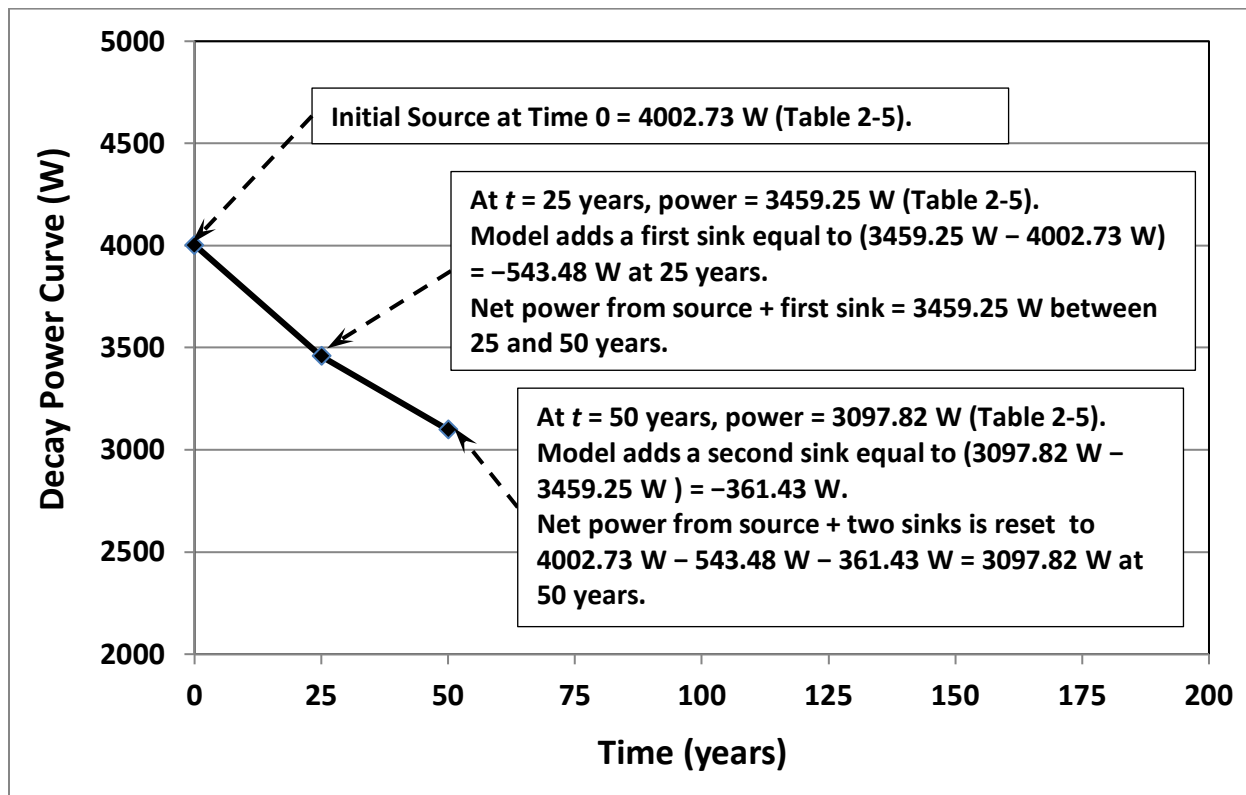


Figure 2-8. Illustration of Using Multiple Point Sources or Point Sinks to Represent the Variable Heat Output for the Thermal Conduction Model

In summary, combining the 5 discrete locations per DPC with multiple point sources at each location and with the 11 DPCs creates a triple sum in the mathematical model: first over the multiple sources/sinks at a given location (to provide the variable power level), second over the 5 discrete locations in each DPC (to provide a more uniform heat output per DPC), and third over the multiple DPCs adjacent to the critical DPC (to represent the temperature change from the 10 adjacent DPCs). This triple sum is explicitly derived in the following discussion of the analytic solution for multiple sources and multiple DPCs.

Mathematical Model for Thermal Response to Heat Conduction

This section describes the analytic solution for a continuous thermal point source with a constant power output and defines the triple sum for the temperature change from the multiple point sources in the model.

Analytic Solution for a Continuous Point Source—If heat is liberated at a rate $\phi(t)\rho c_p$ per unit time from time $t = 0$ to time t at point (x', y', z') , then the temperature change $v(x, y, z, t)$ at time t due to heat conduction in an infinite, homogenous medium with constant thermal properties is given by the following (Carslaw and Jaeger 1959, Section 10.4, Equation (1)):

$$v(x, y, z, t) = \frac{1}{8(\pi\kappa)^{3/2}} \int_0^t \phi(t') e^{-[(x-x')^2 + (y-y')^2 + (z-z')^2]/4\kappa(t-t')} \frac{dt'}{(t-t')^{3/2}} \quad \text{Equation 2-2}$$

where κ is thermal diffusivity (m²/s). The parameter $\phi(t)$ is defined as a function of the heating rate, $h(t)$:

$$\phi(t) \equiv \frac{h(t)}{\rho c_p} \quad \text{Equation 2-3}$$

where ρ is the density (kg/m³), c_p is the specific heat of the medium (J/[kg·K]), and the values for $h(t)$ are interpolated from the data in Table 2-5 for the critical DPC or for the surrounding DPCs with decay heat (only). Equation 2-2 and Equation 2-3 are referred to as a continuous point source of strength $\phi(t)$ from $t = 0$ onwards. If $\phi(t)$ is constant and equal to q , then the integral can be evaluated as the following (Carslaw and Jaeger 1959, Section 10.4, Equation (2)):

$$v(x, y, z, t) = \frac{q}{4\pi\kappa r} \operatorname{erfc} \frac{r}{\sqrt{4\kappa t}} \quad \text{Equation 2-4}$$

with

$$r = \sqrt{(x-x')^2 + (y-y')^2 + (z-z')^2} \quad \text{Equation 2-5}$$

representing the distance from the point source at (x', y', z') to the observation point at (x, y, z) . The *erfc* is the complementary error function, whose value is tabulated in numerous mathematical tables and also available as a function in Excel®. The units of q and $\phi(t)$ are “°C·m³/s”.

Each DPC is assumed to have a 1 m outer radius and is 5.6 m in length. The observation point for the temperature change at the critical DPC is at the top center point on the outer wall of the overpack. This point is 1 m above the cylindrical axis of the DPC.

The analytic solution for heat conduction near a continuous point source cannot represent a phase change (specifically evaporation or boiling of the groundwater around a DPC), so this solution is restricted to sub-boiling conditions. The solution also cannot represent a DPC surrounded by multiple materials, such as backfill in a host rock, if the backfill and host rock have different thermal properties. To address the latter case, separate calculations were performed using the thermal properties in Table 2-6 for the backfill and host rock; results are presented in Section 3.3.2.1.

Analytic Solution for Multiple Sources and Multiple DPCs—Using Equation 2-4, the temperature change from the multiple point sources at each location—the 5 spatial locations in each DPC and the 11 DPCs in the model—has been generalized as a triple sum in Equation 2-6:

$$v(x, y, z, t_i) = \sum_{m=1}^{ND} \sum_{k=1}^{NL} \sum_{j=1}^i \frac{\phi_m(t_j)}{4\pi\kappa r_{k,m}} \operatorname{erfc}\left(\frac{r_{k,m}}{\sqrt{4\kappa(t_i - t_j)}}\right), \quad i = 1, 2, 3, \dots, NP \quad \text{Equation 2-6}$$

The key input parameters in Equation 2-6 are as follows:

- i* is the index for the set of start times, $\{t_i\}$, for the individual point sources at each location in the DPCs. For the current model, the value of t_i is the same for all locations and all DPCs in the model, so subscripts k and m are not needed for t_i . The subscript $i = 1, 2, 3, \dots, NP$. The value of NP is 38 for the current model.
- j* is a summation index over the individual point sources at each location in each DPC that have started by time t_i . The subscript $j = 1, 2, 3, \dots, i$. Note that the innermost summation in Equation 2-6 does not end at NP , the total number of time points, because not all of the point sources are producing heat by time t_i .
- k* is the index for point source locations on the axis of each DPC. The subscript $k = 1, 2, 3, \dots, NL$. The value of NL is 5 for the current model.
- m* is the index for the number of DPCs in the model, $m = 1, 2, 3, \dots, ND$. The value of ND is 11 for the current model.
- $\phi_m(t_j)$ is the value for the “strength” of the point source beginning at time t_j , based on interpolation of data in Table 2-5 for the m^{th} DPC. The interpolated value of $\phi_k(t_j)$ differs for the critical (central) DPC versus the adjacent DPCs, which only have heat from radionuclide decay. Once a point source starts to generate heat, the value of $\phi_k(t_j)$ remains constant for all $t > t_j$. The relationship between the “strength” of a point source and the heating rate interpolated from Table 2-5 at time t_i is defined in Equation 2-7 and Equation 2-8 below.
- $r_{k,m}$ is the distance from an observation point to the k^{th} location in the m^{th} DPC.

Within the m^{th} DPC, heat is liberated at a constant rate per unit time, $h_m(t_j)$, beginning at time t_j and continuing until t_{NP} . The value of $h_m(t_j)$ is defined by interpolation of the data in Table 2-5 for a DPC with criticality or for a DPC without criticality. The “strength” at time t_j at each of the NL source locations in the m^{th} DPC, $\phi_k(t_j)$, is defined by Equation 2-7 and Equation 2-8:

$$\phi_m(t_1) \equiv \frac{h_m(t_1)}{(NL)\rho c_p}, \text{ for } j=1 \quad \text{Equation 2-7}$$

$$\phi_m(t_j) \equiv \frac{h_m(t_j) - h_m(t_{j-1})}{(NL)\rho c_p}, \text{ for } j=2, 3, 4, \dots, NP \quad \text{Equation 2-8}$$

Equation 2-7 and Equation 2-8 represent the variability of the power output by superposing the different strengths for multiple point sources with varying start times and with varying strengths at each location within a DPC, as explained in Section 2.3.2.1, subsection “Conceptual Model for Thermal Response to Heat Conduction”. The factor NL in Equation 2-7 and Equation 2-8 represents the equal distribution of power among the $NL = 5$ locations for point sources within each DPC. Equation 2-7 and Equation 2-8 are consistent with Equation 2-3 because the total heat in each DPC is split equally among NL discrete locations. The units of $\phi_k(t_j)$ are “°C·m³/s”.

Equation 2-6, Equation 2-7, and Equation 2-8, plus the data in Table 2-5, are the mathematical basis for the thermal conduction calculations presented in Section 3.3.2.1. The numerical solutions were evaluated in Excel spreadsheets.

Limitations of this Approach—Equation 2-8 is a solution for the heat conduction equation using a finite number of point sources. The following list presents the limitations of this methodology:

- The potential for boiling or rapid evaporation of the groundwater is not represented by the point source solution. For a repository in saturated shale at a depth of 500 m, the maximum hydrostatic pressure is estimated as 50 bars (725 psi). The boiling point of water at depth is then 264°C. Solutions of Equation 2-8 are not accurate if significant boiling occurs.
- The analytic solution for a point source assumes an infinite homogeneous medium with constant thermal properties. Multiple materials with different thermal properties, such as bentonite backfill and shale host rock, cannot be represented in a single calculation. Separate calculations—one with backfill thermal properties and a second with the shale host rock thermal properties (Table 2-6)—have therefore been performed to evaluate the sensitivity of temperature changes to these thermal properties. Results in Section 3.3.2.1 show a typical increase of about 30°C for the shale host rock properties versus the bentonite backfill properties.
- The analytic solution cannot represent the multiple materials, such as UO₂, steel, water, and Zircaloy, inside a DPC. Given the thick steel shell (on the order of 2.5 in. thick), each DPC has relatively high conductivity in comparison to the bentonite backfill and shale host rock surrounding each DPC. For a given power output, such as during criticality, the thermal gradients within the DPC are generally less than the thermal gradients in the geologic materials because of the relative high conductivity of materials in the DPC. In this situation, it is possible that the current models over predict peak temperatures on the surface of the DPC. However, further study and analysis are required to verify this hypothesis.
- The DPC model assumes that heat is generated at five discrete locations along the axis of a DPC: the center of the DPC, at each end of the DPC, and midway between the center and each end of

the DPC. A sensitivity calculation was performed to test the sensitivity of results to nine discrete locations versus five locations. This sensitivity calculation produces a $\sim 5^{\circ}\text{C}$ temperature rise with nine discrete locations versus five discrete locations. This increase is minor, as explained in Section 3.3.2.1, and is not significant for these calculations.

- This model does not include convective or radiative heat transfer. Separate calculations with conductive and convective heat transfer are described in Section 2.3.2.2 with results presented in Section 3.3.2.2. These calculations demonstrate that the permeability of the backfill needs to be greater than $5 \times 10^{-15} \text{ m}^2$ for convection to have a significant effect on thermal response, and this permeability level is much higher than for bentonite backfill or shale host rock in the shale reference case. Radiative heat transfer is not considered here because the emplacement drifts are backfilled. These statements may need to be revisited for a specific site and repository design.

Thermal Properties and Values for $\{t_i\}$

The thermal properties for the conduction-only calculations that were performed separately for the bentonite backfill and shale host rock are listed in Table 2-6.

Table 2-6. Thermal Properties for Calculations for Bentonite Backfill and Shale Host Rock

Property	Bentonite Backfill	Shale Host Rock
Saturated Thermal Conductivity (W/[m·°C])	1.5	1.2
Heat Capacity (J/[kg·°C])	830	830
Grain Density (kg/m ³)	2,700	2,700
Porosity (–)	0.35	0.2
Bulk Density (kg/m ³)	2,105	2,360
Thermal Diffusivity (m ² /s)	8.59×10^{-7}	6.13×10^{-7}

NOTE: Bulk Density = $(1 - \text{Porosity}) \times (\text{Grain Density}) + (1,000 \text{ kg/m}^3) \times (\text{Porosity})$; assumes water-saturated pore space.

Source: Mariner et al. 2017, Table 4-11.

The solution of Equation 2-6, Equation 2-7, and Equation 2-8 requires values for the set of time points, $\{t_i\}$, that define the start time for the i^{th} point source at each location in each DPC. Time values were selected to provide adequate resolution for the thermal response during rapid changes in power and to provide smooth temperature history curves.

2.3.2.2 Analytical Model with Heat Conduction and Heat Convection

Section 2.3.2.1 describes the analytical model for including heat conduction in the evaluation of temperature changes due to a steady-state criticality. This subsection (Section 2.3.2.2) considers an analytical model that adds buoyancy-induced convection due to the nonuniform heating of the saturated medium. As a first approximation for the inclusion of convective effects using an analytical approach, the SNF may be represented as a heat line source in which the heat generation rate is time-independent. This initial assessment assumes a saturated homogenous medium and a constant heat generation rate for a period of 10,000 years.

The calculations are based on an analytical solution for heat conduction and convection from a horizontal line source that represents a string of DPCs in a porous medium. The initial condition is a uniform temperature throughout, and the analysis provides the temperature increase as a function of depth and horizontal distance. For low Rayleigh numbers, an analytical asymptotic solution is available for the evolving temperature profile. Appendix A provides the mathematical details of the derivation for the analytical solution.

Table 2-7 presents the values of the input parameters for determining the contours of temperature increase above ambient for a line source of heat in a saturated porous medium. Values for heat capacity and thermal conductivity are based on the shale reference case (Mariner et al. 2017, Table 4-11). The fluid viscosity and thermal expansion coefficient are those of water. The rate of heat generation per unit length of line source is defined as $(4,000 \text{ W})/(20 \text{ m}) = 200 \text{ W/m}$, where the power level from steady-state criticality is 4 kW per DPC and the center-to-center spacing between adjacent DPCs is 20 m. Note that a power level of 200 W/m assumes that each DPC in the line source (i.e., in an emplacement drift) has a 4 kW criticality event simultaneously. This assumption is very conservative.

Table 2-7. Parameters for Determining Contours of Temperature Increase above Ambient for a Line Source in a Saturated Porous Medium

Parameter	Definition	Value	Units
c_m	porous media heat capacity	830	J/(kg·°C)
K	permeability	1×10^{-15} and 5×10^{-15}	m^2
k_m	porous media thermal conductivity	1.5	W/(m·°C)
q'	line source heat generation rate	200	W/m
α_m	porous media thermal diffusivity	8.585×10^{-7}	m^2/s
β	thermal expansion coefficient	2.9×10^{-4}	1/°C
μ	fluid viscosity	8.6×10^{-4}	kg/(m·s)
ρ	density	2,105	kg/m ³
σ	density times heat capacity of porous media divided by this product for the fluid	0.2	(-)

Section 3.3.2.2 presents the computational results for the analytical temperature contours. The results show that, for the parameters of interest, convective heat transfer may be neglected for rock permeabilities of 10^{-15} m^2 or less. This value is four orders of magnitude higher than the host rock shale permeability of 10^{-19} m^2 (Mariner et al. 2017, Table 4-11). However, as shown in Section 3.3.2.1, if the rock permeability increases to about $5 \times 10^{-15} \text{ m}^2$, then buoyancy-driven convective flow starts to become noticeable.

2.3.3 Thermal Analysis with PFLOTRAN

A set of simulations was run in PFLOTRAN considering heat flow and mass transport of air and water without consideration for radionuclide chemistry and transport. The model set up is similar to that described in Section 2.8. The purpose of these simulations is to analyze the thermal impacts of DPC direct disposal. Because radionuclide chemistry and transport are not included, these simulations can be run in PFLOTRAN under conditions for which dry-out could occur. Therefore, these simulations use a more

realistic set of initial conditions, and the results with these initial conditions were compared to results that do consider radionuclide chemistry and transport. Section 3.3.3 shows the analysis results in the form of temperature and water saturation distributions over time.

2.4 Chemistry

Steady-state criticality increases fission product concentrations, raise temperatures, and enhance radiolysis inside breached DPCs. The quantitative consequences of criticality—namely change in dose to a receptor—depends on the degree to which each of these factors affect mobilization and retardation of radionuclides from the package, which in turn depends upon the coupled chemical processes that control in-package chemistry. For the saturated shale+backfill case, in-package temperatures are calculated to reach between ~170°C and 200°C during steady-state criticality events and are set by the heat output of criticality, 4 kW (Section 3.3.2.1). In the alluvial case, temperatures cannot exceed the boiling point of water, 100°C. For reference, post-thermal pulse subcritical temperatures at Yucca Mountain were calculated to not exceed 60°C. Increased temperature is expected to accelerate corrosion of DPC internals, primarily 316 stainless steel, and to produce hydrogen gas in the process. The extent of corrosion and its impact on steel lifetime are calculated in Section 3.4.

Particularly in the shale case, steel corrosion makes in-package conditions reducing which inhibits fuel dissolution and stabilizes many of the actinides in lower solubility states. Radiolysis produces oxidants, such as hydrogen peroxide, and in the alluvial case, nitric acid. Acid production by radiolysis is important because it has the potential to increase concentrations of actinides, radionuclides which are solubility-limited and whose solubilities increase under acid conditions. Preliminary reaction path calculations done to constrain how effectively acid production from radiolysis would be buffered by reaction with corrosion products are described in Section 3.4.

2.5 Solubility

Spent fuel degradation produces relatively insoluble actinide oxides containing Pu, U, Am, Np, and Th, the solubilities of which control actinide release and tend to decrease with temperature. Increased temperature also decreases the solubilities of the oxides and carbonates of neutron poisons produced during steady-state criticality, such as ¹⁴⁹Sm, ¹⁵⁷Gd, and ¹⁴³Nd. Temperature-dependent actinide solubilities and their impact are documented in Section 3.5.

Again, a key question is how much radiolytic production of nitric acid in the alluvial case can lower the in-package pH and release actinides. In general, actinide solubilities are higher away from neutral pH: acidic or basic conditions favor actinide release. In-package pH is buffered to a near-neutral level by equilibria between steel corrosion product phases. Radiolytic production of nitric acid only occurs in the alluvial case where N₂ from the soil zone is present in the breached DPC.

2.6 EBS Degradation

A repository is typically designed with multiple engineered barriers that serve to reduce the rate of movement of water or radionuclides from the repository, prevent the release of radionuclides from the waste, or substantially reduce the release rate of radionuclides from the waste (40 CFR 197). Various man-made components can function as engineered barriers: a waste form that significantly decreases radionuclide mobility, a canister, a waste package, or even a material that is placed over and around the

waste to delay movement of water or radionuclides. In the analyses described in this report, the engineered barriers in the hypothetical repositories consist of the waste package, the fuel itself (cladding), and the backfill surrounding the waste package.

As stated in Section 1.4.1, it is assumed that, for a criticality event to occur, the waste package has failed, water has entered the waste package, and the configuration of water and SNF in the waste package is such that the configuration has an effective neutron multiplication factor (k_{eff}) greater than or equal to 1.0. For the analyses described in this report, the waste package consists of the DPC inside a larger disposal overpack. Thus, consistent with the assumption in Section 1.4.1, the waste package has failed and no longer functions as a barrier.

It is assumed, however, that both the DPC and the disposal overpack maintain their geometries as right circular cylinders. This assumption is reasonable for the hypothetical unsaturated alluvial repository, where the pressure on the waste package is roughly atmospheric. However, the assumption may not be reasonable for the hypothetical saturated repository in shale, where the hydrostatic pressure is on the order of 5 MPa (about 50 atm) and where there may be additional swelling pressure from the bentonite buffer on the order of 15 MPa (Posiva Oy 2012; SKB 2011). The effect of these pressures on the waste package and how the response of the waste package might affect criticality will be examined as this research effort moves forward.

In Section 1.4.2, it is assumed that, for the purposes of the work discussed in this report, the cladding on every fuel rod has small perforations that, while small enough to preserve the fuel assembly in a critical configuration, are also large enough to permit radionuclides to be released into a breached waste package and be transported into and beyond the EBS external to the waste package. This assumption enables a critical configuration to be maintained for 10,000 years while still allowing radionuclides to be released from the fuel rods. As such, it represents a reasonable starting point for the purposes of the analyses described in this report. This assumption will be investigated as the research effort moves forward.

It should be noted that cladding that has failed, even with small cracks or holes, is likely to split along its axis once the waste package fails and permits water or moist air into the waste package. This splitting is caused by interaction of the water or moist air with the fuel pellets and the interior of the cladding. These interactions release soluble fission products from the pellet, increase the volume of the pellet by forming less dense phases, and permit corrosion of the interior of the cladding (BSC 2005a). This axial splitting is likely to happen quickly relative to the regulatory period, which is assumed to be 1,000,000 years per Section 1.4.3. Fuel degradation tests were performed with two intentionally failed Zircaloy-clad fuel rods in humid air at 175° (BSC 2005a). The cladding on both test samples split axially in less than two years. The swelling of fuel pellets, corrosion of the interior of the cladding, and axial splitting of the fuel rod would change the geometry and chemistry of the SNF in the DPC, perhaps rendering the SNF in the DPC subcritical. While these degradation processes should be investigated further, as discussed below and for the purposes of the analyses described in this report, it is necessary to maintain a critical configuration for 10,000 years and, thus, to assume that these degradation processes do not occur.

In the PA for the Yucca Mountain repository, it was assumed that all cladding in a waste package splits instantly at the time of waste package failure (SNL 2008; DOE 2008b). A waste package was considered to be failed at the time of the first penetration of the waste package by any process that allowed the ingress of oxygen and water vapor into the package. This assumption is conservative with respect to the

model used in the Yucca Mountain PA, which did not include the occurrence of criticality. However, this assumption is not necessarily conservative if criticality is included in the model; the lower reactivity associated with immediate cladding axial splitting could preclude the occurrence of criticality. That is, assuming all cladding splits axially at the time of waste package failure is not conservative for modeling the occurrence and consequences of criticality in the waste package.

As research into the occurrence and consequences of postclosure criticality continues, the degradation processes that could affect the performance of Zircaloy as a barrier will be investigated. These processes include general corrosion, pitting corrosion, crevice corrosion, creep rupture, internal pressurization, stress corrosion cracking, and hydride cracking (SNL 2008; DOE 2008b). Of particular importance are the effects of postclosure criticality on these degradation processes; unlike the reactor in which the SNF was originally irradiated, the environment inside a disposed DPC is not controlled (e.g., water chemistry is not controlled to avoid cladding corrosion [EPRI 2002; EPRI 2005]).

The third barrier in the hypothetical repositories modeled in this report is the backfill: crushed alluvium for the unsaturated alluvial repository and bentonite for the saturated shale repository. Bentonite is proposed as a backfill material because (1) it swells when it resaturates, preventing the drift from becoming the preferential flow path for ground water, and (2) it has low permeability ($\sim 10^{-20}$ m²) (Liljenfeldt et al. 2017). However, the barrier performance of clay-rich materials, such as bentonite, is thought to be sensitive to temperatures above 100°C, particularly in the presence of water. The behavior of bentonite at temperatures above 100°C is currently being studied (Mariner et al. 2018). As shown in Section 3.3 and Section 3.8, the temperature of the waste package surface in a steady-state criticality event in the hypothetical saturated repository rises well above 100°C; hence, the bentonite backfill temperature also exceeds 100°C. Therefore, for the purposes of the analyses conducted in this report, it is assumed that the bentonite backfill in the hypothetical saturated repository does not sorb radionuclides as well during the steady-state criticality event when the backfill temperature is above 100°C. Crushed alluvium is not sensitive to temperature in the same way that bentonite is. The behavior of crushed alluvium is not affected by the steady-state criticality event, except to the extent that (1) its thermal conductivity is sensitive to temperature and (2) the absence of water precludes radionuclide transport.

Much of the foregoing discussion focuses on the effects of steady-state criticality on engineered barriers. In the event of a transient criticality event, it is assumed that, similar to the steady-state criticality event, the waste package has failed such that a quantity of water sufficient to cause a transient criticality event has entered the waste package. The model for a transient analysis that is being developed (Section 2.1.4) will yield the time-dependent power, reactivity, and delayed neutron precursor density. These results will be used to calculate damage to the EBS surrounding the critical package and to evaluate whether the transient event could damage the EBS in the vicinity of other waste packages.

2.7 Permanent Criticality Termination Processes

The potential for postclosure criticality in a DPC could diminish if certain processes or characteristics cause permanent reduction in DPC reactivity. An analysis was conducted to evaluate the DPC characteristics and geologic disposal processes that could render the potential for criticality in a DPC permanently insignificant, thereby eliminating the need for further consideration or analysis. The goal of the analysis is to answer the following questions:

What SNF or DPC characteristics could be impacted by disposal events and processes, including decay, corrosion, dissolution, and criticality, such that the potential for criticality initiation or continuation becomes permanently significantly diminished? How and when would those impacts occur?

While the approach used for the analysis is described below, the actual results are provided in Section 3.7. For this analysis, the term “permanent termination of criticality” is used to denote the significant diminishment of criticality potential, but not to imply absolute prevention of criticality potential. The “equivalent” ²³⁵U enrichment of SNF in a typical DPC could exceed 2.5 wt.% and the total mass of ²³⁹Pu could exceed 100 kg, both of which are well above minimum critical limits for idealized conditions (ANSI/ANS 8.1 2014). However, even though the potential for criticality in a DPC cannot be completely ruled out, that potential can become very low because of the presence of absorbers, changes in geometry, and limited moderation (as explored further in this analysis).

Criticality states (k_{eff}) for several hundred DPCs were evaluated based on as-loaded configurations with full burnup credit in a disposal analysis basis configuration (DABC), which represents intact SNF assemblies without any credit for fixed neutron absorber plates (i.e., absorber plates are assumed corroded, constituents dissolved, and removed from DPC) and with no credit for baskets with carbon steel components. Based on these calculations, the DPCs that could support a critical configuration have a range of excess reactivity from essentially 0 (i.e., $k_{eff} = 1$) to over 0.1 (i.e., $k_{eff} > 1.1$) (Liljenfeldt 2017).

Parametric analyses for various commercial SNF degraded configurations are documented in *Commercial Spent Nuclear Fuel Igneous Scenario Criticality Evaluation* (SNL 2007). These calculations demonstrate that degraded fuel configurations, even when the fuel degrades into self-moderated schoepite and the remaining porosity in the fuel and the canister void space are filled with water, are less reactive than configurations with an intact fuel lattice. The caveat is that the fuel composition must remain unchanged. Table 2-8 (excerpted from SNL 2007, Table 6-5) presents k_{eff} values for a base case representing intact fuel in a TAD canister and for a bounding degraded configuration that is potentially credible.

Table 2-8. Comparison of k_{eff} Values for PWR SNF Configurations

Case Description	k_{eff}	Delta from Base Case
Base Case —PWR SNF assemblies at 4 wt.%, 30 GWd/MTU in a TAD canister in a tightly packaged geometry (assemblies separated by 6 mm of borated stainless steel plates). No basket.	0.954	N/A
Degraded Configuration —PWR SNF assemblies at 4 wt.%, 30 GWd/MTU in a TAD canister with the fuel represented as fully hydrated schoepite with 15% porosity (assuming the stable form of schoepite that maximizes the amount of hydrogen present). The degraded fuel assemblies are separated by 6 mm of borated stainless steel plates and no basket.	0.858	0.096

A number of sensitivity cases with fresh fuel comparing intact configurations to various configurations of schoepite at a range of porosities and water saturation levels demonstrate that, although some “theoretical” combination of parameters for degraded configurations could approach the reactivity of intact SNF, none would exceed it (SNL 2007, Table A-12). Therefore, the most reactive configuration for commercial SNF in a DPC consists of an intact fuel lattice (i.e., fuel pitch does not change) with closely grouped assemblies and without a fuel basket or neutron absorber plates. This configuration is denoted in this report as the DABC.

The occurrence of disposal processes and events is a direct function of disposal time. For fundamental processes (e.g., decay), time is absolute; however, for other processes (e.g., corrosion), time is relative because it is driven by a combination of DPC characteristics (e.g., fuel condition and basket composition), geologic parameters (e.g., infiltration rate), engineered barrier design, and other processes and events that impact in-package chemistry. The following is a list of typical criticality control parameters as well as the basis for selecting those parameters of relevance to criticality potential in disposed DPCs:

- **Reflection**—Reflection is often bounded in criticality analyses based on the potential materials that could be present. Because DPCs are relatively large systems and the potential for criticality with the depleted low-enriched uranium (LEU) fuel can exist only at thermal neutron energies, reflection plays a secondary role and could change during disposal. Therefore, reflection does not influence the determination of permanent termination of criticality potential in disposed DPCs.
- **Leakage**—Similar to reflection, leakage plays a minor role in determination of criticality state because the DPCs are large thermal systems. Once the system is fully degraded, leakage impacts due to the increase in surface-to-volume ratio could significantly reduce system reactivity; however, these systems are much less reactive than the DABC for DPCs. Therefore, leakage is not evaluated as a separate mechanism for permanent termination of criticality potential in disposed DPCs.
- **Neutron Absorption**—There are several neutron absorbers that could be present in a DPC, including fixed neutron absorber plates/rods, soluble absorbers in incoming water, and absorbers integral to the SNF. Absorber plates are not credited (i.e., assumed not present) in the DABC. Dissolved species in incoming water are repository dependent. Retention of neutron absorbers from corrosion products is repository and time-dependent (i.e., not permanent). Therefore, the only absorption parameter evaluated is that associated with the SNF composition based on the burnup credit analysis.
- **Geometry**—The primary geometry parameters relate to baskets that maintain separation between the fuel assemblies, grid spacers that maintain separation between the fuel rods, and cladding/fuel that maintain the lumped configuration (i.e., most reactive configuration for LEU systems). DPCs have a variety of basket designs. The DABC does not credit baskets (i.e., assumed not present) for most DPC designs. Therefore, the geometry parameters evaluated are the grid spacers, which maintain fuel pin separation, and the cladding/fuel.
- **Fissile Material Mass/Concentration/Enrichment**—These parameters have a direct influence on permanent criticality termination and, thus, are evaluated collectively ensuring that decay, depletion, ingrowth, and dissolution are taken into account.

- **Interaction**—Neutronic coupling between the SNF disposed in neighboring DPCs is not meaningful for the large DPCs. Neutronic coupling between the fuel assemblies within a DPC is an inherent assumption of the criticality analysis. Materials that were intended to reduce interaction between fuel assemblies (e.g., neutron absorber palates, baskets) will eventually corrode and are not credited in the DABC; therefore, changes in interaction cannot lead to permanent termination of criticality potential in disposed DPCs.
- **Temperature**—Temperature can impact the oscillatory behavior of criticality; however, it cannot lead to permanent termination of criticality.
- **Moderation**—Moderation is the most important parameter in establishing the potential for criticality in DPCs. Availability of water inside a disposed DPC is highly dependent on repository geology (e.g., unsaturated tuff versus saturated shale) as well as engineering barrier design. If water pooling inside a DPC can be permanently prevented, then there is no potential for criticality with intact fuel configurations. Evaluating the ability of the waste package to contain sufficient moderator over long time scales is beyond the scope of this report; therefore, it is assumed for the purposes of this study that sufficient moderator is present.

To determine the point at which criticality potential for a DPC is permanently terminated, the change in reactivity due to perturbations during disposal must be greater than the excess reactivity for the DABC of a specific DPC. Given the analysis approach summarized above, Section 3.7 explores the potential magnitudes of permanent reactivity changes resulting from irreversible geometry changes, burnup, decay, and compositional changes due to corrosion/dissolution. The purpose is to determine whether there are DPCs for which criticality can be permanently terminated and, if so, to identify the associated processes and timing of termination.

It is important to note that the results and specific values provided in Section 3.7 are not intended to be absolute or applicable to all DPCs with any level of precision. They are presented to provide perspective and to guide follow-on analyses using specialized codes with detailed criticality state models that are based on potential material compositions and take into account decay, depletion, and dissolution.

2.8 Repository Simulations

The initial examination of the impacts of direct DPC disposal in a hypothetical geologic repository is described in this subsection. Using PFLOTRAN, this study simulated 3D multiphase flow and aqueous radionuclide transport in the near field immediately surrounding a single DPC waste package in a repository drift (Figure 2-9). By modeling a single waste package in one repository drift, this study developed an initial understanding of the impact that the unique size and thermal loading of a DPC can have on repository performance.

Section 2.8.1 presents material properties for repositories and host rock media in two hypothetical geologic environments. Base case analyses were performed for the saturated shale host rock scenario considering decay heat and radionuclide inventory of a 37-PWR DPC that stays subcritical for the duration of the simulation. Section 2.8.2 provides a description of comparison simulations that are similar to the base case simulations except the fuel in the waste package was assumed to experience a steady-state criticality. Among other things, the inclusion of a steady-state criticality causes a change to the decay heat, an additional heat released due to the criticality event, and a change in the waste package

radionuclide inventory. The results of the base case and comparison simulations are provided in Section 3.8.1 and Section 3.8.2, respectively.

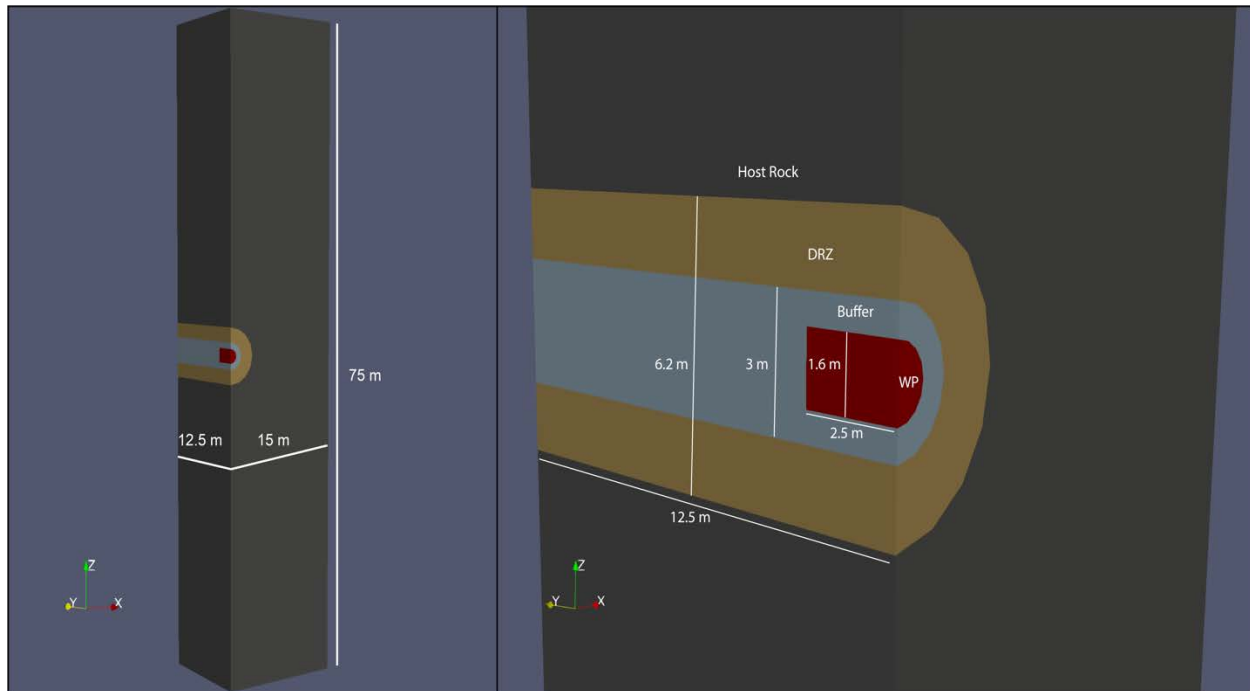
2.8.1 Base Case Simulations (without Criticality)

2.8.1.1 Introduction

This subsection focuses on the design of the near-field repository models used in this and subsequent subsections, with particular emphasis on heat and mass flow in a conceptual model that is consistent with simulations considering an in-package criticality. The saturated shale reference case is simulated using a single waste package near-field model. However, it was not possible to model radionuclide transport in the hypothetical alluvial repository because some grid cells became fully gas saturated under a 37-PWR heat load (i.e. there is no liquid phase). The capability to model radionuclide transport in gas-saturated regions is currently being developed in PFLOTRAN. Therefore, this subsection outlines the material properties that will be used in the unsaturated alluvium reference case simulations. The more detailed thermal analysis of the reference shale repository presented in Section 2.3.3 uses more physically representative initial conditions but is unable to track radionuclide transport because of simulator capability restrictions. The associated analysis results in Section 3.3.3 show, however, that the different initial conditions used for consideration of radionuclide transport in the repository simulations described in Section 2.8 should still produce appropriate results for the shale host rock scenario. In Section 3.8, repository simulations that include effects of in-package criticality on heat generation and radionuclide transport are compared to the base-case simulations that do not consider in-package criticality.

2.8.1.2 Model Design

A 3D model was developed to examine near-field mass and energy transport processes in the immediate vicinity of a single waste package in a repository drift (Figure 2-9). This model uses quarter symmetry to reduce computational complexity: symmetry is assumed between halves of the waste package across the x - z plane and also across the y - z plane. No flow boundaries are employed along the side boundaries of the model assuming that more waste packages are spaced evenly along the drift and that other drifts are present in the repository parallel to the one being modeled (similar to Rutqvist et al. 2011). Symmetry is not assumed across the x - y plane because gravity acts vertically, which can result in buoyant flow. The entire simulation domain is 15 m perpendicular to the drift in x , by 12.5 m parallel to the drift, by 75 m vertically (z). The drift is modeled as a half cylinder (representing a quarter of the waste package) with a diameter of 3 m, the disturbed rock zone (DRZ) extends to a diameter of 6.2 m, and the 37-PWR DPC waste package is discretized as 1.6 m in diameter. The length of the quarter waste package is set to 2.5 m in this model, which corresponds to a full waste package length of 5 m.



NOTE: DRZ = disturbed rock zone.
 WP = waste package.

Figure 2-9. Model Domain for a 3D, Single-Drift, Single-Waste Package Simulation using Quarter Symmetry Boundaries

Two different hypothetical repository host rocks are considered in this analysis: a shale host rock and an alluvium host rock. The shale host rock is modeled as a homogeneous, water-saturated medium with the repository drift set at approximately 500 m below ground surface. In contrast, future analysis of the alluvium host rock will use the same single-drift model, but the medium will be unsaturated with a repository located 250 m below ground surface. Material properties of each host rock and their corresponding repositories are listed in Table 2-9.

The analysis of simulation results for saturated shale without criticality (Section 3.8.1) compares profiles of temperature, pressure, and liquid/gas saturation at four different locations in the model domain: in the center of the waste package, at the outside edge of the waste package in the drift, at the outer edge of the drift in the DRZ, and in the host rock along the outer boundary of the drift. Outlined in Figure 2-10, these four observation points represent locations where there are abrupt contrasts in material properties and/or initial conditions.

Table 2-9. Physical Properties of Model Materials

Property	Waste Package ^b	Buffer (shale) ^b	Shale DRZ ^b	Shale Host Rock ^b	Buffer (alluvium) ^a	Alluvium DRZ ^a	Alluvium Host Rock ^a
Porosity (-)	0.5	0.35	0.2	0.2	0.4	0.4	0.4
Permeability (m ²)	1×10 ⁻¹⁶	1×10 ⁻²⁰	1×10 ⁻¹⁸	1×10 ⁻¹⁹	1×10 ⁻¹³	1×10 ⁻¹²	1×10 ⁻¹³
Density (kg/m ³)	5,000	2,700	2,700	2,700	2,700	2,700	2,700
Thermal Conductivity (W/[m·K])	16.7	1.5	1.2	1.2	2.0	2.0	2.0
Heat Capacity (J/[kg·K])	466	830	830	830	830	830	830
Liquid Residual Saturation (S _{rl})	0.1	0.1	0.1	0.1	0.1	0.1	0.1
Gas Residual Saturation (S _{rg})	0.1	0.1	0.1	0.1	0.1	0.1	0.1
Saturation Function		Van Genuchten Function					
alpha (Pa ⁻¹)	1×10 ⁻⁴	6.25×10 ⁻⁸	6.67×10 ⁻⁷	6.67×10 ⁻⁷	1×10 ⁻³	1×10 ⁻³	1×10 ⁻³
m (-)	0.5	0.375	0.333	0.333	0.5	0.5	0.5
Liquid Relative Permeability		Mualem Function					
m (-)	0.5	0.375	0.333	0.333	0.5	0.5	0.5
S _{rl} (-)	0.1	0.1	0.1	0.1	0.1	0.1	0.1
Gas Relative Permeability		Mualem Function					
m (-)	0.5	0.375	0.333	0.333	0.5	0.5	0.5
S _{rl} (-)	0.1	0.1	0.1	0.1	0.1	0.1	0.1
S _{rg} (-)	0.1	0.1	0.1	0.1	0.1	0.1	0.1

NOTE: Details of van Genuchten saturation function and Mualem relative permeability functions can be found in PLFOTRAN (2016).

Source: ^a Sevougian et al. 2019a.

^b Sevougian et al. 2019b.

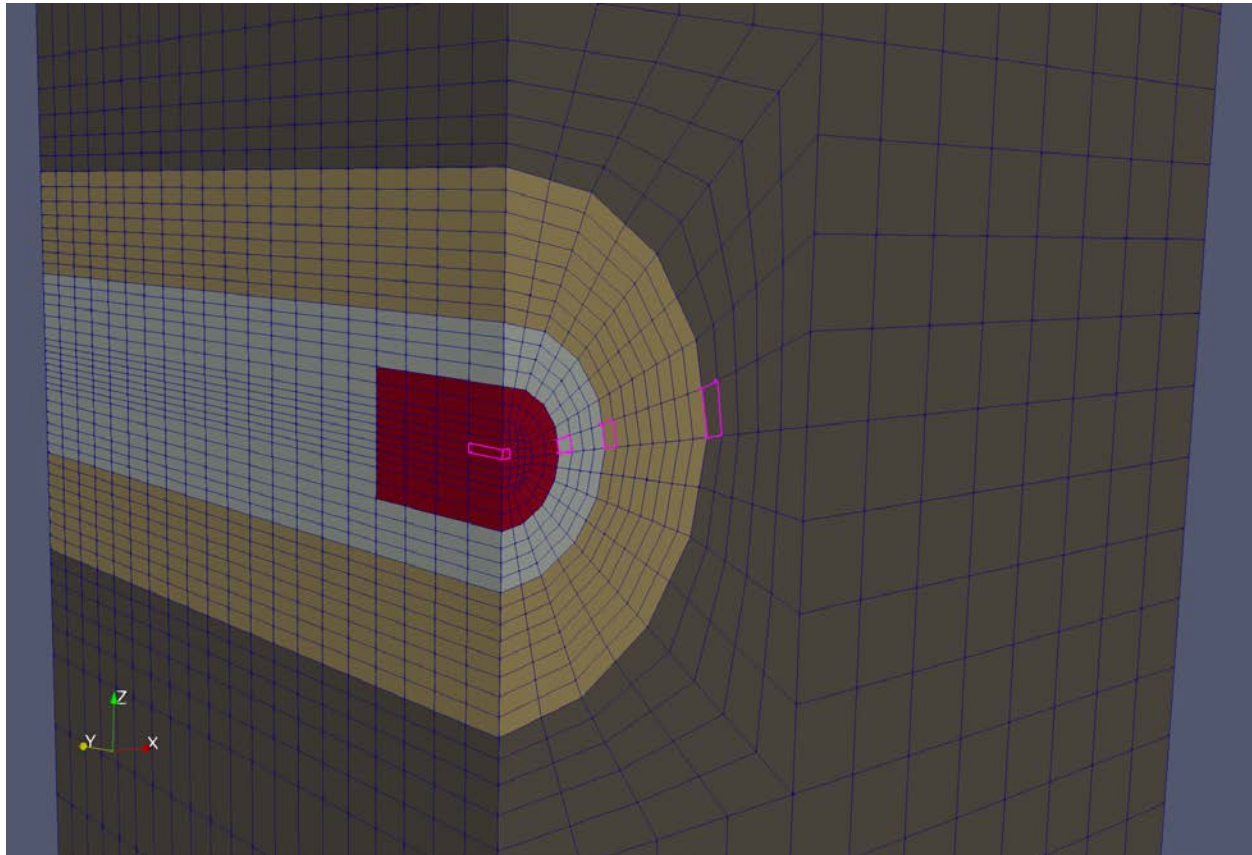


Figure 2-10. Locations of Four Observation Cells: Center of the Waste Package, in the Drift near the Edge of the Waste Package, in the DRZ at the Edge of the Drift, and in the Host Rock at the Edge of the DRZ

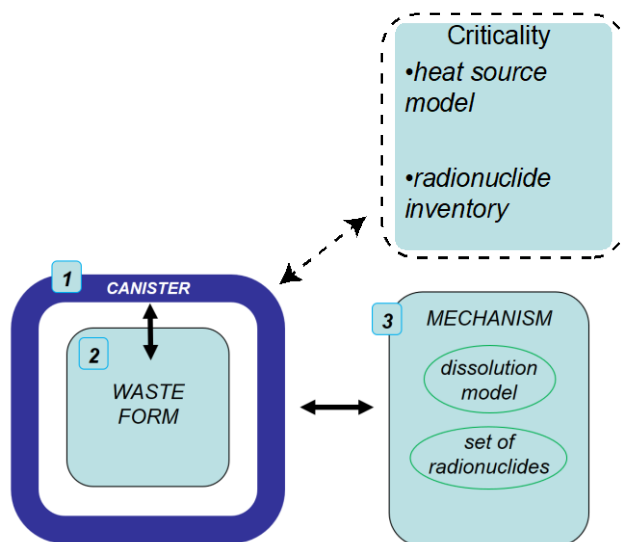
It is generally understood that decay heat from the radionuclide inventory of a 37-PWR DPC exerts a greater thermal load than other smaller (e.g., 21-PWR) waste packages. A decay heat source corresponding to the radionuclide inventory of one quarter of a representative 37-PWR DPC is imposed on this model (Painter et al. 2019). If the SNF in a DPC were to become critical, changes in radionuclide inventory will result in additional changes to the decay heat; in subsequent simulations that consider an in-package criticality, decay heat is correspondingly adjusted.

2.8.2 Comparison Simulations (with Criticality)

Modifications to PFLOTRAN were made to simulate in-package criticality and to take input from external neutronics codes. This subsection details the development of a criticality submodule that is attached to the waste form process model in PFLOTRAN. Additionally, this subsection discusses the current state of development of an interface to convert output of external neutronics codes into PFLOTRAN input.

2.8.2.1 Criticality Submodule Development

The criticality submodule in PFLOTRAN was developed as part of this work as an attachment to the waste form process model (Figure 2-11). In this way, criticality parameters are associated with individual waste forms in a simulation, which allows for flexibly assigning heterogeneous criticality events to different waste packages in a repository-scale simulation. For instance, different criticality start and end times can be applied to different waste forms, or waste forms that go critical can give off different heat output.



NOTE: Dashed lines indicate new functionality added through the criticality submodule.

Figure 2-11. Criticality Parameters Are Associated with Individual Waste Forms through a Submodule Built onto the Waste Form Process Model

To use the criticality submodule, a user must first define a waste form in a PFLOTRAN input deck (PFLOTRAN 2016). Currently, steady-state criticality is implemented as a constant heat of criticality added on top of a variable decay heat source. Decay heat and radionuclide inventory are both read in from external files. Within the waste form block, the `CRITICALITY` keyword is used to associate a criticality mechanism (defined by `MECH_NAME`) with a start time and an end time (`CRIT_START` and `CRIT_END`, respectively). In a subsequent block, the criticality mechanism (the `CRITICALITY_MECH` block) is defined by a name (`NAME`), a steady-state heat of criticality (`HEAT_OF_CRITICALITY`), a decay heat (`DECAY_HEAT`) that can be prescribed or read in from a dataset as either the total decay heat (`TOTAL`) or the additional decay heat due to the criticality (`ADDITIONAL`), and a radionuclide inventory (`INVENTORY`) that can be read in as a dataset that describes the radionuclide inventory as a function of time.

2.8.2.2 Interface with Neutronics Codes

As described above, the criticality submodule modifies the waste form process model in PFLOTRAN to take an external file as input to modify the radionuclide inventory in the waste package and the decay heat during a criticality event. The decay heat file must contain a table with decay heat output and associated postclosure time; at any given time PFLOTRAN uses heat input values that are linearly interpolated between times provided in the input table. Similarly, radionuclide inventories are read in from an external table that describes radionuclide mass fractions (mass of radionuclide per total mass of all radionuclides) at different times postclosure, and inventories at any given time are linearly interpolated between times specified in the table. A Python script was developed to assemble radionuclide inventories exported from external neutronics codes (Section 2.1) into inventories that the PFLOTRAN criticality submodule can read and apply. Future work will expand integration with neutronics calculations to model criticality power output as a function of water saturation, as water content plays a key role in moderating criticality.

A subset of the total radionuclide inventory presented in Section 3.2 was used to test the criticality submodule and the interface with neutronics code outputs, as described above. This subset contains ten radionuclides: ^{129}I , which is one of the most soluble and does not adsorb; the decay chain including ^{241}Am , ^{237}Np , ^{233}U , and ^{229}Th ; three actinides whose inventory increases significantly as a result of the criticality event (^{238}Pu , ^{240}Pu , and $^{242\text{m}}\text{Am}$); and two fission products whose inventory increases significantly as a result of the criticality event (^{90}Sr and ^{137}Cs).

In simulations both with and without an in-package criticality event, waste package breach occurs at 9,000 years simulation time, at which point the waste form is considered exposed to water in the drift. Radionuclide inventories in the solid waste form as a function of time are read in externally through the criticality submodule, and these inventories differ depending on whether there was a criticality event or not. In the case of a criticality event, the event is considered to be concurrent with waste package breach.

Aqueous radionuclide concentration is tracked after waste package breach with consideration for solubility limits, adsorption, and decay/ingrowth. Adsorption is modeled in PFLOTRAN using a linear isotherm: the distribution coefficient (K_d) characterizes the distribution of the solute between the adsorbed phase and the aqueous dissolved phase. Decay and ingrowth in the aqueous phase are calculated using a three-generation analytical solution (Mariner et al. 2016) through the UFD Decay process model in PFLOTRAN. Parameters are listed in Table 2-10; parameter selection and model implementation are consistent with the shale reference case outlined in Mariner et al. (2017). For simulations that include a steady-state criticality event, K_d values in the backfill are assumed to be zero, a very conservative assumption that represents lack of sorption capability of the backfill as a result of temperatures being above 100°C. As this work progresses, the effects of a postclosure steady-state criticality event (Section 2.5) on radionuclide solubilities will be studied and quantified to the extent possible.

Table 2-10. Inputs to PFLOTRAN for Each Radionuclide

Isotope	Solubility ^a (M)	K_d in Backfill ^b (mL/g)	K_d in DRZ and Shale ^b (mL/g)	Daughter Product	Decay Constant ^c (s ⁻¹)
¹²⁹ I	Infinitely soluble	Nonsorbing	Nonsorbing	¹²⁹ Xe	1.4×10^{-15}
²⁴¹ Am	4×10^{-7}	12,000 0 ^d (criticality event)	50,000	²³⁷ Np	5×10^{-11}
²³⁷ Np	4×10^{-9}	1000 0 ^d (criticality event)	900	²³³ U	1.03×10^{-14}
²³³ U	7×10^{-7}	100,000 0 ^d (criticality event)	8000	²²⁹ Th	1.38×10^{-13}
²²⁹ Th	6×10^{-7}	3,000 0 ^d (criticality event)	8000	²²⁵ Ra	2.77×10^{-12}
²³⁸ Pu	2×10^{-7}	1,000 0 ^d (criticality event)	900	²³⁴ U	2.50×10^{-10}
²⁴⁰ Pu	2×10^{-7}	1,000 0 ^d (criticality event)	900	²³⁶ U	3.35×10^{-12}
^{242m} Am	4×10^{-7}	12,000 0 ^d (criticality event)	50,000	²³⁸ Np	1.56×10^{-10}
¹³⁷ Cs	Infinitely soluble	380 0 ^d (criticality event)	400	^{137m} Ba	7.30×10^{-10}
⁹⁰ Sr	Infinitely soluble	Nonsorbing	Nonsorbing	⁹⁰ Y	7.60×10^{-10}

Source: ^aClayton et al. 2011, Table 3.3-23.

^bClayton et al. 2011, Table 3.3-23.

^cDecay constants from ORIGEN (Croff 1983) or NNDC (National Nuclear Data Center; BNL n.d.).

^dDuring criticality.

See Mariner et al. (2017) for more detail on parameter values, and PFLOTRAN (2016) for process model implementation.

DRZ = disturbed rock zone.

3. CRITICALITY ANALYSES RESULTS

Section 2 provides descriptions of various analyses designed to develop an understanding of the effects of postclosure criticality on different aspects of repository performance. Section 3 presents the associated results of these analyses: neutronics in Section 3.1, inventory in Section 3.2, thermal effects in Section 3.3, chemistry in Section 3.4, solubility in Section 3.5, EBS degradation in Section 3.6, permanent criticality termination processes in Section 3.7, and repository simulations in Section 3.8.

3.1 Neutronics

To demonstrate the new Terrenus code, simulations of a simplified, small DPC-style canister containing a 3×3 array of PWR fuel pins were conducted. In these simulations, the canister is 370.0 cm tall, and the fission heat is calculated at 12 evenly spaced axial levels along the canister height. A total power of 100 W is assumed. The temperature at the outer boundary of the canister is assumed to be fixed at an ambient temperature of 60° F.

A relative convergence criterion of 10^{-3} is imposed on calculations for the water density, water temperature, and fuel temperature, which are determined by COBRA. For each iteration, a Monte Carlo radiation transport simulation is performed with 300 inactive cycles, 300 active cycles, and 100,000 histories per cycle, which are sufficient in number to demonstrate the coupling capability. Because of the low power of this 3×3 array, the thermal hydraulics and neutronics are loosely coupled, and convergence occurs after two iterations. The converged fission source from previous iterations is not currently used; however, the intent is to add this capability in the future to reduce the number of inactive cycles necessary for all iterations after the first. Since the only concern is to demonstrate the coupling machinery, simplified compositions are used to reduce the computational expense of the radiation transport calculation. The fuel is low-enriched, fresh UO_2 containing only ^{16}O , ^{235}U , and ^{238}U . The gap is pure ^4He , and the clad is pure ^{90}Zr . The water is slightly borated to reduce the reactivity of the fresh fuel. Obviously, though not realistic for SNF, the reduced number of nuclides in fresh fuel significantly decreases the computational expense of the radiation transport without having any effect on the coupling performance under investigation here.

Fission power is calculated using a mesh tally placed over the pin cell boundaries spanning 18 evenly spaced axial levels. The energy released per fission is calculated using the values in the ENDF-VII.1 (evaluated nuclear data file) libraries, which are 194.02 MeV/fission in ^{235}U and 198.122 MeV/fission in ^{238}U . Because COBRA-SFS does not support radiative heating in the channel, gamma heating is neglected. Future calculations could compute the gamma heating to gain more understanding of the consequence of this assumption.

3.1.1 3×3 Assembly Power Distributions

Figure 3-1 shows the radial power distribution at the midplane, $z = 185$ cm, of the 3×3 geometry. Physically, the power distribution should be perfectly flat. Some statistical noise can be observed in the converged solution at iteration 1, although the variation is fairly modest (note the ranges of the color bars on the right of each image). Nevertheless, it may be necessary to run more particles to obtain reduced variance and a more tightly converged fission source in future calculations.

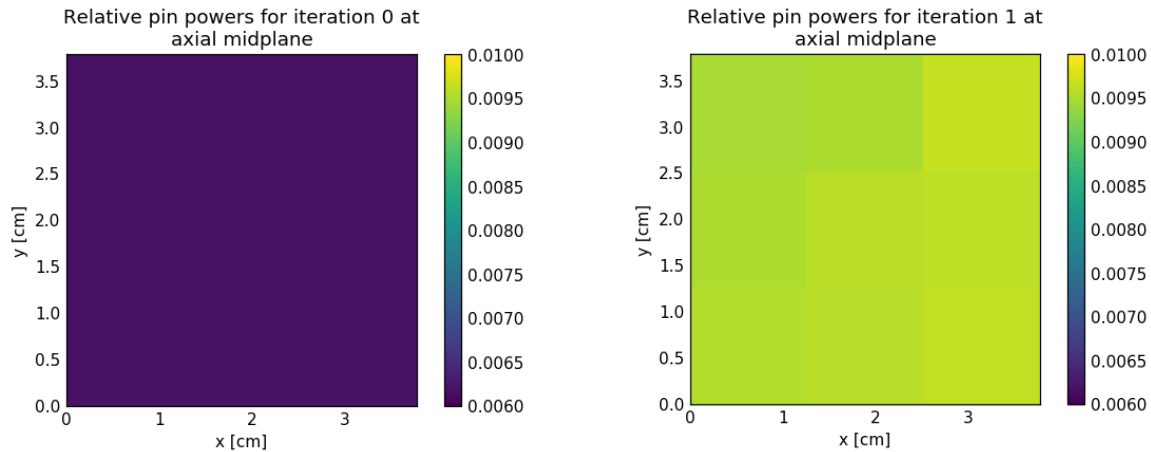


Figure 3-1. 3x3 Radial Power Distribution over Two Iterations at $z = 185$ cm

3.1.2 3x3 Assembly Channel Temperature Distributions

Figure 3-2 shows channel temperatures for two iterations. Iteration 0 starts with a uniform channel temperature at the ambient temperature of 60°F . The converged solution for iteration 1 is obtained using the fission powers calculated by Shift. Convergence is rapid because the very low power of this critical assembly results in only a loose coupling between the neutronics and the thermal hydraulics. A higher power would result in a tighter coupling requiring more iterations to converge. As expected, the inner channels are at a higher temperature because they are not adjacent to the cooler ambient temperature.

Figure 3-3 shows the axial distribution of the temperature in one of the central channels. In this case, only iteration 0 and iteration 1 are shown since, as before with the radial distribution, the axial distribution converges immediately with the first iteration. The axial temperature distribution behaves as expected, with temperatures rising from the bottom to the top of the model.

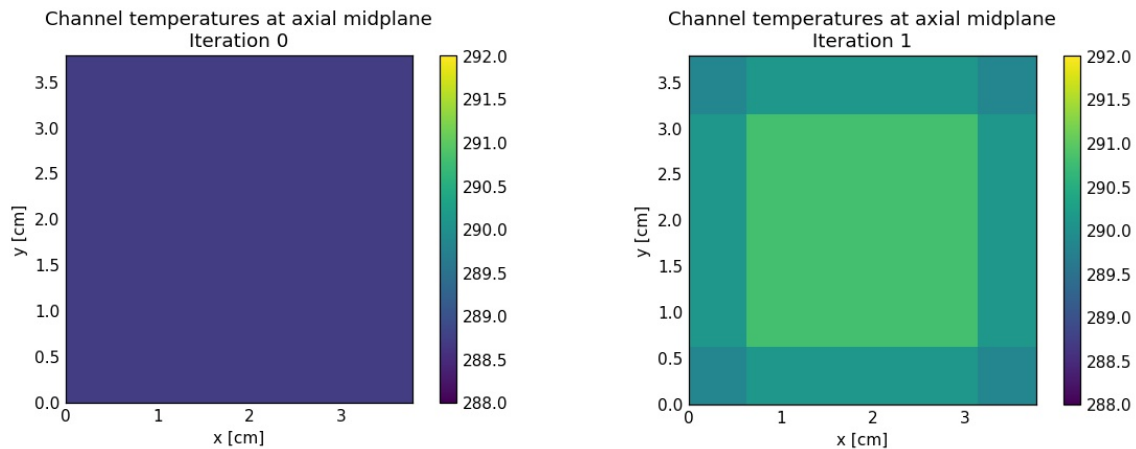


Figure 3-2. 4x4 Channel Temperatures over Two Iterations at $z = 185$ cm

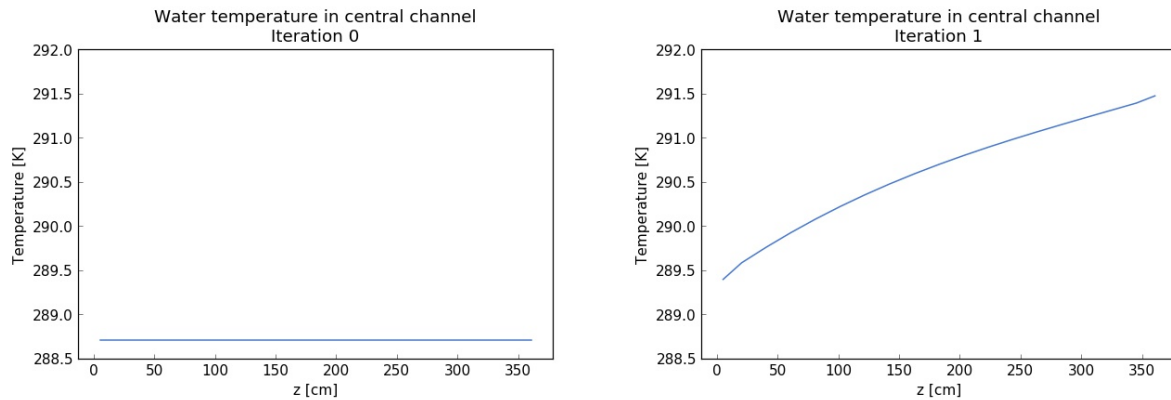


Figure 3-3. Axial Temperatures Distributions for Iterations 0 and 1

3.1.3 3x3 Assembly Channel Density Distributions

Figure 3-4 shows the channel water densities. The initial condition is a channel water density of 1.0 g/cc. The channel densities converge in the first iteration. As expected, there is an inverse relationship between density and temperature, with lower densities in the center channels.

Figure 3-5 shows the axial water density distribution in a central channel. As expected, the density of the water is reduced as the temperature increases up the channel. As before, the axial density distribution is converged after the first iteration.

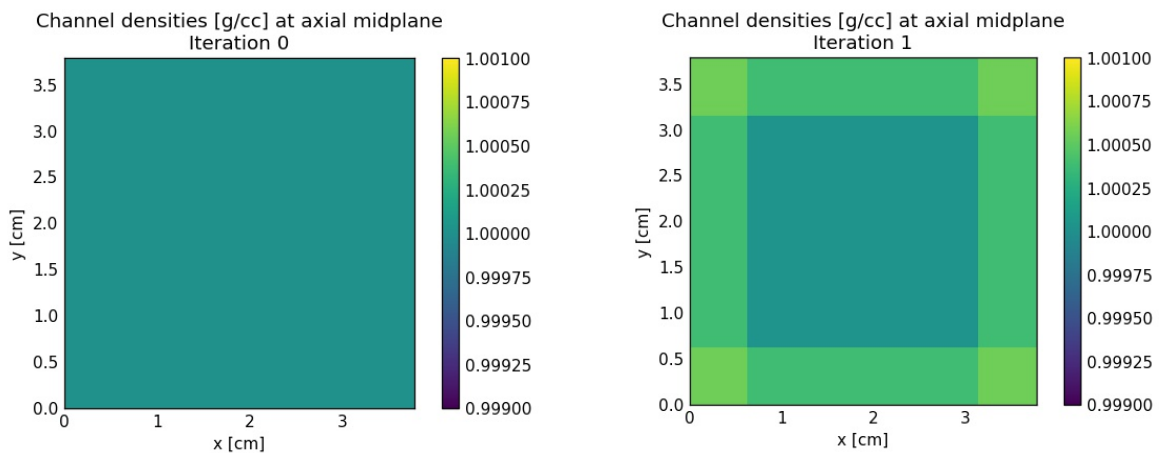


Figure 3-4. Channel Water Densities

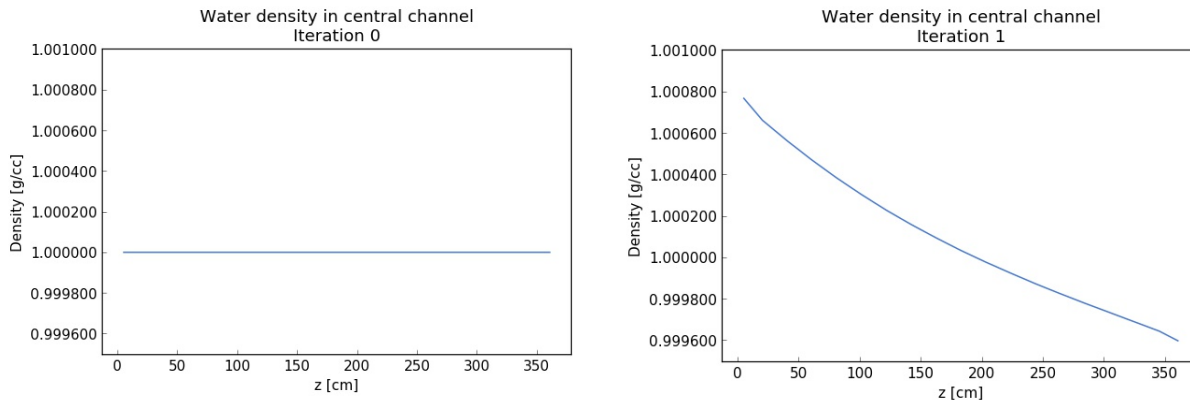


Figure 3-5. Axial Channel Water Densities in a Central Channel

3.1.4 Initial Use of Terrenus on a 17x17 PWR Assembly

To further test the performance of Terrenus, a multiphysics analysis of a standard 17x17 PWR assembly was performed. The model for this assembly is taken from Godfrey (2016). The layout of a PWR assembly is given in Figure 3-6. The pin diameters and material properties can be found in Godfrey (2016). For this problem, the fuel enrichment is set at 2.0 wt % ²³⁵U to maintain a moderate supercriticality. The water properties are the same as for the 3x3 pin array discussed previously, and the boundaries of the problem are maintained at 60°F, just as with the 3x3 pin array. Total assembly power is set at 200 W.

Figure 3-7 (left) shows a plot of the pin powers at the axial midplane, and Figure 3-7 (right) shows a plot of the pin powers axially along one of the fuel pins adjacent to the central instrument tube. In both images, the powers behave as expected. Power is zero in non-fuel pin cells (i.e., in guide tubes and the instrument tubes) and has roughly a cosine shape axially.

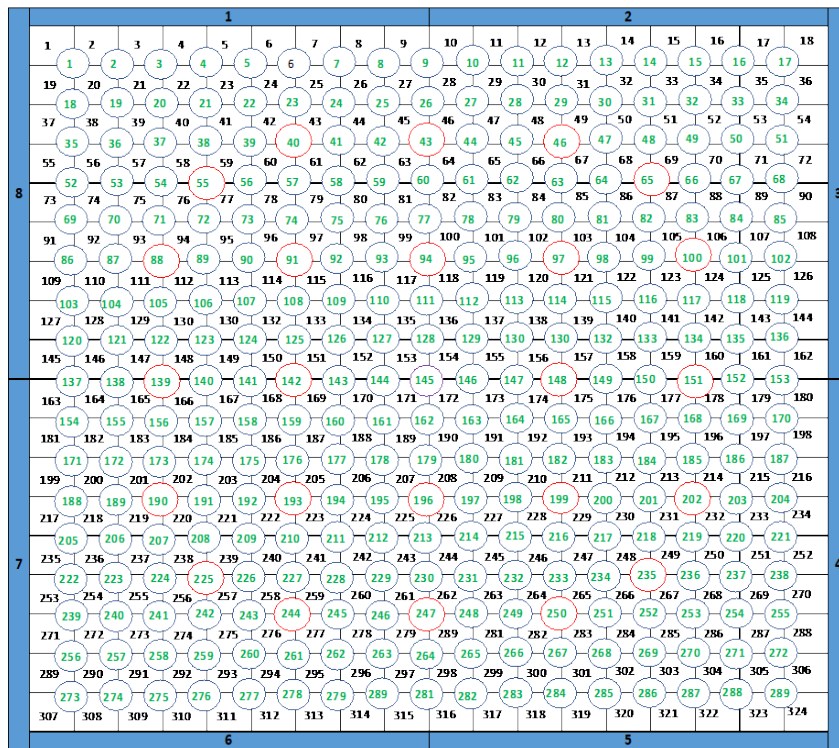


Figure 3-6. Pin Layout of a Standard 17x17 PWR Assembly

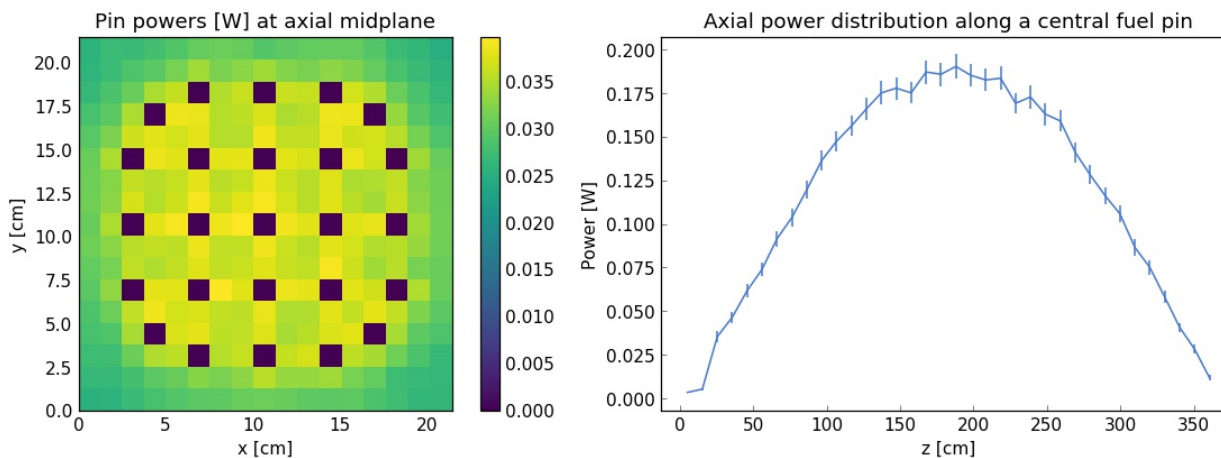


Figure 3-7. Pin Powers at the Axial Midplane (left) and Axial Distribution of Pin Power along a Fuel Pin adjacent to the Central Instrument Tube (right)

Figure 3-8 (left) presents the radial channel temperatures at the axial midplane, and Figure 3-8 (right) shows the channel temperature axially through the central instrument tube. These results look as expected, with temperatures higher in the center of the PWR assembly and lower near the cooler boundary conditions. The temperature rises monotonically axially through the assembly, as expected.

Figure 3-9 (left) shows the radial water density in the channels at the axial midplane, and Figure 3-9 (right) shows the axial water density in the central instrument tube. As expected, the density decreases with increased temperature, with higher density on the cooler boundaries of the PWR assembly and lower density in the warmer interior. The density also decreases monotonically axially through the assembly.

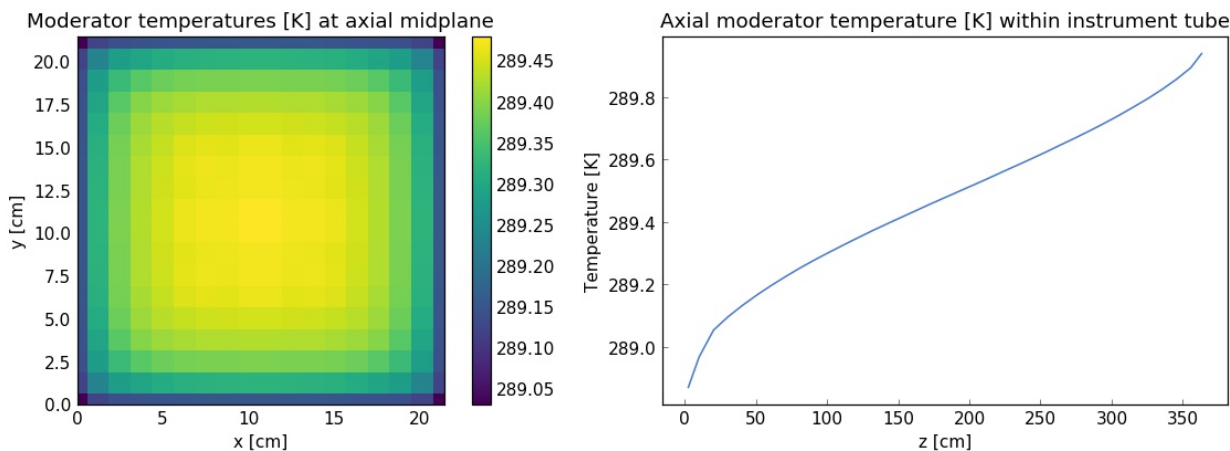


Figure 3-8. Temperature of the Water Moderator in Each Channel at the Axial Midplane (left) and Axial Temperature Distribution in the Central Instrument Tube (right)

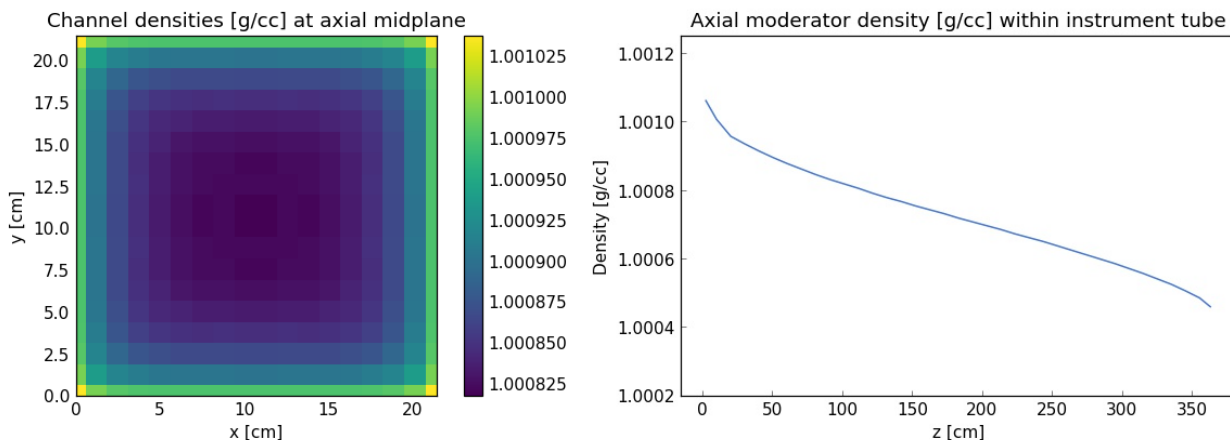


Figure 3-9. Water Moderator Density in Each Channel at the Axial Midplane (left) and Axial Distribution of the Moderator Density in the Central Instrument Tube (right)

Figure 3-10 (left) shows the fuel pin temperatures radially at the axial midplane, and Figure 3-10 (right) shows the fuel pin temperature axially in a fuel pin adjacent to the central instrument tube. Again, the results are consistent with the channel temperatures and calculated powers and are consistent with the earlier 3×3 results presented.

Finally, Figure 3-11 (left) and (right) show the axial water temperature and water density in the central instrument tube for various power levels, respectively. Both plots reveal the expected behavior: increased power generates increased water temperature and decreased water density.

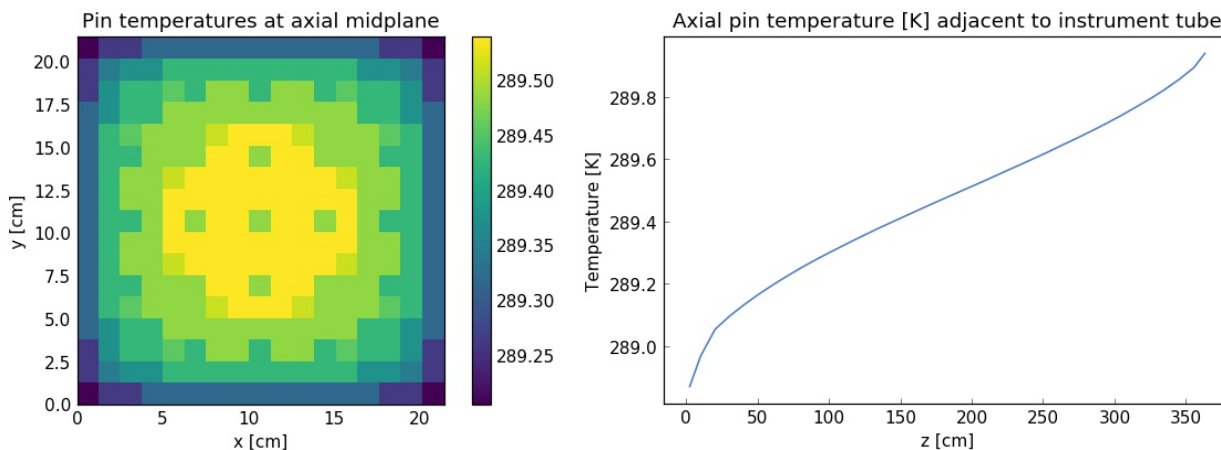


Figure 3-10. Pin Temperature in Each Pin Cell at the Axial Midplane (left) and the Axial Temperature Distribution in a Fuel Pin adjacent to the Central Instrument Tube (right)

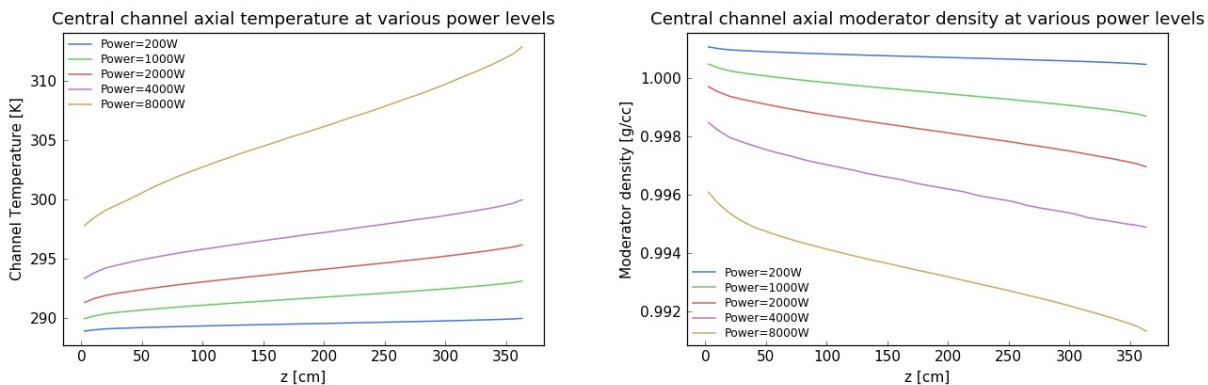


Figure 3-11. Axial Distribution of Temperature (left) and Moderator Density (right) in the Central Instrument Tube for Various Power Levels

3.1.5 Investigation of Negative Reactivity Phenomena

This subsection discusses an initial investigation into the negative reactivity induced by various physical phenomena. First, the negative reactivity caused by increased temperature is examined. As the power level increases, the water temperature increases as well (as shown on left in Figure 3-11). The water density also decreases, but that effect is not captured because reflective neutron boundary conditions are assumed. Figure 3-12 shows the effect of power level on reactivity for the 17×17 PWR problem. The modest increase in channel temperature has no effect on the reactivity of the system. This situation corresponds to the typical experience in reactor physics: negative temperature reactivity does not become significant until temperatures over 600 K are achieved.

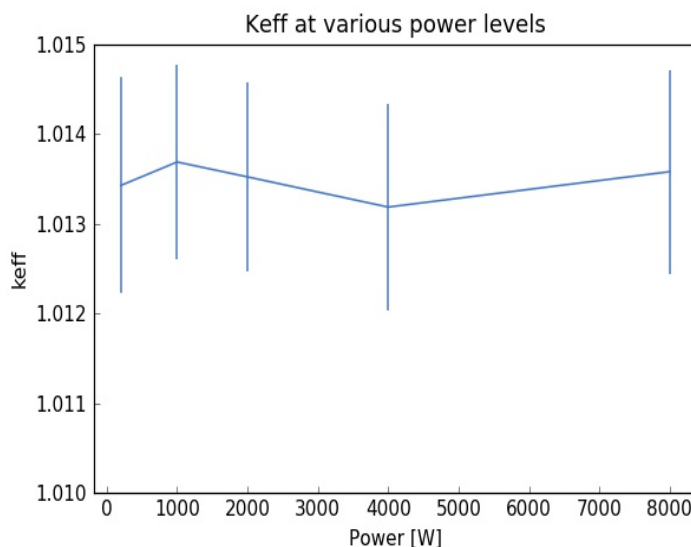


Figure 3-12. Reactivity in a Fully Reflected 17×17 PWR Assembly at Various Power Levels

Because the 17×17 assembly is surrounded by a reflective boundary condition, decreases in moderator density have no effect, as a decrease in the mean free path through an infinite array of pins has very little impact. Therefore, to investigate the effect of changing moderator density on criticality, an array of assemblies was created to be similar to that of a loaded DPC, except that the canister walls are omitted and the assemblies contain fresh fuel with a reduced enrichment of 1.0 wt % ^{235}U . The model geometry is shown in Figure 3-13. The properties of each assembly are identical to those discussed in Section 3.1.4, except the change to the fuel enrichment. A vacuum boundary condition is applied at all boundaries. Although Terrenus does not yet have the ability to perform multiphysics simulations of multiple assemblies, the underlying Shift Monte Carlo code can perform transport simulations of multiple assemblies. Therefore, the PWR model was simulated with Shift, varying the water density. The effect of varied water density on the reactivity is shown in Figure 3-14.

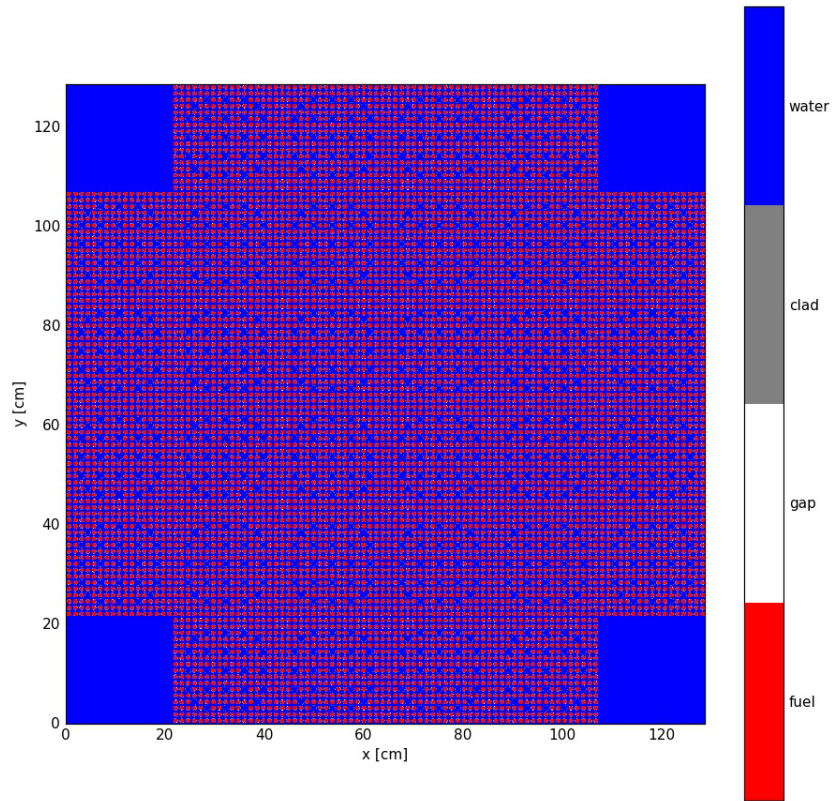


Figure 3-13. A Simplified Neutronic Model of a Loaded Canister

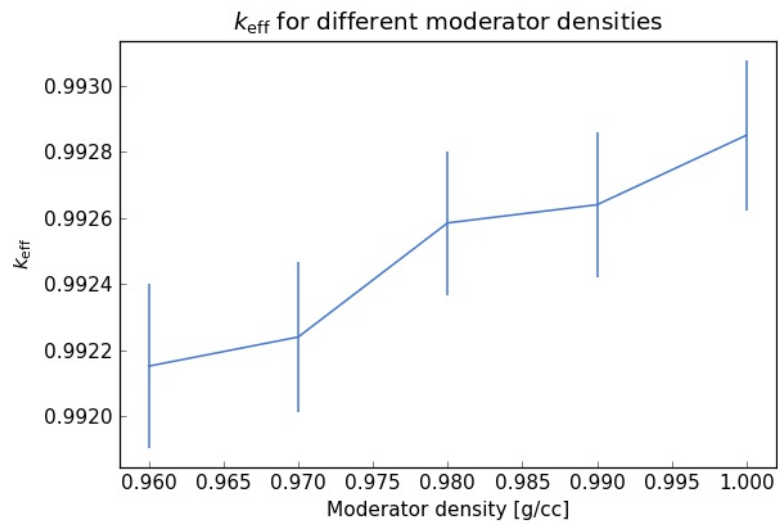


Figure 3-14. Effect of Moderator Density on Reactivity

As moderator density decreases, leakage from the system increases, and therefore k_{eff} decreases. Water density is varied from 0.96 to 1.0 g/cc, which is approximately the range of densities that water can experience at 1 atm of pressure. While there was a clear trend in the value of k_{eff} , the differences are quite modest, spanning only 50 percent mille (pcm).

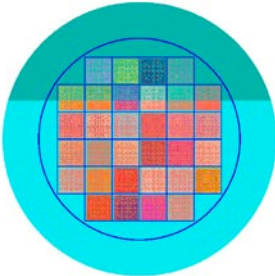
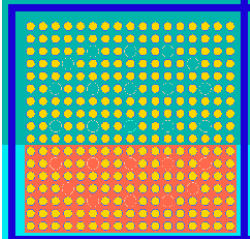
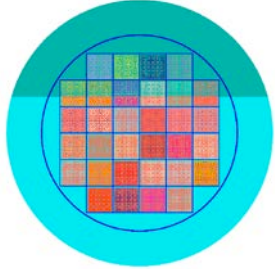
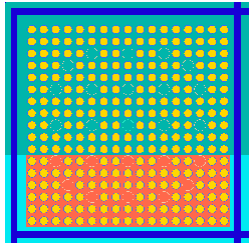
Although these results are still preliminary, it is unlikely that there is sufficient negative reactivity in a purely liquid water scenario to balance the excess reactivity of a critical canister. Therefore, it is likely that, in most situations, the water will boil and the reduction in moderation due to that boiling will drive the system subcritical.

The current thermal-hydraulic code, COBRA-SFS, is single-phase and does not support boiling. The plans for addressing this shortcoming are addressed in Section 3.1.7.

3.1.6 Calculating Critical Water Level

To gain insight into critical configurations for typical SNF canisters, a series of criticality calculations was performed using Shift to determine the critical water level for a realistic MPC-32-TSC canister. The radiation transport models were generated with the Used Nuclear Fuel–Storage, Transportation & Disposal Analysis Resource and Data Systems, or UNF-ST&DARDS (Banerjee et al. 2016), which uses operational data to build as-loaded canisters with used fuel assemblies. All of the modeled canisters generated with the UNF-ST&DARDS tool were completely submerged in water and had to be modified to simulate a canister that was only partially filled. Moving forward, the intent is to simplify this process by enhancing Terrenus so that it can be used to create the necessary models automatically for calculating a critical water level. Once the models were generated, a simple criticality search was conducted to narrow down the precise water level that yielded a multiplication factor nearest to unity. The final result is illustrated in Table 3-1, which shows the two bounding cases that narrowed down the critical water level for the Sequoyah MPC-32-TSC 079 canister. Note that a similar analysis can be performed for any potentially critical canister. For this particular canister, the critical water level is approximately 103 cm from the bottom of the first row of assemblies.

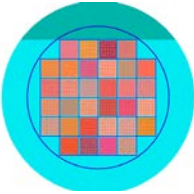
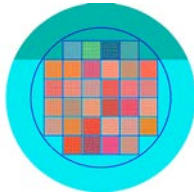
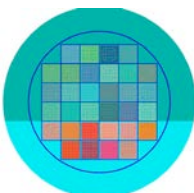
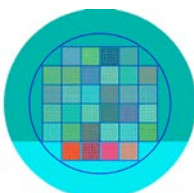
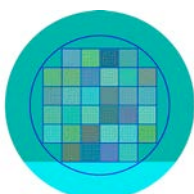
Table 3-1. Critical Water Level for the MPC-32-TSC 079 Sequoyah Canister

Canister Cross Section	Water Level	Assembly Cross Section	Multiplication Factor (k_{eff})
	~103.61 cm		1.00016506 ± 6
	~102.37 cm		0.9994745 ± 5

Before the Sequoyah MPC-32-TSC 079 canister was selected for study, a couple of other cases were simulated, including a run using a canister with fresh fuel and another using a canister that did not achieve criticality even when completely flooded. The results from these cases are shown in Table 3-2 alongside the Sequoyah 079 case.

Note that the majority of the canisters considered in this investigation do not have a multiplication factor above unity, even when completely flooded. Of the ~27 canisters available in the UNF database from the Sequoyah facility, only 4 are critical when completely submerged in water. All of the investigated cases are decayed for approximately 20,000 years and include no neutron absorbers.

Table 3-2. Test Cases for Critical Water Level Search

Canister CrossSection	Water Level (cm)	Multiplication Factor (k_{eff})		
		Fresh Fuel	Used Fuel	Sequoyah 079
	~141	1.10353	0.99773	1.00957
	~117.5	1.10023	0.99629	1.00743
	~94	1.09115	0.98744	0.99824
	~70.5	1.07437	0.96796	0.97979
	~47	1.03492	0.93414	0.93941
	~23.5	0.93026	0.84492	0.84941
	~0	0.33254	0.27118	0.27183

3.1.7 Critical Power Search

Terrenus was used to calculate the power produced by a fully loaded, fully or partially flooded, SNF canister. The power produced by a critical canister is determined by a balance between the thermal-hydraulic and heat-transfer properties of the system and the neutronics. A canister with excess reactivity ($k_{eff} > 1.0$) causes an increase in moderator and fuel pin temperature and a decrease in moderator density. As was discussed previously, these phenomena are insufficient to reduce k_{eff} by a significant amount. However, once the water begins to boil, the increased void fraction causes a substantial reduction in the population of thermal neutrons, thereby bringing the reaction into balance.

To calculate this critical power, the first step is to make an initial guess of the power level, as well as an initial guess of the negative power reactivity coefficient (i.e., the negative change in the reactivity for every increased watt of power). It is required by the physics of the system that the reactivity decreases as the power increases. Using the initial guess of the power, the thermal-hydraulic properties and the reactivity are computed by COBRA-SFS and Shift, respectively. Using the reactivity calculated by Shift, a new power level and new negative reactivity coefficient are calculated. These parameters are then iterated to convergence.

This capability has been implemented into Terrenus but cannot be tested until boiling can be modeled. Approaches for achieving this goal are discussed in the following subsection.

3.1.8 Conclusions and Future Work

Currently, the Terrenus code is capable of coupling Shift and COBRA-SFS for a simplified canister model containing a single PWR assembly. The Terrenus framework has been tested using fresh fuel in a simplified 3×3 fuel pin geometry as well as a full 17×17 assembly. The multiphysics simulations produce results consistent with expectations regarding water temperatures and density, as well as power profiles. An investigation into physical phenomena that are likely to balance excess reactivity in a flooded canister was also conducted. Neither increased fuel temperature nor decreased water density is likely to be sufficient to balance even small amounts of excess reactivity. Therefore, it is likely that the water temperature increases until boiling occurs. Note that boiling is only likely in the case for which the canister is saturated, as elucidated in Section 3.3.1.

Future work will expand the geometric capabilities of Terrenus so that a canister full of assemblies can be modeled, along with the canister internals. Completing this task requires adding an assembly-aware metadata layer onto the SCALE general geometry package within Shift, and it also requires a much more general-purpose COBRA input template. Additionally, Terrenus currently requires four input files: a Terrenus input file, a Shift input file, a model geometry file, and a COBRA-SFS file. Ensuring that all of these input files are correct and consistent with one another is time consuming and error prone. In the future, the intent is to use a single Terrenus input file with Terrenus automatically generating any other input files that are required.

Moreover, Terrenus currently requires the user to specify the total power of the system. Future work will include enabling Terrenus to calculate the negative temperature coefficient of the canister system so that a critical temperature search can be performed. The coupled transport thermal-hydraulics system will be able to iterate to the actual power. A new convergence criterion that uses the more stable thermal-

hydraulics parameters (channel temperature and density) rather than the stochastically noisy radiation transport parameter (power) will also be developed.

Finally, COBRA-SFS may not be able to provide the thermal-hydraulic functionality needed for this project over the long term. COBRA-SFS is a stand-alone code without any built-in coupling interface, which necessitated the complex Python coupling module that was developed. Because COBRA-SFS is single phase only, it cannot model boiling, nor can it calculate vapor pressure, which may be a major source of canister failure in criticality events. The near-term plans for Terrenus include the introduction of boiling physics for the thermal-hydraulic solver. One method for achieving this goal is to attempt to approximate boiling using COBRA-SFS with a homogeneous equilibrium model. This approximation will likely calculate the conduction of heat away from the fuel pins nearly correctly, but it also will introduce error into the calculation of heat convection. An alternative is to replace COBRA-SFS with a thermal-hydraulic code that has a boiling model such as the Reactor Excursion and Leak Analysis Program-5 (RELAP-5) or RELAP-7 (INEL 1995). Future work will include consideration of other thermal-hydraulic codes that may better meet the needs of the criticality consequence project.

3.2 Inventory

As discussed in Section 2.2, the effects of a steady-state criticality on inventory were evaluated based on data from actual assemblies of 37 Westinghouse 15×15 loaded in the NAC TSC-37 from a reactor that was shut down prior to CY2000. The analysis assumed a steady-state criticality with a 4 kW power distribution lasting from 9,000 to 19,000 years after closure, and the radionuclides selected for evaluation are those shown in Price et al. (2019). Note that the power generated in the steady-state criticality event is a linear function of the number of fissions; therefore, the results of evaluating the change in inventory associated with a 4 kW steady-state event can be extrapolated to other power levels.

The results of the evaluation are shown in three tables and three corresponding figures: one table and one figure showing the change in inventory of actinides and their decay products (Table 3-3 and Figure 3-15), one table and one figure showing the change in inventory of radioactive fission products and activation products (Table 3-4 and Figure 3-16), and one table and one figure showing the change in inventory of stable fission products (Table 3-5 and Figure 3-17).

A subset of the total radionuclide inventory presented in this subsection was used in PFLOTRAN calculations to test the criticality submodule and the interface with neutronics code outputs (Section 3.8.2). This subset consists of ten radionuclides: seven are among the actinides and their decay products shown in Table 3-3, and three are among the fission products shown in Table 3-4. The specific radionuclides are identified and discussed in further detail below.

As shown in Table 3-3 and Figure 3-15, at 19,000 years after repository closure the inventory of some actinides (^{241}Am , $^{242\text{m}}\text{Am}$, ^{242}Cm , ^{244}Cm , ^{238}Pu , ^{241}Pu , and ^{232}U) increases significantly when comparing the case without criticality to that with criticality. This result is due to the short half-lives of these radionuclides, shown in Table 3-3; by 19,000 years after repository closure in the absence of a criticality, the inventories of these radionuclides have decayed to either very low levels or to zero. The assumed 10,000-year steady-state criticality event produces orders-of-magnitude less power than what is produced in a reactor, but it still produces these radionuclides, which leads to the significant percent increases seen in Table 3-3. Some of the short-lived radionuclides that have not previously been included in a PA may

need to be included if criticality is included. The PFLOTRAN calculations that include criticality (Section 3.8.2) incorporate seven of these radionuclides: the decay chain that includes ²⁴¹Am, ²³⁷Np, ²³³U, and ²²⁹Th; two actinides whose inventory increases from zero (²³⁸Pu and ^{242m}Am); and another actinide whose inventory increase is only moderate (²⁴⁰Pu). In addition, in this criticality simulation the inventory of some actinides decreases with the occurrence of the criticality event (²⁴⁵Cm, ²³⁹Pu, ²⁴²Pu, ²²⁹Th, ²³³U, ²³⁵U, and ²³⁸U). This outcome is caused by fission of that radionuclide or its parent, and/or neutron capture.

Table 3-3. Inventory of Actinides and Their Decay Products 19,000 Years after Repository Closure, with and without 10,000-Year Steady-State Criticality Event

Nuclide	Half-life (years) ^a	Mass (g) without Criticality	Mass (g) with Criticality	Percent Change (%)
²²⁷ Ac	21.77	1.98E-03	3.42E-03	72.64
²⁴¹ Am	432.6	2.05E-01	5.97E+01	28991.65
^{242m} Am	141	0.00E+00	1.64E-06	N/A
²⁴³ Am	7,364	2.09E+02	2.76E+02	32.30
²⁴² Cm	4.46E-01	0.00E+00	3.31E-04	N/A
²⁴⁴ Cm	18.1	0.00E+00	2.28E-02	N/A
²⁴⁵ Cm	8,423	4.09E+00	3.65E+00	-10.70
²³⁷ Np	2.14E+06	2.84E+04	2.93E+04	3.30
²³¹ Pa	3.28E+04	3.03E+00	5.09E+00	67.88
²¹⁰ Pb	22.2	5.51E-02	5.58E-02	1.42
²³⁸ Pu	87.7	0.00E+00	9.14E+00	N/A
²³⁹ Pu	24,110	5.93E+04	5.81E+04	-1.93
²⁴⁰ Pu	6,561	4.45E+03	5.99E+03	34.55
²⁴¹ Pu	14.33	6.77E-03	1.94E+00	28476.70
²⁴² Pu	3.75E+05	6.01E+03	5.90E+03	-1.86
²²⁶ Ra	1,600	4.27E+00	4.33E+00	1.43
²²⁸ Ra	5.75	1.67E-08	1.68E-08	0.50
²²⁹ Th	7,932	3.92E+00	3.80E+00	-3.12
²³⁰ Th	7.54E+04	2.30E+02	2.36E+02	2.31
²³² Th	1.40E+10	4.15E+01	4.17E+01	0.50
²³² U	68.9	3.05E-07	2.24E-03	733837.08
²³³ U	1.59E+05	1.62E+02	1.57E+02	-2.61
²³⁴ U	2.46E+05	4.65E+03	5.23E+03	12.52
²³⁵ U	7.04E+08	2.17E+05	2.07E+05	-4.47
²³⁶ U	2.34E+07	8.43E+04	8.65E+04	2.58
²³⁸ U	4.47E+09	1.60E+07	1.60E+07	-0.06

NOTE: ^a Half-lives taken from the National Nuclear Data Center (BNL n.d.).

For nuclides not present (i.e., mass = 0 g) in the no-criticality case, the percent change cannot be calculated, hence the N/A (not applicable) designation.

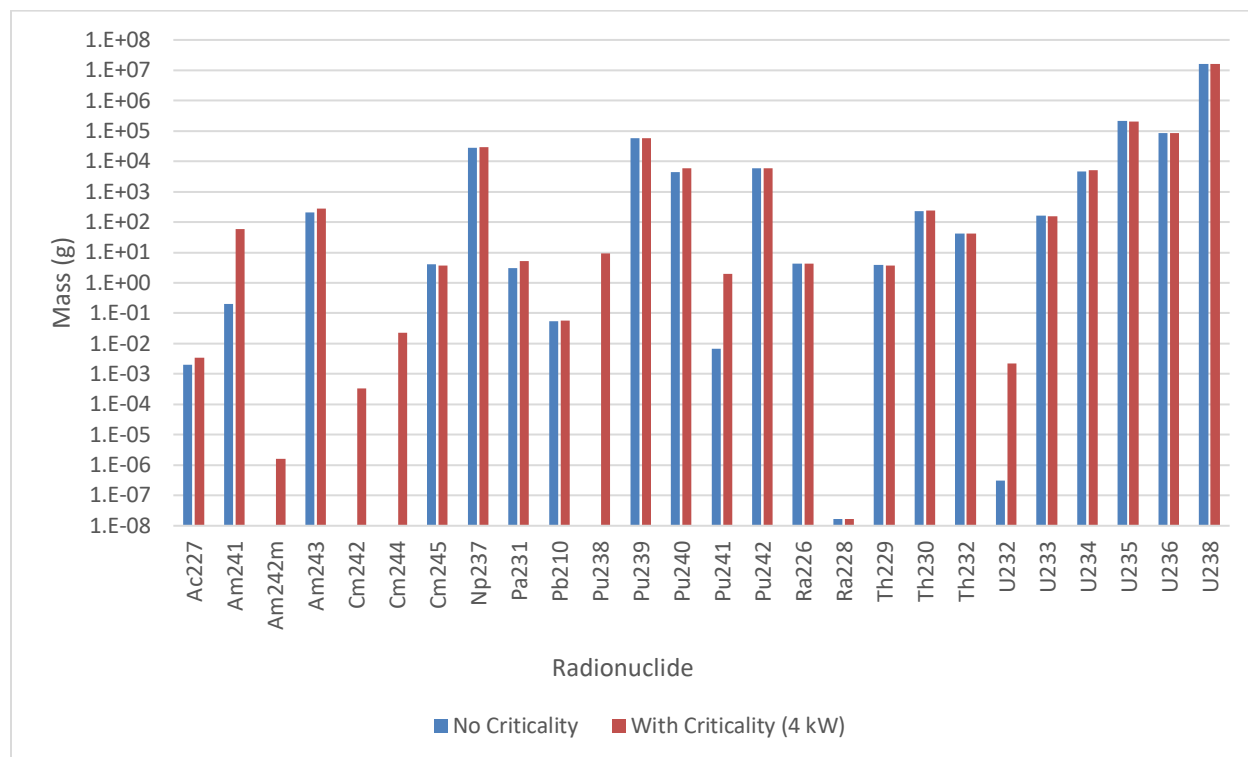


Figure 3-15. Inventory of Actinides and Their Decay Products 19,000 Years after Repository Closure, with and without 10,000-Year Steady-State Criticality Event

As shown in Table 3-4 and Figure 3-16, a comparison without and with criticality at 19,000 years after closure indicates that the inventory of the long-lived fission and activation products increases by a few percent, reflecting their production by the 10,000-year steady-state event. The inventory of the short-lived fission and activation products increases from zero to the values shown in Table 3-4 and Figure 3-16, commensurate with the fission product yield of the different fissile isotopes. Three radioactive fission products are included in the PFLOTRAN calculations described in Section 3.8.2: ⁹⁰Sr and ¹³⁷Cs, which are relatively short-lived, and ¹²⁹I, which is long-lived.

Table 3-5 and Figure 3-17 show that, in a comparison without and with criticality at 19,000 years after closure, the inventory of most of the stable fission products increases a few percent, representing production of these fission products during the 10,000-year criticality event. The inventory of some stable fission products decreases because they are neutron absorbers; they absorb neutrons as the criticality event progresses and become a different isotope.

Table 3-4. Inventory of Radioactive Fission and Activation Products 19,000 Years after Repository Closure, with and without 10,000-Year Steady-State Criticality Event

Nuclide	Half-life (years) ^a	Mass (g) without Criticality	Mass (g) with Criticality	Percent Change (%)
^{137m} Ba	4.85E-06	0.00E+00	3.70E-07	N/A
¹⁴ C	5,700	1.23E-01	1.42E-01	15.46
¹⁴⁴ Ce	7.80E-01	0.00E+00	4.97E-02	N/A
³⁶ Cl	3.01E+05	3.51E-25	7.20E-24	1948.44
¹³⁴ Cs	2.0652	0.00E+00	3.53E-02	N/A
¹³⁵ Cs	2.30E+06	6.30E+03	6.91E+03	9.57
¹³⁷ Cs	30.08	0.00E+00	2.42E+00	N/A
¹⁶⁴ Eu	8.601	0.00E+00	7.87E-02	N/A
¹²⁹ I	1.57E+07	2.11E+03	2.18E+03	3.45
¹⁴⁷ Pm	2.6234	0.00E+00	7.82E-02	N/A
¹⁴⁴ Pr	3.29E-05	0.00E+00	2.09E-06	N/A
¹⁰⁶ Rh	2.49E-04	0.00E+00	1.93E-08	N/A
¹²⁵ Sb	2.75856	0.00E+00	2.83E-03	N/A
⁷⁹ Se	3.26E+05	6.01E+01	6.21E+01	3.33
¹⁴⁷ Sm	1.96E+11	3.84E+03	3.99E+03	3.84
¹⁵¹ Sm	90	0.00E+00	1.24E+00	N/A
¹²⁶ Sn	2.30E+05	2.67E+02	2.77E+02	3.75
⁹⁰ Sr	28.9	0.00E+00	1.01E+00	N/A
⁹⁹ Tc	2.11E+05	1.01E+04	1.04E+04	3.28
⁹⁰ Y	7.31E-03	0.00E+00	2.58E-04	N/A

NOTE: ^a Half-lives taken from the National Nuclear Data Center (BNL n.d.).

For nuclides not present (i.e., mass = 0 g) in the no-criticality case, the percent change cannot be calculated, hence the N/A (not applicable) designation.

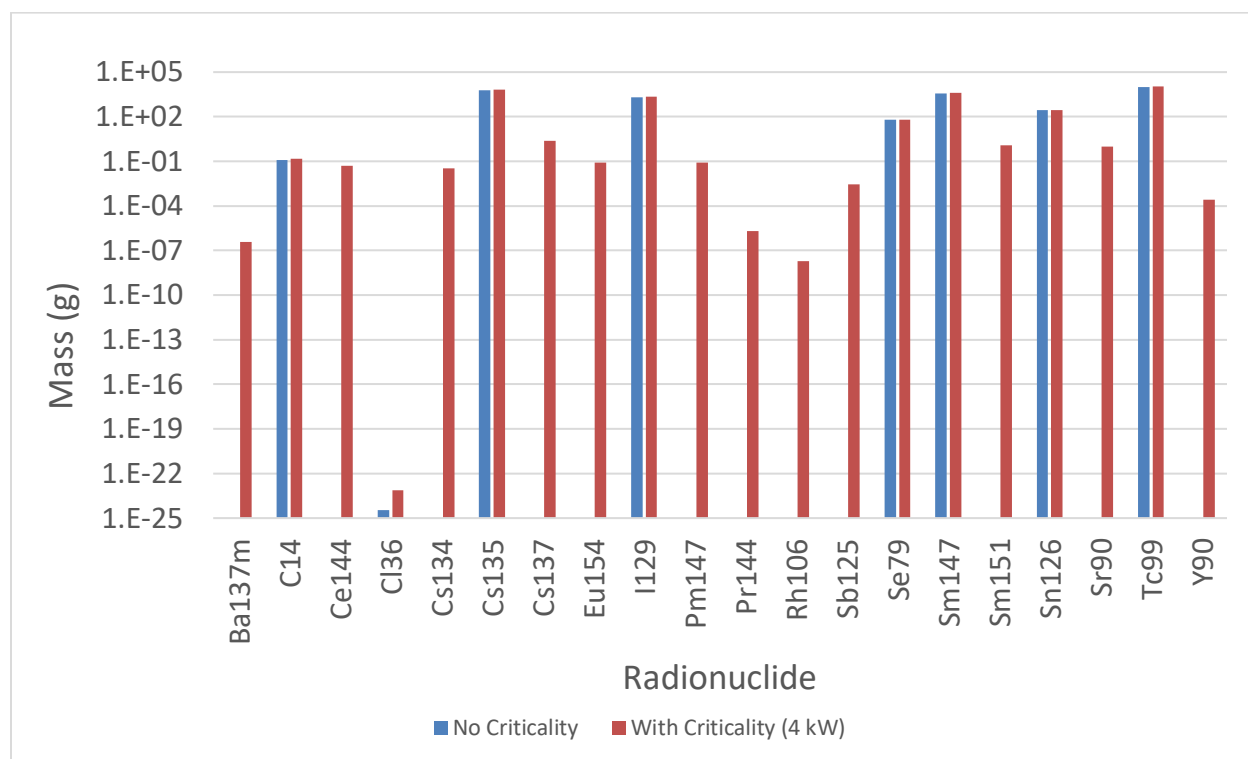


Figure 3-16. Inventory of Radioactive Fission and Activation Products 19,000 Years after Repository Closure, with and without 10,000-Year Steady-State Criticality Event

Table 3-5. Inventory of Stable Fission Products 19,000 Years after Repository Closure, with and without 10,000-Year Steady-State Criticality Event

Nuclide	Half-life (years) ^a	Mass (g) without Criticality	Mass (g) with Criticality	Percent Change (%)
¹⁰⁹ Ag	stable	1.10E+03	1.13E+03	2.59
¹³³ Cs	stable	1.55E+04	1.60E+04	3.10
¹⁵¹ Eu ^b	≥ 1.7E+18	2.02E+02	1.81E+02	-10.38
¹⁵³ Eu	stable	1.54E+03	1.59E+03	3.01
¹⁵⁵ Gd	stable	1.02E+02	1.99E+01	-80.44
⁹⁵ Mo	stable	1.06E+04	1.09E+04	3.17
¹⁴³ Nd	stable	1.15E+04	1.18E+04	1.99
¹⁴⁵ Nd	stable	9.04E+03	9.31E+03	3.03
¹⁰¹ Ru	stable	1.05E+04	1.09E+04	3.28
¹⁴⁹ Sm	stable	5.45E+01	1.92E+01	-64.70
¹⁵⁰ Sm	stable	3.83E+03	3.94E+03	2.99
¹⁵² Sm	stable	1.52E+03	1.55E+03	1.88

NOTE: ^a Half-lives taken from the National Nuclear Data Center (BNL n.d.).

^b The half-life of this radionuclide is long enough that it is considered stable for these analyses.

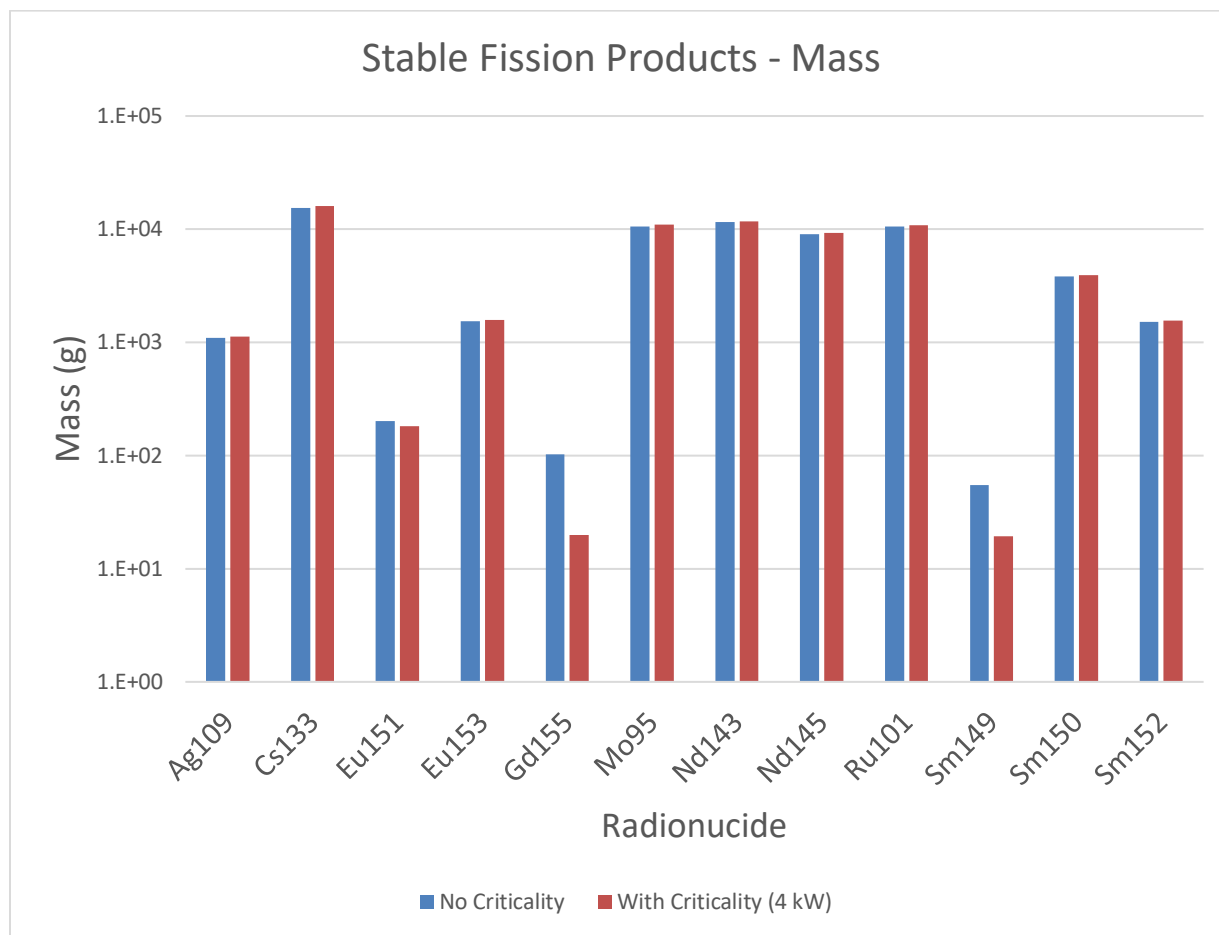


Figure 3-17. Inventory of Stable Fission Products 19,000 Years after Repository Closure, with and without 10,000-Year Steady-State Criticality event

As discussed above, a subset of the radionuclides presented above was selected for PFLOTRAN simulations: ^{241}Am , ^{237}Np , ^{233}U , ^{229}Th , ^{238}Pu , ^{240}Pu , $^{242\text{m}}\text{Am}$, ^{137}Cs , ^{90}Sr , and ^{129}I . These radionuclides were selected for the reactive transport simulations because they are part of decay chains; because they are long-lived, nonsorbing, and highly soluble; or because their inventories increase significantly during the postulated criticality event compared to no-criticality case. Two different radionuclide inventories that have been read from neutronics code calculations and formatted as input to PFLOTRAN are given for the simulation case without a criticality event (Table 3-6) and with a criticality event (Table 3-7). Figure 3-18 is a graphical representation of the data in Table 3-6 and Table 3-7.

Table 3-6. Inventory of Selected Radionuclide Inventories as Input into PFLOTRAN, without Criticality

Time (years)	Mass Fraction (g/g)									
	²⁴¹ Am	²³⁷ Np	²³³ U	²²⁹ Th	²³⁸ Pu	²⁴⁰ Pu	^{242m} Am	¹³⁷ Cs	⁹⁰ Sr	¹²⁹ I
0	1.19E-03	5.59E-04	1.97E-08	6.09E-12	5.17E-05	2.01E-03	6.57E-12	6.49E-05	2.51E-05	1.28E-04
100	1.02E-03	7.33E-04	4.04E-08	1.87E-11	2.36E-05	1.99E-03	4.02E-12	6.48E-06	2.26E-06	1.28E-04
200	8.66E-04	8.81E-04	6.60E-08	4.10E-11	1.08E-05	1.97E-03	2.46E-12	6.47E-07	2.03E-07	1.28E-04
300	7.37E-04	1.01E-03	9.60E-08	7.50E-11	4.92E-06	1.95E-03	1.50E-12	6.46E-08	1.83E-08	1.28E-04
400	6.28E-04	1.11E-03	1.30E-07	1.22E-10	2.26E-06	1.93E-03	9.20E-13	6.44E-09	1.65E-09	1.28E-04
500	5.35E-04	1.21E-03	1.67E-07	1.84E-10	1.04E-06	1.91E-03	5.63E-13	6.43E-10	1.48E-10	1.28E-04
600	4.56E-04	1.28E-03	2.06E-07	2.62E-10	4.81E-07	1.89E-03	3.44E-13	6.42E-11	1.34E-11	1.28E-04
700	3.88E-04	1.35E-03	2.48E-07	3.56E-10	2.24E-07	1.87E-03	2.11E-13	6.41E-12	1.20E-12	1.28E-04
800	3.31E-04	1.41E-03	2.92E-07	4.67E-10	1.05E-07	1.85E-03	1.29E-13	6.40E-13	1.08E-13	1.28E-04
900	2.82E-04	1.45E-03	3.37E-07	5.97E-10	4.97E-08	1.83E-03	7.88E-14	6.39E-14	9.75E-15	1.28E-04
1400	1.27E-04	1.61E-03	5.81E-07	1.53E-09	1.10E-09	1.73E-03	6.74E-15	6.33E-19	5.77E-20	1.28E-04
1900	5.68E-05	1.68E-03	8.41E-07	2.94E-09	3.91E-11	1.65E-03	5.77E-16	6.28E-24	3.41E-25	1.28E-04
2400	2.55E-05	1.71E-03	1.11E-06	4.84E-09	5.44E-12	1.56E-03	4.94E-17	6.22E-29	2.02E-30	1.28E-04
2900	1.15E-05	1.72E-03	1.38E-06	7.22E-09	4.46E-13	1.48E-03	4.23E-18	6.17E-34	1.19E-35	1.28E-04
3900	2.35E-06	1.73E-03	1.92E-06	1.33E-08	3.23E-15	1.33E-03	3.10E-20	0.00E+00	0.00E+00	1.28E-04
4900	5.05E-07	1.73E-03	2.46E-06	2.11E-08	2.37E-17	1.20E-03	2.27E-22	0.00E+00	0.00E+00	1.28E-04
5900	1.31E-07	1.73E-03	3.00E-06	3.03E-08	1.73E-19	1.08E-03	1.67E-24	0.00E+00	0.00E+00	1.28E-04
6900	5.23E-08	1.73E-03	3.53E-06	4.10E-08	1.27E-21	9.70E-04	1.22E-26	0.00E+00	0.00E+00	1.28E-04
7900	3.46E-08	1.73E-03	4.06E-06	5.28E-08	9.32E-24	8.73E-04	8.94E-29	0.00E+00	0.00E+00	1.28E-04
8900	2.91E-08	1.73E-03	4.59E-06	6.57E-08	6.83E-26	7.85E-04	6.56E-31	0.00E+00	0.00E+00	1.28E-04
9000	2.88E-08	1.73E-03	4.65E-06	6.71E-08	4.18E-26	7.77E-04	4.01E-31	0.00E+00	0.00E+00	1.28E-04
9050	2.86E-08	1.73E-03	4.67E-06	6.78E-08	3.27E-26	7.73E-04	3.14E-31	0.00E+00	0.00E+00	1.28E-04
9100	2.85E-08	1.73E-03	4.70E-06	6.84E-08	2.55E-26	7.69E-04	2.45E-31	0.00E+00	0.00E+00	1.28E-04
9500	2.73E-08	1.73E-03	4.91E-06	7.40E-08	3.57E-27	7.37E-04	3.43E-32	0.00E+00	0.00E+00	1.28E-04
10000	2.61E-08	1.73E-03	5.18E-06	8.11E-08	3.06E-28	6.99E-04	2.94E-33	0.00E+00	0.00E+00	1.28E-04
11000	2.39E-08	1.73E-03	5.70E-06	9.60E-08	2.24E-30	6.29E-04	2.15E-35	0.00E+00	0.00E+00	1.28E-04
12000	2.20E-08	1.73E-03	6.22E-06	1.12E-07	1.64E-32	5.66E-04	1.58E-37	0.00E+00	0.00E+00	1.28E-04
15000	1.73E-08	1.72E-03	7.78E-06	1.63E-07	6.47E-39	4.12E-04	6.21E-44	0.00E+00	0.00E+00	1.28E-04
18000	1.35E-08	1.72E-03	9.31E-06	2.19E-07	0.00E+00	3.00E-04	0.00E+00	0.00E+00	0.00E+00	1.28E-04
19000	1.24E-08	1.72E-03	9.82E-06	2.38E-07	0.00E+00	2.70E-04	0.00E+00	0.00E+00	0.00E+00	1.28E-04
20000	1.15E-08	1.72E-03	1.03E-05	2.58E-07	0.00E+00	2.43E-04	0.00E+00	0.00E+00	0.00E+00	1.28E-04
21025	1.06E-08	1.72E-03	1.08E-05	2.78E-07	0.00E+00	2.18E-04	0.00E+00	0.00E+00	0.00E+00	1.28E-04

Table 3-6. Inventory of Selected Radionuclide Inventories as Input into PFLOTRAN, without Criticality (continued)

Time (years)	Mass Fraction (g/g)									
	²⁴¹ Am	²³⁷ Np	²³³ U	²²⁹ Th	²³⁸ Pu	²⁴⁰ Pu	^{242m} Am	¹³⁷ Cs	⁹⁰ Sr	¹²⁹ I
21100	1.05E-08	1.72E-03	1.09E-05	2.80E-07	0.00E+00	2.16E-04	0.00E+00	0.00E+00	0.00E+00	1.28E-04
21250	1.04E-08	1.72E-03	1.09E-05	2.83E-07	0.00E+00	2.13E-04	0.00E+00	0.00E+00	0.00E+00	1.28E-04
21500	1.02E-08	1.72E-03	1.11E-05	2.88E-07	0.00E+00	2.07E-04	0.00E+00	0.00E+00	0.00E+00	1.28E-04
22000	9.75E-09	1.72E-03	1.13E-05	2.98E-07	0.00E+00	1.97E-04	0.00E+00	0.00E+00	0.00E+00	1.28E-04
23000	8.98E-09	1.72E-03	1.18E-05	3.18E-07	0.00E+00	1.77E-04	0.00E+00	0.00E+00	0.00E+00	1.28E-04
49900	1.00E-09	1.71E-03	2.43E-05	8.85E-07	0.00E+00	1.03E-05	0.00E+00	0.00E+00	0.00E+00	1.28E-04
99900	1.70E-11	1.68E-03	4.37E-05	1.81E-06	0.00E+00	5.25E-08	0.00E+00	0.00E+00	0.00E+00	1.28E-04
199900	5.15E-15	1.63E-03	7.08E-05	3.25E-06	0.00E+00	2.60E-12	0.00E+00	0.00E+00	0.00E+00	1.27E-04
499900	1.22E-25	1.48E-03	1.01E-04	4.60E-06	0.00E+00	1.25E-12	0.00E+00	0.00E+00	0.00E+00	1.26E-04
999900	0.00E+00	1.26E-03	9.73E-05	4.42E-06	0.00E+00	1.24E-12	0.00E+00	0.00E+00	0.00E+00	1.23E-04

Table 3-7. Inventory of Selected of Radionuclides as Input into PFLOTRAN, with Criticality

Time (years)	Mass Fraction (g/g)									
	²⁴¹ Am	²³⁷ Np	²³³ U	²²⁹ Th	²³⁸ Pu	²⁴⁰ Pu	^{242m} Am	¹³⁷ Cs	⁹⁰ Sr	¹²⁹ I
0	1.19E-03	5.59E-04	1.97E-08	6.09E-12	5.17E-05	2.01E-03	6.57E-12	6.49E-05	2.51E-05	1.28E-04
100	1.02E-03	7.33E-04	4.04E-08	1.87E-11	2.36E-05	1.99E-03	4.02E-12	6.48E-06	2.26E-06	1.28E-04
200	8.66E-04	8.81E-04	6.60E-08	4.10E-11	1.08E-05	1.97E-03	2.46E-12	6.47E-07	2.03E-07	1.28E-04
300	7.37E-04	1.01E-03	9.60E-08	7.50E-11	4.92E-06	1.95E-03	1.50E-12	6.46E-08	1.83E-08	1.28E-04
400	6.28E-04	1.11E-03	1.30E-07	1.22E-10	2.26E-06	1.93E-03	9.20E-13	6.44E-09	1.65E-09	1.28E-04
500	5.35E-04	1.21E-03	1.67E-07	1.84E-10	1.04E-06	1.91E-03	5.63E-13	6.43E-10	1.48E-10	1.28E-04
600	4.56E-04	1.28E-03	2.06E-07	2.62E-10	4.81E-07	1.89E-03	3.44E-13	6.42E-11	1.34E-11	1.28E-04
700	3.88E-04	1.35E-03	2.48E-07	3.56E-10	2.24E-07	1.87E-03	2.11E-13	6.41E-12	1.20E-12	1.28E-04
800	3.31E-04	1.41E-03	2.92E-07	4.67E-10	1.05E-07	1.85E-03	1.29E-13	6.40E-13	1.08E-13	1.28E-04
900	2.82E-04	1.45E-03	3.37E-07	5.97E-10	4.97E-08	1.83E-03	7.88E-14	6.39E-14	9.75E-15	1.28E-04
1400	1.27E-04	1.61E-03	5.81E-07	1.53E-09	1.10E-09	1.73E-03	6.74E-15	6.33E-19	5.77E-20	1.28E-04
1900	5.68E-05	1.68E-03	8.41E-07	2.94E-09	3.91E-11	1.65E-03	5.77E-16	6.28E-24	3.41E-25	1.28E-04
2400	2.55E-05	1.71E-03	1.11E-06	4.84E-09	5.44E-12	1.56E-03	4.94E-17	6.22E-29	2.02E-30	1.28E-04
2900	1.15E-05	1.72E-03	1.38E-06	7.22E-09	4.46E-13	1.48E-03	4.23E-18	6.17E-34	1.19E-35	1.28E-04

Table 3-7. Inventory of Selected of Radionuclides as Input into PFLOTRAN, with Criticality (continued)

Time (years)	Mass Fraction (g/g)									
	²⁴¹ Am	²³⁷ Np	²³³ U	²²⁹ Th	²³⁸ Pu	²⁴⁰ Pu	^{242m} Am	¹³⁷ Cs	⁹⁰ Sr	¹²⁹ I
3900	2.35E-06	1.73E-03	1.92E-06	1.33E-08	3.23E-15	1.33E-03	3.10E-20	0.00E+00	0.00E+00	1.28E-04
4900	5.05E-07	1.73E-03	2.46E-06	2.11E-08	2.37E-17	1.20E-03	2.27E-22	0.00E+00	0.00E+00	1.28E-04
5900	1.31E-07	1.73E-03	3.00E-06	3.03E-08	1.73E-19	1.08E-03	1.67E-24	0.00E+00	0.00E+00	1.28E-04
6900	5.23E-08	1.73E-03	3.53E-06	4.10E-08	1.27E-21	9.70E-04	1.22E-26	0.00E+00	0.00E+00	1.28E-04
7900	3.46E-08	1.73E-03	4.06E-06	5.28E-08	9.32E-24	8.73E-04	8.94E-29	0.00E+00	0.00E+00	1.28E-04
8900	2.91E-08	1.73E-03	4.59E-06	6.57E-08	6.83E-26	7.85E-04	6.56E-31	0.00E+00	0.00E+00	1.28E-04
9000	2.88E-08	1.73E-03	4.65E-06	6.71E-08	4.18E-26	7.77E-04	4.01E-31	0.00E+00	0.00E+00	1.28E-04
9050	3.50E-07	1.73E-03	4.67E-06	6.77E-08	1.57E-07	7.74E-04	7.54E-15	1.01E-07	4.01E-08	1.28E-04
9100	8.16E-07	1.73E-03	4.70E-06	6.84E-08	2.62E-07	7.70E-04	1.80E-14	1.33E-07	5.22E-08	1.28E-04
9500	3.51E-06	1.73E-03	4.90E-06	7.39E-08	4.75E-07	7.44E-04	8.20E-14	1.48E-07	5.76E-08	1.28E-04
10000	5.04E-06	1.73E-03	5.15E-06	8.08E-08	4.90E-07	7.13E-04	1.21E-13	1.48E-07	5.78E-08	1.29E-04
11000	5.67E-06	1.74E-03	5.65E-06	9.54E-08	4.99E-07	6.56E-04	1.40E-13	1.48E-07	5.83E-08	1.29E-04
12000	5.49E-06	1.74E-03	6.15E-06	1.11E-07	5.07E-07	6.04E-04	1.38E-13	1.48E-07	5.88E-08	1.30E-04
15000	4.56E-06	1.76E-03	7.64E-06	1.60E-07	5.29E-07	4.79E-04	1.19E-13	1.47E-07	6.00E-08	1.31E-04
18000	3.83E-06	1.78E-03	9.09E-06	2.13E-07	5.49E-07	3.88E-04	1.04E-13	1.47E-07	6.12E-08	1.32E-04
19000	3.62E-06	1.78E-03	9.57E-06	2.31E-07	5.55E-07	3.64E-04	9.95E-14	1.47E-07	6.16E-08	1.33E-04
20000	7.64E-07	1.78E-03	1.01E-05	2.50E-07	2.14E-10	3.27E-04	7.40E-17	1.47E-17	2.19E-18	1.33E-04
21025	1.56E-07	1.78E-03	1.06E-05	2.70E-07	8.25E-14	2.94E-04	4.81E-19	8.23E-28	4.26E-29	1.33E-04
21100	1.39E-07	1.78E-03	1.07E-05	2.72E-07	4.83E-14	2.92E-04	3.33E-19	1.46E-28	7.02E-30	1.33E-04
21250	1.11E-07	1.78E-03	1.07E-05	2.75E-07	2.72E-14	2.87E-04	1.59E-19	4.62E-30	1.90E-31	1.33E-04
21500	7.76E-08	1.78E-03	1.09E-05	2.80E-07	6.33E-15	2.79E-04	4.67E-20	1.46E-32	4.64E-34	1.33E-04
22000	3.97E-08	1.78E-03	1.11E-05	2.90E-07	4.45E-16	2.65E-04	4.00E-21	1.46E-37	2.77E-39	1.33E-04
23000	1.46E-08	1.78E-03	1.16E-05	3.10E-07	3.07E-18	2.39E-04	2.94E-23	0.00E+00	0.00E+00	1.33E-04
49900	8.97E-10	1.77E-03	2.47E-05	8.92E-07	0.00E+00	1.39E-05	0.00E+00	0.00E+00	0.00E+00	1.33E-04
99900	1.53E-11	1.74E-03	4.49E-05	1.85E-06	0.00E+00	7.11E-08	0.00E+00	0.00E+00	0.00E+00	1.32E-04
199900	4.64E-15	1.68E-03	7.31E-05	3.36E-06	0.00E+00	3.11E-12	0.00E+00	0.00E+00	0.00E+00	1.32E-04
499900	1.12E-25	1.53E-03	1.04E-04	4.77E-06	0.00E+00	1.26E-12	0.00E+00	0.00E+00	0.00E+00	1.30E-04
999900	0.00E+00	1.30E-03	1.01E-04	4.58E-06	0.00E+00	1.26E-12	0.00E+00	0.00E+00	0.00E+00	1.27E-04

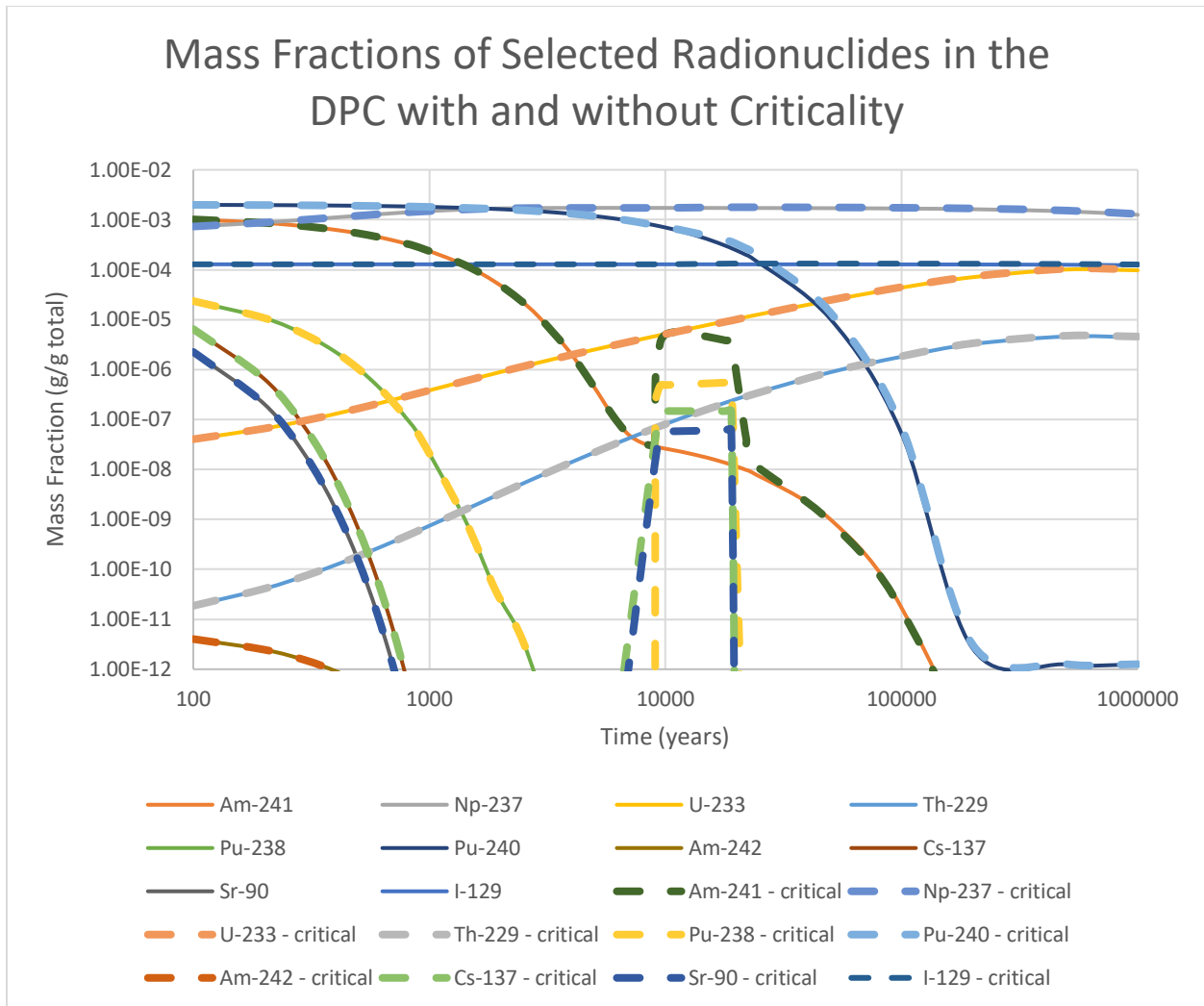


Figure 3-18. Comparison of Selected Radionuclide Mass Fractions in the DPC with and without a Steady-State Criticality Event

3.3 Thermal Effects

Section 2.3 presents three analyses designed to help develop an initial understanding of the effect of a steady-state criticality event on thermal behavior in a repository with DPCs. The corresponding results are presented in the subsections below. As described in Section 2.3.1, the first analysis uses PFLOTRAN to explore the thermal-hydrologic constraints on criticality power output for DPCs disposed in unsaturated alluvium. The simulation results (Section 3.3.1) indicate what conditions might lead to retaining enough water in a breached waste package to maintain a criticality event.

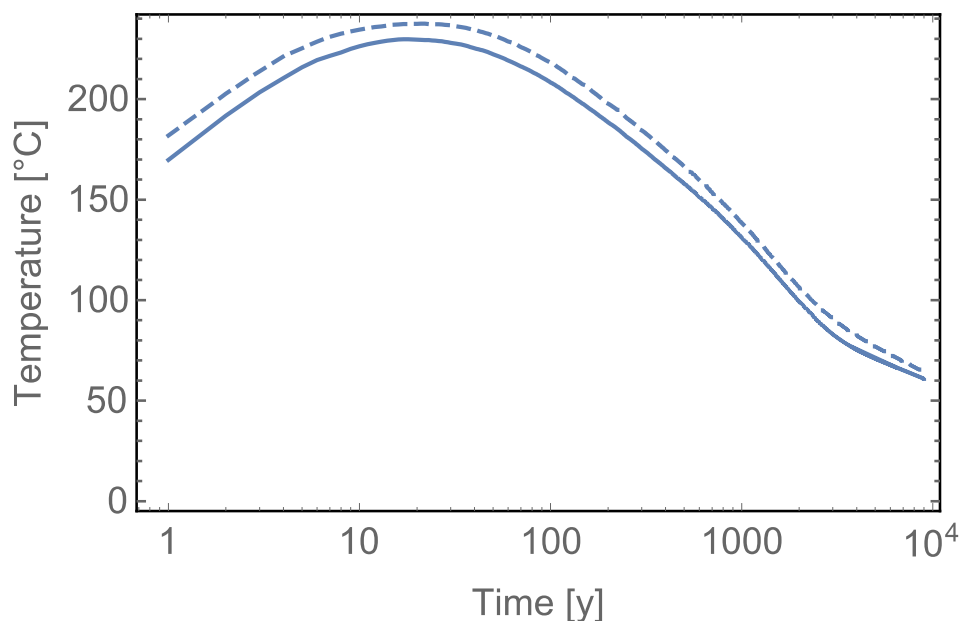
The second analysis relies on analytical models to investigate the thermal response to a steady-state criticality in a DPC disposed in a saturated, homogenous medium (e.g., saturated shale). Section 2.3.2.1 describes a model that considers conduction only; the results are provided in Section 3.3.2.1. The model described in Section 2.3.2.2 and Appendix A includes conduction and convection, with the associated results provided in Section 3.3.2.2.

The final analysis is similar to the second except it uses PFLOTRAN to simulate the thermal response to a steady-state criticality in a DPC disposed in saturated shale. This analysis, which is described in Section 2.3.3, allows for a comparison to be made for simulations with and without criticality. This comparison is included in the results of the third analysis discussed in Section 3.3.3.

3.3.1 Thermal-Hydrologic Constraints on Criticality Power Output for DPCs in Unsaturated Alluvium

As described in Section 2.3.1, an analysis was done to identify what thermal-hydrologic conditions and criticality power output might lead to retaining enough water in a breached waste package in unsaturated alluvium to maintain a steady-state criticality event. Rather than assuming that a criticality begins at 9,000 years (Assumption 1 in Section 1.4.1), this analysis assumes that 9,000 years is the time at which the waste package is breached. The criticality event starts only after the waste package has filled with water. Two different deep percolation rates are considered: approximately 10 mm/yr and approximately 2 mm/yr. In addition, different power outputs from the criticality event are evaluated. The analysis results are presented below.

Temperature versus time in the center of the waste package is shown in Figure 3-19 for both infiltration cases. These plots stop at 9,000 years, the time of waste package breach. In the 10 mm/yr case, the temperature peaks at 233°C after 10–20 years postclosure. By the time of waste package breach, the waste package temperature has decayed to about 61°C. The 2 mm/yr case has slightly higher temperatures because of less latent heat of vaporization to overcome and the slightly lower thermal conductivity in the drier 2 mm/yr case.

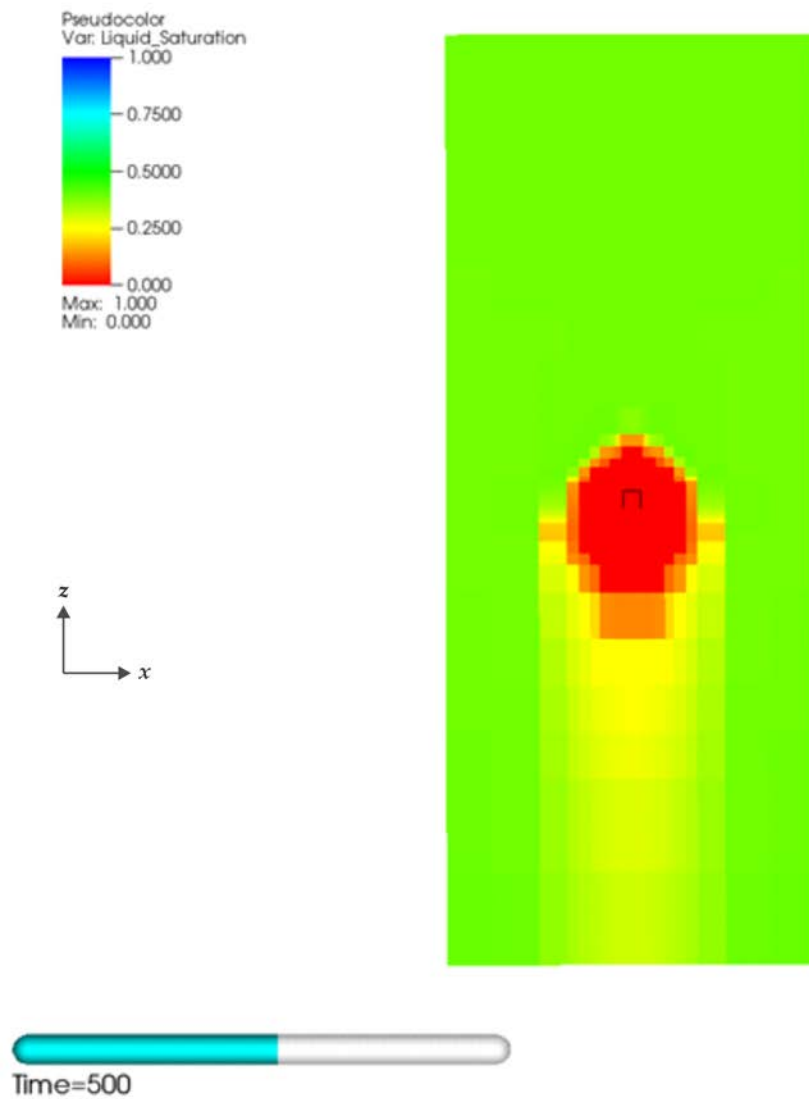


NOTE: Solid curves are for the 10 mm/yr case, dashed curves are for 2 mm/yr.

Figure 3-19. Waste package Temperature versus Time prior to Waste Package Breach

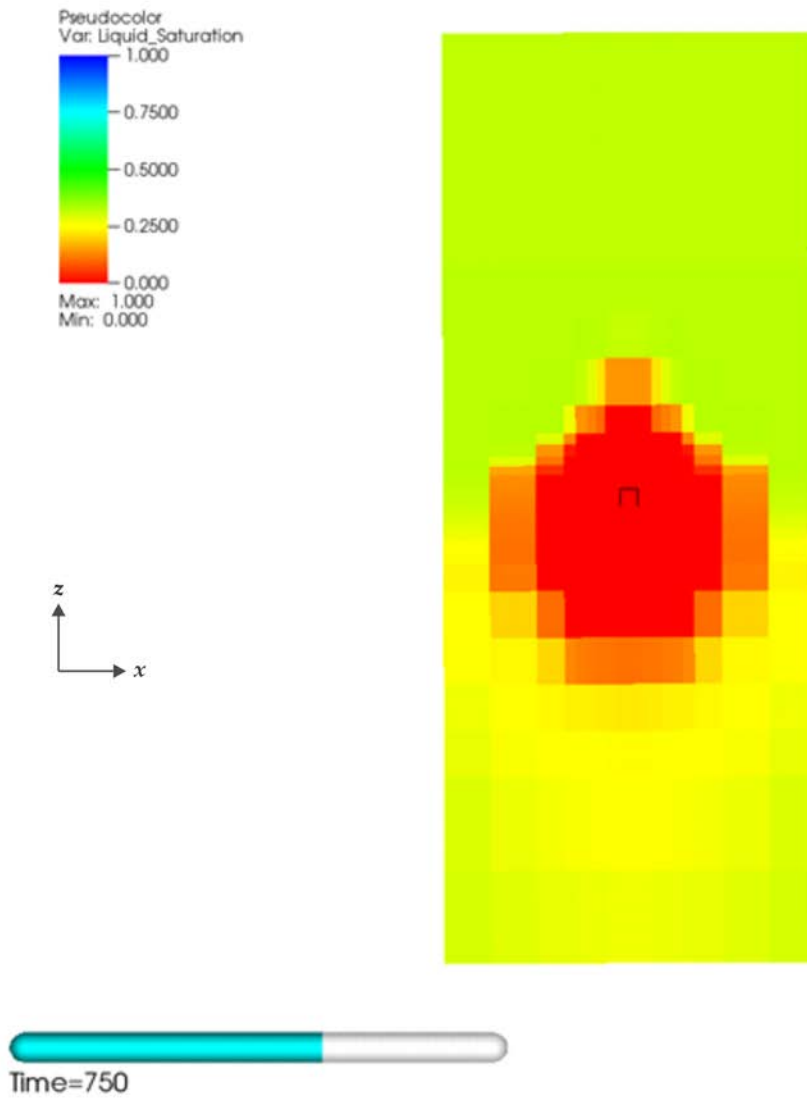
The liquid saturation index field for the 10 mm/yr case is shown in Figure 3-20 at 500 years postclosure, which is near the time of the maximum extent of the dry zone. The black box in the center is the waste package shell. The region of zero liquid saturation extends several meters into the host formation in all directions. It is vertically asymmetric, extending farther in the downward direction. A region of reduced liquid content below the drift—the drift shadow—forms because the drift and surrounding dryout zone block downward flowing water. Significantly, the dry-out zone does not extend to the pillar centerline between drifts. As a result, water drains between drifts without forming a perched zone of higher water content above the repository.

The liquid saturation index field for the 2 mm/yr case is shown in Figure 3-21 at 750 years postclosure, the time of maximum dry-out for this case. The dry-out zone is larger and the vertical asymmetry more pronounced. The dry-out zone extends approximately 20 m in the downward direction and nearly to the pillar center in the horizontal direction.



NOTE: The black box is the waste package outer shell. The subdomain shown is a 40×80 m, vertical cross section at the center of the waste package and perpendicular to the drift.

Figure 3-20. Liquid Saturation Index for the 10 mm/yr Case at 500 Years Postclosure, the Time of Maximum Dry-out



NOTE: The black box is the waste package outer shell. The subdomain shown is a 40×80 m, vertical cross section at the center of the waste package and perpendicular to the drift.

Figure 3-21. Liquid Saturation Index for the 2 mm/yr Case at 750 Years Postclosure, the Time of Maximum Dry-out

Following the waste package breach at 9,000 years, the waste package fills with water in about 100 years in the 10 mm/yr scenario, potentially triggering a criticality event. Two steady-state criticality scenarios are considered for the 10 mm/yr infiltration case: one producing 300 W and one producing 400 W. The criticality event is assumed to initiate 9,100 years after repository closure, after the waste package fills with water.

Temperature versus time for the 300 W scenario is shown in Figure 3-22. In this scenario, the waste package temperature increases to about 78°C. The waste package remains filled with water for 1,000 years after the initiation of the criticality event (result not shown), suggesting that the 300 W criticality event could be sustained.

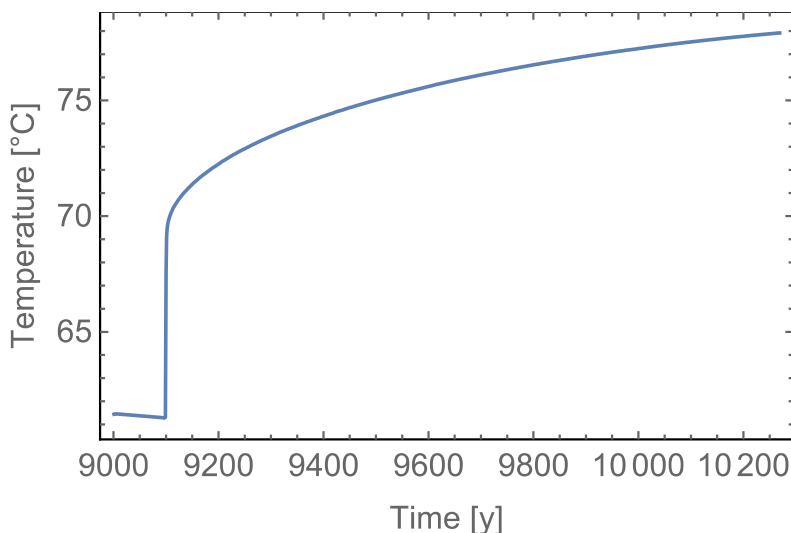
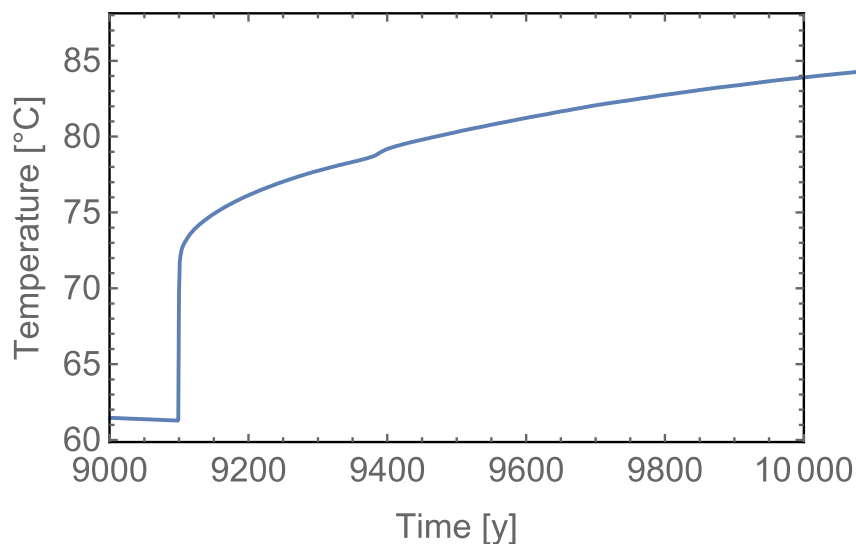


Figure 3-22. Waste Package Temperature versus Time after Waste Package Breach at 9,000 Years for the 10 mm/yr Case, 300 W Scenario

In the 400 W scenario, the temperature initially increases rapidly following the initiation of the criticality event (Figure 3-23), reaching 76°C at 9,200 years, 200 years after the breach. The temperature continues to slowly increase after that, tipping the balance between infiltrating water and evaporation more toward evaporation. Water loss becomes rapid at around 9,300 years and by 9,310 years, the waste package is nearly dry (Figure 3-24), even though the waste package temperature has not reached 100°C. Because loss of water moderator would terminate the criticality event, the 400 W criticality scenario is not sustainable long term.



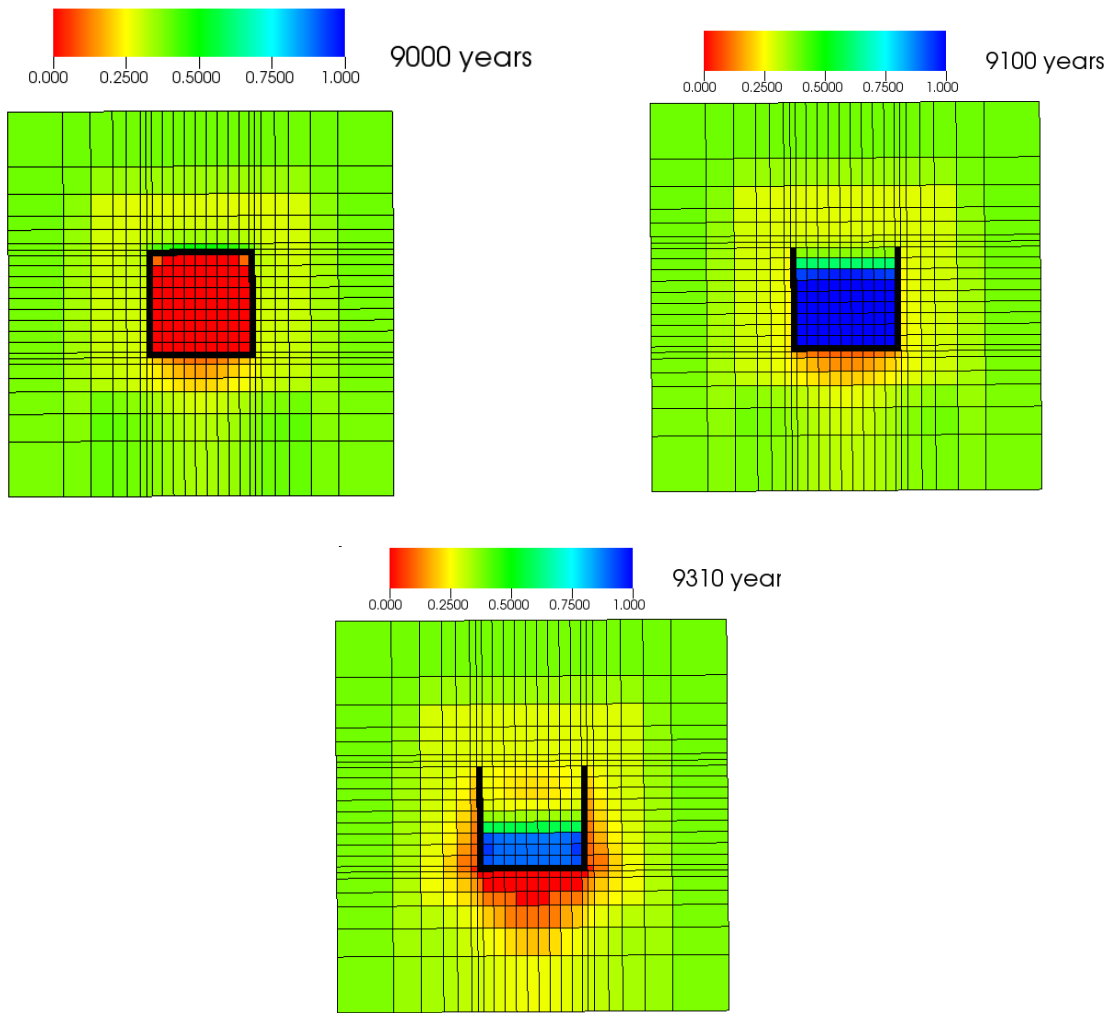
NOTE: In the 10 mm/yr case, 400 W criticality scenario, the waste package temperature increases, thereby driving away water.

Figure 3-23. Waste Package Temperature versus Time after Waste Package Breach for the 10 mm/yr Case, 400 W Criticality Scenario

In the 2 mm/yr case, decay heat alone keeps the waste package dry for thousands of years. The rewetting front reaches the waste package around 16,000 years and the waste package fills with water by 17,000 years. Assuming a 100 W criticality event is initiated at that time, the water in the waste package is driven away by 18,000 years (Figure 3-25). Thus, a 100 W event is sustainable for several hundred years in the 2 mm/yr case, but it cannot be sustained indefinitely because of evaporation. The waste package temperature is only 57°C at 18,000 years in this scenario, further underscoring that evaporation without boiling is sufficient to keep the waste package dry in low infiltration unsaturated alluvium.

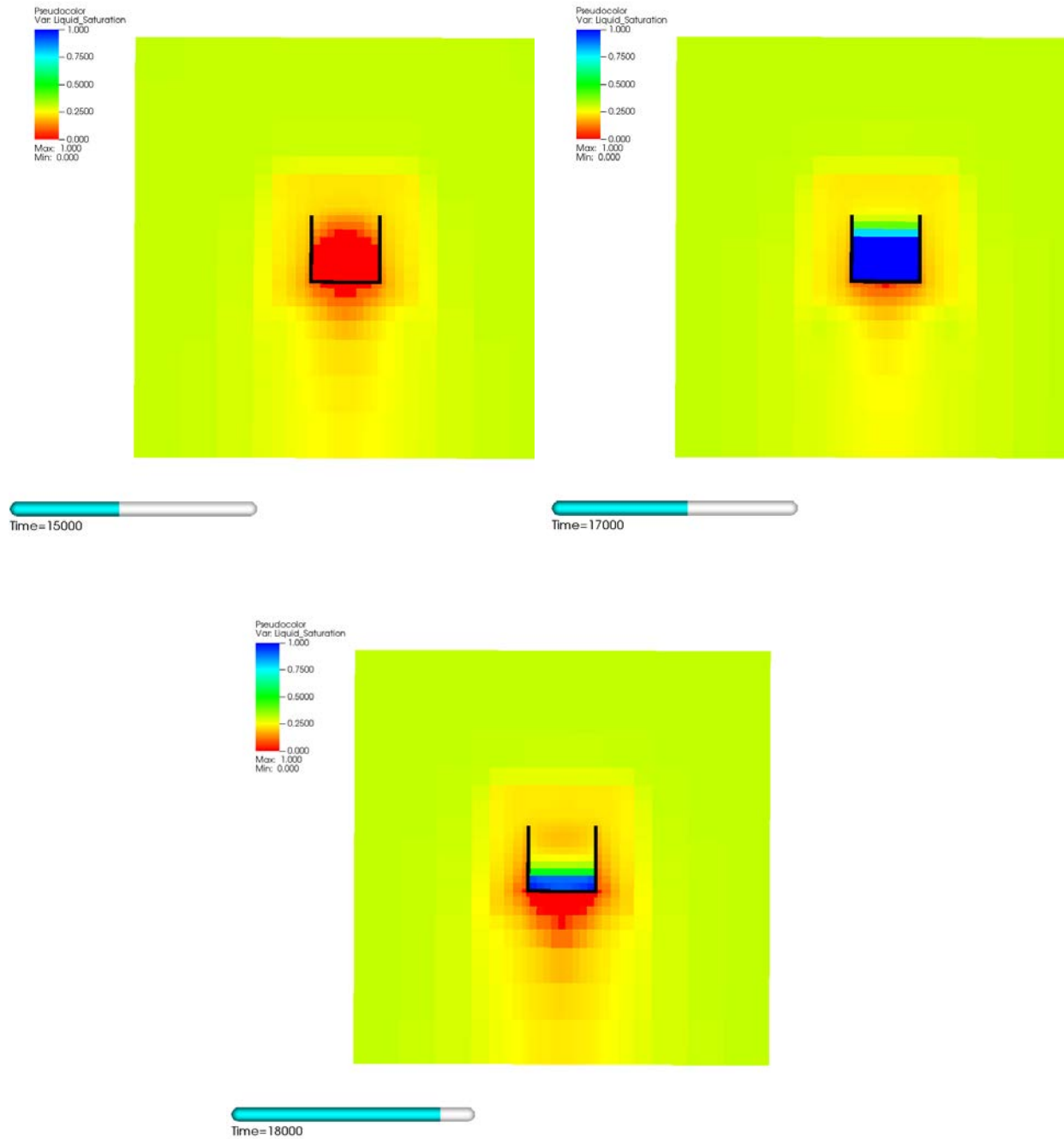
For the conditions analyzed here, the alluvial formation can supply enough water to allow the waste package to fill with water and trigger a criticality event following a waste package breach. In the 10 mm/yr scenario, the waste package fills with water about 100 years after a breach at 9,000 years. However, long-term average power output that can be sustained is limited to between 300 W and 400 W for a single waste package. In the 2 mm/yr scenario, decay heat alone is sufficient to keep the waste package dry until approximately 16,000 years postclosure. Moreover, in these dry conditions, criticality events with power outputs as low as 100 W cannot be sustained long term because evaporation and vapor diffusion remove water moderator from the waste package.

Liquid Saturation Index



NOTE: Blue means the cell is saturated; red means the cell is completely dry. Upper left—9,000 years is the time just before waste package breach. Upper right—9,100 years marks the initiation of a 400 W criticality event. Bottom—9,310 years is 210 years after the event starts.

Figure 3-24. Liquid Saturation Index for the 10 mm/yr Scenario shown on Vertical Cross Section Perpendicular to Emplacement Drifts



NOTE: Blue means the cell is saturated; red means the cell is completely dry. The waste package fills with water around 17,000 years postclosure, at which time a 100 W criticality event is assumed to start. Even that modest power output is sufficient to cause water to evaporate and leave the waste package in these dry conditions.

Figure 3-25. Liquid Saturation Index for the 2 mm/yr Scenario in a Vertical Cross Section Perpendicular to the Emplacement Drifts at Different Times

3.3.2 Computational Results for Analytical Models of Thermal Response to Steady-State Criticality

Two analytical models were constructed to evaluate the thermal response to a steady-state criticality. The model considering conduction only is described in Section 2.3.2.1; the model considering conduction and convection is described in Section 2.3.2.2. Section 3.3.2.1 below discusses the results of the conduction-only model, including the temperatures at the central (critical) DPC and at the nearest DPC in the same emplacement drift. The results for the analytical model featuring conduction and convection are discussed in Section 3.3.2.2.

3.3.2.1 Results for Analytical Model with Heat Conduction

Temperature at the Central (Critical) DPC

Figure 3-26 shows the (total) temperature on the surface of the critical DPC at its top center (1 m above the central axis) for bentonite backfill thermal properties. The temperature in Figure 3-26 includes the contributions from 11 thermal sources (Figure 2-6) and an ambient temperature of 30°C. Note that the initial peak temperature, 164°C, and the temperature during criticality, 165°C, are both significantly below the boiling point (assumed to be 264°C) for a saturated shale repository at 500 m depth. In an unsaturated system, the spacing between adjacent DPCs, currently 20 m, may be increased to reduce the peak temperature in the bentonite backfill to below 100°C.

Figure 3-37 shows the temperature rise from the central (critical) DPC (black curve) and from the adjacent DPCs (colored curves) with spacing of 20 m, 30 m, 36.1 m, and 40 m from the central DPC. As expected, the contribution from the critical DPC between 9,000 and 19,000 years dominates the thermal response and the adjacent DPCs make an insignificant contribution to temperature change after 9,000 years. Figure 3-27 shows that the temperature change at the central DPC from DPCs with 36.1 m spacing is greater than that from DPCs with 30 m spacing because the location of DPCs in adjacent drifts results in four DPCs with 36.1 m spacing but only two DPCs with 30 m spacing, as shown in Figure 2-6.

Figure 3-28 shows the (total) temperature on the surface of the critical DPC at its top center (1 m above the central axis) for shale host rock thermal properties. The temperature in Figure 3-28 includes the contributions from 11 thermal sources (Figure 2-6) and an ambient temperature of 30°C. The general features of the thermal response in Figure 3-28 are identical to Figure 3-26 for bentonite backfill, although the initial peak temperature and the temperature during criticality are approximately 30°C greater for the shale host rock than for the bentonite backfill. This behavior is reasonable because the thermal diffusivity of the backfill, $8.59 \times 10^{-7} \text{ m}^2/\text{s}$, is about 40% greater than the thermal diffusivity of the shale host rock, $6.13 \times 10^{-7} \text{ m}^2/\text{s}$, resulting in higher temperatures in the shale due to its lower thermal diffusivity.

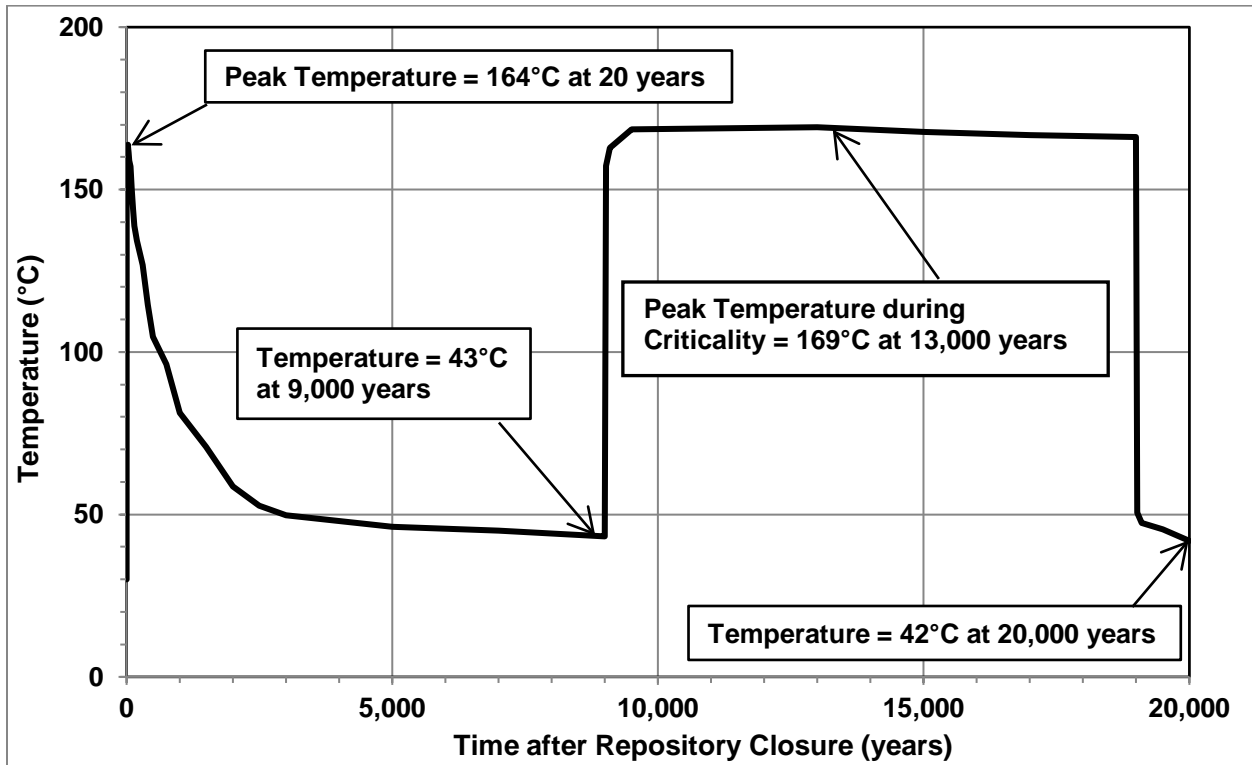
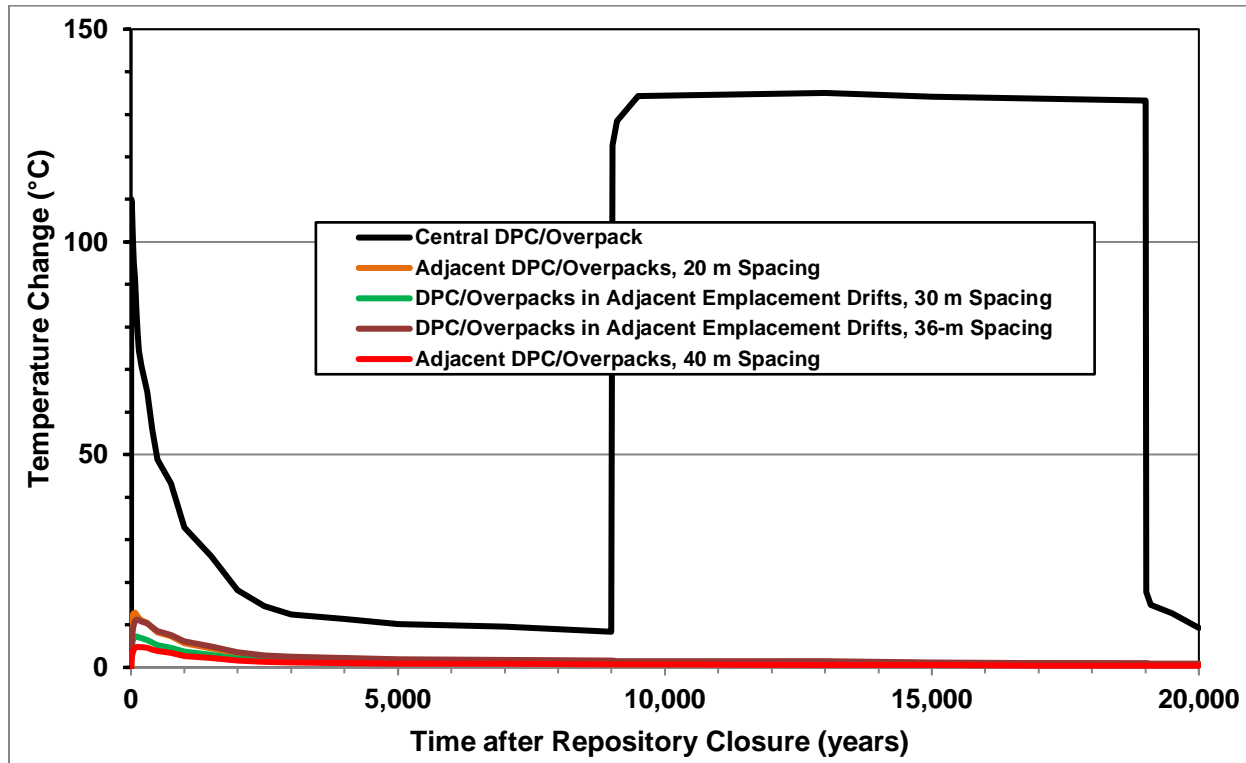


Figure 3-26. Temperature History for 4 kW Criticality from 9,000 to 19,000 Years with Thermal Properties for Bentonite Backfill



NOTE: There is less temperature change on the central DPC from DPCs with 30 m versus 36.1 m spacing because the spacing of the adjacent drifts results in four DPCs with 36.1 m spacing but only two DPCs with 30 m spacing (Figure 2-6). DPC = dual-purpose canister.

Figure 3-27. Contribution to Temperature Change from the Central (Critical) DPC and from the Adjacent DPCs with the Thermal Properties for Bentonite Backfill

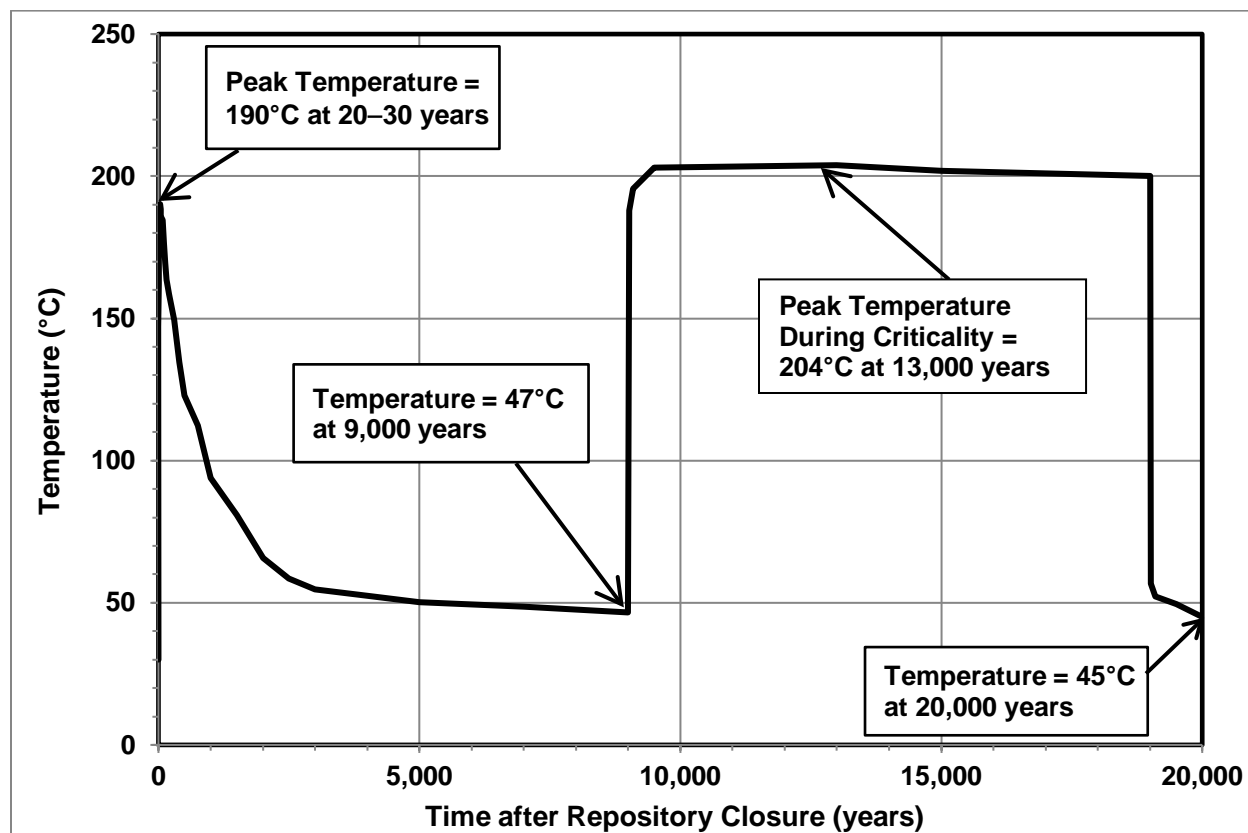


Figure 3-28. Temperature History for 4 kW Criticality from 9,000 to 19,000 years with Thermal Properties for Shale Host Rock

Temperature Change at the Adjacent DPC from Criticality in the Central DPC

The results presented above focus on the temperature history at the central (critical) DPC from a 4 kW criticality event in the same DPC. It is also of interest to determine the temperature changes at adjacent DPCs from a 4 kW criticality in the central DPC. In other words, does the thermal pulse from the critical DPC produce large temperature changes (and possibly collateral damage) in adjacent DPCs that are 20 to 40 m away from the central DPC?

Figure 3-29 and Figure 3-30 show the temperature changes on the surface of adjacent DPCs that are spaced 20 m, 30 m, and 40 m from the critical DPC using thermal properties for bentonite backfill and for shale host rock, respectively. The observation point on each adjacent DPC is again at top center, 1 m above the central axis. Figure 3-29 shows peak temperature rises of 11.6°C at 13,000 to 19,000 years for a 20 m separation, 7.4°C at 15,000 to 19,000 years for a 30 m separation, and 5.5°C at 15,000 to 19,000 years for a 40 m separation in bentonite backfill. Figure 3-30 shows peak temperature rises of 14.5°C at 13,000 to 19,000 years for a 20 m separation, 9.4°C at 15,000 to 19,000 years for a 30 m separation, and 7.0°C at 15,000 to 19,000 years for a 40 m separation in the shale host rock. These temperature changes are relatively small, so a steady-state 4 kW criticality in a DPC is very unlikely to produce “collateral damage” in an adjacent DPC from thermal effects.

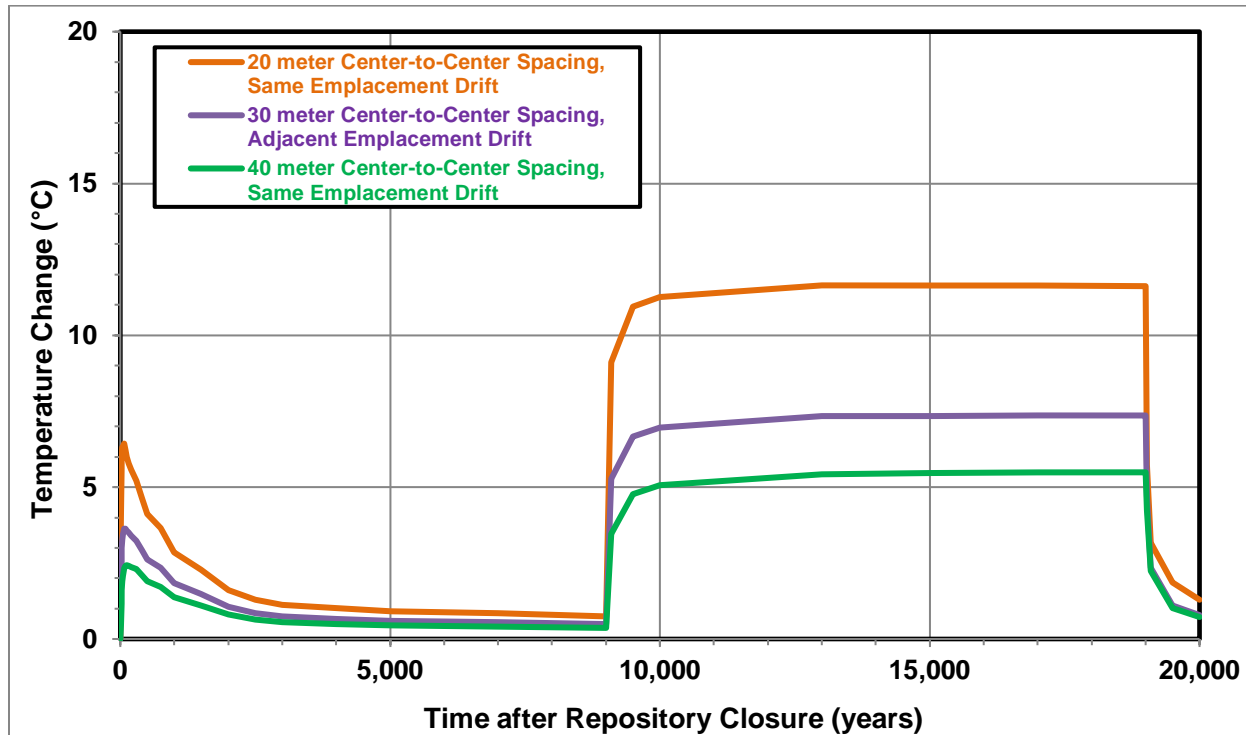


Figure 3-29. Temperature Change in Adjacent DPCs Separated by 20, 30, and 40 m from the Central (critical) DPC in Bentonite Backfill

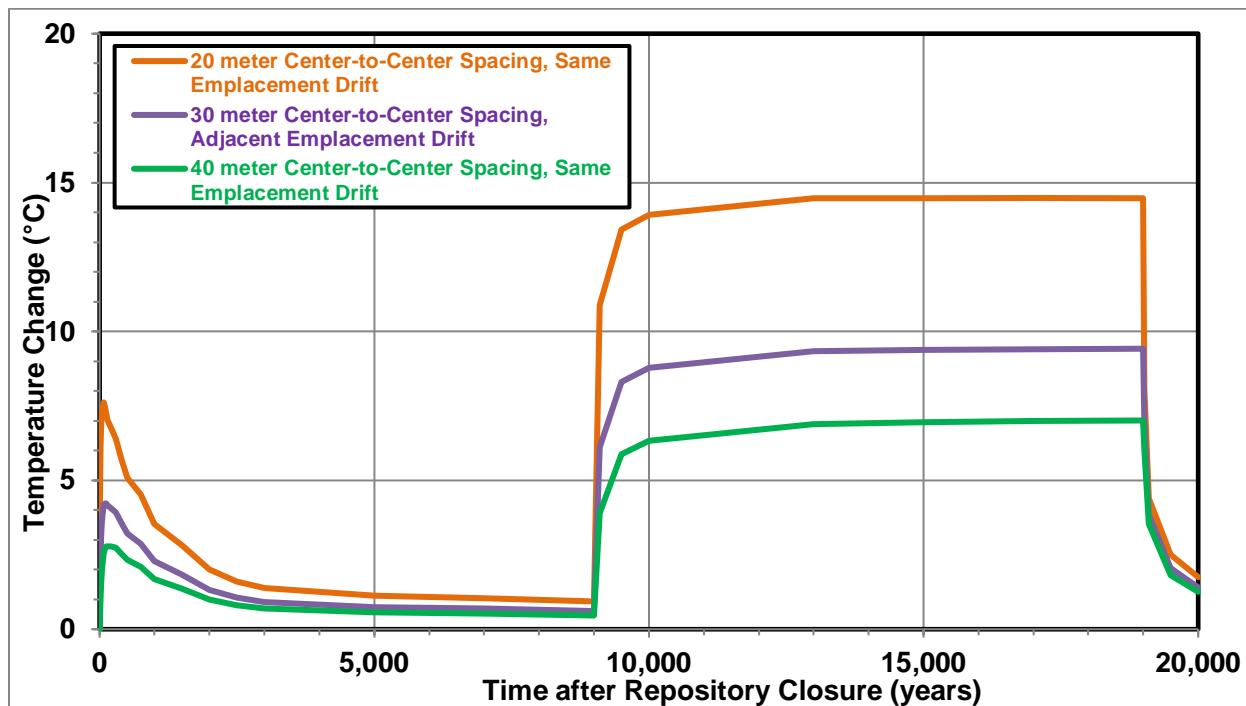


Figure 3-30. Temperature Change in Adjacent DPCs Separated by 20, 30, and 40 m from the Central (critical) DPC in Shale Host Rock

Sensitivity of Results to Five Versus Nine Discrete Locations for Thermal Point Sources

Figure 3-31 is a comparison of the thermal response at the top center of the central (critical) DPC from models with five versus nine discrete locations for point sources. To be clear, the thermal response in Figure 3-26 is only for the central DPC and does not include the effect of adjacent DPCs to provide a clear comparison of five versus nine discrete locations for a single DPC. The total power for both models is based on the data in Table 2-5; the total power is equally divided among five or nine discrete locations, and the discrete locations are equally spaced on the axis of the critical DPC in both models.

Figure 3-31 presents a comparison of the results for five versus nine discrete locations for the central DPC (only). The initial peak temperature change in the model with nine discrete locations is 115.4°C at 10 years versus 110.12°C at 10 years for the model with five discrete locations. This comparison yields a difference of 5.3°C or +4.8%. Between 100 and 9,000 years, the difference drops monotonically from 3.9°C to 0.4°C. During criticality, the temperature change in the model with nine discrete locations is 136.6°C at 9,500 years versus 130.7°C at 9,500 years for the model with five discrete locations. This comparison yields a difference of 5.9°C, or +4.5%.

An increase of 4.5% is consistent with the analytic solution for the steady-state temperature field around a continuous point source of constant strength. As $t \rightarrow \infty$ in Equation 2-4, $erfc(r / \sqrt{4\kappa t}) \rightarrow 1$ and $v \rightarrow q/(4\pi\kappa r)$ (Carslaw and Jaeger 1959, Section 10.4). This simple formula means that the temperature change in steady state from each point source is (1) directly proportional to $q(t_i)$, the strength of the point source for the time interval in question, and (2) inversely proportional to r , the distance from the point source to the observation point.

Applying this result for a model with five discrete locations equally spaced on the axis and an observation point on the top center of the DPC:

$$v_5 \propto \frac{q/5}{1.0} + \frac{2q/5}{1.7205} + \frac{2q/5}{2.9732} = (0.5670)q \quad \text{Equation 3-1}$$

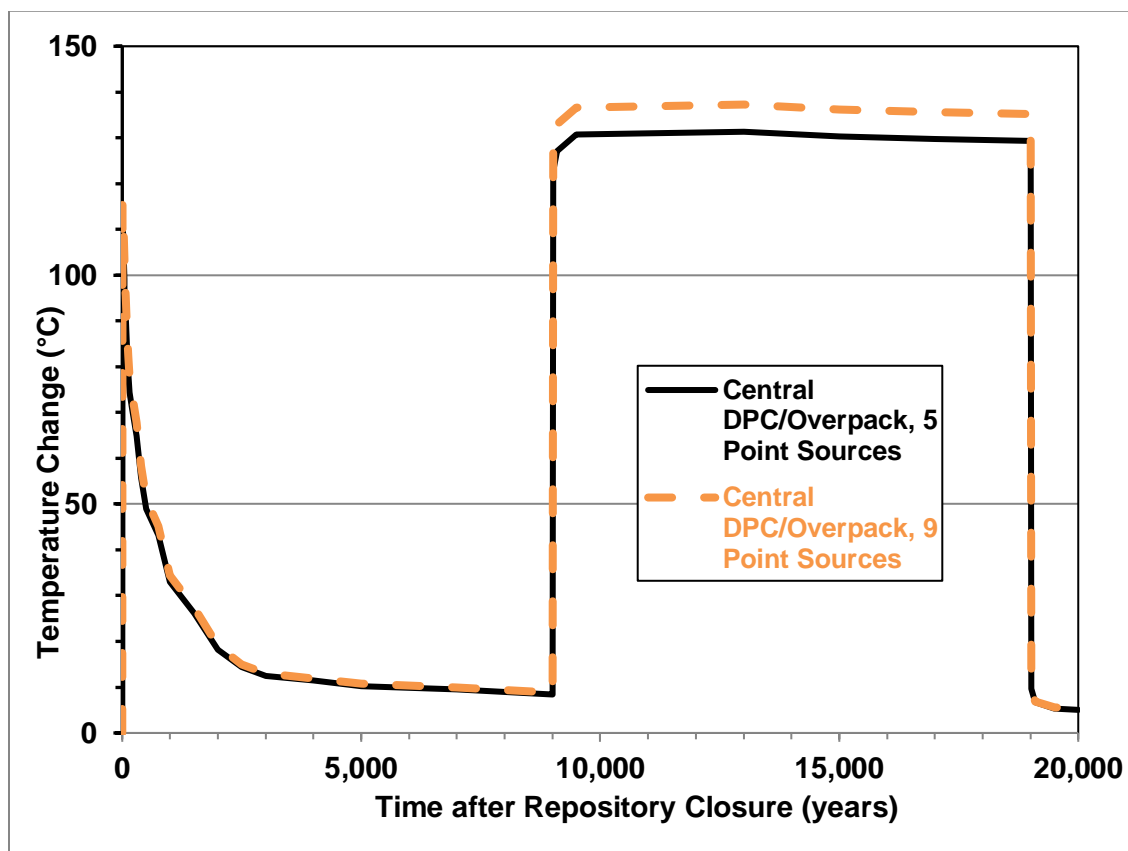
In Equation 3-1, the first term represents the ratio of the power to the distance to the observation point for the central location in the DPC, with one-fifth of the total power divided by the distance from the center point source to the top center of the DPC surface ($r = 1$ m). The second term represents the ratio of the power to the distance to the observation points for two point sources (with two-fifths of the total power) that lie midway between the center and ends of the DPC. The distance from these two point sources to the observation point at the top center of the DPC surface is $r = \sqrt{(1)^2 + (1.4)^2} = 1.7205$. The third term represents the ratio of power to the distance to the two point sources that are located at the ends of the DPC with $r = \sqrt{(1)^2 + (2.8)^2} = 2.9732$. Similar logic for a model with nine discrete locations gives Equation 3-2:

$$v_9 \propto \frac{q/9}{1.0} + \frac{2q/9}{1.7205} + \frac{2q/9}{2.9732} + \frac{2q/9}{1.2207} + \frac{2q/9}{2.3250} = (0.5926)q \quad \text{Equation 3-2}$$

Then the ratio of v_9 to v_5 is

$$\frac{v_9}{v_5} = \frac{0.5926q}{0.5670q} = 1.045 \quad \text{Equation 3-3}$$

The increase is 4.5% for nine versus five discrete locations at steady-state. So a model with five discrete locations tends to underestimate temperature changes by 4% to 5% relative to a model with nine discrete locations. This difference is negligible compared to the other uncertainties in these calculations, such as the uncertainty in the parameters and repository design for the shale reference case. Given that these calculations are considered preliminary for a generic reference case in a saturated shale site, the model with five discrete locations per DPC is adequate for these calculations.



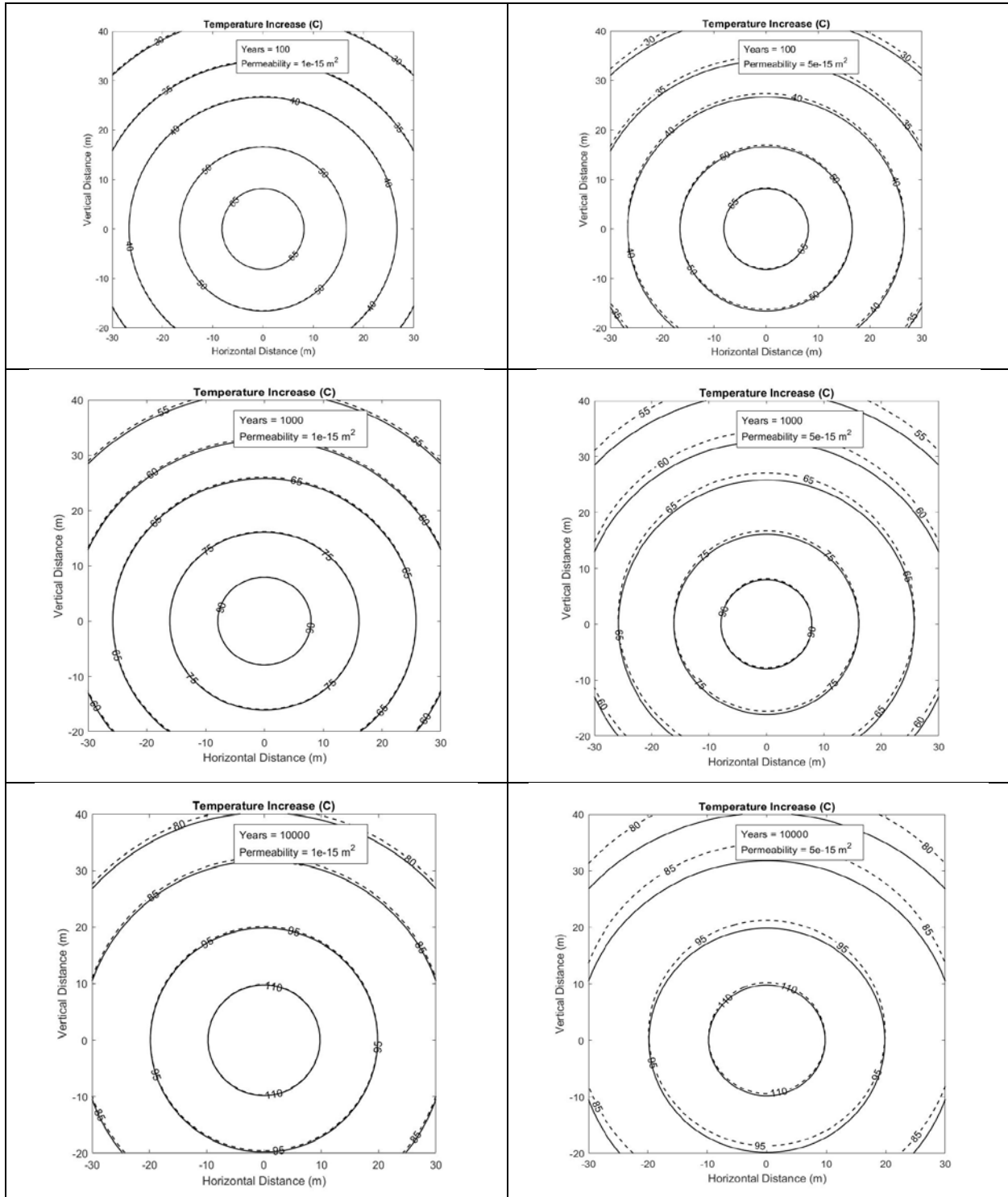
NOTE: DPC = dual-purpose canister.

Figure 3-31. Comparison of Temperature Change with Five Versus Nine Discrete Locations for Thermal Point Sources on the Axis of the Central (critical) DPC in Bentonite Backfill

3.3.2.2 Results for Analytical Model with Heat Conduction and Heat Convection

The analytical model for evaluating the thermal response to a steady-state criticality with conduction and convection is described in Section 2.3.2.2 and Appendix A. The calculations consider a saturated homogenous medium and a constant heat generation rate for a period of 10,000 years. Table 2-7 presents the values of the input parameters for determining the contours of temperature increase above ambient for a line source of heat in a saturated porous medium. The results of the calculations are provided below.

Figure 3-32 presents the increase in temperature as contours at 100, 1,000 and 10,000 years, from the top to the bottom of the figure, respectively. The right and left sides of the figure are for permeabilities of 10^{-15} and $5 \times 10^{-15} \text{ m}^2$, respectively. The conduction-only temperature contours are always circular because there is no convection and thus no angular dependence. However, heated water has a lower density than water at the temperature far from the line source. This difference induces buoyancy that drives convective flow around the line source. Since the heating rate, density, and heat capacity are constant, the temperature contours with and without convection must encompass the same area. Therefore, in Figure 3-32 the dashed curves for the same temperature are shifted slightly higher in vertical distance. This effect is small even for $K = 5 \times 10^{-15} \text{ m}^2$ as given on the right side which is much higher than the expected permeability. For $K = 1 \times 10^{-15} \text{ m}^2$ as given on the left side of the figure, the effect of convection is negligible even after 10,000 years of heating. Thus, unless there is a dramatic change in the permeability with time, possibly due to cracking or mineral leaching, induced buoyancy can be neglected.



NOTE: Solid lines are conduction only, and dashed lines are conduction and convection.

Figure 3-32. Contours of Increased Temperature Above Ambient at 100, 1,000, and 10,000 years with Rock Permeabilities of $1 \times 10^{-15} \text{ m}^2$ and $5 \times 10^{-15} \text{ m}^2$ on the Left and Right Sides, Respectively

3.3.3 Results for Thermal Analysis with PFLOTRAN without Criticality

As described in Section 2.3.3, PFLOTRAN was used to simulate the thermal impacts of disposal of SNF in a DPC in saturated shale. The simulations rely on more physically realistic initial conditions, but in turn cannot consider radionuclide transport because of capability restrictions. Simulation and boundary conditions are consistent with those described in Section 3.8.

For the shale reference case, material properties are consistent with those outlined in Table 2-9. The only difference in the simulations presented here is that the initial water saturation is set to 65% (Rutqvist et al. 2011; Rutqvist et al. 2014). As shown in Figure 3-33, temperature peaks at around 190°C at the very center of the waste package. The temperature in the buffer peaks at about 185°C after 40 years, and host rock temperature peaks at 113°C after 70 years (Figure 3-35). Similarly, liquid saturations remain below 100% in the drift throughout the first 10 years of simulation time (Figure 3-34); complete dry-out only occurs at the center of the waste package, which is fully re-saturated by 2,000 years (Figure 3-36). Notable asymmetry in the liquid saturation distribution here is likely due to material property contrasts and localized thermal loading. In particular, the ring of high liquid saturation at the 1-year snapshot is likely due to permeability contrasts between the waste package and buffer, and the behavior of the liquid saturation front captured at 10 years is likely due to the heat source being localized in the waste package and maintaining low water saturation there (Figure 3-34).

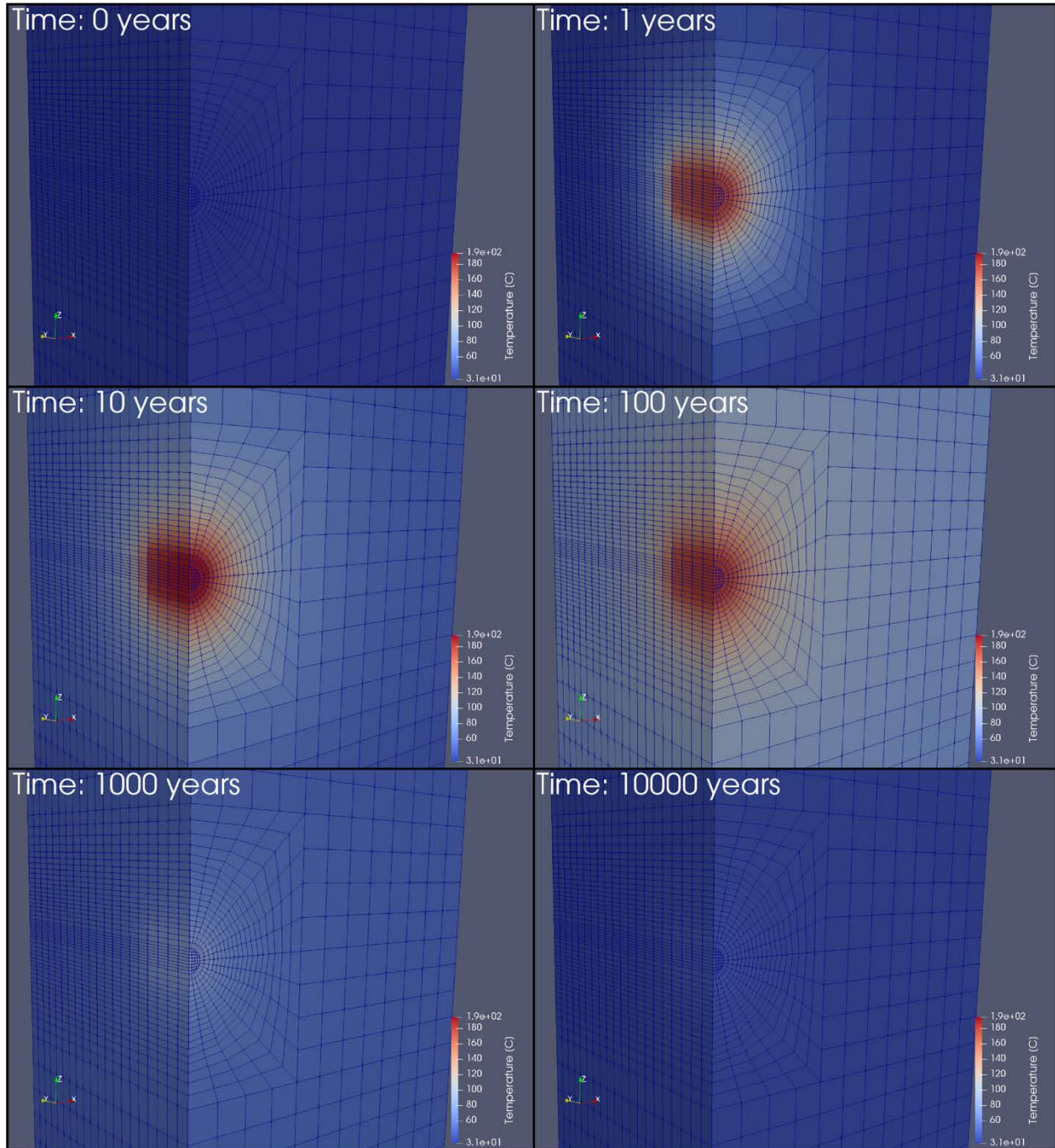


Figure 3-33. Snapshots of 3D Temperature Distribution

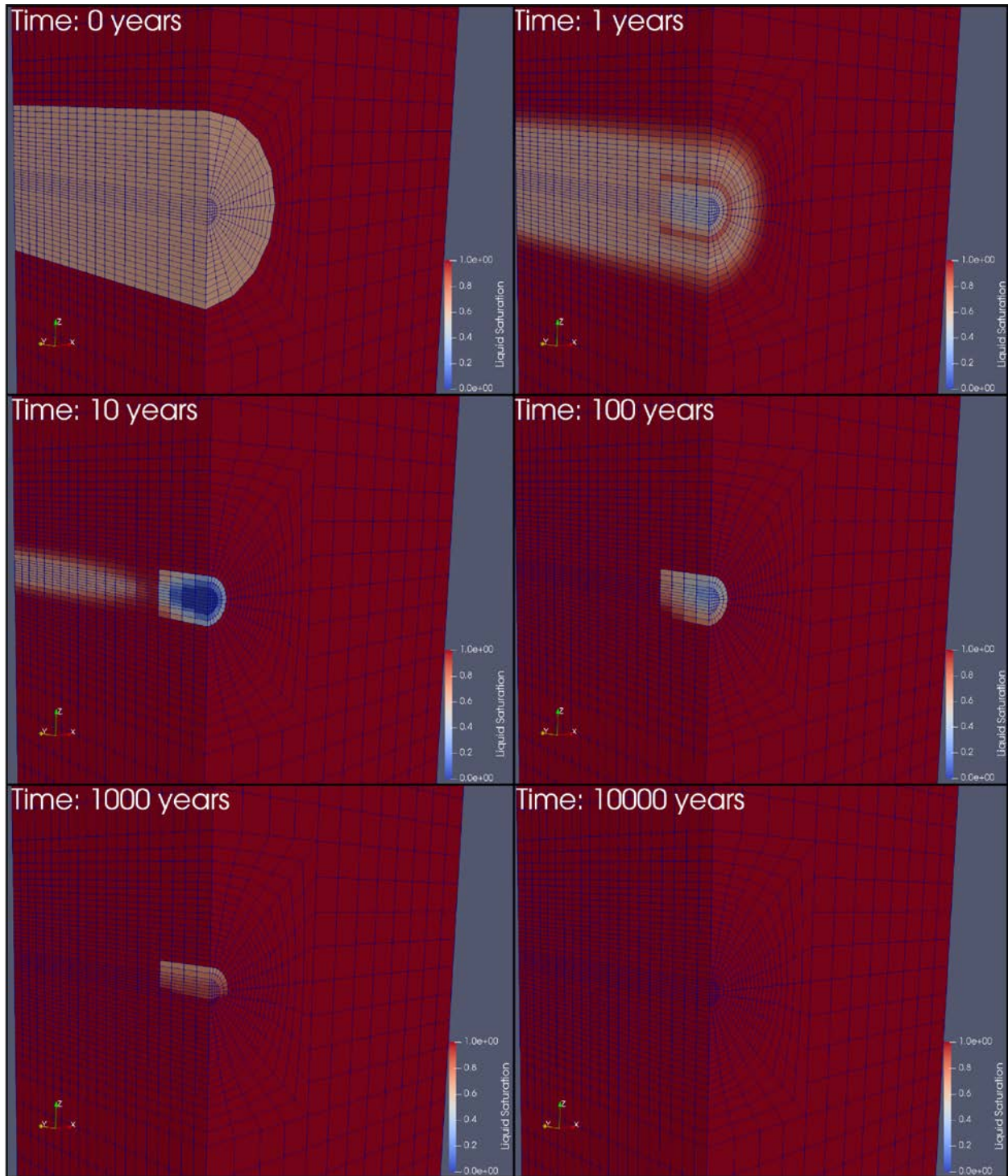
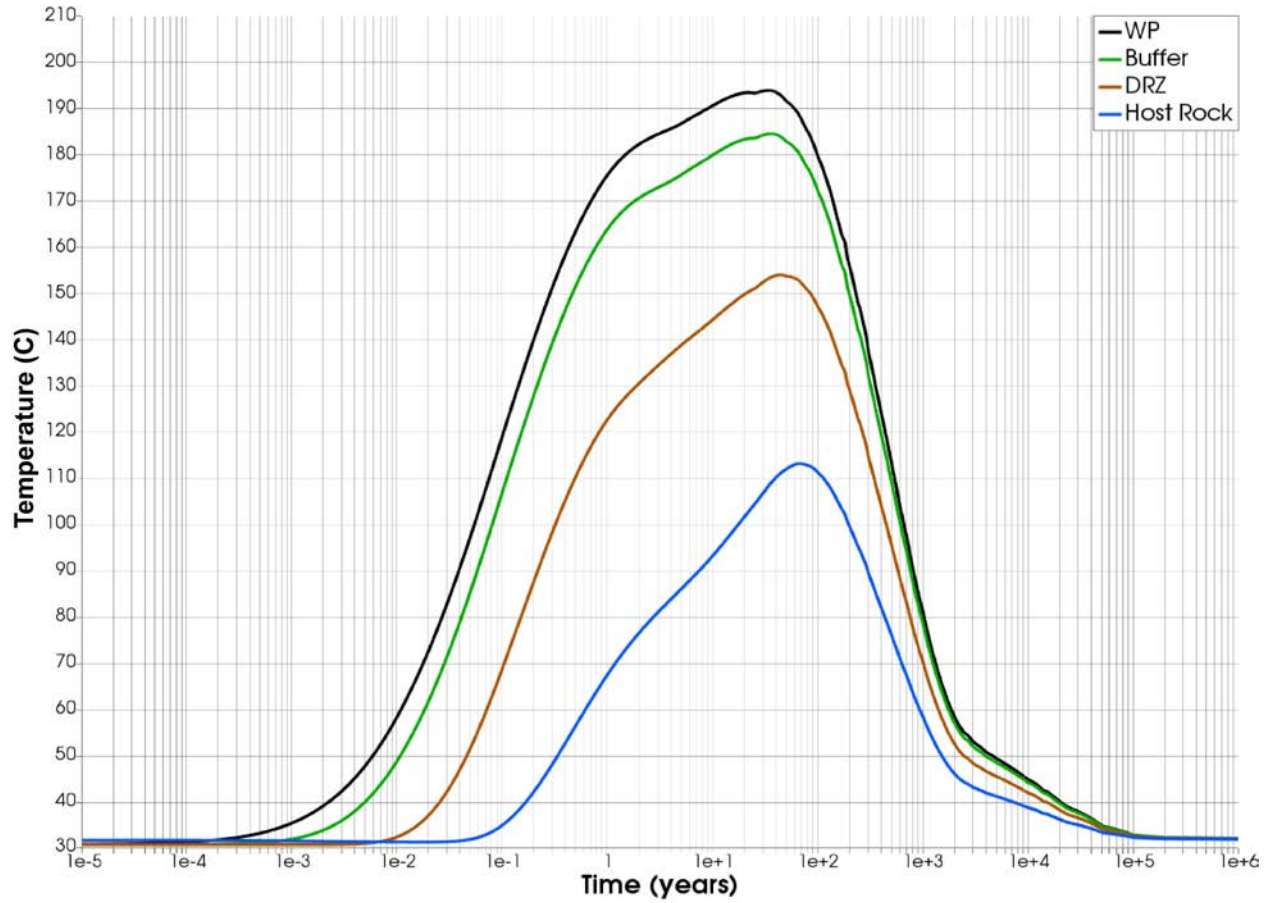
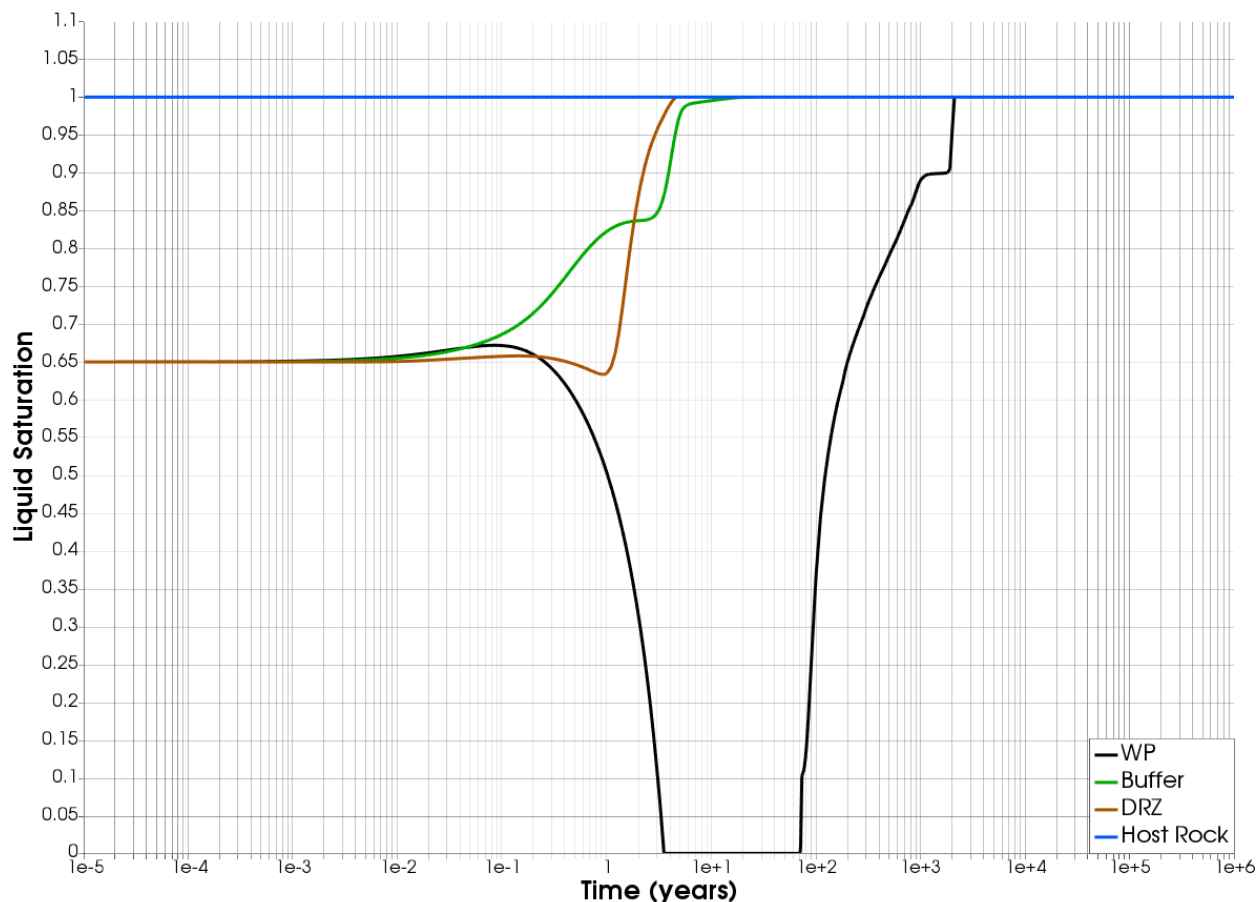


Figure 3-34. Snapshots of 3D Liquid Saturation Distribution



NOTE: DRZ = disturbed rock zone.
 WP = waste package.

Figure 3-35. Temperature versus Time at Observation Points Specified in Figure 2-10



NOTE: DRZ = disturbed rock zone.
 WP = waste package.

Figure 3-36. Liquid Saturation versus Time at Observation Points Specified in Figure 2-10

Simulations presented in this subsection demonstrate that, under representative initial liquid saturation conditions, peak temperatures due to decay heat thermal loading are very similar to those observed in Section 3.8, and the entire repository is fully saturated with water after about 2,000 years. Therefore, for shale reference case simulations, the initial water saturation likely exerts minimal influence on heat flow and radionuclide transport in the event of waste package breach and in-package criticality occurring at 9,000 years. By then, temperatures are within about 10°C of ambient temperature and the repository is fully water-saturated. This situation supports the simulated pressure and temperature response due to an in-package criticality event presented in Section 3.8.

3.4 Chemistry

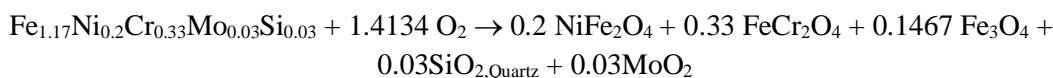
Key components of in-package chemistry are the coupled processes of stainless steel corrosion, radiolysis, and SNF degradation. The discussion below quantifies some of the effects of radiolysis and increased temperatures from postclosure criticality on the processes that affect in-package chemistry.

These effects are not included in the PFLOTRAN simulations described in Section 3.8, but they will be captured in future PFLOTRAN simulations.

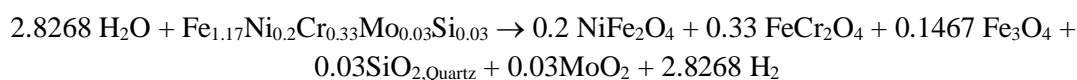
3.4.1 Steel Corrosion

The 316 stainless steel corrosion in J-13 well water at 50°C was measured at 0.000443 μm/d. Corrosion rates of 316 stainless steel at 80°C in anoxic alkaline media range from 0.001 to 0.1 μm/yr, or 0.0000027 to 0.00027 μm/d (Kurstin et al. 2004). Hydrothermal corrosion rates of 316 stainless steel in contact with low Eh redox-buffered bentonite at 300°C decrease over time (Cheshire et al. 2014; Jove-Colon et al. 2017) because of the accumulation of corrosion product layers, which diminish the access of water and/or depletion of oxidants (Jove-Colon et al. 2017). Corrosion over 38 to 59 days averaged 0.26 μm/d. Corrosion over 6 months was measured at 0.07 μm/d. Corrosion rates are higher when fluids are more saline. An Arrhenius equation developed from the 300°C corrosion data and the mid-point (0.000027 μm/d) 80°C data predicts a 100°C (alluvial) steel corrosion rate of 0.00008 μm/d and a 169°C (shale) steel corrosion rate of 0.002 μm/d.

General corrosion of stainless steel produces an assemblage of iron (hydr)oxides, magnetite (Fe₃O₄), possibly hydrated Cr₂O₃, chromite (FeCr₂O₄), trevorite (NiFe₂O₄), and possibly metal sulfides and silicates (Stockman 2006; Jove-Colon et al. 2017). Steel corrosion also produces H₂ gas and low Eh conditions particularly in the shale case. Oxidation of stainless steel (Fe_{1.17}Ni_{0.2}Cr_{0.33}Mo_{0.03}Si_{0.03}) to trevorite, chromite, quartz and magnetite is shown in the following example reaction:



Oxidation of steel under reducing conditions (shale) produces H₂ instead of consuming O₂, as seen, for example, in the following:



There is a large positive volume change entailed in the conversion of a mole (100 g) of stainless steel (12.53 cm³/mol) to corrosion products (31.44 cm³/mol for the oxidizing conditions case above); the net volume change is calculated to be 18.91 cm³ per mole of steel corroded. However, the actual volume change, hence void-filling potential, is expected to be greater because the corrosion products contain water as thin films and in pores. Water content in soils typically range from 20% to 50%. Calculations done for the Yucca Mountain Project assumed a water pore volume of 40% in steel corrosion products (BSC 2005c).

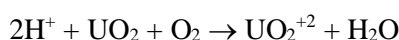
The TAD 21-PWR canister (BSC 2005c, Section 6.3.4.3.4.2) is used to roughly constrain consequences of temperature-dependent stainless steel corrosion during criticality inside a DPC. The initial 316 steel surface area of the TAD internals is 1196 m²; the interior volume is 14.77 m³; and the void volume is 7.99 m³, or 7,990 l. This value corresponds to an initial porosity of 54%. The mass of 316 stainless steel internals in the TAD (minus the shield plug) is 30,880 kg (CSNF waste products and corrosion products domains in BSC 2005c, Table 6.3-8). A maximum stainless steel corrosion rate of 0.002 μm/d (shale) corresponds to 0.07 kg/yr of 316 corrosion, which is equal to 0.0013 m³/yr of pore volume filling (i.e., corrosion product accumulation minus steel dissolution). Assuming that entrained water amounts to

40% of the volume (as was done for Yucca Mountain) points to a rate of DPC void filling of $1.40 \times 0.0013 \text{ m}^3/\text{yr} = 0.0018 \text{ m}^3/\text{yr}$. At this rate, the DPC is calculated to be self-sealed in 4,320 years in the shale criticality scenario. In the lower temperature alluvial case, corrosion is ~25 times slower at 0.0028 kg/yr of stainless steel corroded, and DPC pore volume reduction of $7.2\text{e-}5 \text{ m}^3/\text{yr}$.

Trevorite dissolution can consume acid and to a degree counteract acidic pHs from occurring (e.g. by radiolytic production of nitric acid in the alluvial case):



The surfaces of iron and chromium corrosion products also work to buffer pHs near neutral because they tend to sorb hydroxyls above a pH of ~9 and H^+ below a pH of ~7, thus keeping adjacent fluids near the oxide surface pH of zero surface charge (7–9). Degradation of SNF also consumes acid:



The actual degree to which in-package pH buffering of radiolysis in the alluvial case will occur depends upon the amount of trevorite, and other corrosion products, formed prior to criticality and the rate at which fuel dissolves. The calculated trevorite pH buffering effect goes away if total radiolytic production of nitric acid exceeds the total amount of trevorite produced by steel corrosion. The pH buffering effect of fuel dissolution goes away if fuel dissolution does not occur because of, for example, high clad coverage. A coupled calculation of radiolysis and steel and SNF degradation is needed to establish how much pH buffering will occur. In the absence of pH buffering in the alluvial case, actinides become more soluble upon criticality.

3.4.2 Radiolysis

Morco et al. (2017) showed for Canadian SNF that the γ dose rate is dominated by the decay of the fission products in the fuel, decreasing nearly exponentially with time from 500 to 1,000,000 years. Humid air radiolysis is estimated to produce a maximum internal-to-the-package nitric acid concentration of 0.1 mol/l. Preliminary PHREEQC (Parkhurst and Appelo 1999) calculations show that reaction of this quantity of nitric acid (pH = 1) with a steel corrosion product assemblage of trevorite and hematite dissolves ~0.06 mol/l (~14 g/l) of trevorite and buffers in-package pH upwards to 5.7 (25°C). Note though that this amount of trevorite needed for in-package pH buffering is ~5 times greater than the maximum amount of trevorite calculated to form in the 9,000 years before criticality is assumed to occur. Trevorite accumulates faster at the higher temperatures of steady-state criticality in the shale case. But again, a more involved, coupled calculation of the interplay between radiolysis, corrosion, and SNF degradation with PFLOTRAN would better constrain the extent of pH buffering by trevorite.

Radiolytic production of hydrogen peroxide occurs in both the alluvial and shale cases but has little impact on in-package chemistry other than to possibly keep actinides in their higher, least soluble, valence states. Radiolytic production of hydrogen peroxide also favors more oxidized corrosion products.

3.4.3 CSNF Degradation

The increased temperature caused by criticality should have relatively less effect on fuel degradation because accelerated steel corrosion raises ambient H_2 levels, which inhibit oxidative degradation of fuel. Spent fuel then degrades by slower, non-oxidative chemical processes (Jerden et al. 2015). Again, effluent

levels of dose-important fission product radionuclides that are not solubility-limited, such as $^{137,135}\text{Cs}$ and ^{129}I , depend on the temperature effect on SNF degradation rates and, in the case of cationic radionuclides, the uptake by bentonite clay backfill. Coupling of the Fuel Matrix Dissolution Model (FMDM) with PFLOTRAN would better constrain the interplay between temperature, hydrogen production, and SNF degradation.

3.5 Solubility

The increased temperatures associated with a steady-state criticality event could result in lower calculated doses from actinides for two reasons: (1) actinide solubilities tend to decrease with temperature (Bernot 2007, Appendix VI), and (2) higher temperatures favor formation of more crystalline and anhydrous radionuclide-bearing solids, which have lower solubilities. Effluent levels of dose-important fission product radionuclides that are not solubility-limited, such as $^{137,135}\text{Cs}$ and ^{129}I , depend on the temperature effect on SNF degradation rates and, in the case of cationic radionuclides, the uptake by bentonite clay backfill. Changes in radionuclide solubilities with increased temperature are not included in the PFLOTRAN simulations presented in Section 2.8 and Section 3.8, but will be captured in future PFLOTRAN simulations.

The chemistry of the lanthanide fission product poisons is similar, which means that the retrograde solubility seen for Nd (Wood et al. 2002) should prevail for the others. Table 8.1-1 of CRWMS M&O (2001) shows minimal calculated release of Gd from SNF. At 50°C, 93.5% of the Gd is calculated to remain in CSNF; 87.7% is calculated to be retained at 90°C. Similar retention is expected for the other lanthanide fission product poisons.

Stainless steel corrosion products and SNF reactions with seepage may keep in-package pH levels near neutral during criticality (this observation is less certain in the alluvial case). High pH excursions are limited by the growth of Fe(II) silicates and hydroxides, which both decrease pH. A more involved calculation that couples PFLOTRAN and FMDM at 100°C would set more precise limits on pH levels inside breached DPCs with a steady-state criticality as well as effluent concentrations of radionuclides for the alluvial case.

3.6 EBS Degradation

As noted in Section 2.6, for the purposes of this work, the performance of several components of the EBS has been fixed by assumption. The waste package is assumed to fail (Section 1.4.1), and the cladding remains intact enough to remain in a critical configuration but permits radionuclide transport through small holes for the duration of the steady-state criticality event (Section 1.4.2). For the saturated repository, when the temperature of the backfill is modeled to exceed 100°C, the backfill is not as effective as a barrier in terms of radionuclide retardation via sorption, with the K_d values in the postclosure criticality case being half of their values in the case without criticality.

3.7 Time of Termination

An analysis was conducted to evaluate the DPC characteristics and geologic disposal processes that could render the potential for criticality in a DPC permanently insignificant, thereby eliminating the need for further consideration or analysis. Section 2.7 introduces the general approach used for the analysis while the subsections below provide the analysis results. In particular, the potential for irreversible geometry

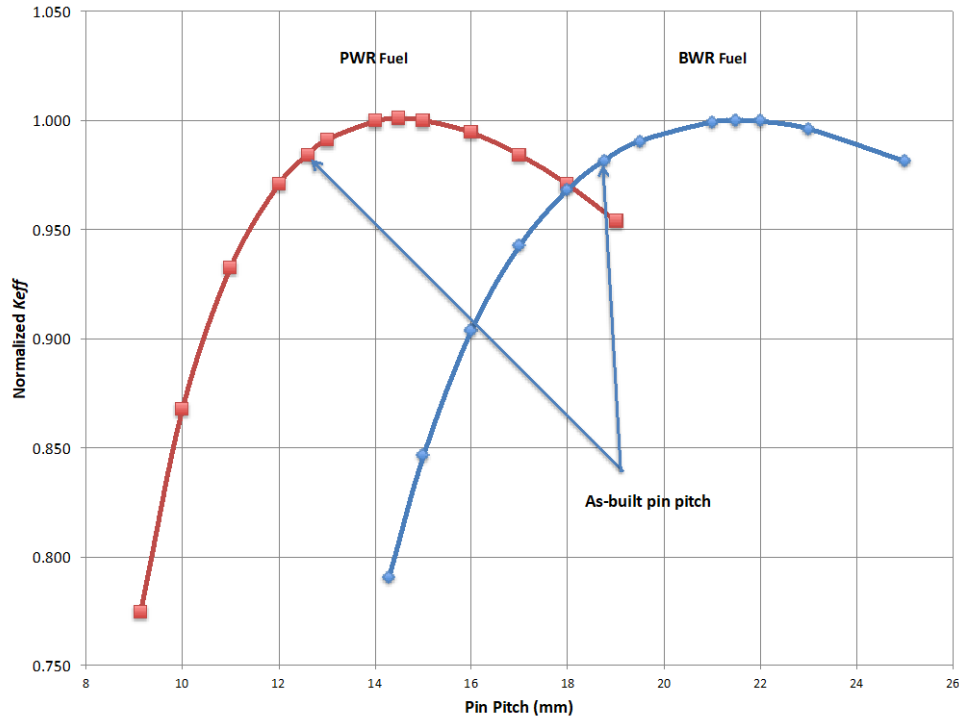
changes, burnup, decay, disruptive events, criticality thermal cycle, and compositional changes due to corrosion/dissolution to cause permanent change in reactivity magnitudes is examined to determine whether there are DPCs for which criticality can be permanently terminated and, if so, to identify the associated processes and timing of termination.

As was pointed out in Section 2.7, it is important to note that the analyses and specific values provided in Section 3.7 are not intended to be absolute or applicable to all DPCs with any level of precision. They are presented to provide perspective and to guide follow-on analyses using specialized codes with detailed criticality state models based on potential material compositions, while accounting for decay, depletion, and dissolution.

3.7.1 Reactivity Perturbations due to Fuel Geometry Changes

Given that the most reactive credible geometry for commercial SNF is tightly packed assemblies (i.e., no baskets or neutron absorbers), the reactivity perturbations due to fuel geometry changes are based on pin pitch changes only (i.e., separation between fuel pins). Commercial SNF is designed to be under moderated; therefore, a slight pin pitch expansion would increase reactivity. However, uniform pin pitch expansion in the fuel assemblies is not considered credible for disposal configurations. Figure 3-37 presents normalized k_{eff} as a function of pin pitch for individual, reflected, fully moderated, PWR and BWR assemblies. These figures are adapted from BSC (2005b, Tables 6.3-4 and 6.3-6). Pin pitch reduction has a significant impact on reducing reactivity. For the modeled PWR fresh fuel, reducing the pin pitch by 1 mm from as-manufactured conditions reduces k_{eff} by 0.023. The reduction in reactivity becomes more significant for additional pin pitch reduction. A uniform pin pitch reduction of ~3 mm would likely be sufficient to render the higher reactivity DPCs (with excess DABC reactivity of 0.1) permanently subcritical, since reversal of pin pitch reduction is not plausible during disposal.

SNF assembly geometry changes can be induced by either corrosion or disruptive events. Corrosion is time-based once initiated, whereas disruptive events are less predictable. Fuel grid spacers vary in design, but generally use zircaloy as the primary material of construction of grid straps and dimples and either zircaloy or inconel for the springs. A typical thickness of grid spacer straps and dimples is ~0.5 mm (Jiang et al. 2016). Cladding thickness for a typical PWR fuel is 0.57 mm and for a typical BWR fuel is 0.74 mm (BSC 2005b, Tables 5.1-2 and 5.1-4).



NOTE: Normalized k_{eff} is determined by dividing the k_{eff} for each pin pitch by the highest k_{eff} associated with the optimum pin pitch.
 BWR = boiling water reactor.
 PWR = pressurized water reactor.

Figure 3-37. Normalized k_{eff} as a Function of Pin Pitch

If the in-package chemistry is conducive to zircaloy corrosion, it is plausible that the grid spacers would degrade at a slower rate than fuel cladding primarily because the grid spacers experience less degradation during irradiation. Primary contributors to cladding degradation are oxidation, creep, and hydride formation/reorientation, several of which are a direct function of hoop stress. Commercial SNF rods are subject to relatively significant hoop stresses, whereas there are no such stresses on grid spacers. Cladding could also fail from unzipping due to fuel oxidation. These mechanisms tend to impact select fuel rods or even segments of fuel rods (e.g., those with hairline cracks or high peak burnup). Figure 3-38 shows typical fuel unzipping, which does not seem to result in significant fuel releases. The impact of failure of a few fuel rods on system reactivity is difficult to predict because, depending on the location and what the removed fuel is replaced with, localized removal could result in either a positive or a negative reactivity change. Replacing a few fuel rods with water generally increases reactivity because it increases moderation for the normally under-moderated assemblies (Figure 3-37), whereas replacing a few fuel rods with corrosion products could slightly decrease reactivity (or result in no change).

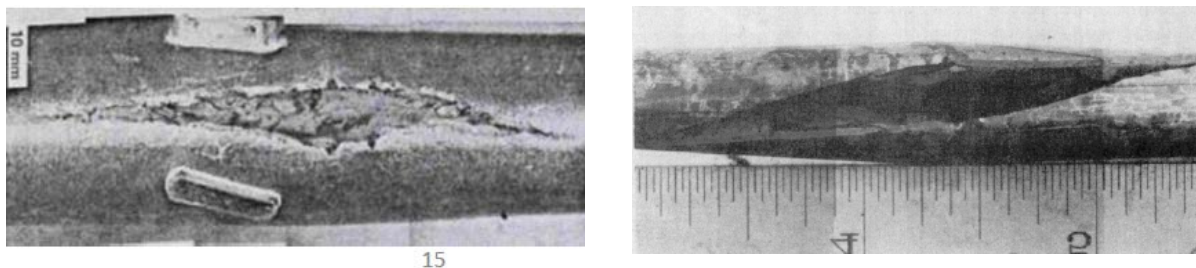


Figure 3-38. Example Cladding Unzipping

The corrosion rate of zircaloy is highly dependent on the composition of the specific zircaloy alloy, its condition (e.g., oxide layer, hydrides), and in-package chemistry. In-package chemistry varies widely based on repository geology (e.g., unsaturated tuff, saturated shale, salt), in-package components (DPC internal designs vary significantly), radiolysis, and evaporation/concentration (due to decay heat or criticality events). Therefore, predicting a specific timeframe for when the grid spacers would degrade after water intrusion is highly uncertain without a detailed PA. No credit was taken for the cladding for the unsaturated tuff Yucca Mountain Repository (DOE 2008b, Section 2.3.7.6); the licensing PA assumed that cladding has failed and the fuel is exposed upon waste package failure. This assumption was conservative from a release standpoint; however, for the purposes of this study, the assumption is not necessarily conservative. Therefore, representative and defensible corrosion modeling of cladding and grid spacers based on the anticipated range of environments and chemical conditions is warranted since the conservative bases for radionuclide release run counter to those required for postclosure criticality analysis. Without significant corrosion modeling of the cladding and grid spacers, a licensing basis of geometry-based permanent termination of criticality would likely not be defensible within the first few hundred thousand years after water intrusion.

3.7.2 Reactivity Perturbations due to Burnup

Burnup changes the composition of the fuel from a reactivity perspective in two ways:

- **Depletion of Fissile Material**—The only fissile isotope in fresh fuel is ^{235}U , which starts depleting rapidly with burnup. For SNF with relatively high burnup, there are several fissile isotopes that contribute to fission and power generation including ^{239}Pu , ^{241}Pu and ^{243}Am . Figure 3-39 provides the concentration of the various fissile isotopes as a function of burnup for PWR SNF with an initial enrichment of 4.5 wt.% ^{235}U . Figure 3-39 illustrates that with increased burnup, the primary fissile isotope becomes ^{239}Pu and essentially reaches an equilibrium concentration at ~ 30 GWd/MTU (i.e., the generation rate is essentially equivalent to the depletion rate).

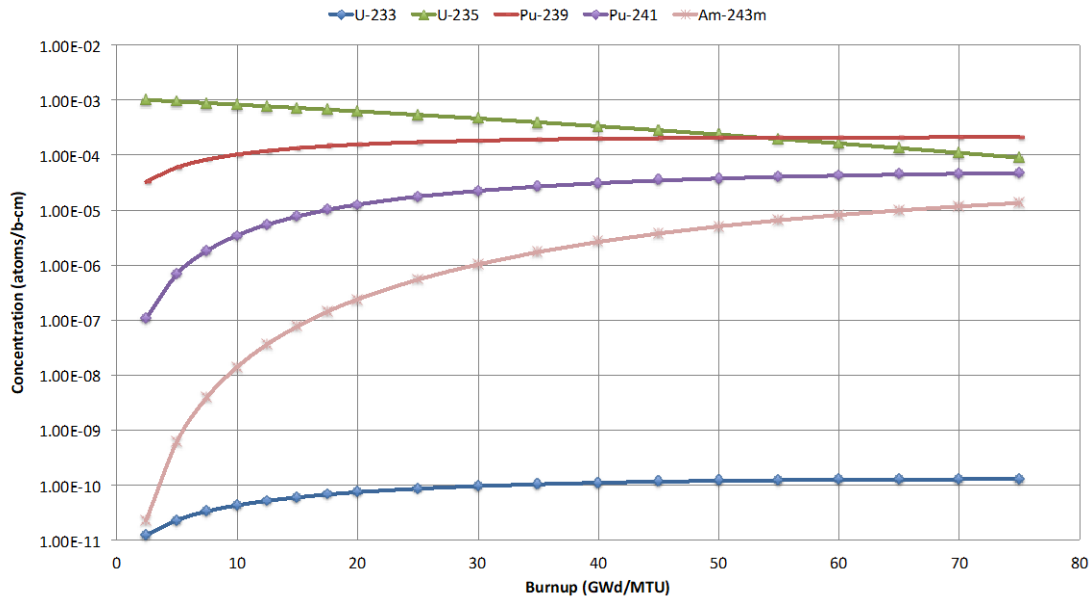


Figure 3-39. Concentration of Fissile Isotopes as a Function of PWR SNF Burnup

- Generation of Neutron Absorbers**—Fuel depletion generates neutron absorbers through either fission (i.e., fission products) or parasitic neutron absorptions (i.e., higher actinides). The primary neutron absorbers with importance to long-term disposal criticality are ^{155}Gd , ^{143}Nd , ^{149}Sm , ^{151}Eu , and ^{103}Rh (Section 3.7.4). Figure 3-40 provides the concentrations of these isotopes or their parent nuclides (in the case of ^{151}Eu , the daughter of ^{151}Sm) as a function of burnup for PWR SNF with an initial enrichment of 4.5 wt.% ^{235}U . Figure 3-40 illustrates that fission products concentration growth rates drop with burnup because of their relatively high absorption cross sections. Nonetheless, with the exception of ^{149}Sm , their generation rate remains higher than their depletion rate.

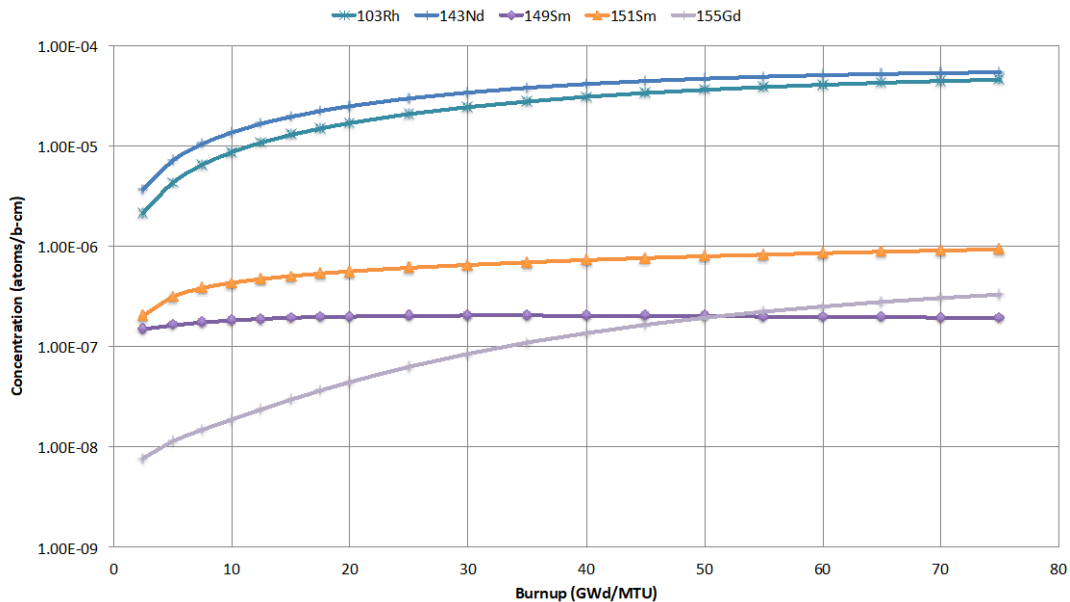
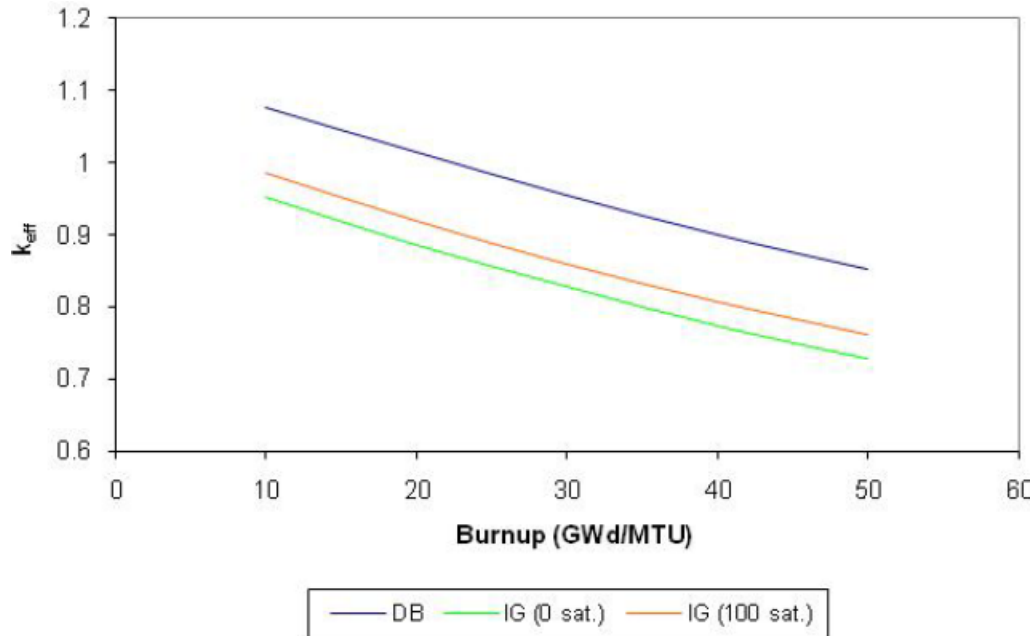


Figure 3-40. Concentration of Neutron Absorber Isotopes as a Function of PWR SNF Burnup

Because burnup-induced composition changes are strongly correlated to the level of burnup with different generation/depletion rates for the various isotopes, their impact on reactivity is treated collectively in this subsection. Figure 3-41 provides k_{eff} as a function of burnup for both intact and fully degraded configurations (SNL 2007). The intact configuration represents closely packed SNF assemblies with an initial enrichment of 4.0 wt.%, separated with 6 mm of borated stainless steel (i.e., Yucca Mountain Repository TAD design basis [DB] configuration). For the degraded igneous (IG) configurations (denoted IG in Figure 3-41), the fuel is represented as fully hydrated schoepite with 15% porosity. Figure 3-41 demonstrates that k_{eff} essentially decreases linearly with burnup, with an average rate of change of approximately $-0.005 \Delta k_{eff}$ per GWd/MTU for PWR SNF. For example, a DPC with excess reactivity of 0.05 for the DABC would require an additional burnup of ~ 9 GWd/MTU to become permanently subcritical. Note that this observation is based on uniform burnup of SNF within the canister. For actual DPCs loaded with SNF at a range of burnup values, the reactivity-to-burnup ratio would likely be different.

A quasi-steady-state criticality during disposal would result in some level of additional burnup. For example, a steady-state criticality at a power level of 400 W (potentially representative of a criticality in an unsaturated repository at atmospheric pressure) lasting for 10,000 years would result in an additional ~ 0.1 GWd/MTU average burnup in a typical DPC. A steady-state criticality at a power level of 4 kW (potentially representative of a criticality in a saturated repository at elevated pressure) lasting for 10,000 years would result in an additional ~ 1 GWd/MTU average burnup in a typical DPC. This incremental burnup would result in insignificant changes to the composition and DPC reactivity.



Burnup (GWd/ MTU)	PWR					
	DB		IG (0% sat.)		IG (100% sat.)	
	k_{eff}	σ	k_{eff}	σ	k_{eff}	σ
10	1.07748	0.00051	0.95310	0.00052	0.98538	0.00052
20	1.01336	0.00051	0.88606	0.00056	0.91823	0.00054
30	0.95411	0.00050	0.82742	0.00050	0.85826	0.00054
40	0.89881	0.00049	0.77373	0.00049	0.80624	0.00055
50	0.85200	0.00049	0.72866	0.00045	0.76040	0.00047

NOTE: DB = design basis.
 IG = igneous.
 PWR = pressurized water reactor.
 sat. = saturation.

Figure 3-41. k_{eff} as a Function of PWR Burnup for the TAD DB Configuration and Degraded IG Configuration with Varying Levels of Saturation

3.7.3 Reactivity Changes due to Decay

The reactivity of commercial SNF changes as a function of decay time because several of the fissionable isotopes and absorbers considered in the burnup credit analysis are radioactive with a range of half-lives from tens of years to millions of years. The relative reactivity change as a function of decay highly depends on the SNF composition used in the model to determine the criticality state. Figure 3-42 provides k_{eff} as a function of time for a generic 32-PWR canister with fuel enriched to 4 wt.% ^{235}U and a burnup of 40 GWd/MTU (Wagner and Parks 2003, Figure 3). Because the DPC disposal criticality analysis is based on full burnup credit, the lowest line in Figure 3-42 is more representative of the reactivity changes as a function of time.

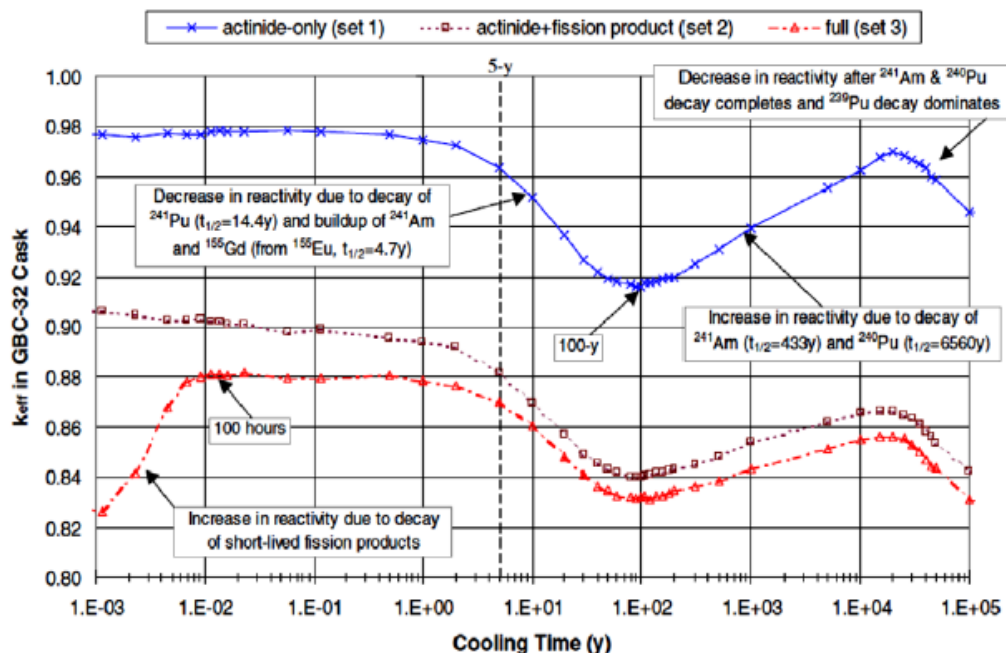


Figure 3-42. k_{eff} as a Function of Decay Time

Figure 3-42 is limited to 100,000 years of decay and demonstrates that this decay duration accounts for approximately $-0.03 \Delta k_{eff}$ from the reactivity peak at $\sim 20,000$ years. Therefore, barring any other changes, a DPC DABC with excess reactivity less 0.03 would no longer have the potential for criticality at 100,000 years, as long as there is no preferential separation between the various fuel constituents. To determine the impact of longer decay times and the reactivity worth of the various isotopes considered in the modeling of the criticality state, an equivalency analysis was performed for a representative burnup enrichment pair on the Yucca Mountain Repository TAD PWR loading curve (4.5 wt.% enrichment and 40 GWd/MTU burnup) (BSC 2003). The equivalency analysis represents the 29 principal isotopes considered in the burnup credit analysis by a single fissile isotope (^{235}U) using fissile material equivalency (Lakes and Ashley 2017, Table B-2) and a single absorber isotope (^{150}Sm) using thermal neutron cross section ratios. This approximation is considered reasonable for this scoping evaluation since only thermal criticality events are possible for the LEU commercial SNF. Table 3-8 provides a summary of the equivalency analysis. The equivalent ^{235}U initial enrichment drops by 19% due to decay from 5 years to 10,000,000 years, whereas, the equivalent absorption drops by 25% for the same decay duration.

Table 3-8. Fissile and Absorber Material Equivalency at 5 and 10,000,000 Years for PWR SNF (4.5 Wt.% ²³⁵U and 40 GWd/MTU)

Equivalent Isotope	5 years (initial)		~ 10,000,000 years (final)		%Change (final – initial / initial)
	Equivalent Concentration (atoms/b-cm)	Equivalent Enrichment at 5 Years (wt.%)	Equivalent Concentration (atoms/b-cm)	Equivalent Enrichment (wt.%)	
²³⁵ U	7.64E-4	3.33 wt.%	6.19E-4	2.7 wt.%	-19%
¹⁵⁰ Sm	2.42E-3	N/A	1.82E-3	N/A	-25%

Figure 3-43 (OECD/NEA 2012, Figure 1) shows that isotopic composition changes important to criticality occur within the first 100,000 years, after which the only remaining change is growth of ²³³U. Assuming full buildup of ²³³U (i.e., complete decay of ²³⁷Np with a half-life of 2,100,000 years), ²³³U accounts for an equivalent ~0.3 wt.% ²³⁵U (12.5% of the total ²³⁵U) based on an equivalency evaluation. As shown in Table 3-8, the relative reduction in absorption after long-term decay is ~25%, which is slightly higher than the 19% relative reduction in fission. Therefore, the reactivity of SNF is likely rise slowly but not significantly over several million years. Based on the burnup equivalency described in Section 3.7.2, this reactivity increase would be negated by ~5 GWd/MTU burnup during a postclosure criticality event.

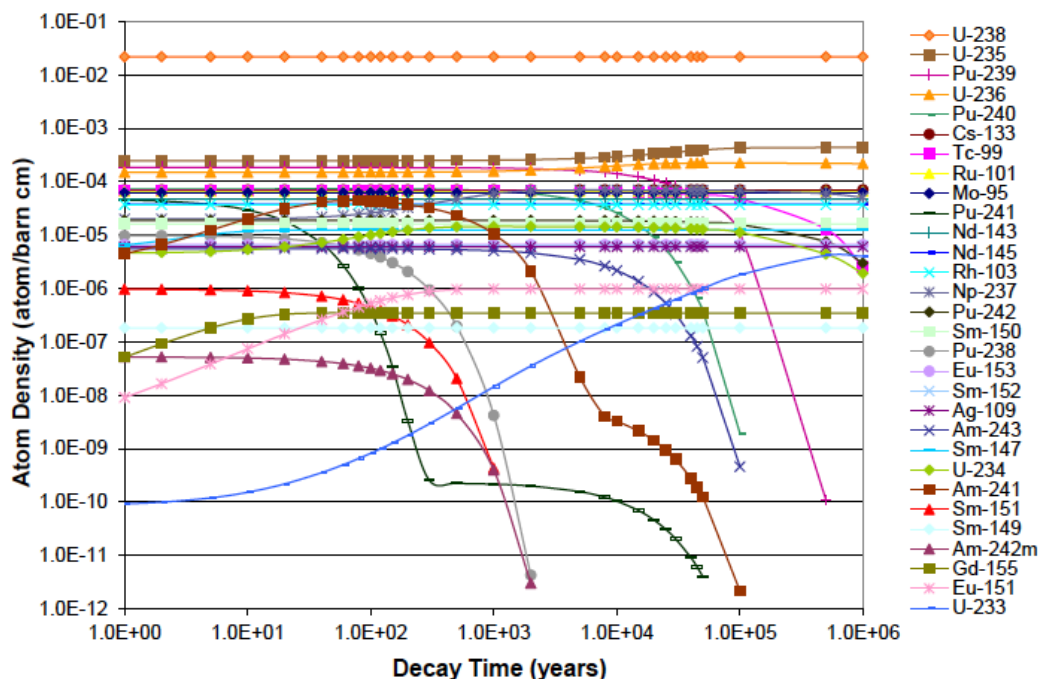


Figure 3-43. Isotopic Concentrations of Radionuclides Important to Criticality

3.7.4 Reactivity Perturbations due to Compositional Changes from Corrosion/Dissolution

The relative reactivity worth (i.e., contribution to fission and/or absorption) of the various isotopes of relevance to criticality state evaluation—based on their concentration, fissile equivalency and thermal neutron absorption cross sections at 5 and 10,000,000 years—is provided in Table 3-9.

Dissolution and removal of uranium does not change the relative enrichment of the fuel, only the total mass. Because of the large mass of uranium in a DPC, uniform removal of uranium is likely to have a small impact on system reactivity until a significant amount of uranium has been removed. The impact of localized removal of uranium (e.g., from select failed rods) on system reactivity is difficult to predict because, as discussed in Section 3.7.2, localized removal of uranium could increase or decrease reactivity. Preferential removal of neutron poisons, on the other hand, could increase system reactivity, potentially significantly. Therefore, corrosion, dissolution, and release evaluations for the following isotopes are more meaningful for permanent criticality termination considerations:

- Removal of plutonium from the fuel could significantly reduce reactivity if it were to occur prior to decay of ^{239}Pu , which has a half-life of 2.41E4 years. As shown in Table 2-8, ^{239}Pu makes up ~40% of the fissile material at 5 years. Therefore, if the package chemistry does not allow for preferential plutonium dissolution from the fuel, or a significant amount could not be removed from the fuel within 100,000 years, then plutonium dissolution would not be a factor in permanent criticality termination.
- Removal of absorber isotopes negatively impacts the permanent criticality termination argument. Therefore, in order to ensure that criticality can be considered permanently terminated based on the demonstration that the DABC is subcritical because of decay, burnup, or geometry change, a defensible argument must be developed to demonstrate that the absorber isotopes listed in Table 3-9 cannot be preferentially separated from the fuel based on their relative importance. The primary fission product absorbers for long-term criticality state determination are ^{155}Gd , ^{143}Nd , ^{149}Sm , ^{151}Eu , and ^{103}Rh .

Table 3-9. Relative Worth of SNF Isotopes

Isotope	Absorption		Fission	
	Relative Worth at 5 Years	Relative Worth at ~1,000,000 Years	Relative Worth at 5 Years	Relative Worth at ~10,000,000 Years
¹⁶ O	0.00%	0.00%		
⁹⁵ Mo	0.31%	0.41%		
⁹⁹ Tc	0.52%	0.00%		
⁹⁹ Ru	0.00%	0.22%		
¹⁰¹ Ru	0.11%	0.15%		
¹⁰³ Rh	1.83%	2.43%		
¹⁰⁹ Ag	0.19%	0.25%		
¹⁴³ Nd	5.55%	7.38%		
¹⁴⁵ Nd	0.66%	0.88%		
¹⁴⁷ Sm	0.22%	0.30%		
¹⁴⁹ Sm	3.36%	4.47%		
¹⁵⁰ Sm	0.56%	0.74%		
¹⁵¹ Sm	4.56%	0.00%		
¹⁵² Sm	0.46%	0.61%		
¹⁵¹ Eu	0.11%	3.83%		
¹⁵³ Eu	0.66%	0.88%		
¹⁵⁵ Gd	3.42%	9.08%		
²³³ U	0.00%	1.24%	0.00%	12.52%
²³⁴ U	0.23%	0.00%		
²³⁵ U	13.78%	29.29%	44.24%	87.29%
²³⁶ U	0.29%	0.55%		
²³⁸ U	24.43%	32.49%		
²³⁷ Np	1.17%	4.81%	0.05%	0.19%
²³⁸ Pu	1.29%	0.00%	0.13%	0.00%
²³⁹ Pu	22.22%	0.00%	40.71%	0.00%
²⁴⁰ Pu	6.78%	0.00%	0.26%	0.00%
²⁴¹ Pu	4.66%	0.00%	14.29%	0.00%
²⁴² Pu	0.08%	0.00%	0.02%	0.00%
²⁴¹ Am	2.45%	0.00%	0.04%	0.00%
^{242m} Am	0.01%	0.00%	0.26%	0.00%
²⁴³ Am	0.08%	0.00%	0.01%	0.00%

3.7.5 Summary and Conclusions

The following can be concluded based on the evaluation of several processes that could cause permanent criticality termination in disposed DPCs:

- Reflection, leakage, interaction, and temperature have an insignificant impact on criticality potential and on permanent criticality termination in disposed DPCs. However, they could affect the oscillatory behavior of potential criticality events.
- There is no criticality potential without moderation. However, evaluating the ability of the waste package to contain sufficient moderator over long time scales is beyond the scope of this study.
- The most reactive credible configuration for disposed DPCs is the DABC, which comprises closely packed SNF assemblies without any neutron absorbers or baskets.
- The additional burnup due to a steady-state disposal criticality event could reduce DPC k_{eff} by 0.005 per GWd/MTU. For a DPC with excess reactivity of ~ 0.1 , an additional burnup of 20 GWd/MTU would be required to cause permanent criticality termination. Such a DPC could sustain a steady-state criticality at a power level of 4 kW (potentially representative of a criticality in a saturated repository at elevated pressure) for 200,000 years, assuming no changes to fuel configuration.
- Decay provides limited changes in DPC reactivity after $\sim 100,000$ years. Buildup of ^{233}U from decay of ^{237}Np results in a relatively small reactivity increase over a few million years.
- Changes in geometry due to grid spacer corrosion/collapse resulting in uniform pin pitch reduction by ~ 3 mm essentially results in permanent termination of criticality for most DPCs.
 - The impact of cladding corrosion or failure on reactivity is uncertain and, if localized, could result in slight increase in reactivity. Representative and defensible corrosion modeling of grid spacers and cladding based on the anticipated range of environments and chemical conditions is warranted since the conservative bases for radionuclide release (for dose evaluations) run counter to those required for postclosure criticality analysis.
 - If a waste package were to fill with enough water such that a critical configuration was obtained, the heat generated would eventually evaporate the water, providing negative feedback and ending the criticality event. The waste package would cool, water would re-enter the waste package, and the criticality event could start again once enough water was present, only to evaporate once the criticality event began and enough heat was generated.
- Removal of absorber isotopes negatively impacts the permanent criticality termination argument. To ensure that criticality can be considered permanently terminated, a defensible argument must be developed to demonstrate that key absorber isotopes (^{155}Gd , ^{143}Nd , ^{149}Sm , ^{151}Eu , and ^{103}Rh) cannot be preferentially separated from the fuel.

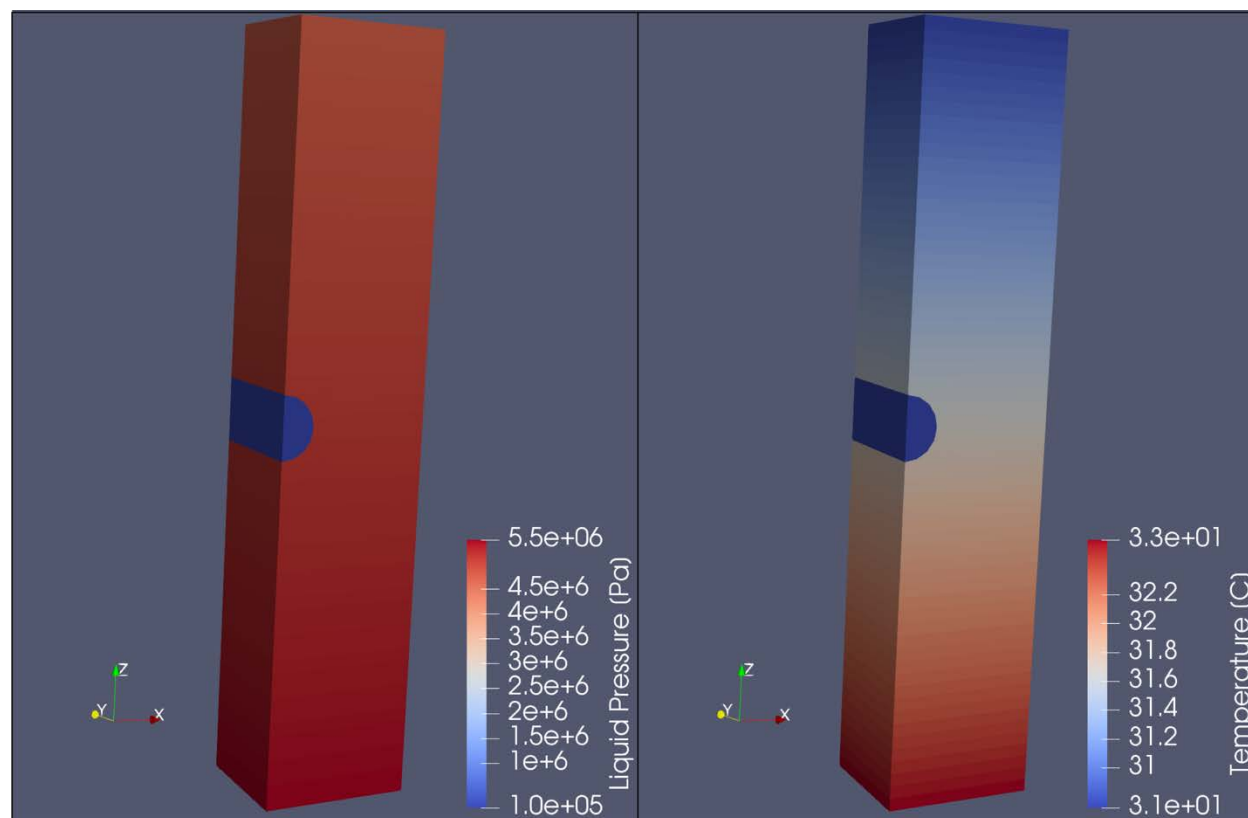
3.8 Repository Simulations

Section 3.8 presents the results of the base-case and comparison simulations, which were conducted using PFLOTRAN as described more fully in Section 2.8. The base case includes saturated shale as the host rock, decay heat effects, and the radionuclide inventory of a 37-PWR DPC that stays subcritical for the duration of the simulation. The comparison simulations include all of the above, but also include the effects of a steady-state criticality. The results of the base-case and comparison simulations are provided in Section 3.8.1 and Section 3.8.2 respectively.

3.8.1 Base-Case Simulations (without Criticality)

The simulation results presented here correspond to the saturated shale host rock reference case model for near-field heat and mass transport near a single waste package without a steady-state criticality event for the duration of the simulation. The simulations include multiphase flow and heat transport coupled to radionuclide decay/ingrowth and aqueous transport. Multiphase flow and heat transport are discussed in this subsection, while radionuclide transport is discussed in Section 3.8.2.

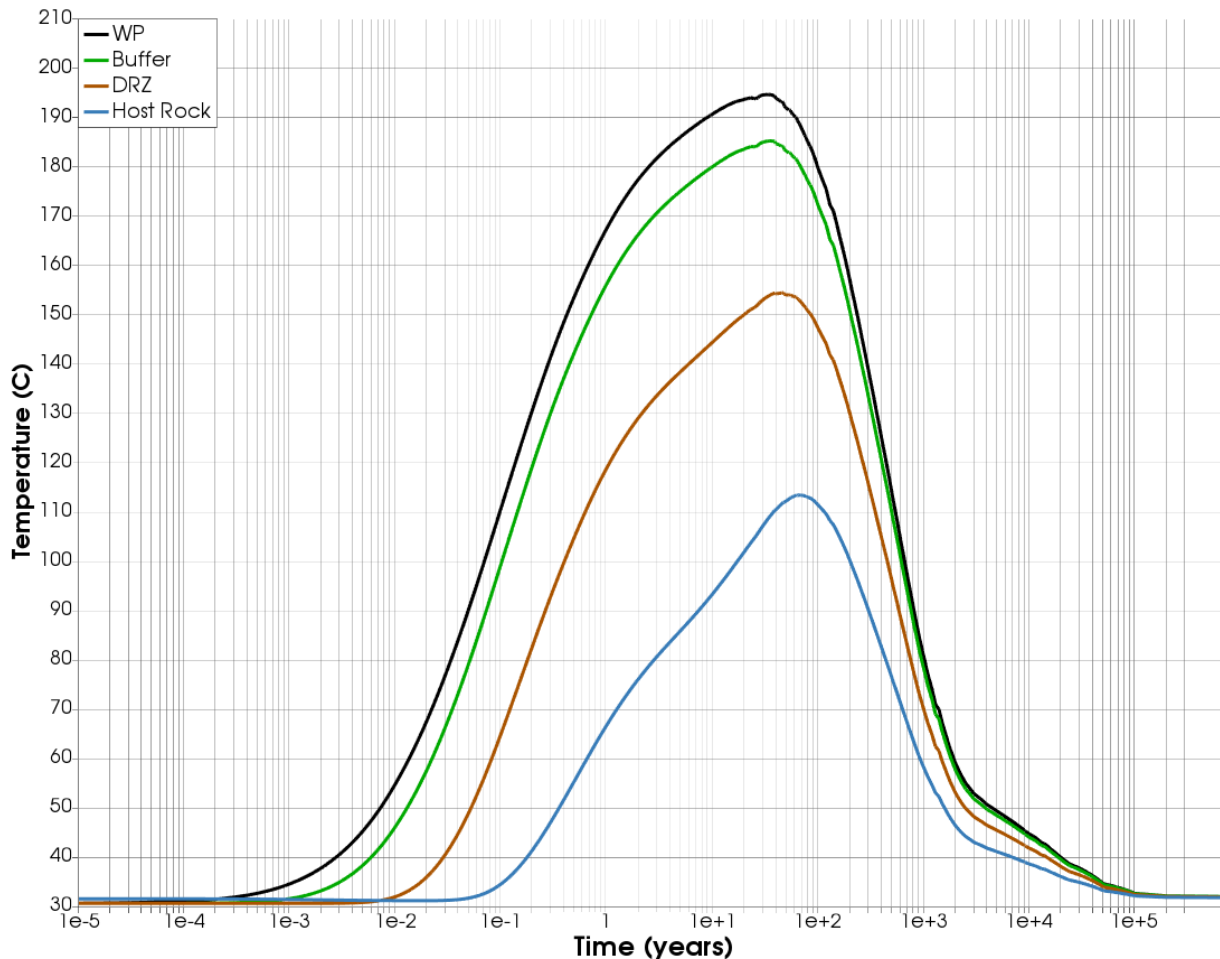
The shale host rock is modeled as a fully water-saturated medium assuming a vertical geothermal gradient of 25°C/km and a hydrostatic pressure gradient. At the land surface, 450 m above the top of the model domain, surface pressure is set at 101 kPa and temperature is set at 18°C. Initial liquid pressure in the host rock inside of the model domain therefore ranges from roughly 4 MPa at the top to 5.5 MPa at the bottom (Figure 3-44). Similarly, initial temperature in the host rock ranges from 31°C to 33°C. Within the drift and the DRZ, initial conditions are set to atmospheric pressure and a temperature of 31°C. Initial water saturation in the drift is set artificially high, at 90% for simulations involving radionuclide decay/ingrowth and aqueous transport. This modeling choice reflects current limitations of PFLOTRAN with respect to tracking radionuclide transport in gas-saturated cells. The simulation time frame is 1,000,000 years.



NOTE: Outside of the repository liquid pressure is hydrostatic, and temperature follows a geothermal gradient. Inside the repository conditions are set at atmospheric pressure and temperature.

Figure 3-44. Initial Pressure and Temperature Conditions for Shale Case at the Time of Repository Closure

Temperature profiles for the four observation cells depicted in Figure 2-10 are shown in Figure 3-45. Cell locations represent (1) the hottest cell in the domain at the center of the waste package, (2) a cell in the buffer immediately adjacent to the waste package (buffer), (3) a cell in the DRZ immediately adjacent to the buffer (DRZ), and (4) a cell in the host rock bordering the DRZ (host rock). The waste package modeled here is 1.6 m in diameter and 5 m in length when considering reflection boundaries, for a total canister volume of approximately 10 m³. As expected, the center of the waste package reaches the highest temperature of anywhere in the model domain, peaking at around 195°C. The hottest temperature the host rock experiences is significantly lower, at approximately 113°C. Peak temperature at the waste package occurs at around 40 years, and host rock temperature peaks at around 70 years.

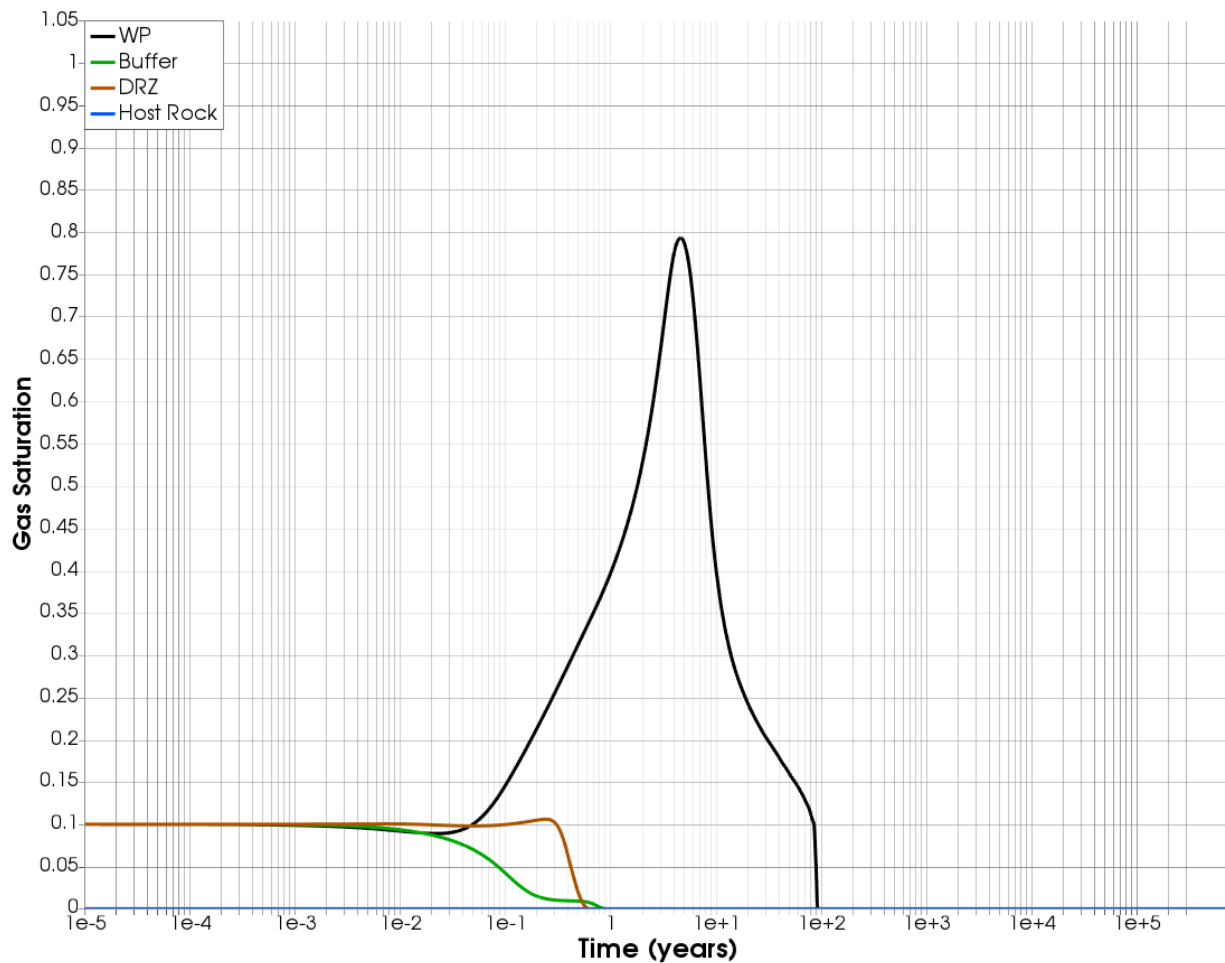


NOTE: DRZ = disturbed rock zone.
 WP = waste package.

Figure 3-45. Temperature versus Time at Observation Points Listed in Figure 2-10

These simulations consider a drift that is initially partially water saturated. To prevent complete dry-out of any grid cells, an initial water saturation of 90% is used. Since the waste package is represented as a porous medium, the aqueous phase is initially connected between waste package and repository. Therefore, since the waste package is the source of heat, water is driven off most significantly in the waste package grid cells, leading to increased gas saturations (depicted in Figure 3-46) while the decay heat load is high. More realistically, the waste package would be initialized as gas-saturated and disconnected from the drift until waste package breach, but imposing such a discontinuity can be numerically difficult because it introduces stiffness into the problem. Efforts are underway to explore how to appropriately consider the waste package material given the importance of liquid saturation for moderating criticality.

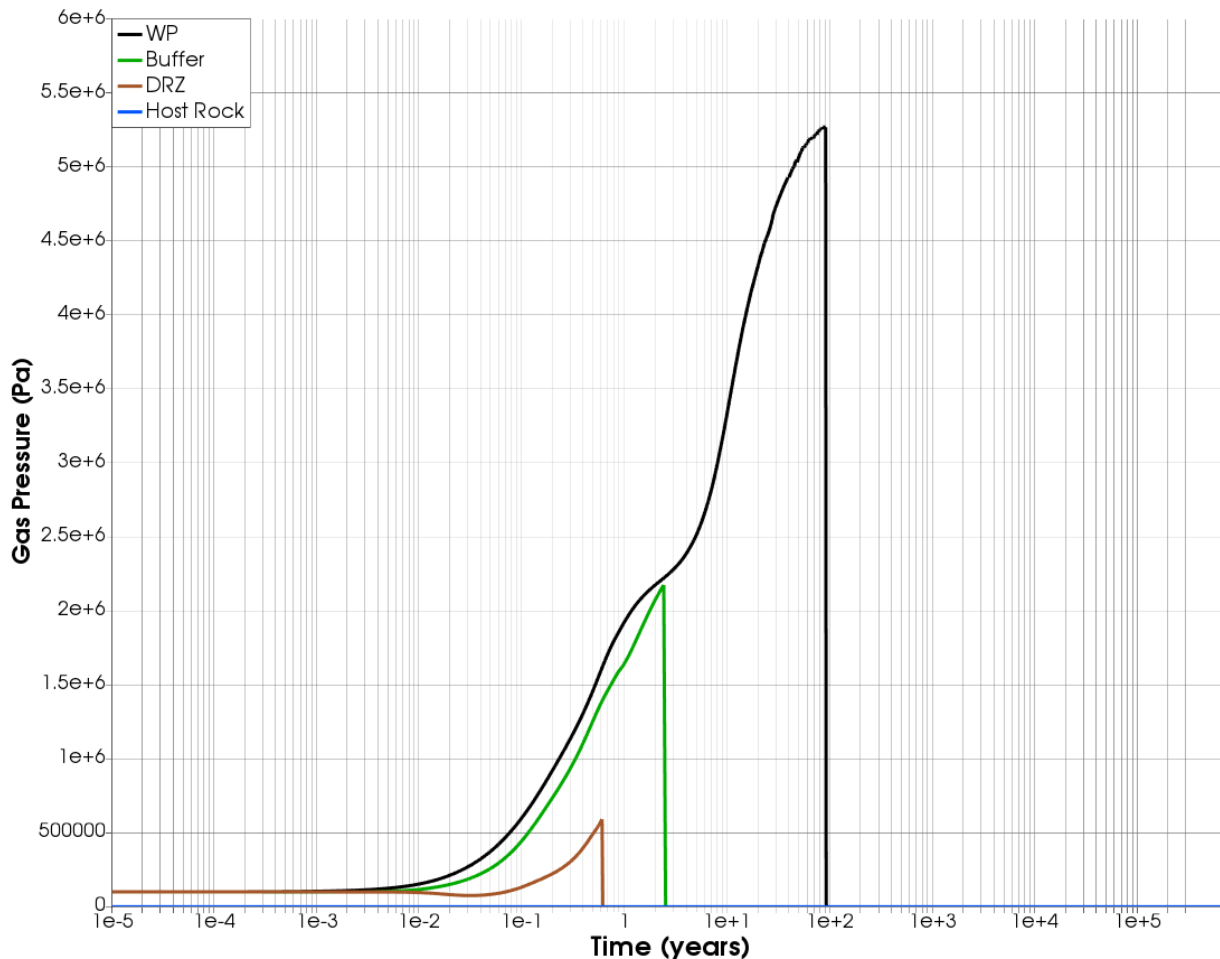
Outside of the waste package, the buffer exhibits strong capillary suction, which decreases its gas saturation even while it is being heated. Water drained from DRZ to the buffer initially outpaces imbibition into the DRZ from the host rock, leading to a slight increase in gas saturation in the DRZ before it ultimately becomes fully saturated with water. The host rock is water saturated for the duration of the simulation.



NOTE: DRZ = disturbed rock zone.
WP = waste package.

Figure 3-46. Gas Saturation versus Time at Observation Points Specified in Figure 2-10

Gas pressures in the drift increase throughout the duration of the simulation, from atmospheric pressure to a maximum of over 2 MPa in the buffer (Figure 3-47); this outcome is due mostly to thermal pressurization. Gas pressures are reported as zero when the gas phase disappears, a situation that occurs in the DRZ and buffer at around 0.6 years and 2.2 years, respectively. The entire model domain is fully water saturated by 100 years.



NOTE: DRZ = disturbed rock zone.
 WP = waste package.

Figure 3-47. Gas Pressure versus Time at Observation Points Specified in Figure 2-10

Concentrations of selected radionuclides (Section 3.2) in the shale adjacent to the drift wall are shown in Figure 3-48. As expected, concentrations of ^{242m}Am , ^{241}Am , ^{238}Pu , ^{137}Cs , and ^{90}Sr are below 1×10^{-20} M, which is the value used in PFLOTRAN to represent a concentration of zero, and thus are not shown in the figure.

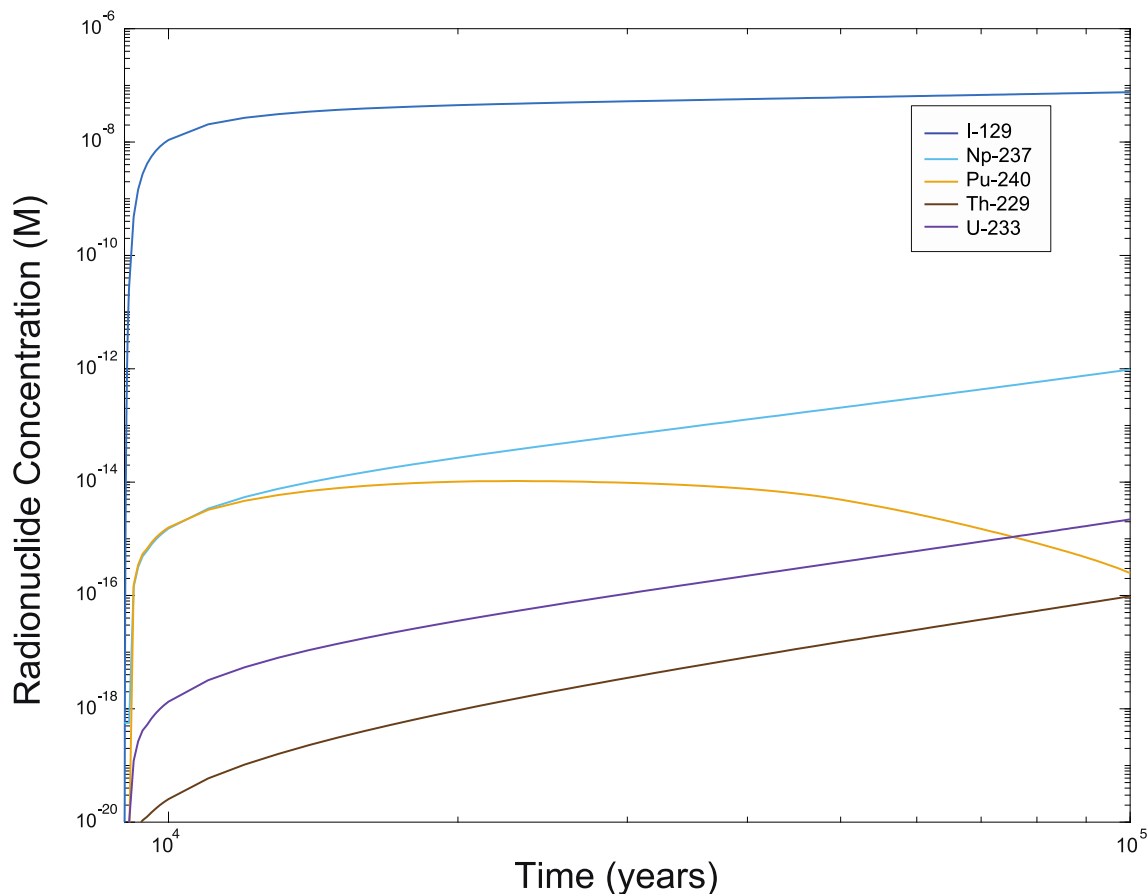


Figure 3-48. Concentrations of Selected Radionuclides in the Shale adjacent to the Drift Wall with no Criticality Event and a Waste Package Breach at 9,000 Years

3.8.2 Comparison Simulations (with Criticality)

As described more fully in Section 2.8.2, the simulations that include a steady-state criticality event model the heat of criticality as a constant heat source (in addition to decay heat) over a specified period of time. In these simulations, the heat source of criticality is determined from thermal analysis (Section 2.3.2.1) as the average heat output at which liquid water could remain present at a given set of pressure and temperature conditions within a waste package. Criticality parameters are summarized in Table 3-10. Radionuclide inventories are read in through the criticality module for simulations both with criticality and without criticality; heat of criticality and start time are zeroed for simulations without in-package criticality.

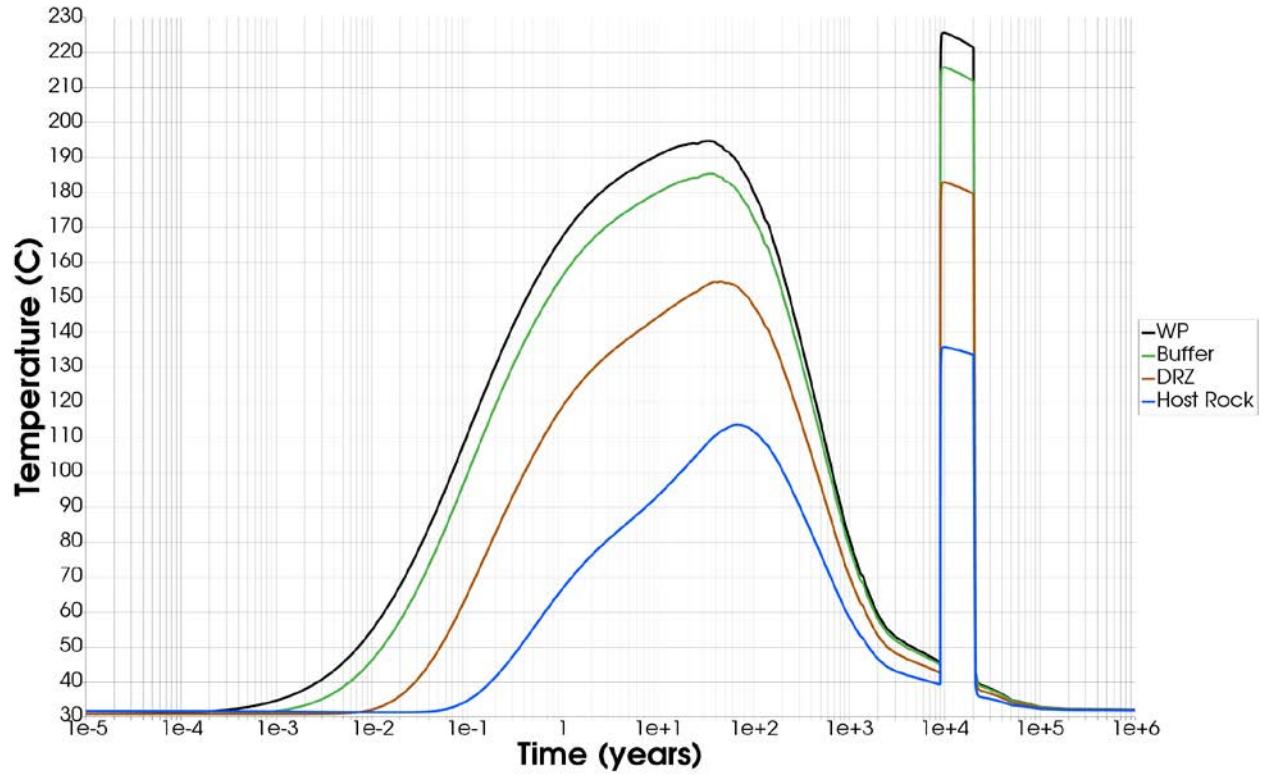
Table 3-10. Criticality Parameters Specified in the Criticality Submodule

Host Rock	Criticality Start Time (years)	Criticality End Time (years)	Heat of Criticality (W)
Shale	9,000	20,000	4,000
Alluvium	9,000	20,000	400

NOTE: Total simulation time period is 20,000 years. Once steady-state criticality initiates at 9,000 years, it continues to the end of the simulation resulting in an 11,000-year duration.

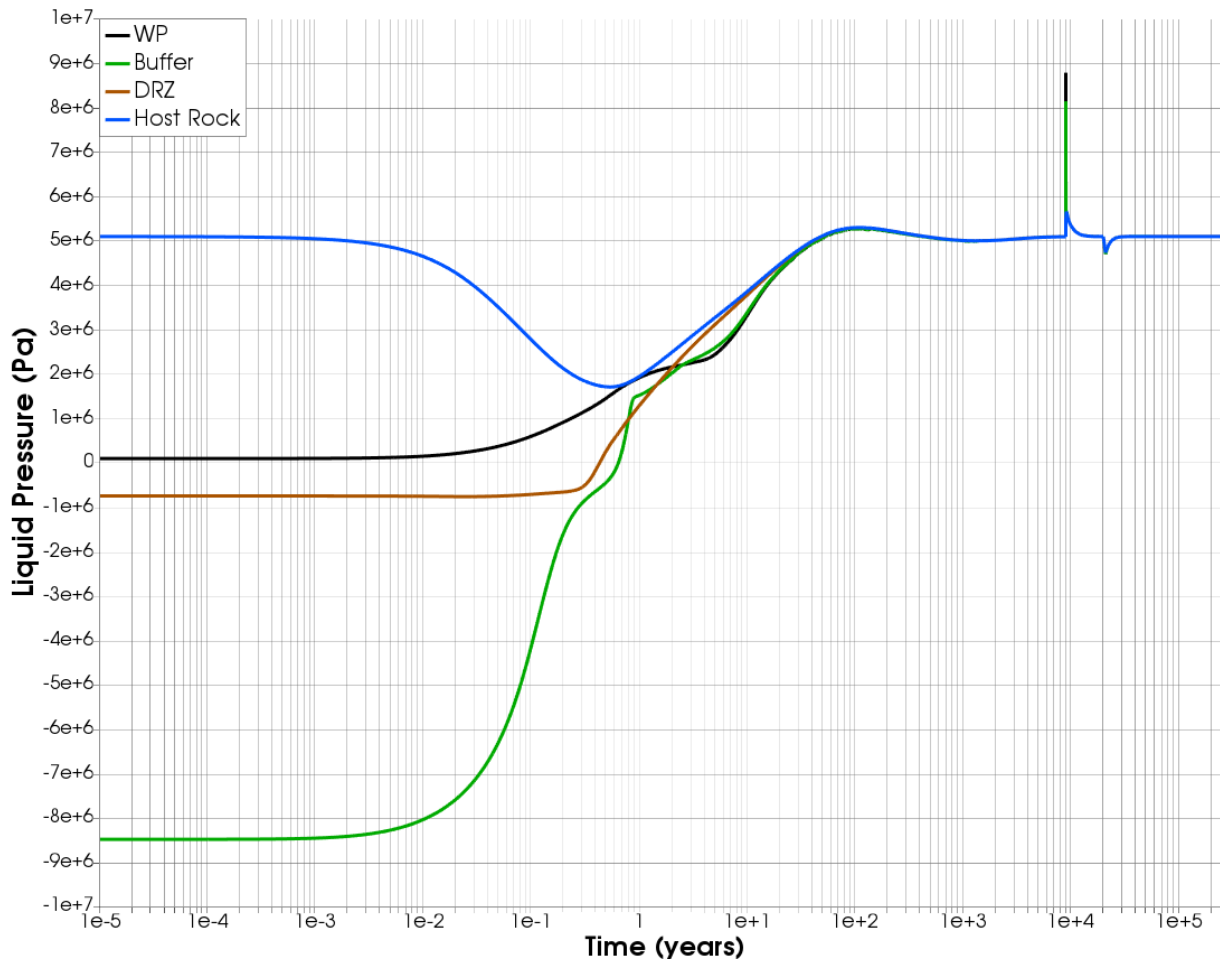
Initial water saturations were chosen to avoid total dry-out, thereby enabling radionuclide transport modeling in PFLOTRAN. As shown in the thermal analysis conducted with PFLOTRAN (Figure 3-46), the entire shale-hosted repository becomes fully re-saturated within 2,000 years. Thus, by the time criticality and waste package breach are initiated, water saturation throughout the whole domain is 100%; therefore, the degree to which the drift is initially unsaturated likely plays a minimal role in affecting heat and mass flow or in-package chemistry during the period of criticality. The same cannot be said for the simulation of the hypothetical repository in unsaturated alluvium—no set of initial conditions avoids dry-out with the given thermal load for a 37-PWR DPC. Thus, simulations of the hypothetical unsaturated repository in alluvium were not run. Development of PFLOTRAN chemistry capability under dried-out conditions is currently underway.

For simulations in a saturated shale host rock, the heat produced by the criticality event generates temperatures at all observation points that are above the peak temperatures experienced when radionuclide decay heat is the only heat source (Figure 3-49). At the center of the waste package, temperatures peak at about 225°C with a constant 4 kW heat source over the course of the 11,000-year criticality event. Temperature in the host rock peaks at over 130°C during this period. Elevated temperatures are concurrent with thermal pressurization (Figure 3-50), and the system remains completely water saturated throughout the course of the criticality event (Figure 3-51).



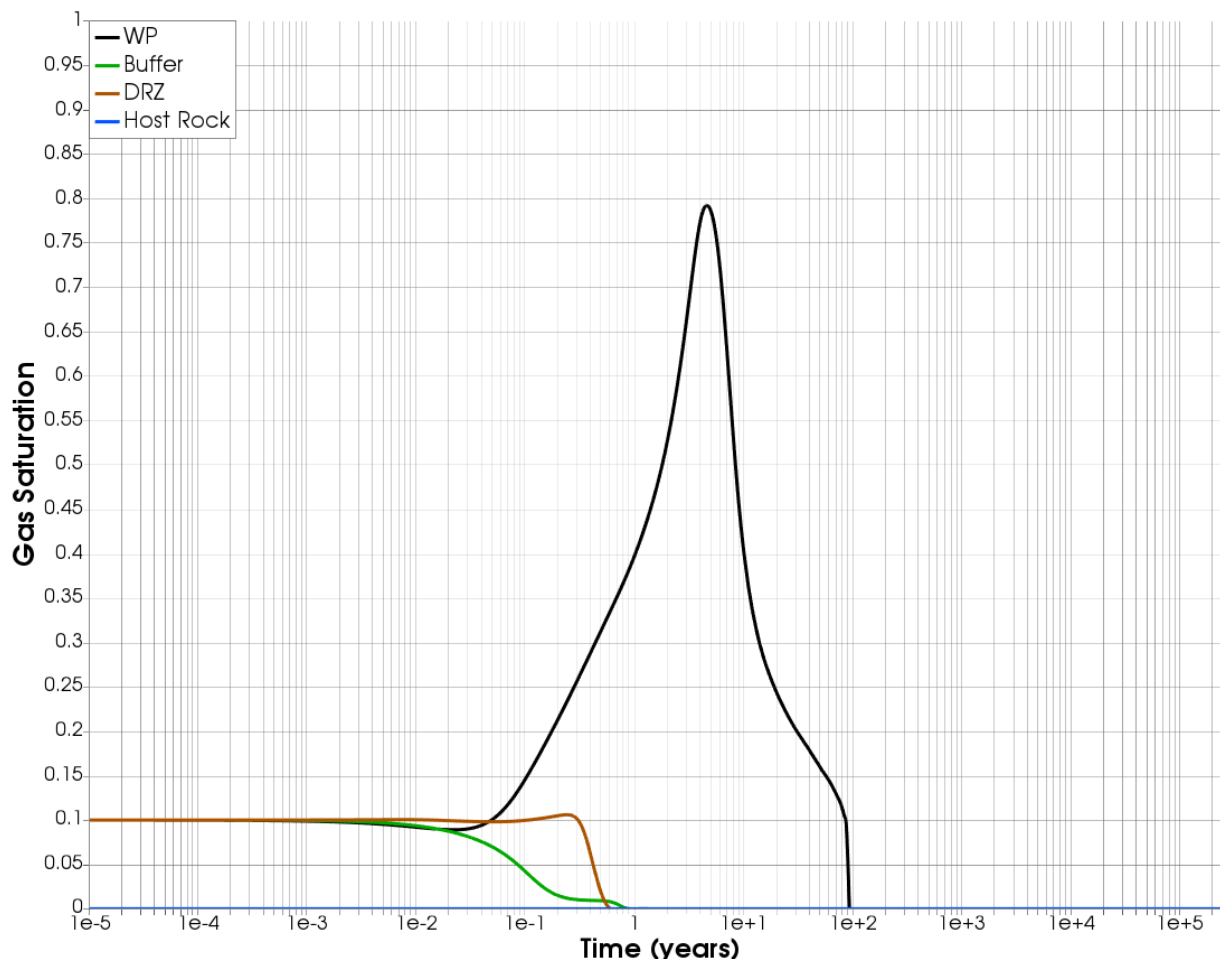
NOTE: DRZ = disturbed rock zone.
WP = waste package.

Figure 3-49. Temperature versus Time at Observation Points Indicated in Figure 2-10, with a Criticality Event Lasting from 9,000 to 20,000 Years



NOTE: Negative liquid pressure indicates capillary suction.
 DRZ = disturbed rock zone.
 WP = waste package.

Figure 3-50. Liquid Pressure versus Time at Observation Points Indicated in Figure 2-10, with a Criticality Event Lasting from 9,000 to 20,000 Years



NOTE: DRZ = disturbed rock zone.
 WP = waste package.

Figure 3-51. Gas Saturation versus Time at Observation Points Indicated in Figure 2-10, with a Criticality Event Lasting from 9,000 to 20,000 Years

Gas pressure in the drift is initialized to atmospheric pressure, and due to the drift being undersaturated, an associated capillary pressure generates capillary suction that is represented in PFLOTRAN with negative liquid pressures (Figure 3-50). The buffer material exhibits the strongest capillary suction, drawing in water rapidly early on. After the decay heat declines enough, water condenses and imbibes from the surrounding formation until the gas phase disappears after about 100 years (Figure 3-51). When the criticality event initiates, a sudden heat pulse causes expansion of the liquid phase and thus thermal pressurization, leading pressure to spike to over 8 MPa in the buffer. This elevated pressure rapidly declines back to the pressure of the host rock, but it could be important to consider when modeling PA-scale fluid flow between multiple drifts in a repository.

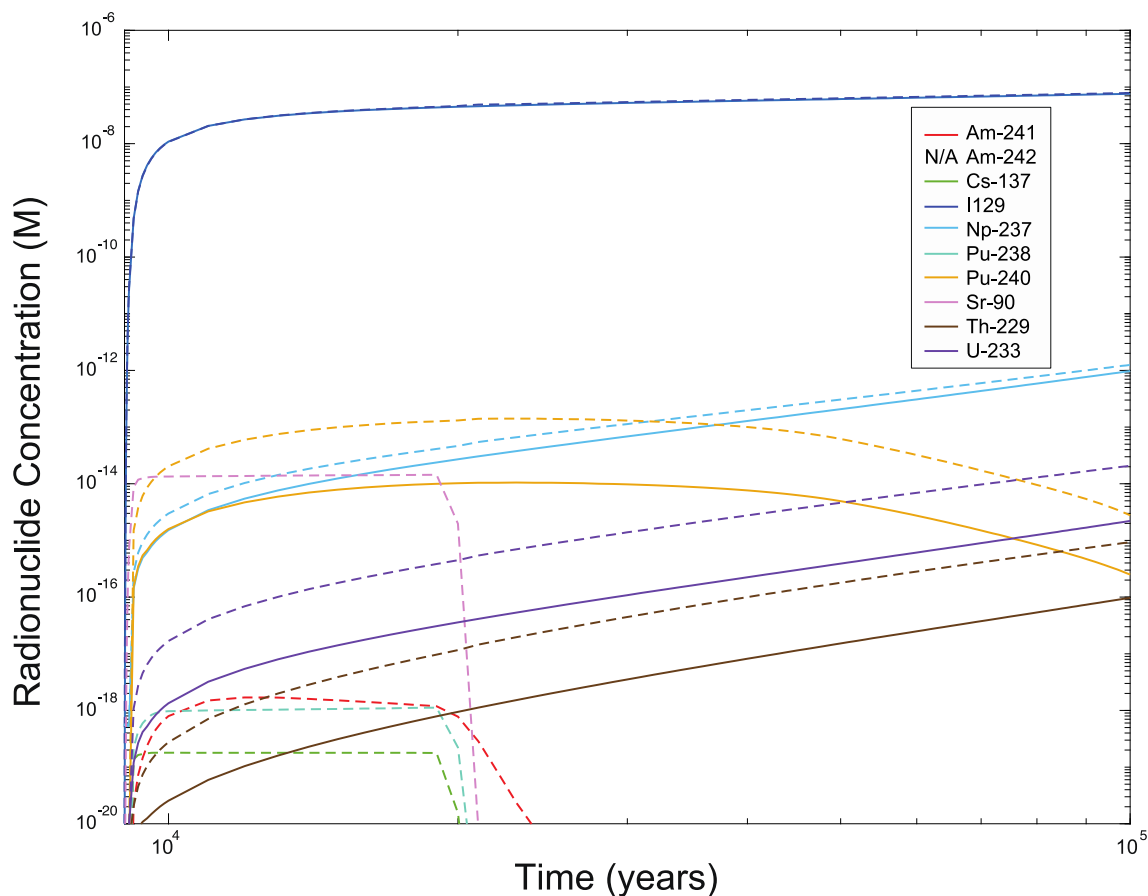
Plotted in Figure 3-52 are the simulated concentrations of the selected subset of radionuclides (Section 3.2) in the observation point within the host rock at the edge of the drift (Figure 2-10), both with and without a criticality event. Table 3-11 gives the percentage change in concentrations of these radionuclides that results when the simulation includes the occurrence of the criticality event relative to when the simulation does not include a criticality event. Only radionuclides with concentrations greater than 1×10^{-20} M in either case are given in this table, as concentrations at or below this value represent a value of zero.

Results in Figure 3-52 are plotted starting at 9,000 years, when waste package breach and criticality are initiated. Changes in radionuclide concentrations relative to the base case reflect changes in the radionuclide inventory because of the criticality event and the lack of radionuclide sorption capability in the backfill. It should be noted that these concentrations are simulated in the hypothetical shale host rock adjacent to the repository, not in the far-field where a water well to the hypothetical member of the public would likely be located. It is not appropriate to use these near-field concentrations to calculate dose to a member of the public; a model that includes far-field radionuclide transport is necessary to be able to calculate dose to a member of the public. Concentrations of the short-lived radionuclides, the ones that show a substantial increase in concentration with the occurrence of the steady-state event, will be orders of magnitude lower in the far field because of decay and, in most cases, sorption onto the host rock. How much lower is a function of the properties of the host rock and the travel time.

As shown in Figure 3-52, concentrations of ^{90}Sr , ^{137}Cs , ^{238}Pu , and ^{241}Am , are orders of magnitude larger in simulations with criticality as compared to simulations without criticality. The reason is that the inventories of these radionuclides, which have half-lives between about 30 and 430 years, decay significantly by 9,000 years after repository closure, as shown in Table 3-3 and Table 3-4. The criticality event in the DPC creates additional quantities of these radionuclides, so that by 20,000 years after repository closure, there are much more of these radionuclides than there would have been had the criticality event not occurred (Table 3-3 and Table 3-4). Concentrations of $^{242\text{m}}\text{Am}$ are not shown because they are below 1×10^{-20} M both with and without a criticality event.

Concentrations of ^{237}Np , ^{233}U , ^{229}Th , ^{240}Pu , and ^{129}I in the shale increase compared to their concentrations without the criticality event, even though the inventory of two of these radionuclides (^{233}U and ^{229}Th) decreases during the criticality event (Section 3.2). The result is due to the assumption that the heat generated by the criticality event causes the backfill to no longer be able to retard radionuclide transport by sorption; thus, the K_d is set to 0 in the backfill for all radionuclides for simulations that include criticality (Table 2-10). This effect is evident in Table 3-11, where the percentage increase in the concentration of ^{129}I , which is a nonsorbing radionuclide whether or not a criticality event occurs, is similar to the percentage increase in its inventory as a result of the criticality event (Table 3-4 and Table 3-11), about 4%. On the other hand, even though their inventories in the DPC decrease as a result of a criticality event (Table 3-3), the concentrations of ^{233}U and ^{229}Th increase by about an order of magnitude in the shale when a criticality event occurs. The reason is that the transport of these radionuclides is not retarded by sorption in the backfill when a criticality event occurs. Uranium is highly sorbing in backfill in the absence of a criticality event (Table 2-10); assuming that the backfill is no longer capable of sorbing radionuclides in the elevated temperatures associated with a critical event leads to an order of magnitude increase in ^{233}U concentrations in the shale, and in its daughter product, ^{229}Th . The concentrations of ^{240}Pu and ^{237}Np also increase by about an order of magnitude and by about 30%,

respectively. It should be noted that, for the simulations that include a criticality event, the value of the K_d in the backfill is set to 0 for the entire simulation period, not just the period of time during which the backfill temperature is higher than 100°C. Being able to vary K_d values during a PFLOTRAN simulation to reflect changes in barrier capability when the backfill temperature is elevated is an area for future development.



NOTE: Dashed lines correspond to comparison simulations considering a criticality event at 9,000 years concurrent with waste package breach, and solid lines correspond to base case simulations without criticality.
N/A = not applicable.

Figure 3-52. Concentration versus Time after Waste Package Breach in the Shale Host Rock at the Edge of the Drift for a Selection of Radionuclides, with and without a Criticality Event

Table 3-11. Percentage Change in Concentrations of Selected Radionuclides at the Edge of the Drift Shale with a Postclosure Criticality Event from 9,000 to 20,000 Years after Repository Closure

Time after Repository Closure (years)	²⁴⁰ Pu	²³⁷ Np	²³³ U	²²⁹ Th	¹²⁹ I
9,000	0.00E+00	0.00E+00	0.00E+00	0.00E+00	0.00E+00
10,000	1.18E+03	9.66E+01	1.16E+03	9.73E+02	-1.34E+00
11,000	1.18E+03	9.21E+01	1.17E+03	1.10E+03	-3.90E-01
12,000	1.17E+03	8.96E+01	1.17E+03	1.13E+03	2.54E-01
13,000	1.17E+03	8.71E+01	1.17E+03	1.14E+03	7.11E-01
14,000	1.17E+03	8.47E+01	1.17E+03	1.14E+03	1.08E+00
15,000	1.16E+03	8.22E+01	1.16E+03	1.14E+03	1.40E+00
16,000	1.16E+03	7.99E+01	1.16E+03	1.14E+03	1.70E+00
17,000	1.16E+03	7.75E+01	1.16E+03	1.14E+03	1.98E+00
18,000	1.16E+03	7.53E+01	1.15E+03	1.13E+03	2.27E+00
19,000	1.17E+03	7.31E+01	1.15E+03	1.13E+03	2.55E+00
20,000	1.18E+03	7.21E+01	1.15E+03	1.13E+03	3.29E+00
30,000	1.24E+03	6.57E+01	1.18E+03	1.16E+03	3.58E+00
40,000	1.21E+03	5.53E+01	1.13E+03	1.12E+03	3.47E+00
50,000	1.15E+03	4.78E+01	1.08E+03	1.08E+03	3.46E+00
60,000	1.08E+03	4.20E+01	1.03E+03	1.03E+03	3.46E+00
70,000	1.04E+03	3.75E+01	9.81E+02	9.88E+02	3.47E+00
80,000	1.04E+03	3.39E+01	9.32E+02	9.43E+02	3.47E+00
90,000	1.04E+03	3.09E+01	8.85E+02	9.01E+02	3.48E+00
100,000	1.02E+03	2.85E+01	8.41E+02	8.60E+02	3.48E+00

4. CONCLUSIONS

A two-phase study was initiated to begin examining the potential consequences, with respect to long-term repository performance, of criticality events that might occur during the postclosure period in a hypothetical repository containing DPCs. Phase I, a scoping phase, consisted of generating an approach intended to be a starting point for the development of the modeling tools and techniques that may eventually be required either to exclude criticality from or include criticality in a PA as appropriate; Phase I is documented in Price et al. (2019). The Phase I approach was used to guide the analyses and simulations done in Phase II to further the development of these modeling tools and techniques as well as the overall knowledge base. This report documents the results of the analyses conducted during Phase II. While the work summarized in Section 4.1 advances both capability and understanding, the research into potential criticality consequences is still in the early stages. Section 4.2 outlines plans for future work recommended to continue moving the research forward to a scientifically justifiable conclusion on the impact of criticality.

4.1 Summary of Results

Even though the potential for criticality in a DPC cannot be completely ruled out, that potential can become very low because of the presence of absorbers, changes in geometry, and limited moderation. The new modeling capabilities developed in Phase II include coupling Shift and COBRA-SFS within the Terrenus framework and adding a submodel to PFLOTRAN to be able to model the additional heat and radionuclide inventory associated with a steady-state criticality event for a specified duration after repository closure. Coupling Shift, a high-performance Monte Carlo radiation transport solver, and COBRA-SFS, a subchannel single-phase thermal-hydraulic code featuring natural circulation, represents significant progress toward being able to perform neutronic calculations of postclosure criticality in a DPC. The criticality submodule of PFLOTRAN was tested using a near-field, single waste package model that considers multiphase flow coupled with transport, decay, and ingrowth of radionuclides. Adding the criticality submodule to PFLOTRAN also represents significant progress toward being able to model the consequences of a postclosure criticality event on long-term repository performance.

To gain insight into critical configurations for typical SNF canisters, a series of criticality calculations was performed using Shift to determine the critical water level for a realistic MPC-32-TSC canister. For this particular canister, the critical water level is approximately 103 cm from the bottom of the first row of assemblies; about 75% of the fuel is submerged.

Changes in the radionuclide inventory as a result of a 4 kW steady-state criticality event in a hypothetical saturated shale repository that lasts from 9,000 to 19,000 years after closure were evaluated (Section 3.2). As expected, short-lived radionuclides, which had undergone significant decay, show the largest increase in their respective inventories. Some longer-lived and stable radionuclides show an increase of about 3%. In contrast, the inventory of some longer-lived and stable radionuclides decreases as a result of the steady-state criticality event because of fission or neutron capture. Inventory decreases in the 37 PWR assemblies analyzed in this study range from about 2% (e.g., ^{239}Pu) to as much as 80% (e.g., ^{155}Gd). Changes in the radionuclide inventory from a 400 W steady-state criticality event in a hypothetical unsaturated repository were not specifically evaluated. However, given the linear relationship between number of fissions and power generated, it is expected that changes in the radionuclide inventory

resulting from a 400 W steady-state criticality event would be about 10% of those associated with a 4 kW steady-state criticality event.

Several different thermal analyses were conducted to investigate the effects of heat produced by the steady-state criticality event on the waste package and beyond (Section 3.3). One conclusion that can be drawn is that the power that can be generated by a steady-state criticality event in a waste package disposed in a saturated environment is much greater than that which can be generated in a waste package disposed in an unsaturated environment. In simulations of the two hypothetical repositories, the maximum power generated in the saturated repository, 4 kW, is an order of magnitude greater than the power generated in the unsaturated repository, less than 400 W. Accordingly, temperature increases in the unsaturated repository from a criticality event are substantially less than those in a saturated repository, on the order of 15°C versus 130°C or more, respectively.

Another conclusion that can be drawn from the analyses is that the heat generated by a 10,000-year, 4 kW, steady-state criticality event in a saturated repository is not likely to affect waste packages in the same drift (20 m center-to-center spacing) or waste packages in an adjacent drift. Further, it can be concluded that convective heat transfer is unimportant in the low-permeability backfill typically planned in a saturated repository.

A preliminary investigation of chemistry in the waste packages during a steady-state criticality event (Section 3.4) and solubilities of radionuclides (Section 3.5) indicates that the increased radiolysis associated with a criticality event could lead to the production of acid, thereby lowering the pH in the waste package. Some of the acid produced would be buffered by corrosion products produced by the corrosion of stainless steel and by the dissolution of the SNF. In the absence of pH buffering, actinides would become more soluble. On the other hand, solubilities of actinides tend to decrease with temperature, and higher temperatures favor formation of radionuclide-bearing solids that have lower solubilities. These competing processes have not yet been quantified and are therefore not included in the simulations documented in this report.

As a first step toward investigating the effects of criticality on the EBS (Section 3.6), this study assumes that, for the hypothetical saturated shale repository, the higher temperatures associated with the steady-state criticality event decrease the barrier capability of the backfill. To implement this assumption in simulations with criticality, the bentonite K_d is reduced (relative to that used for the case without criticality) to inhibit radionuclide sorption during transport through the backfill.

Several processes that could cause permanent criticality termination in disposed DPCs were also evaluated (Section 3.7). One conclusion is that radioactive decay provides limited changes in DPC reactivity after ~100,000 years. To the contrary, buildup of ^{233}U from decay of ^{237}Np results in a small reactivity increase over a few million years. Additional burnup due to a steady-state postclosure criticality event reduces DPC k_{eff} by 0.005 per GWd/MTU. For a DPC with excess reactivity of ~0.1, an additional burnup of 20 GWd/MTU would be required to cause permanent criticality termination. Such a DPC could sustain a steady-state criticality at a power level of 4 kW for 200,000 years, assuming no changes to fuel configuration. Changes in geometry due to grid spacer corrosion/collapse and effects of thermal and moderator removal/restoration resulting in uniform pin pitch reduction by ~3 mm would essentially result in permanent termination of criticality for most DPCs. The impact of cladding corrosion or failure on reactivity is uncertain and, if localized, could result in slight increase in reactivity. Finally, loss of

absorber isotopes negatively affects the criticality termination argument. Potential loss of key absorber isotopes through dissolution or other means must be considered.

PFLOTRAN was used to simulate radionuclide releases from a single waste package in a hypothetical saturated shale repository both without a steady-state criticality event and with a steady-state criticality event (Section 3.8). Radionuclide releases from a single waste package in a hypothetical unsaturated alluvium repository were not modeled because no set of initial conditions avoid dry-out given the decay heat from the 37-PWR DPC. In the simulations of the hypothetical saturated repository, the heat generated during the criticality event leads to rapid thermal pressurization of the surrounding backfill and DRZ and to temperatures exceeding those attained by decay heat alone.

In the PFLOTRAN simulations, a selected subset of ten radionuclides was chosen to demonstrate differences in aqueous radionuclide concentrations at the shale next to the drift that can accompany waste package breach depending on whether the waste package has gone critical or not. Concentrations of the short-lived isotopes increase by several orders of magnitude relative to the no-criticality-event case until about a few thousand years after the criticality event ceases, depending on the half-life of the radionuclide. Concentrations of longer-lived radionuclides selected for modeling in PFLOTRAN increase over the course of a hundred thousand years, relative to the case in which a criticality event did not occur. The largest increases in concentrations (about an order of magnitude) occur for those radionuclides that exhibit the most retardation in the backfill in the absence of a criticality event; that is, the radionuclides that have the highest K_d values in the backfill in the absence of a criticality event. For nonsorbing radionuclides, the increase in concentration is much smaller, only a few percent. Note that these concentrations are in the shale right next to the waste disposal drift, not in the far field where a water well might be drilled by a member of the public at some time in the future. As such, it is not appropriate to use these near-field concentrations to estimate dose to a member of the public.

4.2 Future Work

Several different areas for future work were identified in this preliminary research. To continue to build neutronic capabilities, the geometric capability of Terrenus should be expanded so that a full cask of arbitrary reactor assemblies can be modeled, along with cask internals. Moreover, future work should include enabling Terrenus to calculate the negative temperature coefficient of the system so that a critical temperature search can be performed, and the coupled transport-hydraulics system can iterate to the actual power. In addition, consideration should be given as to whether other thermal-hydraulic codes exist that better meet the needs of this project. With respect to modeling a transient event, an approach has been proposed and is under development (Section 2.1.6); further development should continue.

For the purposes of the work described herein, it is assumed that the steady-state criticality events are not cyclic. However, particularly in the unsaturated repository, a postclosure criticality event is likely to have a cyclic nature. If a waste package were to fill with enough water such that a critical configuration was obtained, the heat generated would eventually evaporate the water, providing negative reactivity feedback and ending the criticality event. The waste package would cool, water would re-enter the waste package, and the criticality event could start again once enough water was present, only to evaporate once the criticality event began and enough heat was generated. Future work should investigate and parameterize the cyclic nature of this “steady-state” criticality event.

Evaluation of the chemistry inside a DPC during a steady-state criticality event is complex and needs further study. Specifically, a coupled calculation considering radiolysis, steel degradation, and SNF degradation and geometry changes at different temperatures is needed. The results of this calculation will contribute to the technical basis for estimating radionuclide solubilities in the waste package, as well as modeling possible degradation of the cladding and grid spacers that could lead to permanent termination of the criticality event. Representative and defensible corrosion modeling of grid spacers and cladding based on the anticipated range of environments and chemical conditions is warranted because assuming cladding has failed and SNF is exposed upon waste package failure runs counter to the basis required for postclosure criticality analysis. In addition, the reactivity of SNF in DPCs over repository time scales, including in the presence of corrosion products, should be studied.

In the future, the capabilities of PFLOTRAN should be expanded (1) to incorporate more radionuclides that might be important to model during a criticality event, (2) to consider the power level of a criticality event as a function of water saturation and/or water density, (3) to expand the grid from a single package to an entire repository, (4) to develop the far-field modeling including calculating the dose to a member of the public, (5) to be able to model a criticality event in a hypothetical unsaturated repository, and (6) to be able to change radionuclide solubilities and radionuclide sorption coefficients during the simulation to account for time-variant potential effects of criticality on solubility and sorption.

The capabilities being developed can be used not only to assess the conditions, time-scales, and effects of criticality, but also to consider engineering modifications that may inhibit criticality conditions. Once the tools and techniques become available, studies could be done to investigate how repository geometry, backfill chemical additives, placement of neutron absorbers, and the like impact the potential for criticality.

5. REFERENCES

10 CFR 63. *Disposal of High-level Radioactive Waste in a Geologic Repository at Yucca Mountain, Nevada.*

10 CFR 71. *Packaging and Transportation of Radioactive Material.*

10 CFR 72. *Licensing Requirements for the Independent Storage of Spent Nuclear Fuel, High-level Radioactive Waste, and Reactor-related Greater than Class C Waste.*

40 CFR 197. *Public Health and Environmental Radiation Protection Standards for Yucca Mountain, Nevada.*

ANSI/ANS 8.1-2014. *Nuclear Criticality Safety in Operations with Fissionable Materials outside Reactors.* La Grange Park, IL: American Nuclear Society.

Avallone, E.A., T. Baumeister III, and A.M. Sadegh. 2007. *Marks' Standard Handbook for Mechanical Engineers.* Eleventh Edition. New York, NY: McGraw Hill.

Avramova, M.N. 2009. *CTF: A Thermal Hydraulic Sub-Channel Code for LWR Transient Analyses, User's Manual.* Pennsylvania State University.

Banerjee, K., K. Robb, G. Radulescu, and J. Scaglione. 2016. "Estimation of Inherent Safety Margins in Loaded Commercial Spent Nuclear Fuel Casks," *Nuclear Technology* 195 (2): 124–142. doi: 10.13182/NT15-112.

Bernot, P. 2007. *Dissolved concentration limits of elements with radioactive isotopes.* ANL-WIS-MD-000010 REV 06. Las Vegas, NV: Sandia National Laboratories.

Bhatt, S. 2019. E-Mail dated 9/23/2019 from Santosh Bhatt to Mike Gross with Subject: "Thermal Calculations in SCALE" and Attachments: "decayHeat.xlsx" and "Results.zip".

BNL (Brookhaven National Laboratory). n.d. *National Nuclear Data Center (NNDC).* www.nndc.bnl.gov.

BSC (Bechtel SAIC Company). 2003. *Isotopic Generation and Confirmation of the PWR Application Model.* CAL-DSU-NU-000004 REV 00A. Las Vegas, NV: Bechtel SAIC Company.

BSC. 2005a. *Cladding Degradation Summary for LA.* ANL-WIS-MD-000021 REV03. Las Vegas, NV: Bechtel SAIC Company.

BSC. 2005b. *Dry Transfer Facility Criticality Safety Calculations.* 100-00C-WHS0-00100-000-00C. Las Vegas, NV: Bechtel SAIC Company..

BSC. 2005c. *EBS Radionuclide Transport Abstraction.* ANL-WIS-PA-000001, REV 02. Las Vegas, NV: Bechtel SAIC Company.

BSC. 2005d. *Steady-State Criticality Consequence Model Report.* CAL-DS0-NU-000001 REV00A. Las Vegas, NV: Bechtel SAIC Company.

Carslaw, H.S. and J.C. Jaeger. 1959. *Conduction of Heat in Solids*. Second Edition. Oxford, Great Britain: Oxford University Press.

Cheshire, M.C., F.A. Caporuscio, M.S. Rearick, C. Jové-Colón, and M.K. McCarney. 2014. "Bentonite evolution at elevated pressures and temperatures: An experimental study for generic nuclear repository designs." *American Mineralogist* 99 (8–9): 1662–1675.

Clayton, D., G. Freeze, T. Hadgu, E. Hardin, J. Lee, J. Prouty, R. Rogers, W.M. Nutt, J. Birkholzer, H.H. Liu, L. Zheng, and S. Chu. 2011. *Generic Disposal System Modeling – Fiscal Year 2011 Progress Report*. FCRD-USED-2011-000184; SAND2011-5828P. Washington, DC: U.S. Department of Energy, Office of Nuclear Energy.

CNWRA (Center for Nuclear Waste Regulatory Analyses). 2005. *System-Level Performance Assessment of the Proposed Repository at Yucca Mountain Using the TPA Version 4.1 Code*. CNWRA 2002-5, Rev. 2. San Antonio, TX: Center for Nuclear Waste Regulatory Analyses.

Croff, A.G. 1983. "ORIGEN2: A Versatile Computer Code for Calculating the Nuclide Compositions and Characteristics of Nuclear Materials." *Nuclear Technology* 62 (3): 335–352. doi: [dx.doi.org/10.13182/NT83-1](https://doi.org/10.13182/NT83-1).

CRWMS M&O (Civilian Radioactive Waste Management System Management and Operating Contractor). 1996. *Probabilistic Criticality Consequence Evaluation*. BBA000000-01717-0200-00021 REV00. Las Vegas, NV: Civilian Radioactive Waste Management M&O.

CRWMS M&O. 1999. *Criticality Consequence Calculation Involving Intact PWR MOX SNF in a Degraded 21 PWR Assembly Waste Package*. CAL-EBS-NU-000008 REV00. Las Vegas, NV: Department of Energy, Office of Civilian Radioactive Waste Management.

CRWMS M&O. 2001. *Geochemistry Model Validation Report: Material Degradation and Release Model*. ANL-EBS-GS-000001 REV 00. Las Vegas, NV: Department of Energy, Office of Civilian Radioactive Waste Management.

Davidson, G.G. and K. Banerjee. 2017. *Initial Development of a Large Facility Dose Analysis Approach*. SFWD-PO-2017-000084; ORNL/SPR-2017-/439. Oak Ridge, TN: Oak Ridge National Laboratory.

Davidson, G.G., M. Swinney, S. Johnson, S. Bhatt, and K. Banerjee. 2019. *Initial Neutronics and Thermal-Hydraulic Coupling for Spent Nuclear Fuel Canisters*. M3SF-19OR010305015; ORNL/SPR-2019/1333. Oak Ridge, TN: Oak Ridge National Laboratory.

Davidson, G.G., T.M. Pandya, S.R. Johnson, T.M. Evans, A.E. Isotalo, C.A. Gentry, and W.A. Wieselquist. 2018. "Nuclide depletion capabilities in the Shift Monte Carlo code." *Annals of Nuclear Energy* 114:259–276. doi: <https://doi.org/10.1016/j.anucene.2017.11.042>.

DOE (Department of Energy). 2008a. *Yucca Mountain Repository License Application*. DOE/RW-0573, Rev. 0. Las Vegas, NV: U.S. Department of Energy, Office of Civilian Radioactive Waste Management.

DOE. 2008b. *Yucca Mountain Repository License Application*. DOE/RW-0573, Rev. 1. Las Vegas, NV: U.S. Department of Energy, Office of Civilian Radioactive Waste Management.

Dulla, S., E.H. Mund, and P. Ravetto. 2008. "The quasi-static method revisited." *Progress in Nuclear Energy* 50:908–920. doi: 10.1016/j.pnucene.2008.04.009.

EPA (Environmental Protection Agency) 2008. *Public Health and Environmental Radiation Protection Standards for Yucca Mountain, Nevada*. 73 FR 61256.

EPRI (Electric Power Research Institute). 2002. *BWR Performance Monitoring*. 1003600. Palo Alto, CA: Electric Power Research Institute, Inc.

EPRI. 2005. *Proceedings: 2005 Condensate Polishing Workshop*. 1013173. Palo Alto, CA: Electric Power Research Institute, Inc.

Gill, D.F., D.P. Griesheimer, and D.L. Aumiller. 2017. "Numerical Methods in Coupled Monte Carlo and Thermal- Hydraulic Calculations." *Nuclear Science and Engineering* 185 (1): 194–205. doi: 10.13182/NSE16-3.

Godfrey, A.T. 2016. *VERA Core Physics Benchmark Progression Problem Specifications*. CASL-U-2012-0131-004, Rev. 4. Oak Ridge, TN: Oak Ridge National Laboratory.

Hamilton, S.P. and T.M. Evans. 2019. "Continuous-energy Monte Carlo neutron transport on GPUs in the Shift code." *Annals of Nuclear Energy* 128:236–247. doi: <https://doi.org/10.1016/j.anucene.2019.01.012>.

Hammond, G.E., Lichtner, P.C., and R.T. Mills. 2014. "Evaluating the performance of parallel subsurface simulators: An illustrative example with PFLOTRAN." *Water Resources Research* 50 (1): 208–228. doi: 10.1002/2012wr013483.

Hardin, E. and E. Kalinina. 2016. *Cost Estimation Inputs for Spent Nuclear Fuel Geologic Disposal Concepts*. SAND2016-0235. Albuquerque, NM: Sandia National Laboratories.

Hardin, E., L. Price, E. Kalinina, T. Hadgu, A. Ilgen, C. Bryan, J. Scaglione, K. Banerjee, J. Clarity, R. Jubin, V. Sobes, R. Howard, J. Carter, T. Severynse, and F. Perry. 2015. *Summary of Investigations on Technical Feasibility of Direct Disposal of Dual-Purpose Canisters*. FCRD-UFD-2015-000129, Rev. 0. Washington, D.C.: U.S. Department of Energy.

INEL (Idaho National Engineering Laboratory). 1995. *RELAP5/MOD3 Code Manual; Volume I: Code Structure, System Models, and Solution Methods*. NUREG/CR-555; INEL-95/0174. Idaho Falls, ID: Idaho National Engineering Laboratory.

Jiang, H., J. Qu, R. Lu, and J.-A.J. Wang. 2016. "Grid-to-rod flow-induced impact study for PWR fuel in reactor." *Progress in Nuclear Energy* 91:355–361. doi: <https://doi.org/10.1016/j.pnucene.2016.06.003>.

Jerden, J.L., K. Frey, and W. Ebert. 2015. "A multiphase interfacial model for the dissolution of spent nuclear fuel." *Journal of Nuclear Materials* 462:135–146. doi: <https://doi.org/10.1016/j.jnucmat.2015.03.036>.

- Jo, Y., B. Cho, and N. Z. Cho. 2016. "Nuclear Reactor Transient Analysis by Continuous-Energy Monte Carlo Calculation Based on Predictor-Corrector Quasi-Static Method." *Nuclear Science and Engineering* 183 (2): 229–246. doi: 10.13182/NSE15-100.
- Jove Colón, C.F., Y. Wang, T. Hadgu, L. Zheng, J. Rutqvist, H. Xu, K. Kim, M. Voltolini, X. Cao, P.M. Fox, P.S. Nico, F.A. Caporuscio, K.E. Norskog, M. Zavarin, T.J. Wolery, C. Atkins-Duffin, J.L. Jerden, V.K. Gattu, and W.L. Ebert. 2017. *Evaluation of Used Fuel Disposition in Clay-Bearing Rock*. SFWD-SFWST-2017-000006; SAND2017-10533 R. Albuquerque, NM: Sandia National Laboratories.
- Kursten, B., E. Smailos, I. Azkarate, L. Werme, N.R. Smart, G. Marx, M.A. Cuñado, and G. Santarini. 2004. "Corrosion Evaluation of Metallic HLW/Spent Fuel Disposal Containers—Review." In *Proc. of the 2nd International Workshop on Prediction of Long-Term Corrosion Behavior in Nuclear Waste Systems (Eurocorr 2004)*, 153–161.
- Lakes, M.E. and R.J. Ashley. 2017. *Hanford Site Solid Waste Acceptance Criteria*. HNF-EP-0063, Rev. 17. Richland, WA: CH2M HILL Plateau Remediation Company.
- Liljenfeldt, H., K. Banerjee, J. Clarity, J. Scaglione, R. Jubin, V. Sobes, R. Howard, E. Hardin, L. Price, E. Kalinina, T. Hadgu, A. Ilgen, C. Bryan, J. Carter, T. Severynse, F. Perry. 2017. *Summary of Investigations on Technical Feasibility of Direct Disposal of Dual-Purpose Canisters*. SFWD-SFWST-2017-000045; ORNL/SPR-2017/443. Oak Ridge, TN: Oak Ridge National Laboratory.
- Mariner, P.E., E.R. Stein, J.M. Frederick, S.D. Sevougian, and G.E. Hammond. 2017. *Advances in Geologic Disposal System Modeling and Shale Reference Case*. SFWD-SFWST-2017-000044; SAND2017-10304R. Albuquerque, NM: Sandia National Laboratories.
- Mariner, P.E., E.R. Stein, J.M. Frederick, S.D. Sevougian, G.E. Hammond, and D.G. Fascitelli. 2016. *Advances in Geologic Disposal System Modeling and Application to Crystalline Rock*. FCRD-UFD-2016-000440; SAND2016-9610R. Albuquerque, NM: Sandia National Laboratories.
- Mariner, P.E., E.R. Stein, S.D. Sevougian, L.J. Cunningham, J.M. Frederick, G.E. Hammond, T.S. Lowry, S. Jordan, and E. Basurto. 2018. *Advances in Geologic Disposal Safety Assessment and an Unsaturated Alluvium Reference Case*. SFWD-SFWST-2018-000509; SAND2018-11858R. Albuquerque, NM: Sandia National Laboratories.
- Merzari, E., W.D. Pointer, and P. Fischer. 2013. "Numerical Simulation and Proper Orthogonal Decomposition of the Flow in a Counterflow T-Junction." *Journal of Fluids Engineering* 135 (9): 091304. doi: <https://doi.org/10.1115/1.4024059>.
- Michener, T.E., D.R. Rector, and J.M. Cuta. 2017a. "COBRA-SFS Thermal-Hydraulic Analysis Code for Spent-Fuel Storage and Transportation Casks: Models and Methods." *Nuclear Technology* 199 (3): 330–349. doi: <https://doi.org/10.1080/00295450.2017.1305190>.
- Michener, T.E., D.R. Rector, and J.M. Cuta. 2017b. "Validation of COBRA-SFS with Measured Temperature Data from Spent-Fuel Storage Casks" *Nuclear Technology* 199 (3): 350–368. doi: <https://doi.org/10.1080/00295450.2017.1327253>.

Morco, R.P., J.M. Joseph, D.S. Hall, C. Medri, D.W. Shoemith, and J.C. Wren. 2017. "Modelling of radiolytic production of HNO₃ relevant to corrosion of a used fuel container in deep geologic repository environments." *Corrosion Engineering, Science and Technology* 52 (sup1): 141–147. doi: 10.1080/1478422X.2017.1340227.

Nield, D.A. and A. Bejan. 1999. *Convection in Porous Media*. 2nd edition. New York, NY: Springer-Verlag. doi: 10.1007/978-1-4757-3033-3.

OECD/NEA (Organisation for Economic Co-operation and Development/Nuclear Energy Agency). 2012 *Burn-Up Credit Criticality Safety Benchmark—Phase VII.: UO₂ Fuel: Study of Spent Fuel Compositions for Long-Term Disposal*. NEA No. 6998. Paris, France: Organisation for Economic Co-operation and Development/Nuclear Energy Agency. www.oecd-nea.org/science/docs/2012/burn-up-credit-phaseVII.pdf.

Painter, S., Z. Fang, R. Howard, and K. Banerjee. 2019. *ORNL Input to GDSA Repository Systems Analysis FY19*. M4SF-19OR010304072. Oak Ridge, TN : Oak Ridge National Laboratory.

Pandya, T.M., S.R. Johnson, T.M. Evans, G.G. Davidson, S.P. Hamilton, and A.T. Godfrey. 2016. "Implementation, Capabilities, and Benchmarking of Shift, a Massively Parallel Monte Carlo Radiation Transport Code." *Journal of Computational Physics* 308:239–272. doi: <https://doi.org/10.1016/j.jcp.2015.12.037>.

Parkhurst, D.L. and C.A.J. Appelo. 1999. *User's Guide to PHREEQC (Version 2)—A Computer Program for Speciation, Batch-Reaction, One-Dimensional Transport, and Inverse Geochemical Calculations*. Water-Resources Investigations Report 99-4259. Denver, CO: United States Geological Survey.

Perry, F.V., E. Swanson, D.M. Milazzo, G.Y.A. Bussod, R.E. Kelley. 2018. *Regional Geologic Evaluations for Disposal of HLW and SNF: Alluvial Basins of the Basin and Range Province*. LA-UR-18-28909, Rev. 01. Los Alamos, NM: Los Alamos National Laboratory. doi: 10.2172/1479910.

PFLOTRAN. 2016. *PFLOTRAN Documentation*. www.pflotran.org/documentation.

Posiva Oy. 2012. *Safety Case for the Disposal of Spent Nuclear Fuel at Olkiluoto – Design Basis 2012*. 2012-03. Eurajoki, Finland: Posiva Oy.

Price, L.L., A.A. Alsaed, P.V. Brady, M.B. Gross, E.L. Hardin, M. Nole, J.L. Prouty, K. Banerjee, and G.G. Davidson. 2019. *Postclosure Criticality Consequence Analyses—Scoping Phase*. M3SF-19N010305061; SAND2019-4644R. Albuquerque, NM: Sandia National Laboratories.

Rechard, R.P., L.C. Sanchez, and H.R. Trellue. 2003. "Consideration of Nuclear Criticality When Directly Disposing Highly Enriched Spent Nuclear Fuel in Unsaturated Tuff—II: Geochemical Constraints." *Nuclear Technology* 144 (2): 222–251. doi: [dx.doi.org/10.13182/NT03-5](https://doi.org/10.13182/NT03-5).

Rector, D.R., C.L. Wheeler, and N.J. Lombardo. 1986. *COBRA-SFS: A Thermal-Hydraulic Analysis Computer Code; Volume I: Mathematical Models and Solution Method*. PNL-6049 Vol. I. Richland, WA: Pacific Northwest Laboratory.

- Rutqvist, J., L. Zheng, F. Chen, H.-H. Liu, and J. Birkholzer. 2014. "Modeling of Coupled Thermo-Hydro-Mechanical Processes with Links to Geochemistry Associated with Bentonite-Backfilled Repository Tunnels in Clay Formations." *Rock Mechanics and Rock Engineering* 47 (1): 167–186. doi: <https://doi.org/10.1007/s00603-013-0375-x>.
- Rutqvist, J., Y. Ijiri, and H. Yamamoto. 2011. "Implementation of the Barcelona Basic Model into TOUGH-FLAC for simulations of the geomechanical behavior of unsaturated soils." *Computers & Geosciences* 37 (6): 751–762. doi: <https://doi.org/10.1016/j.cageo.2010.10.011>.
- Sevougian, S.D., E.R. Stein, T. LaForce, F.V. Perry, M. Nole, and K.W. Chang. 2019a. *GDSA Repository Systems Analysis FY19 Update*. M3SF-19SN010304052. Albuquerque, NM: Sandia National Laboratories.
- Sevougian, S.D., E.R. Stein, T. LaForce, F.V. Perry, T.S. Lowry, L. Cunningham, M. Nole, C.B. Haukwa, K.W. Chang, and P.E. Mariner. 2019b. *GDSA Repository Systems Analysis Progress Report*. M2SF-19SN010304051; SAND2019-5189R. Albuquerque, NM: Sandia National Laboratories.
- SKB (Svensk Kärnbränslehantering AB). 2011. *Long-term Safety for the Final Repository for Spent Nuclear fuel at Forsmark – Main Report of the SR-Site Project, Volume I*. TR-11-01. Stockholm, Sweden: Svensk Kärnbränslehantering AB.
- SNL. 2007. *Commercial Spent Nuclear Fuel Igneous Scenario Criticality Evaluation*. ANL-EBS-NU-000009 REV 00 ERD 2. Las Vegas, NV: Sandia National Laboratories.
- SNL. 2008. *Features, Events, and Processes for the Total System Performance Assessment: Analyses*. ANL-WIS-MD-000027 REV00. Las Vegas, NV: Sandia National Laboratories.
- Stockman, H.W. 2006. *The Choice of Solid Phases for Modeling the Corrosion of Stainless Steel*. Internal Yucca Mountain Project Memo from Harlan W. Stockman dated August 31, 2006.
- Wagner, J.C. and C.V. Parks. 2003. *Recommendations on the Credit for Cooling Time in PWR Burnup Credit Analyses*. NUREG/CR-6781; ORNL/TM-2001/272. Oak Ridge, TN: Oak Ridge National Laboratory.
- Wagner, J.C., S.W. Mosher, T.M. Evans, D.E. Peplow, and J.A. Turner. 2011. "Hybrid and Parallel Domain-Decomposition Methods Development to Enable Monte Carlo for Reactor Analyses." *Progress in Nuclear Science and Technology* 2:815–820.
- Weast, R.C. and M.J. Astle. 1979. *CRC Handbook of Chemistry and Physics*. Boca Raton, FL: CRC Press.
- Wood, S.A., D.A. Palmer, D.J. Wesolowski, and P. Bénézech. 2002. "The aqueous geochemistry of the rare earth elements and yttrium. Part XI. The solubility of Nd(OH)₃ and hydrolysis of Nd³⁺ from 30 to 290°C at saturated water vapor pressure with in-situ pH_m measurement." In *Water–Rock Interactions, Ore Deposits, and Environmental Geochemistry: A Tribute to David Crerar*, Special Publication 7, ed. R. Hellman and S.A. Wood, 229–256. St. Louis, MO: Geochemical Society.

YMP (Yucca Mountain Project). 2003. *Disposal Criticality Analysis Methodology Topical Report*. YMP/TR-004Q, Rev. 02. Las Vegas, NV: U.S. Department of Energy, Yucca Mountain Site Characterization Office.

Zhu, A. 2016. "Transient Methods for Pin-Resolved Whole-Core Neutron Transport." PhD thesis, University of Michigan.

Zhu, A., Y. Xu, and T. Downar. 2016. "A Multilevel Quasi-Static Kinetics Method for Pin-Resolved Transport Transient Reactor Analysis." *Nuclear Science and Engineering* 182 (4): 435–451. doi: <https://doi.org/10.13182/NSE15-39>.

This page is intentionally left blank.

APPENDIX A

MATHEMATICAL DERIVATION FOR ANALYTICAL MODEL WITH CONDUCTION AND CONVECTION

A-1. Introduction

Section 2.3.2.2 describes the analytical model that considers both heat conduction and convection in the evaluation of the thermal response of DPCs to a steady-state criticality. The mathematical details of the derivation supporting that analytical model appear below. The results of this analysis are provided in Section 3.3.2.2.

Because this analytical model is considered to be an initial assessment, it uses several simplified representations. The SNF is characterized as a horizontal heat line source in which the heat generation rate is time-dependent primarily because of changes in water content and radionuclide concentration in the canisters. The host rock is treated as a saturated, homogenous, porous medium, and the heat generation rate is assumed to be constant for a period of 10,000 years. In addition, the initial condition is a uniform temperature throughout, and the analysis provides the temperature increase as a function of depth and horizontal distance. For low Rayleigh numbers, an analytical asymptotic solution is available for the evolving temperature profile.

A-2. Mathematical Derivation

The three basic equations describing the process are (1) Darcy's Law with the Oberbeck-Boussinesq approximation for the fluid density variation with temperature, (2) continuity for an incompressible fluid, and (3) the energy balance that includes conduction and convection. These equations are respectively (Nield and Bejan 1999)

$$\bar{v} = -\frac{K}{\mu} [\nabla p - \rho_{f\infty} [1 - \beta(T - T_{\infty})] \bar{g}] \quad \text{Equation A-1}$$

$$\nabla \cdot \bar{v} = 0 \quad \text{Equation A-2}$$

$$(\rho c)_m \frac{\partial T}{\partial t} + (\rho c)_f \bar{v} \cdot \nabla T = k_m \nabla \cdot \nabla T + q''' \quad \text{Equation A-3}$$

The thermal conductivity and thermal capacity of the porous medium are given respectively by

$$k_m \equiv (1 - \varphi)k_s + \varphi k_f \quad \text{Equation A-4}$$

$$(\rho c)_m = (1 - \varphi)(\rho c)_s + \varphi(\rho c)_f \quad \text{Equation A-5}$$

The symbols have the following meaning:

\bar{g} = gravitational constant vector (m/s²)

K = permeability (m²)

k = thermal conductivity (W/[m·°C])

p = pressure (Pa)

q''' = volumetric heat generation rate (W/m³)

T = temperature (°C)

t = time (s)

\bar{v} = fluid Darcy velocity vector (m/s)

β = fluid thermal expansion coefficient (1/°C)

φ = porosity

ρ = density (kg/m³)

μ = fluid viscosity (kg/[m·s])

The subscripts have the following meaning:

f = fluid

s = solid

m = porous media

∞ = conditions far from canister

The solution for a line source in homogenous media is given in Nield and Bejan (1999), but all the steps in the derivation and solution are not given. In the following, a detailed derivation is given, and the resulting expression for the increase in temperature was used to create the contour plots given in Figure 3-32.

The derivation starts by taking the curl of Equation A-1 to get

$$\nabla \times \bar{v} = -\frac{K\rho_f\infty\beta}{\mu}\nabla T \times \bar{g} \quad \text{Equation A-6}$$

For the 2D model in r - θ coordinates, where θ is measured counter-clockwise from the horizontal plane, the gravitational constant vector is given by

$$\bar{g} = -g\sin(\theta)\hat{\mathbf{a}}_r - g\cos(\theta)\hat{\mathbf{a}}_\theta \quad \text{Equation A-7}$$

and the temperature gradient is given by

$$\nabla T = \frac{\partial T}{\partial r}\hat{\mathbf{a}}_r + \frac{1}{r}\frac{\partial T}{\partial \theta}\hat{\mathbf{a}}_\theta \quad \text{Equation A-8}$$

where $\hat{\mathbf{a}}_r$ and $\hat{\mathbf{a}}_\theta$ are unit vectors in the r and θ directions, respectively, and $g = 9.81 \text{ m/s}^2$. Substituting Equation A-7 and Equation A-8 into Equation A-6 results in

$$\frac{\partial v_\theta}{\partial r} + \frac{v_\theta}{r} - \frac{1}{r}\frac{\partial v_r}{\partial \theta} = \frac{K\rho_\infty\beta g}{\mu}\left[\cos(\theta)\frac{\partial T}{\partial r} - \frac{\sin(\theta)}{r}\frac{\partial T}{\partial \theta}\right] \quad \text{Equation A-9}$$

Equation A-2 in cylindrical coordinates is given by

$$\frac{\partial}{\partial r}(rv_r) + \frac{\partial v_\theta}{\partial \theta} = 0 \quad \text{Equation A-10}$$

Let the stream function ψ be defined such that

$$v_r = \frac{1}{r}\frac{\partial \psi}{\partial \theta} \quad \text{Equation A-11}$$

and

$$v_\theta = -\frac{\partial \psi}{\partial r} \quad \text{Equation A-12}$$

With these definitions, Equation A-10 is automatically satisfied and instead of two variables (v_r and v_θ), only the stream function needs to be determined to determine the flow velocities. Substituting Equation A-11 and Equation A-12 into Equation A-9 yields the following:

$$r \frac{\partial^2 \psi}{\partial r^2} + \frac{\partial \psi}{\partial r} + \frac{1}{r} \frac{\partial^2 \psi}{\partial \theta^2} = \frac{K \rho_o \beta g}{\mu} \left[\sin(\theta) \frac{\partial T}{\partial \theta} - r \cos(\theta) \frac{\partial T}{\partial r} \right] \quad \text{Equation A-13}$$

Similarly, the energy balance given by Equation A-3 reduces to

$$\sigma \frac{\partial T}{\partial t} + \frac{1}{r} \frac{\partial \psi}{\partial \theta} \frac{\partial T}{\partial r} - \frac{1}{r} \frac{\partial \psi}{\partial r} \frac{\partial T}{\partial \theta} = \alpha_m \left[\frac{\partial^2 T}{\partial r^2} + \frac{1}{r} \frac{\partial T}{\partial r} + \frac{1}{r^2} \frac{\partial^2 T}{\partial \theta^2} \right] \quad \text{Equation A-14}$$

where the heat generation term is incorporated into a boundary condition, and α_m and σ are defined as

$$\alpha_m \equiv \frac{(1 - \phi)k_s + \phi k_f}{(\rho c)_f} \quad \text{Equation A-15}$$

and

$$\sigma \equiv \frac{(\rho c)_m}{(\rho c)_f} \quad \text{Equation A-16}$$

Equation A-13 and Equation A-14 represent the system of interest subject to the boundary conditions

$$t = 0: \quad v_r = 0, \quad v_\theta = 0, \quad T = T_\infty \quad \text{Equation A-17}$$

$$r \rightarrow \infty: \quad v_r = 0, \quad v_\theta = 0, \quad T = T_\infty \quad \text{Equation A-18}$$

$$\theta = \pm \frac{\pi}{2}: \quad v_\theta = 0, \quad \frac{\partial v_r}{\partial \theta} = 0, \quad \frac{\partial T}{\partial \theta} = 0 \quad \text{Equation A-19}$$

The linear heat generation rate q' (W/m) is given by

$$q' = \lim_{r \rightarrow 0} \left(-k_m 2\pi r \frac{\partial T}{\partial r} \right) \quad \text{Equation A-20}$$

There is no apparent length scale to nondimensionalized Equation A-13 and Equation A-14. Nield and Bejan (1999) use the square root of the permeability as the length scale. This method results in a very large dimensionless radial distance with the following dimensionless variables

$$t_* = \frac{t\alpha_m}{K\sigma}, \quad r_* = \frac{r}{\sqrt{K}}, \quad T_* = \frac{(T - T_\infty)k_m}{q'}, \text{ and } \psi_* = \frac{\psi}{\alpha_m} \quad \text{Equation A-21}$$

With these definitions, Equation A-13 and Equation A-14 become respectively

$$r_* \frac{\partial^2 \psi_*}{\partial r_*^2} + \frac{\partial \psi_*}{\partial r_*} + \frac{1}{r_*} \frac{\partial^2 \psi_*}{\partial \theta^2} = \text{Ra} \left(\sin(\theta) \frac{\partial T_*}{\partial \theta} - r_* \cos(\theta) \frac{\partial T_*}{\partial r_*} \right) \quad \text{Equation A-22}$$

and

$$\frac{\partial T_*}{\partial t_*} + \frac{1}{r_*} \left(\frac{\partial \psi_*}{\partial \theta} \frac{\partial T_*}{\partial r_*} - \frac{\partial \psi_*}{\partial r_*} \frac{\partial T_*}{\partial \theta} \right) = \frac{\partial^2 T_*}{\partial r_*^2} + \frac{1}{r_*} \frac{\partial T_*}{\partial r_*} + \frac{1}{r_*^2} \frac{\partial^2 T_*}{\partial \theta^2} \quad \text{Equation A-23}$$

The transformed boundary conditions are

$$t_* = 0: \quad \frac{1}{r_*} \frac{\partial \psi_*}{\partial \theta} = 0, \quad \frac{\partial \psi_*}{\partial r_*} = 0, \quad T_* = 0 \quad \text{Equation A-24}$$

$$r_* \rightarrow \infty: \quad \frac{1}{r_*} \frac{\partial \psi_*}{\partial \theta} = 0, \quad \frac{\partial \psi_*}{\partial r_*} = 0, \quad T = T_\infty \quad \text{Equation A-25}$$

$$\theta = \pm \frac{\pi}{2}: \quad \frac{\partial \psi_*}{\partial r_*} = 0, \quad \frac{1}{r_*} \frac{\partial^2 \psi_*}{\partial \theta^2} = 0, \quad \frac{\partial T}{\partial \theta} = 0 \quad \text{Equation A-26}$$

and

$$\lim \left[-k_m 2\pi r \frac{\partial T}{\partial r} \right]_{r \rightarrow 0} = q' \quad \text{Equation A-27}$$

The Rayleigh number in Equation A-22 is

$$\text{Ra} = \frac{g\rho\beta q' K^{3/2}}{\mu\alpha_m k_m} = \frac{(9.81)(1000)(2.9 \times 10^{-4})(210)(10^{-18})^{1.5}}{(5 \times 10^{-4})(1.4 \times 10^{-7})(0.6)} = 1.4 \times 10^{-14} \quad \text{Equation A-28}$$

As given in Equation A-28 and for nominal values of the parameters, the Rayleigh number is much less than 1, and a regular expansion is therefore justified.

An expansion of ψ_* and T_* in a Taylor series for small Ra can be given by

$$T_* = T_{*0} + RaT_{*1} + (Ra)^2T_{*2} + \dots \quad \text{Equation A-29}$$

and

$$\psi_* = \psi_{*0} + Ra\psi_{*1} + (Ra)^2\psi_{*2} + \dots \quad \text{Equation A-30}$$

Using only the first two terms of Equation A-29 and Equation A-30, and substituting into Equations A-22 and Equation A-23 results in

$$\begin{aligned} r_* \frac{\partial^2(\psi_{*0} + Ra\psi_{*1})}{\partial r_*^2} + \frac{\partial(\psi_{*0} + Ra\psi_{*1})}{\partial r_*} + \frac{1}{r_*} \frac{\partial^2(\psi_{*0} + Ra\psi_{*1})}{\partial \theta^2} \\ = Ra \left(\sin(\theta) \frac{\partial(T_{*0} + RaT_{*1})}{\partial \theta} - r_* \cos(\theta) \frac{\partial(T_{*0} + RaT_{*1})}{\partial r_*} \right) \end{aligned} \quad \text{Equation A-31}$$

and

$$\begin{aligned} \frac{\partial(T_{*0} + RaT_{*1})}{\partial t_*} + \frac{1}{r_*} \left(\frac{\partial(\psi_{*0} + Ra\psi_{*1})}{\partial \theta} \frac{\partial(T_{*0} + RaT_{*1})}{\partial r_*} \right. \\ \left. - \frac{\partial(\psi_{*0} + Ra\psi_{*1})}{\partial r_*} \frac{\partial(T_{*0} + RaT_{*1})}{\partial \theta} \right) \\ = \frac{\partial^2(T_{*0} + RaT_{*1})}{\partial r_*^2} + \frac{1}{r_*} \frac{\partial(T_{*0} + RaT_{*1})}{\partial r_*} + \frac{1}{r_*^2} \frac{\partial^2(T_{*0} + RaT_{*1})}{\partial \theta^2} \end{aligned} \quad \text{Equation A-32}$$

Collecting terms of zeroth order in Ra in Equation A-31 and Equation A-32 results respectively in

$$r_* \frac{\partial^2\psi_{*0}}{\partial r_*^2} + \frac{\partial\psi_{*0}}{\partial r_*} + \frac{1}{r_*} \frac{\partial^2\psi_{*0}}{\partial \theta^2} = 0 \quad \text{Equation A-33}$$

$$\frac{\partial(T_{*0})}{\partial t_*} + \frac{1}{r_*} \left(\frac{\partial(\psi_{*0})}{\partial \theta} \frac{\partial(T_{*0})}{\partial r_*} - \frac{\partial(\psi_{*0})}{\partial r_*} \frac{\partial(T_{*0})}{\partial \theta} \right) = \frac{\partial^2(T_{*0})}{\partial r_*^2} + \frac{1}{r_*} \frac{\partial(T_{*0})}{\partial r_*} + \frac{1}{r_*^2} \frac{\partial^2(T_{*0})}{\partial \theta^2} \quad \text{Equation A-34}$$

Equation A-33 is a homogeneous equation with homogeneous conditions, thus $\psi_{*0} = 0$ and Equation A-34 simplifies to

$$\frac{\partial(T_{*0})}{\partial t_*} = \frac{\partial^2(T_{*0})}{\partial r_*^2} + \frac{1}{r_*} \frac{\partial(T_{*0})}{\partial r_*} + \frac{1}{r_*^2} \frac{\partial^2(T_{*0})}{\partial \theta^2} \quad \text{Equation A-35}$$

The solution to Equation A-35 is given in Carslaw and Jaeger (1976, p. 261) as

$$T_{*0} = \frac{q'}{4\pi} \int_0^t \frac{\exp\left[-\frac{r_*^2}{4(t_* - t')}\right]}{t_* - t'} dt' \quad \text{Equation A-36}$$

Let

$$u = \frac{r_*^2}{4(t_* - t')} \quad \text{Equation A-37}$$

then the solution can be expressed as

$$T_{*0} = \frac{(T - T_\infty)k_m}{q'} = \frac{1}{4\pi} \int_{\frac{r_*^2}{4t_*}}^{\infty} \frac{e^{-u}}{u} du = -\frac{1}{4\pi} \text{Ei}\left(-\frac{r_*^2}{4t_*}\right) = \frac{1}{4\pi} \text{E}_1\left(\frac{r_*^2}{4t_*}\right) \quad \text{Equation A-38}$$

where Ei is the exponential integral function given by

$$\text{Ei}(x) \equiv \int_x^{\infty} \frac{e^{-t}}{t} dt = \gamma + \ln(x) + \sum_{k=1}^{\infty} \frac{x^k}{k! k} \quad \text{Equation A-39}$$

The first order solutions given by Nield and Bejan (1999) are

$$\psi_{*1} = \frac{\sqrt{t_*} \cos(\theta)}{4\pi} \left[\frac{\exp(-\eta^2) - 1}{\eta} + \eta \text{Ei}(-\eta^2) \right] \quad \text{Equation A-40}$$

and

$$T_{*1} = \frac{\sqrt{\frac{t\alpha_m}{K\sigma}} \sin(\theta)}{16\pi^2} \left\{ \ln(\eta) [(\gamma - 2)\eta - \eta^3] + \eta \ln^2(\eta) + \eta \frac{2 - \gamma}{2} + \eta^3 \frac{3 - \gamma}{2} + \dots \right\} \quad \text{Equation A-41}$$

where

$$\gamma = \lim_{n \rightarrow \infty} \left\{ -\ln(n) + \sum_{k=1}^n \frac{1}{k} \right\} = 0.5772156649 \quad \text{Equation A-42}$$

and

$$\eta = \frac{r_*}{2\sqrt{t_*}} = \frac{r\sqrt{K\sigma}}{2\sqrt{Kt\alpha_m}} = \frac{r}{2} \sqrt{\frac{\sigma}{t\alpha_m}} \quad \text{Equation A-43}$$

The temperature above ambient is given by

$$(T - T_\infty) = \frac{q'(T_{*0} + \text{Ra}T_{*1})}{k_m} \quad \text{Equation A-44}$$

The expression in Equation A-44 is used to create the contour plots in Figure 3-32.